2017

Quantitative Understanding of Nanoparticle Flocculation in Water Treatment

Sungmin Youn
Marshall University, youns@marshall.edu

Recommended Citation

Youn, S. (2017). Quantitative understanding of nanoparticle flocculation in water treatment [dissertation]. Austin: University of Texas.

The Dissertation Committee for Sungmin Youn Certifies that this is the approved version of the following dissertation:

Quantitative Understanding of Nanoparticle Flocculation in Water Treatment

Committee:

Desmond F. Lawler, Supervisor

Lynn E. Katz

Howard M. Liljestrand

Navid Saleh

Kamy Sepehrnoori

Quantitative Understanding of Nanoparticle Flocculation
in Water Treatment

by

Sungmin Youn, B.S.; M.S.E

Dissertation

Presented to the Faculty of the Graduate School of

The University of Texas at Austin

in Partial Fulfillment

of the Requirements

for the Degree of

Doctor of Philosophy

The University of Texas at Austin

May 2017

Dedication

To Marie and Jina for their support and love

Acknowledgements

Sir Isaac Newton once wrote: "If I have seen further, it is by standing on the shoulders of giants." I would like to thank my advisor, Dr. Desmond F. Lawler, for letting me stand on his shoulders so I could see further and pursue my interests. Dr. Lawler, you have been one of the most influential people in my life. During the past six years, you have taught me how to become a better student, teacher, researcher, and engineer. Thank you for your mentorship and advising. I will make sure that I share your passion and devotion for environmental engineering education with the next generation of engineering students.

I would also like to express my sincere gratitude to my dissertation committee members, Drs. Howard Liljestrand, Lynn Katz, Navid Saleh, and Kamy Sepehrnoori for their guidance and suggestions regarding my research. I would not have been able to finish my dissertation without their help and support.

Furthermore, I have been fortunate to have a group of talented and supportive friends and colleagues here at the University of Texas at Austin. First, I would like to thank the Lawler research group. Ijung, Anne, Tongren, Farith, Catherine, Yasir, Stetson, Kyunghwa, Ki, Soyoon, and Sam, I sincerely thank you for companionship and the encouragement that you have given to me. Special thanks go to Anne who has spent many hours proofreading my dissertation and given me great ideas for improvements. In addition, I am grateful for departmental friendships with Joon, Kyungmin, SH, Seungnam, Jim, Justin, Dipesh, Jaime, Taegyu, Sedat, Nirupam, Aurore, Celina, Babak, Arash, Seungbum and Boonam. Your friendships enriched my life on campus for the last few years. I would also like to extend my appreciation to GETA communities supervised

by Pam. Through my GETA experiences, I was able to cultivate my teaching skills and broaden my horizons in undergraduate engineering education.

Lastly, I would like to acknowledge my family and their endless support and encouragement. Marie, without all the sacrifices that you have made, I would not be here today. Thank you for being a supportive and understanding wife and also a kind mom to Jina. Jina, thank you for bringing so much joy and happiness to my life. I really appreciate your cooperation during the last few months as I was finishing my dissertation and I really thank you (or maybe Marie) for letting me sleep through the nights. I would also like to thank my parents and parents-in-law for their love and prayers during my studies. Mom and Dad, thank you so much for believing in and supporting me from the day I decided to come to the States to study. I would also like thank my brother and brothers-in-laws, Kyungmin, Sam, and Charlie for their love and care.

Most importantly, I give thanks to God who guides me through my ups and downs. Through it all, through it all, my eyes are on You. Through it all, through it all, it is well.

Quantitative Understanding of Nanoparticle Flocculation in Water Treatment

Sungmin Youn, Ph.D.

The University of Texas at Austin, 2017

Supervisor: Desmond F. Lawler

Flocculation is critical in drinking water treatment; in flocculation, the particle size distribution changes from a large number of small particles to a small number of larger particles. Larger particles are effectively removed by settling and filtration processes that follow flocculation. In recent years, manufacturing of engineered nanoparticles has skyrocketed, and these nanoparticles can enter our water supplies, but knowledge of their fate in water treatment is limited. The objective of this research was to update knowledge of flocculation by extending previous work at the microscale to the nanoscale.

Flocculation involves transport of particles to the vicinity of one another and subsequent attachment if interactions at close distances are favorable. Transport and possible collisions are brought about by Brownian motion, differential sedimentation, and fluid shear; these processes, even at the nanoscale, are well understood. Whether collisions and attachment actually occur, however, depend on a balance of hydrodynamic interactions, van der Waals attraction, and electrostatic repulsion; this research quantitatively assessed, for the first time, this balance for collisions of nanoparticles by all three collision mechanisms using a well-established trajectory analysis approach. The collision efficiency (α) is the ratio of the number of successful collisions (attachment) to

the number of collisions predicted by the transport equations. The analysis was performed with and without electrostatic repulsion, which occurs if particles are charged.

In all cases, Brownian motion was the dominant flocculation mechanism. However, without electrostatic repulsion, differential sedimentation and fluid shear were found to be far more important than heretofore expected because the α value can be substantially higher than one, contrary to all previous understanding. With electrostatic repulsion, collisions by these two mechanisms were found to occur only if the particles are substantially different in size.

Experiments in which the changes in particle size distributions of nanoparticles were carefully monitored were also performed, and the results compared to the mathematical predictions. Although not perfect, excellent agreement between the measured and predicted particle size distributions was found. The conclusion is optimistic: if nanoparticles are properly destabilized to reduce or eliminate surface charge, they will be well removed in conventional water treatment plants.

Table of Contents

List of Tables

List of Figures

xvi

Chapter 1: Introduction

The objective of this research is to improve the quantitative understanding of the dynamics of particle size distributions at the nanoscale in conventional water treatment flocculation processes. Previous research has demonstrated that flocculation at the microscale (> 1 μm) can be explained quantitatively. In this research, particle destabilization and size growth at the nanoscale were studied both theoretically and experimentally. Numerical particle number balance equations and trajectory analysis were employed. Mathematical predictions were compared to experimental results obtained from well controlled laboratory scale flocculation. Improved understanding of particle flocculation at the nanoscale will enhance the design and operation of subsequent particle separation processes in conventional water treatment systems. Therefore, not only would the life-cycle pathways of nanoparticles in water treatment be addressed, but the overall quality of treated water would also be improved.

1.1 BACKGROUND

The current agreement on the definition of nanoparticles is natural, incidental, and manufactured materials that have external dimensions between 1 nm and 100 nm and show different properties from their bulk materials (Foss Hansen *et al.*, 2007). The dramatic rise in the use of engineered nanoparticles means that nanoparticles are being discharged into natural water bodies; therefore, life-cycle pathways of nanoparticles in drinking water treatment must be considered (Wiesner *et al.*, 2006).

The present research addresses a critical question for conventional water treatment: can we effectively remove a high percentage of particles in treatment processes, even if the particles are very small? The literature suggests confusion about the effectiveness of conventional particle removal processes on engineered nanoparticles:

some scholars reported that conventional particle separation techniques are adequate (O'Brien and Cummins, 2010), while others disagree (Chalew *et al.*, 2013; Limbach *et al.*, 2008; Reijnders, 2006; Wiesner *et al.*, 2006; Zhang *et al.*, 2008). The present research addresses this question by examining, theoretically and experimentally, changes in (absolute) particle size distributions (number concentrations as a function of particle size) of particles at the nanoscale during laboratory scale flocculation.

Water treatment processes, mainly due to flocculation, remove conventional particles from water, including inorganic particles, viruses, and bacteria. The ultimate removal of these contaminants actually occurs in subsequent particle removal processes (gravitational separation, granular media filtration, and/or membranes), all of which depend on the particle size distribution. Hence, the effluent particle size distribution of the flocculation process, which is the influent to these particle removal processes, is of paramount importance. Because the size of particles determines their settling velocity, surface area, and diffusion coefficient, the ability to predict the particle size distribution is critical in water and wastewater treatment (Benjamin and Lawler, 2013).

Most particles in water are generally stable, and engineered nanoparticles often are coated with stabilizing agents to promote particle stability. Stable particles do not aggregate or attach to other surfaces (and are, therefore, not removed well in water treatment). To overcome the particle stability, destabilizing agents (*e.g.*, alum or iron) are often used in water treatment. Destabilization is essential to successful flocculation and particle removal. Flocculation of particles in water is understood as a two-step process (O'Melia and Stumm, 1967; Stumm and O'Melia, 1968). A particle first travels to the vicinity of another particle through long-range transport and then the particle collides with the other particle through short-range transport to form aggregates and flocs. The long-range transport processes are caused by three predominant mechanisms: Brownian

motion, fluid shear, and differential sedimentation. The collision frequency functions (β) that mathematically describe long-range transport processes of two equal- or unequal-sized spherical particles can be analytically calculated (O'Melia, 1978; Elimelech *et al.*, 1998). However, the collision efficiency (α) that accounts for short-range transport processes of two spherical particles requires numerical analysis due to the complexity of hydrodynamic and interparticle interaction energy (Benjamin and Lawler, 2013).

Lawler and co-workers (Lawler *et al.*, 1980; Lawler and Wilkes, 1984) developed a mathematical model for the evolution of size distributions based on Smoluchowski's (1917) particle number balance with the collision frequency functions (β). Later, Han and Lawler (1991, 1992) summarized previously reported theoretical hydrodynamic interactions for Brownian motion and fluid shear and performed trajectory analysis for the differential sedimentation transport mechanism to generalize α when the larger particle in the two-particle collision was one micrometer or larger. Since then, the α values developed by Han and Lawler have been used to describe short-range transport mechanisms in flocculation processes in conventional water treatment, and the predictions made were in close agreement with experimental results when the destabilization did not involve precipitation (Li, 1996; Lawler and Nason, 2005; Nason, 2006).

1.2 PROBLEM STATEMENT

Despite the previous success, a few limitations need to be addressed. First, the existing α values were calculated only for the conditions where the larger particle in the collision was one micrometer or greater. Because the use and production of engineered nanoparticles are dramatically increasing, life-cycle pathways of nanoparticles in water and wastewater treatment need to be addressed (Wiesner *et al.*, 2006). The collision

efficiency functions (α_{Br}, α_{Sh}, and α_{Ds}) that account for hydrodynamic and interparticle interaction energy for nanoparticles have not been calculated, and some of the short-range transport processes, in particular, might be significantly different for such small particles. To better understand the fate and transport of nanoparticles in water treatment, α values for these small particles need to be calculated.

Secondly, the current α values were calculated under the assumption that the EDL interactions between colliding particles in flocculation would be negligible if particles are well-destabilized by adsorption and charge neutralization. For this reason, the existing α values did not include the EDL interactions in their numerical calculations. In practice, however, perfect neutralization is not always achieved and particles are left with a smaller, but not zero, surface charge. In addition, particle destabilization can also be achieved by compression of the diffuse layer or enmeshment in a precipitate, and in these cases, the surface charge is not negligible. The EDL repulsive interactions must be incorporated into the derivation of α for comprehensive understanding of particle destabilization.

Lastly, the existing collision efficiency functions for fluid shear (α_{Sh}) need to be verified. The existing α_{Sh} was obtained by interpolation and extrapolation of Adler's global capture efficiency values (1981a). Adler's initial trajectory analysis was performed under narrow computational conditions (that had four particle size ratios, $\lambda = 0.1$, 0.2, 0.5, and 1, where λ is the size ratio of the smaller to larger particle in the two-particle collision). Han (1989) extrapolated and interpolated to generate the collision efficiency functions for λ values from near zero to 1. To generate α_{Sh} that is more accurate over a broad size range of spherical particles and particle ratios, Adler's trajectory analysis must be performed under a much greater number of computational conditions.

4

1.3 SIGNIFICANCE

The improved ability to predict particle size distributions precisely at the nanoscale during flocculation will advance our knowledge of particle destabilization and particle removal efficiency in conventional water treatment. The comprehensive understanding of flocculation will enhance the design and operation of conventional particle separation processes in water treatment. The optimized drinking water treatment could possibly promote the cost reduction of treatment while resulting in a better quality of drinking water. In addition, life-cycle pathways of nanoparticles in drinking water treatment would also be addressed.

1.4 OBJECTIVES

The present work sought to improve quantitative understanding of how the particle size changes during flocculation at the nanoscale. The scope of the research was refined to focus on flocculation of nano-sized particles. The objectives of this research were to:

1) compute numerical models (trajectory analyses and particle number balances) to be able to predict the evolution of the particle size distributions at the nanoscale;

2) experimentally measure and quantify the change in absolute particle size distributions during flocculation at the nanoscale under various experimental conditions; and

3) compare experimental results with predictions made from the numerical models

1.5 APPROACH

In the present research, both mathematical modeling and experimental investigation were used to accomplish the objectives stated above. This research methodology has been practiced in the Lawler research group. Prior to the present research, Lawler and Wilkes (1984), Han and Lawler (1992), Li (1996), and Nason

(2006) had given many iterations to minimize the deficiency between theoretical modeling and experimental results. The previous mathematical modeling was done in various programming languages including PL/I, Fortran 77, C and C++. To improve outdated models, both trajectory analysis and numerical particle number balance equations were re-written in MATLAB in this research. Laboratory scale experiments were performed with several independent variables that were systematically controlled. Particle size distributions were measured using a NanoSight instrument. Iterative comparisons between the mathematical predictions and experimental data manifested which areas were well captured by the theoretical models, and which areas require further experiments or modifications to the model.

The dissertation is organized as follows. Chapter 2 explains general background information of particle destabilization, flocculation, and mathematical theories behind flocculation modeling. Chapter 3 contains the experimental methods and design, while the experimental results are presented in Chapter 4. The detailed methods used in mathematical modeling are described in Chapter 5; the predictions of the mathematical model are discussed by comparison to experimental results in Chapter 6. Finally, conclusions and suggestions for future research are deliberated in Chapter 7.

Chapter 2: Literature Review

This literature review provides an overview of flocculation processes, an introduction to particle stability and DLVO theory, and a comprehensive review of previously developed mathematical flocculation models. As summarized in Chapter 1, the objective of the present research is to improve the quantitative understanding of how the size distribution of nanoparticles change in laboratory-scale batch flocculation experiments. To quantitatively explain flocculation at the nanoscale, particle stability, particle destabilization, and particle transport mechanisms are first elucidated.

2.1 FLOCCULATION

Flocculation is a physical treatment process that follows coagulation (particle destabilization). During flocculation, granted enough detention time and gentle mixing, the destabilized particles are encouraged to collide and attach to one another. Due to these collisions and subsequent attachment, the particle size distribution changes from a large number of smaller particles to a smaller number of large particles (*i.e.*, flocs). Because the effectiveness of the downstream particle separation processes such as sedimentation or filtration depends on the particle size distribution, flocculation is one of the most critical processes in water treatment systems.

Flocculation is also known as an integral part of precipitation processes in water and wastewater treatment. For example, along with crystallization, the growth of calcium carbonate ($CaCO_3$) solids in precipitative softening is also explained by flocculation (Nason, 2006). In the present research, precipitation is not considered in the mathematical formulations of flocculation; solid formation is assumed to be completed prior to flocculation.

Mathematical flocculation models employ a differential equation that simulates the rate of changes in a particle number distribution due to particle collisions with respect to time. The existing mathematical models have only been validated for micro-sized particle suspension. Recent advances in computing and analytical technology make it possible to obtain real-time particle size distributions at the nanoscale (Lawler *et al.*, 2015).

2.1.1 Particle Size Distributions

Generally, with very few exceptions, natural water and wastewater contain various sizes of particles. Knowing the distribution of particle sizes in a water source sheds insight into what technologies or processes need to be considered when treating the suspension. By comparing the particle size distributions before and after particle treatment, the treatment effectiveness can be evaluated (Hendricks, 2006). Tiehm *et al.* showed that the removal of chemical oxygen demand (COD) and phosphorus during wastewater treatment is closely related to particle size distributions of suspended solids. Particle size distributions need to be considered to optimize the operation of sedimentation tanks or designing deep bed filtration units (Tiehm *et al.*, 1999). Comprehensive understanding of the particle size distribution is required for membrane processes to optimize and control the membrane fouling (Stoller, 2009). Particle size distributions have a significant impact on the performance of stormwater treatment as well (Hettler *et al.*, 2010).

The particle size distribution function is generated through graphically characterized particle size information or a mathematical model that fits experimentally measured data. The abscissa in a particle size distribution graph can be reported in terms of particle's length, surface (or cross-sectional) area, or volume. The ordinate can be

measured by number, area, or volume. Cumulative, differential, logarithmic, or normalized manners are all accepted ways to plot particle size distribution functions. Although particle size distribution functions in terms of the particle volume have been more commonly used for flocculated suspensions, a number distribution function is employed throughout this study as the primary means of describing the particle size distribution. The number distribution function is different in that it presents the normalized number concentration of particles (*i.e.*, $(\#/mL)/\Delta\log d_p$) as a function of the discretized particle sizes ($\Delta\log d_p$) that is in equal increments on a logarithmic scale. The equal logarithmic increments of particle size capture the effects of different particle treatment processes better than arithmetic increments in particle sizes (Benjamin and Lawler, 2013).

2.1.2 Particle Stability and Destabilization Mechanisms

In general, particles in water are stable due to their electrical surface charges. The electrical surface charges originate in several different manners as detailed by Stumm and Morgan (1996). Regardless of the origin of surface charge, a charged surface will attract and form two surrounding layers of the counterions. The first inner layer is known as stern layer (or Helmholtz layer) where the counterions are temporarily bound to the charged surface. The second outer layer is called the diffuse layer. Here counterions are free in motion but still under the influence of the charged surface (Israelachvili, 2011). The electrical double layer (EDL) refers to these two layers of counterions surrounding the charged surface. In the presence of the EDL, the same sign of charged particles repel and change their trajectories to go around each other, thus creating stable suspensions of particles.

9

Along with the electrical repulsion between charged particles, an attractive interaction, called London-van der Waals (vdW) attraction, also exists. vdW attraction stems from constant oscillations of the electromagnetic fields due to electric dipoles (Elimelech, 1998). vdW attraction is stronger than the EDL repulsion at sufficiently short separation distances. If two approaching particles have enough momentum to overcome the repulsive interaction and obtain a short separation distance where attractive interaction is dominant, then the particles can attach to one another.

Overcoming the EDL repulsion is very rare for most particles in natural water or wastewater; therefore, particle collisions and attachment are prevented. For this reason, particles in water must be destabilized prior to flocculation to foster particle collisions and attachment. Particles can be destabilized by four destabilizing mechanisms (O'Melia, 1978): (a) compression of the double layer, (b) adsorption and charge neutralization, (c) enmeshment in a precipitate, and (d) adsorption and interparticle bridging.

The first destabilizing mechanism, the compression of the double layer, is achieved by increasing the ionic strength of the background solution. Because of increased ionic strength, more counterions are available near the charged surface to form the diffuse layer. Therefore, the thickness that the double layer extends is reduced with increased ionic strength. The reduction in the thickness of the double layer lowers the effect of the EDL repulsion between particles of the same sign charge. Compared to other destabilizing mechanisms, compression of the double layer is mathematically better understood because the ionic strength is a function of molar concentrations and the valency of the dissolved ions. By either increasing or decreasing these parameters, particle stability can be controlled. Hence, double layer compression is a popular destabilizing mechanism in research settings although it is not practical in full-scale engineered systems.

Particular chemical interactions between the particle surfaces and dissolved ions often result in destabilization. Surface charges can be neutralized by the adsorption of oppositely charged ions onto the surface. The adsorption of positively charged hydrated metal species (*e.g.*, aluminum or iron) onto negatively charged particles demonstrate the mechanism of adsorption and charge neutralization. Because the surface charge is neutralized by adsorption of opposite charged ions, the EDL repulsion is effectively minimized or eliminated. However, a reversal of the surface charge can also occur if the neutralizing ions are overdosed. The excessive adsorption of oppositely charged ions overturns the sign of charged surfaces rather neutralizing.

The third destabilizing mechanism occurs when a destabilizing chemical (a metal) is dosed in the solution in such quantity that precipitation takes place. In precipitation, precursors start forming to achieve a thermodynamically more stable state by minimizing the total surface area of the particles in solutions (Voorhees, 1985). The precursors of precipitates first adsorb onto the existing particles rather than form new nuclei. Then, the precursors grow and form insoluble precipitates (usually metal hydroxides) while the existing particles are trapped inside. Because the existing particles work as nucleation sites, the rate of precipitation is correlated to the number of the initial existing particles. If there are some particles left that have not been used as nucleation sites, those particles will be "swept" out by fluffy hydroxide precipitates as they settle. Common examples of enmeshment in a precipitate are aluminum hydroxide, ferric hydroxide, or calcium carbonate.

The last destabilizing mechanism is adsorption and interparticle bridging. This mechanism utilizes long-chain polymer molecules, which possess chemical groups that can reach out to the particle surfaces, as destabilizing agents. When the destabilizing polymers adsorb at the surfaces, the remainder of the polymer extends out searching for

other particles for adsorption. Therefore, the long-chain polymer serves as a bridge between particles. However, this mechanism is rarely used in low particle concentrations because polymers cannot easily find other particles to bind. In this scenario, polymers often start bending around to adsorb onto the same particle surface.

2.2 DLVO THEORY

DLVO stands for the first letters of four names of the scientists who contributed to the theory: Derjaguin and Landau (1941), and Verwey and Overbeek (1948). DLVO theory assesses particle stability by quantifying the total potential energy between two interacting plates, particles, a particle-plate combination, or other shapes. The total potential energy is assumed to be the sum of attractive and repulsive energies induced by the vdW and the EDL interactions, respectively.

There are two approaches to vdW computation. Hamaker (1937) first derived the mathematical expression for attractive energy using a pairwise summation of all the intermolecular energies between the two interacting objects and the medium. Lifshitz (1956) later rectified oversights from Hamker's assumption of simple pairwise addition by incorporating the effect of polarization of atoms (Israelachvili, 2011). However, the Hamaker approach is still commonly used in spite of its shortcoming due to its simplicity with negligible margins of error (Gregory, 1981). In calculation of the vdW energy, the retardation effect must be accounted for (Casimir and Polder, 1948). The retardation effect arises from a time lag of the oscillations of electric fields between interacting dipoles and it becomes significant when the separation distance between the pair of dipoles is greater than 0.1 nm (Anandarajah and Chen, 1995).

Gregory (1981) simplified the complex mathematical expression for the vdW energy that was initially proposed by Clayfield *et al.* (1971) which employed the

12

Hamaker approach and the retardation effect. Throughout the present research, Gregory's simplified vdW energy expression as shown in Equation (2.1) is used:

$$V_a = -\frac{A_H a_1 a_2}{6(a_1 + a_2)d}\left[1 - \frac{bd}{\lambda}\ln\left(1 + \frac{\lambda}{bd}\right)\right] \tag{2.1}$$

where, A_H is the Hamaker constant; a_1 and a_2 are the radii of the two interacting particles; d is the separation distance between their nearest edge particles; λ is the characteristic wavelength (0.1 nm); and b is a constant (b = 5.32) proposed by Gregory to fit exact values.

The computation of the EDL repulsive energy is more complicated. Owing to the nature of electric field interactions, the boundary conditions of the overlapping electromagnetic fields of two approach particles must be specified. The two extreme boundary conditions, which are most widely used, are constant surface potential and constant surface charge. These assumptions provide two different physiochemical views of the relevant surface phenomena upon approach. The constant potential boundary condition assumes that the surface potentials of interacting particles remain constant during the course of interaction (Derjaguin and Landau, 1941; Verwey and Overbeek, 1948; Hogg *et al.*, 1966; Gregory, 1975), whereas the constant charge boundary condition presumes that the surface charge density is maintained constant (Verwey and Overbeek, 1948; Frens and Overbeek, 1972; Usui, 1973; Gregory, 1973). Calculated EDL energies using these two assumptions can be dramatically different from each other, especially at short separation distances. It is generally considered that the constant potential and constant charge models give the lower and upper limits, respectively, of the possible EDL interaction energy.

Once the boundary condition is set, an exact EDL repulsive energy between two approaching particles can be calculated by solving the Poisson-Botlzmann equation. Because the Poisson-Botlzmann equation is a nonlinear second-order differential equation, it requires numerical analysis to find exact solutions to it. To avoid computational complication, a few different approximation methods have been derived by linearization of the exponential function of the Poisson-Botlzmann equation (Gregory, 1975). These approximation methods are sufficient for most relevant environmentally engineered systems; hence, they are frequently employed for routine use despite their shortcomings (Mikelonis *et al.*, 2016).

It takes a few seconds for the disturbed double layers to establish the equilibrium whereas particle collisions through Brownian motion take place approximately in a hundred nanoseconds (Frens and Overbeek, 1972). It is reasonable to assume that the surface charge remains constant during the nanoparticle collision where Brownian motion is the predominant transport mechanism and the surface potential does not maintain its equilibrium. In the present research, the linearized Poisson-Botlzmann approximation was used with the constant charge boundary assumption as following (Gregory, 1975):

$$V_r = \frac{a_1 a_2}{a_1 + a_2} \frac{2\pi n k_B T}{\kappa^2} (y_1{}^2 + y_2{}^2) \left[\frac{2y_1 y_2}{y_1{}^2 + y_2{}^2} \ln\left(\frac{1 + \exp(-\kappa d)}{1 - \exp(-\kappa d)}\right) - \ln\left(1 - \exp(-2\kappa d)\right) \right] \quad (2.2)$$

where, a_1 and a_2 are the radii of the two interacting particles, n is the number concentration of ions, k_B is Boltzmann's constant, T is the temperature in Kelvin, κ is the Debye-Huckel parameter ($\kappa^2 = 2e^2 n z^2 / \varepsilon k_B T$), e is the electron charge, z is the valency of the electrolyte, ε is the permittivity of the medium, y_1 and y_2 are the dimensionless normalized surface potentials (*e.g.*, $y_1 = ze\psi_1 / k_B T$) from the surface potentials (ψ_1 and ψ_2), and d is the separation distance.

Figure 2.1 shows an example of interaction energy between two equal-sized particles, calculated using Equations (2.1) and (2.2). For the calculation, zeta potentials of -25.7 mV, Hamaker constant of 10E-20 J, the ionic strength of 1 mM, temperature of 297 K and the particle diameter of 100 nm were assumed. By convention, the negative interaction energy indicates attractive interaction between the two particles, and the positive energy associates the repulsive interaction. The total interaction energy is the summation of the vdW and EDL energy terms. When the separation distance between the two particles is substantial, the interparticle interaction is inconsequential. As the particles draw near each other, both attractive and repulsive interactions become more notable; however, the repulsive energy outbalances the attractive energy. The maximum positive net energy occurs at a separation of ~3 nm; this maximum energy of interaction is known as the energy barrier. At a very small separation distance beyond the energy barrier where it is called the primary minimum of interaction energy, the attractive energy exceeds the repulsive one; hence, the particles are strongly attracted to each other. A floc will be formed from the two particles only if the momentums of the two approaching particles are sufficient to overcome the barrier.
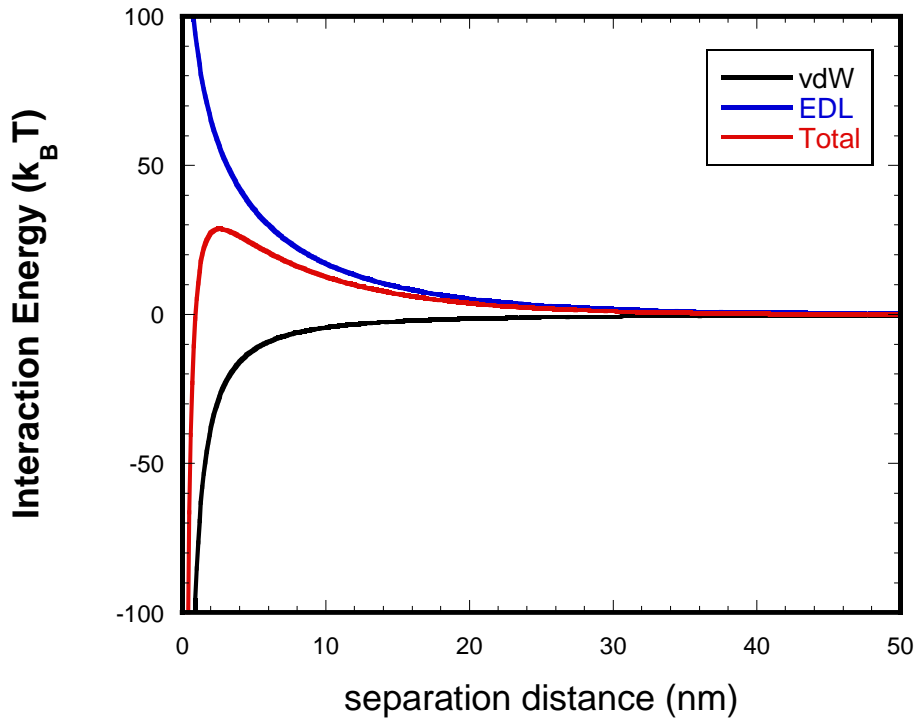
Figure 2.1 Typical interaction energy curves

In addition to the vdW and EDL interactions discussed in DVLO theory, several scholars have suggested other interactions that could affect particle stability in relevant water conditions. These interactions include acid-base interactions (Grasso *et al.*, 2000), magnetic (Considine *et al.*, 1998), hydration (Yotsumoto and Yoon, 1993), hydrophobic (Christenson, 1988; Song *et al.*, 2011), and steric interactions (Lin and Wiesner, 2012). The experimental conditions of the present work were carefully chosen where these non-DLVO interactions were insignificant; therefore, the present work focuses on classical DLVO theory.

2.3 MODELING FLOCCULATION

Flocculation processes are generally explained by Smoluchowski's number balance equation (1917). With a few assumptions and simplifications, Smoluchowski was

the first to derive a mathematical description for flocculation. The assumptions included that (1) flocculation happens from every particle-particle collision; (2) resulting flocs do not break; (3) particles are spherical before and after flocculation and volume is conserved (coalescence assumption); and (4) all collisions are binary (two-particle collisions only). In Smoluchowski's number balance, the number concentration of a particular size particle (k, for example) is defined as the sum of the gain and the loss of k-sized particles (*i.e.*, k-sized particles are created by collision of two smaller particles, and k-sized particles are lost by collision of k-sized particles with any particles). This number balance can be written in words:

Accumulation		*Gain*		*Loss*
Rate of change with time of the number concentration of particles of size k	=	*Rate of creation of particles of size k by flocculation of smaller particles (the sum of whose volumes is size k)*	-	*Rate of loss of particles of size k by flocculation of size k particles with any size particles*

A discretized number concentration balance equation was then derived by Smoluchowski as follows:

$$r_k^{Smoluchowski} = \frac{dn_k}{dt} = \frac{1}{2}\sum_{\substack{all\ i\ and\ j \\ Vi+Vj=Vk}} \beta_{ij}n_in_j - n_k\sum_{all\ i}\beta_{ik}n_i \qquad (2.3)$$

where i, j and k are size classes of particles; n_i is the number concentration of i-sized particles (L^{-3}); V_i is the volume of a size i particle (L^3); and β_{ij} is the collision frequency function for particles of size i and j (L^3/T). The collision frequency function (β_{ij}), which is also known as the aggregation kernel, quantifies physical transport mechanisms of the two colliding particles at long-range. Due to the assumption of an adequate separation distance between the two colliding particles, the collision frequency function does not

consider the movement of water (or fluids) between the two colliding particles (no hydrodynamic effects included).

As mentioned in Chapter 1, the three particle transport mechanisms play important roles in flocculation. Mathematical expressions for Brownian motion and fluid shear were developed by Smoluchowski (1917). Camp and Stein (1943) revised Smoluchowski's fluid shear and derived an equation describing the mechanism of differential sedimentation. Detailed expressions for the collision efficiency function of each transport mechanism are tabulated in Table 2.1.

Table 2.1 Collision frequency functions for three transport mechanisms

Transport	Collision frequency function, β_{ij}	
Brownian motion	$\beta_{ij}^{Br} = \dfrac{2k_B T}{3\mu}\left(\dfrac{1}{d_i} + \dfrac{1}{d_j}\right)(d_i + d_j)$	(2.4)
Fluid shear	$\beta_{ij}^{Sh} = \dfrac{1}{6}G(d_i + d_j)^3$	(2.5)
Differential sedimentation	$\beta_{ij}^{Ds} = \dfrac{\pi g}{72\mu}(\rho_p - \rho_L)(d_i + d_i)^3\lvert d_i - d_j\rvert$	(2.6)

These expressions give collision frequency functions in a unit of volume per time where k_B is Boltzmann's constant; T is temperature in Kelvin; μ is the viscosity of water; d_i and d_j are the diameters of i and j-sized particles; G is the mixing intensity or the velocity gradient; g is standard gravitational acceleration; and ρ_p and ρ_L are the densities of particles and water.

2.3.1 Long-Range Force Model

Because the three principal transport mechanisms are assumed to be independent, the total long-range transport mechanism is the sum of those three collision frequencies (Han, 1989). Lawler and Wilkes (1984) introduced an empirical factor (α_{emp}) into

18

Smoluchowski's number balance to adjust mathematical predictions to fit the experimental data better as shown below:

$$r_k^{Long-range} = \frac{dn_k}{dt} = \frac{1}{2}\alpha_{emp}\sum_{\substack{all\ i\ and\ j \\ Vi+Vj=Vk}}\beta_{ij}^{tot}n_in_j - \alpha_{emp}n_k\sum_{all\ i}\beta_{ij}^{tot}n_i \qquad (2.7)$$

The variables represent the same parameters that are previously defined in Equation (2.3). This equation is referred as the long-range force model herein. The empirical factor (α_{emp}) incorporates observational/measurement errors or physiochemical phenomena that were not accounted for in mathematical modeling. The long-range force model was tested against the collected data from both laboratory-scale experiments and a conventional softening plant (Lawler and Wilkes, 1984; Li, 1996). The predictions made from the long-range force model constantly overestimated flocculation between large and small particles although the model produced good estimations in the intermediate particle size ranges.

2.3.2 Short-Range Force Model

To address the overestimation of flocculation between large and small particles in the long-rage force model, Han and Lawler (1992) introduced the collision efficiency function (α_{ij}) that introduces particle transport at short-range, which had been previously missing, into the mathematical model. Because of the short separation distance assumption, the collision efficiency function took interparticle interactions into account in flocculation modeling. To consider interparticle interaction such as hydrodynamic and the vdW energy at short-range, Han and Lawler executed numerical trajectory analysis. However, the EDL repulsive energy between the particles was not included in Han and Lawler's trajectory analysis for two reasons. First, particles are often destabilized in flocculation which implies that the EDL energy would be very small and negligible.

19

Secondly, the EDL interaction is determined by particle properties and electrolyte conditions and incorporating all these factors would have been burdensome in numerical computation at the time of study. Rather, the EDL interactions between the particles were accounted for by the empirical collision efficiency factor (α_{emp}). The long-range force model with the collision efficiency functions is called the short-range force model and is written as follows:

$$r_k^{Short-range} = \frac{dn_k}{dt} = \frac{1}{2}\alpha_{emp}\sum_{\substack{all\ i\ and\ j \\ Vi+Vj=Vk}}\gamma_{ij}^{tot}n_in_j - \alpha_{emp}n_k\sum_{all\ i}\gamma_{ij}^{tot}n_i \qquad (2.8)$$

$$\gamma_{ij}^{tot} = \alpha_{ij}^{Br}\beta_{ij}^{Br} + \alpha_{ij}^{Sh}\beta_{ij}^{Sh} + \alpha_{ij}^{Ds}\beta_{ij}^{Ds}$$

The short- and long-range force models were examined in laboratory-scale experiments including both flocculation by Li (1996) and precipitative flocculation by Nason (2006). The short-range force model was able to yield better predictions to the experimental data than the long-range force model. In spite of the success of the short-range force model, both short- and long-range force models have not been tested on the flocculation of nanoparticles.

2.3.3 Alternative Models

Alternate mathematical models have been suggested by a number of scholars to enhance mathematical predictions of flocculation by improving the underlying assumptions proposed by Smoluchowski. The fractal dimension was incorporated into the mathematical modeling by Lee *et al.* (2000, 2002) and Thill *et al.* (2001). They argued that the assumption of coalescence flocs differs from the true nature of porous flocs and developed mathematical models that consider the fractal nature of flocs. Some other scholars have focused on floc breakup, and explained that the discrepancy between model predictions and experimental flocculation results arise from the presumption of

20

everlasting flocs without considering breakup of flocs. Particle size distributions were better predicted when a breakup term was included in the flocculation model (Kramer and Clark, 1999; 2000). Unfortunately, none of these models account for nanoparticle flocculation. The main focus of the present research is to verify the original flocculation model with Smoluchowski's assumptions to laboratory-scale experimental results. However, it is possible that the effects of the fractal nature and breakup of flocs will need to be addressed in future work.

2.4 NUMERICAL COMPUTATION AND TRAJECTORY ANALYSIS

As it was mentioned in Chapter 1, the collision frequency functions (β) that mathematically describe long-range transport mechanisms of two equal- or unequal-sized spherical particles can be analytically calculated. However, due to the complexity of hydrodynamic and interparticle interactions, calculating the collision efficiency functions (α) that account for transport mechanisms of two spherical particles at short range require numerical analysis (Benjamin and Lawler, 2013). To accurately quantify particle transport mechanisms in flocculation, both α and β have to be calculated.

2.4.1 Brownian Motion

By definition, stability (W) is the ratio of the aggregation rate in the absence of repulsive interactions between particles to the aggregation rate in the presence of repulsive interactions (Stumm and Morgan, 1996). Smoluchowski's diffusion equation (1917) gives the solution to the aggregation rates in the absence of repulsive interactions, and Fuchs' diffusion equation (1934) provides the solution to the aggregation rate in the presence of repulsive interactions. Spielman (1970) derived the stability ratio (W) considering repulsive interactions including the hydrodynamic and the EDL energy between two particles as follows:

$$W = \left(1 + \frac{a_2}{a_1}\right) \int_2^\infty \frac{D_{12}^\infty}{D_{12}} \frac{\exp\left(\frac{V_T}{k_B T}\right)}{s^2} ds = \frac{1}{\alpha_{Br}} \tag{2.9}$$

where a_1 and a_2 are the radii of two colliding particles (a_1 is always bigger than a_2 by convention), D_{12} is the relative diffusion coefficient, D_{12}^∞ is the diffusion coefficient at infinite separation, V_T is the total interparticle potential energy (*i.e.*, the sum of DLVO energies), k is the Boltzmann constant, and T is temperature in Kelvin. The collision efficiency functions (α_{Br}) for Brownian motion is the reciprocal of the stability ratio (Stumm and Morgan, 1996). Han (1989) solved the hydrodynamic portion of the equation (*i.e.*, D_{12}^∞/D_{12}) using Jeffrey and Onishi's resistance and mobility tensor solutions (1984), and then numerically solved the integral to acquire the collision efficiency functions from the stability ratio (Han *et al.*, 1997). In this research, Han's method was utilized and Equation 2.9 was solved numerically using ordinary differential equation (ODE) solvers in MATLAB. The default value of MATLAB for absolute error tolerance was used in this integration; therefore, the upper bound is chosen large enough that the error becomes less than 1E-10.

2.4.2 Differential Sedimentation

Han and Lawler (1991) summarized theoretical calculations of hydrodynamic effects made by other scholars and performed trajectory analysis to calculate the collision efficiency function during differential sedimentation. Han and Lawler used Batchelor's equation (1982) to convert Jeffrey and Onishi's resistance and mobility tensor solutions (1984) to velocities of two settling particles. The mathematical derivations in the present work closely follow Han and Lawler's paper (1991). The relative trajectory of the smaller particle with respect to the larger particle is depicted in a polar coordinate system shown in Figure 2.2.
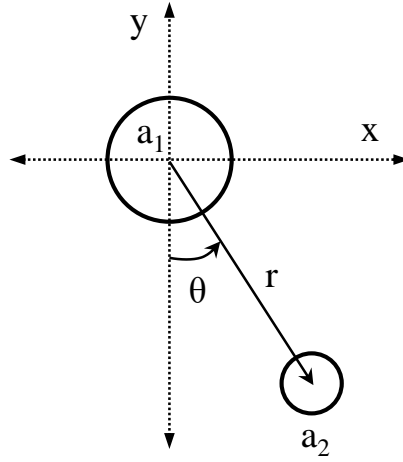
Figure 2.2 Schematic drawing of two settling particles in polar coordinates

From the Lagrangian point of view, the origin of the polar coordinate is at the center of the larger particle (a_1). The angle between the two particles is θ, and the center-to-center distance between the particles is r. Han and Lawler derived a first order differential equation that gives the distance between the two settling particles as a function of the angle between the particles as given below:

$$\frac{dr}{d\theta} = r\frac{[-\cos\theta L(s,\lambda)U_{12} - D_{12}G(s,\lambda)F(s,\lambda)]}{\sin\theta M(s,\lambda)U_{12}} \tag{2.10}$$

where s is the dimensionless separation distance that is normalized by the average size of two particle radii (*i.e.*, s=r/((a_1+a_2)/2)), λ is the ratio of the two particle sizes (a_2 to a_1), $L(s, \lambda)$ and $M(s, \lambda)$ are the hydrodynamic correction terms to a particle's settling velocity, $G(s, \lambda)$ represents the hydrodynamic correction term to the diffusivity coefficient, U_{s12} is differential settling velocity, and $\nabla\Phi_{12}$ represents the gradient of the total interparticle potential energy (*i.e.*, the sum of DLVO energy). Solving the above equation, the distance and the angle of the smaller particle is determined with respect to the larger particle at the

origin. Details of mathematical derivations and computational conditions are provided by Han (1989) and Han and Lawler (1991). In this research, this first order nonlinear differential equation was solved numerically using ODE Solvers in MATLAB.

In trajectory analysis, open trajectories are defined as instances where particles miss each other, and closed trajectories are defined as instances where particle collisions occur during the course of their interaction (*i.e.*, the dimensionless separation distance between the two particles, s, is equal to 1). A critical cross-sectional area is defined for particular particles as the verge of a possible closed trajectory. Figure 2.3 illustrates hypothetical trajectories in differential sedimentation. In the absence of interparticle interactions (Figure 2.3 A), the radius of the critical cross-section is the sum of a_1 and a_2. However, the critical cross-sectional area is reduced in the presence of interparticle interactions (Figure 2.3 B) due to the repulsive effects from hydrodynamics, and the EDL interaction. The collision efficiency function (α_{Ds}) is equal to the ratio of the critical cross-sectional area in the presence of interparticle interactions to the critical cross-sectional area in the absence of those interparticle interactions.
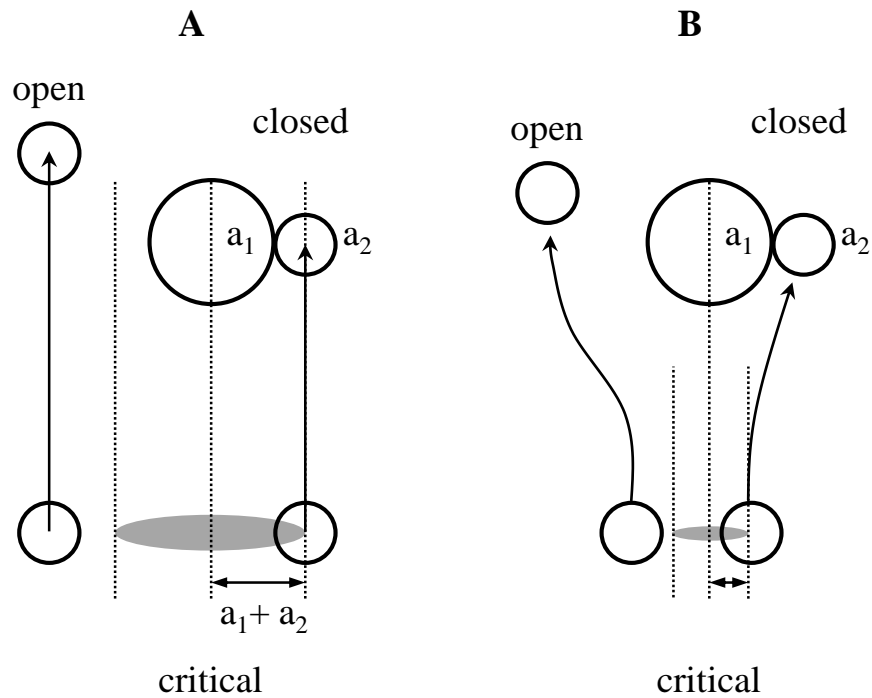
Figure 2.3 Critical areas in the absence (A) and presence (B) of interparticle interactions.

2.4.3 Fluid Shear

Adler presented the global capture efficiencies for collisions of two unequal-sized particles in a linear shear fluid (1981a, 1981b, 1981c, 1981d) by improving van de Ven and Mason's derivation (1976a, 1976b). To calculate the collision efficiency functions for particles in a linear shear flow, Adler's trajectory analysis was performed in this research under traditional interparticle interactions (hydrodynamics and the vdW and EDL energies). The relative trajectory of two particles moving at different velocities due to a linear shear flow in polar coordinates is schematized in Figure 2.4.
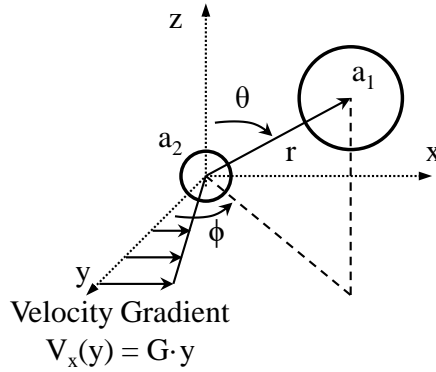
Figure 2.4 Schematic representation of two particles in a linear shear flow

The origin of the polar coordinate is at the center of Particle 2. The angle between Particle 1 and the z-axis is θ, the angle between the projection of Particle 1 on the xy-plane and the y-axis is ϕ, and the center-to-center distance between the two particles is defined as r. Adler used three first order differential equations to describe the changes in r, θ, and ϕ with respect to time, t; as follows:

$$\frac{dr}{dt} = Gr(1 - A) \sin^2 \theta \sin \phi \cos \phi + F_r \tag{2.11}$$

$$r\frac{d\theta}{dt} = (1 - B) \sin \theta \cos \theta \sin \phi \cos \phi + F_\theta \tag{2.12}$$

$$r \sin \theta \frac{d\phi}{dt} = Gr \sin \theta \left(\cos^2 \phi - \frac{B}{2} \cos 2\phi \right) \sin \theta + F_\phi \tag{2.13}$$

where G is a linear velocity gradient, A and B are dimensionless hydrodynamic correction factors which are functions of the ratio of the two particle radii and the distance between them (they are similar to the L, G, M functions in Equation (2.10)), and F is the total interparticle force (*i.e.*, the first derivative of DLVO energy with respect to separation distance). The hydrodynamic correction factors are detailed in Adler's papers

26

(1981b, 1981c). Tandon and Diamond (1997) devised simpler hydrodynamic fitting functions that yield less than 2% error from the exact values of Adler (1981a) and Batchelor and Green (1972). In this research, the Tandon and Diamond simplified hydrodynamic functions were utilized instead of Adler's exact hydrodynamic correction function to reduce the computational burden.

2.5 SUMMARY

Flocculation is a critical process in water treatment. By changing the particle size distribution, flocculation allows subsequent particle separation processes such as sedimentation, granular filtration, or membrane treatment to be more effective. Yet, significant gaps in fundamental understanding still exist at the nanoscale. If nano-sized particles can become large sized particles (micro-scale) due to conventional particle destabilization, nano-sized particles are expected to well removed from water by subsequent particle separation processes. The motivation of the present research stemmed from the previous research of Han and Lawler (1992) and Li (1996). Han and Lawler developed the first flocculation model that considered short-rage interactions between particles and Li verified the mathematical model by comparing it against experimental results. However, the evolution of the particle size distribution in flocculation at the nanoscale cannot be predicted by their work. The mathematical model does not account for the collision efficiency functions for nano-sized particles. Additional motivation for the present research comes from the development of new analytical technologies that enable particle characterization at the nanoscale.

The primary goal of this research is to improve quantitative understanding of flocculation at the nanoscale by comparing the experimental results acquired from laboratory-scale flocculation under various conditions to an extended flocculation model.

Chapter 3: Experimental Methods

3.1 INTRODUCTION

To obtain a quantitative understanding of the destabilization and flocculation of nanoparticles, the evolution of particle size distributions for silver nanoparticles (AgNPs) was studied under various laboratory scale experimental conditions. Experimental data were then systematically evaluated in comparison to each other or against predictions made from the mathematical flocculation model described in Chapter 2. In this Chapter, experimental designs and methods, analytical instruments, and interpretation of collected data are described.

3.2 EXPERIMENTAL DESIGN

Laboratory scale batch flocculation experiments were designed for engineered AgNPs. It is well known that the use of engineered nanoparticles in consumer products has increased over the last few decades and silver is one of the most popular nanomaterials due to its versatility (Lawler *et al.*, 2013). Because engineered nanoparticles such as AgNPs can be released to surrounding environments from consumer products, several scholars have suggested that life-cycle pathways of nanoparticles in water treatment processes must be investigated (Wiesner *et al.*, 2006). In particular, some of the transport processes in water treatment might be significantly different for such small and dense particles like AgNPs. For this reason, silver was selected as the target particle for this study. The size and shape of commercially available AgNPs are well defined (Kim, 2014). In addition, silver has a relatively high refractive index number; therefore, it is relatively easy to measure its sizes with analytical instruments that utilize laser-illumination techniques (Lawler *et al.*, 2015).

3.2.1 Silver Nanoparticles (AgNPs)

Three distinct sizes of spherical AgNPs (NanoXact) stabilized by citrate capping layers (diameters are 30, 50, and 100 nm) were purchased from Nanocomposix (San Diego, CA). Citrate is the most common stabilizing agent for nanoparticles in research settings (Tolymat *et al.*, 2010). The primary stabilizing mechanism of citrate capped AgNPs is electrostatic and the surface charge at natural water conditions (pH 7-9) is negative (Mikelonis, 2015). The hydrodynamic size and zeta potential of AgNPs were confirmed by a NanoSight (LM10, Malvern) and ZetaCompact (Zetameter, CAD instrument), respectively. The measured particle sizes for the three types of AgNPs are shown in Figure 3.1.
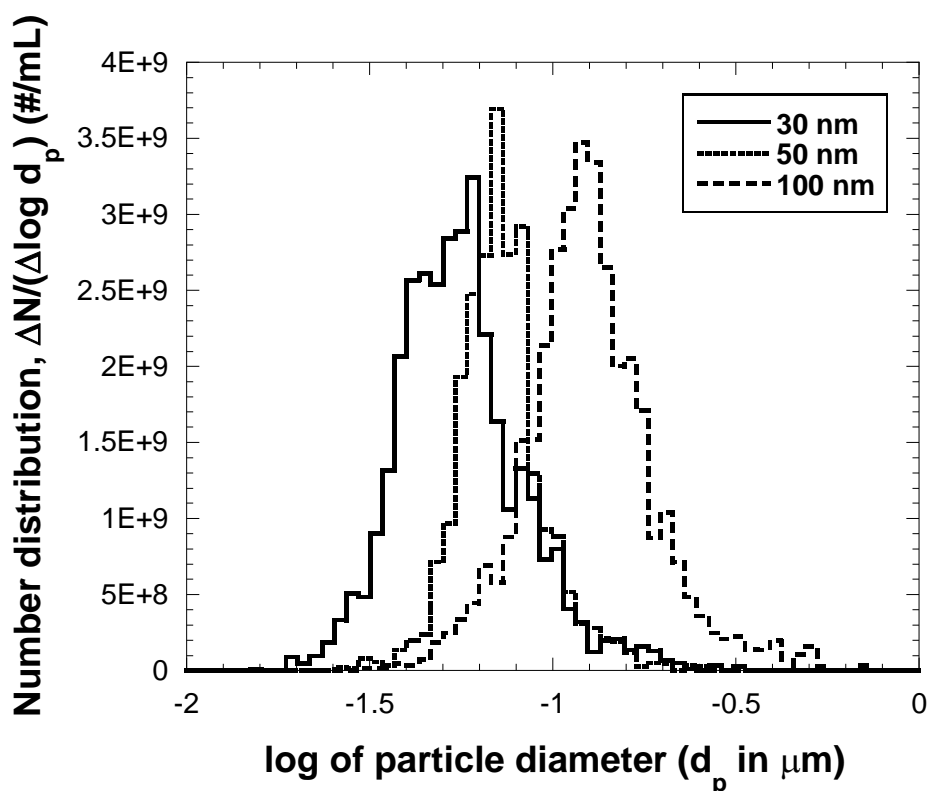
Figure 3.1 Particle number distributions of purchased citrate stabilized AgNPs

The initial zeta potentials measured by ZetaCompact are between -50 and -45 mV at pH 7 for the three purchased AgNPs which agreed with the value reported by the manufacturer. Because the three types of purchased AgNPs differ from each other only in diameters while their zeta potentials were almost identical to each other, direct comparisons between these AgNPs under the same experimental conditions is intended to reveal the effect of particle sizes on nanoparticle flocculation.

3.2.2 Experimental Conditions

Along with the size of AgNPs, the influences of other independent variables (ionic strengths, valencies of the background electrolytes, initial concentrations, and the presence of natural organic matters) were systematically investigated. The experimental conditions during each flocculation experiment are tabulated in Table 3.1.

Table 3.1 Experimental conditions for laboratory-scale flocculation

	Particle size (nm)	Ionic Strength (mM)	Valency	Initial Particle Concentration (#/mL)	NOM*
1	100	30	1	1.3E+09	X
2	100	50	1	1.1E+09	X
3	100	30	2	1.2E+09	X
4	100	30	3	1.2E+09	X
5	100	30	1	1.9E+09	X
6	100	50	1	1.1E+09	O
7	100	30	2	1.3E+09	O
8	30	30	1	1.1E+09	X
9	30	10	1	1.0E+09	X
10	30	3	1	1.1E+09	X
11	30	3	2	1.2E+09	X
12	30	3	1	2.5E+09	X
13	50	3	1	1.2E+09	X
14	50	3	2	1.2E+09	X
15	50	10	1	1.1E+09	X
16	30 & 100	10	1	1.3E+09	X
17	30 & 100	30	1	1.0E+09	X
18	30 & 100	3	2	1.0E+09	X

*NOM = Natural Organic Matter, X = the absence of NOM, and O = the presence of NOM

3.3 LABORATORY-SCALE BATCH FLOCCULATION

3.3.1 Preparation of Materials

To reflect the importance of background electrolytes on nanoparticle flocculation, two different salts were chosen: calcium nitrate ($Ca(NO_3)_2$), and sodium nitrate ($NaNO_3$). It is known that the primary destabilizing mechanisms of calcium nitrate and sodium nitrate on citrate capped AgNPs are charge neutralization and compression of the diffuse layer, respectively (Lawler *et al.*, 2013). By comparing these two types of salts, the destabilization and flocculation of AgNPs could be systematically studied. To prevent any potential reactions with silver, nitrate salts were selected rather than chloride salts (Linnert *et al.*, 1990; Li *et al.*, 2010). The specific ionic strengths in flocculation experiments were determined based on preliminary experimental results. As it was explained earlier in Chapter 2, according to DLVO theory, a higher ionic strength forms a thin diffuse layer which favors particle collisions, while a lower ionic strength fosters an extended diffuse layer that hinders particle collisions. Throughout each flocculation experiment, the pH was kept constant at 7.0 (± 0.3) via sodium bicarbonate (0.1 meq/L $NaHCO_3$) to avoid calcium carbonate precipitation and other adverse effects. In addition, to emulate surface water conditions, some suspensions included Suwannee River natural organic matter (NOM) at a concentration of 3.5 mg/L as DOC. The reference NOM powder was purchased from the International Humic Substances Society. The NOM stock solution was prepared by dissolving the NOM powder into Millipore water (18 Ohm) and filtering through membranes with a pore size of 0.45 μm to filter any unwanted particles. The dissolved carbon content of the NOM stock solution was quantified by a TOC-L analyzer (Shimadzu, Japan). Millipore water was used in all experiments. Laboratory glassware, stir-bars, and pipette tips were cleaned by soaking in 10% nitric acid overnight and kept in a particle-free room prior to each experiment.

3.3.2 Experimental Procedure

For each flocculation experiment, the stock suspensions of AgNPs (0.02 mg/mL) were diluted to desired number concentrations with Millipore water; for different types of experiments, different silver concentrations were used as indicated in Table 3.1. If NOM was to be added, it was added next and allowed to interact with the AgNPs for 24 hours to give sufficient time for adsorption of NOM onto the particle surface. AgNPs could undergo dissolution (Liu and Hurt, 2010; Zhang *et al.*, 2015), aggregation (Li and Lenhart, 2012), or sulfidation (Kim *et al.*, 2010; Levard *et al.*, 2011). To protect the change of particle property, the prepared solutions were stored at 4 °C protected from light. The stock solutions of nitrate and calcium salts were made at a high concentration so that the desired final concentrations could be obtained with a dilution factor of 33.3 (*i.e.*, by adding 30 μL of the salt stock per 970 μL of AgNPs solution to have 1000 μL of the final suspension). The $NaNO_3$ or $Ca(NO_3)_2$ stock solutions were added at time 0 to achieve desired ionic strengths and rapidly mixed for 30 seconds. Samples were collected at various times and particle size distributions were measured immediately. Throughout each flocculation experiment, gentle mixing (with G values estimated as $10s^{-1}$) was applied via a combined rocking and rolling motion in enclosed jars to avoid particle settling. Flocculation experiments were performed by controlling five different independent variables while other environmental conditions were fixed. In addition, heterodisperse samples were produced by adding two sizes of AgNPs together (30 nm & 100 nm) and evaluated.

3.4 CHARACTERIZATION METHODS

3.4.1 Nanoparticle Tracking Analysis (NTA)

In the present study, the particle size distributions of AgNPs were measured exclusively using NanoSight LM10 HS equipped with software version NTA 3.0. This instrument uses laser illuminated microscopy to record the Brownian motion of nanoparticles in suspension. NTA 3.0 is a computer program that tracks each particle from the recorded videos, calculates the particles' mean squared displacements, and from that information and the Stokes-Einstein equation, the particles' diffusion coefficients and sphere-equivalent radius. The Stokes-Einstein equation is

$$D = \frac{k_B T}{6\pi\mu a} \tag{3.1}$$

where D is the diffusion coefficient, k_B is Boltzmann's constant, T is the temperature in Kelvin, μ is the viscosity of water, and a is the particle's radius.

The method and theory of NTA are described by Malloy & Carr (2006). The lower size limit of detection depends on the refractive index of nanoparticles which, for colloidal silver, is approximately 10 nm (Carr *et al.*, 2008; Filipe *et al.*, 2010). For this research, each measurement was taken for 30 s and run in triplicate. The average values of three measurements were used for the analysis. Although the software allows fitting the data to a log-normal distribution, the raw data were used in the data analysis. The absolute, and not just relative, size distributions reflect the changes brought about by flocculation more precisely; these processes promote heterodispersity in the distribution, and a log-normal model fitting would distort the actual data. Therefore, the raw data were used to produce particle size distributions with equally spaced size increments on a logarithmic scale.

The desired number concentrations for the flocculation experiments were chosen based on the optimum number concentration range of NanoSight. The operation manual for NanoSight recommends all samples to be diluted to a particle number concentration greater than 10E7 and lower than 5E9 particles per milliliter. Varying dilution factors to the AgNPs stock solution, it was confirmed that the mass concentration is proportional to number concentrations measured within the suggested operation ranges of NanoSight as shown in Figure 3.2.

$y = 7.99 \times 10^7 + 3.57 \times 10^9 x \quad R = 1 \times 10^0$

$$y = 4.47 \times 10^8 + 3.83 \times 10^9 x \quad R = 0.998$$
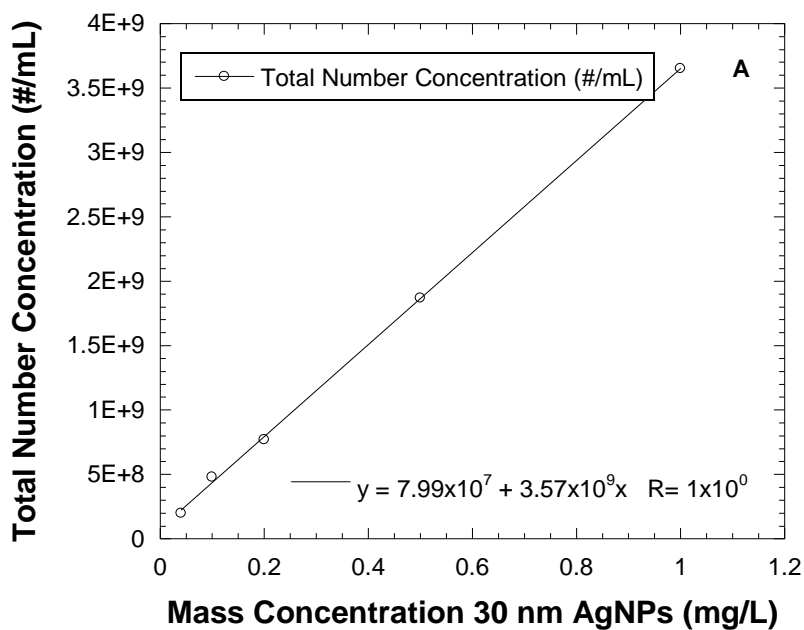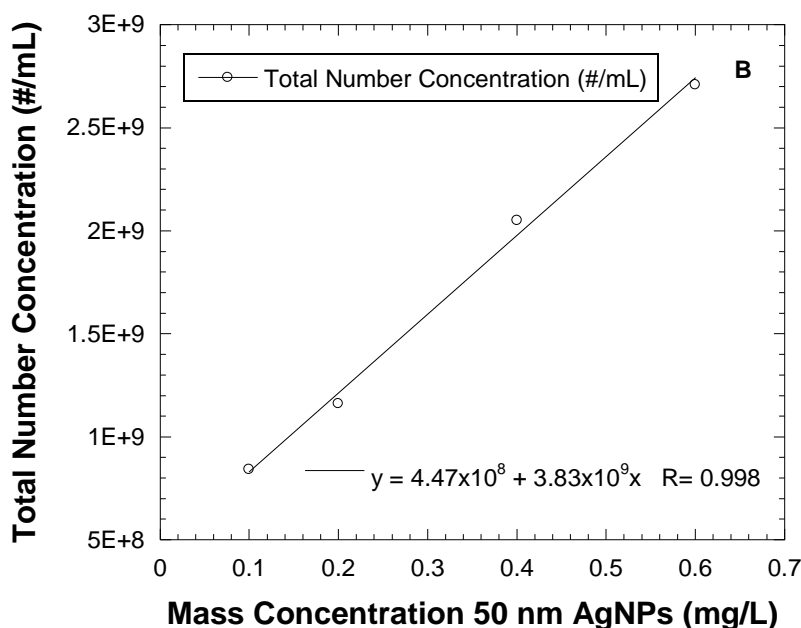
Figure 3.2 Number vs. Mass Concentration for A) 30 nm and B) 50 nm AgNPs

These quantitative measurements could be very difficult to obtain at first, and the optimum configuration of the instrument for particular nanoparticles can only be determined by arduous trial-and-error. Due to its high refractive index number, AgNPs are less challenging than other inorganic nanoparticles to quantify number concentrations using NTA. However, the measured particle number concentrations in the early stage of the present research often differed from the expected number concentrations (*e.g.*, NTA gave higher number concentrations than the estimated number concentrations by the manufacturer of AgNPs). The standard configuration of the instrument will not likely deliver precise number concentrations. The measured number concentrations of NanoSight are strongly influenced by laser intensity during the measurement process and threshold configuration during data acquisitions. These two properties must be carefully controlled during each measurement and cross referenced between each sample.

36

Prior research was used to evaluate the precision of particle number concentrations measured by NanoSight. Results of AgNPs removed during granular filtration (Lawler *et al*., 2015) that were measured on a number basis using NanoSight were compared with results of mass measurements that were measured by inductively coupled plasma optical emission spectrometry (ICP-OES); these measurements are compared in Figure 3.3.
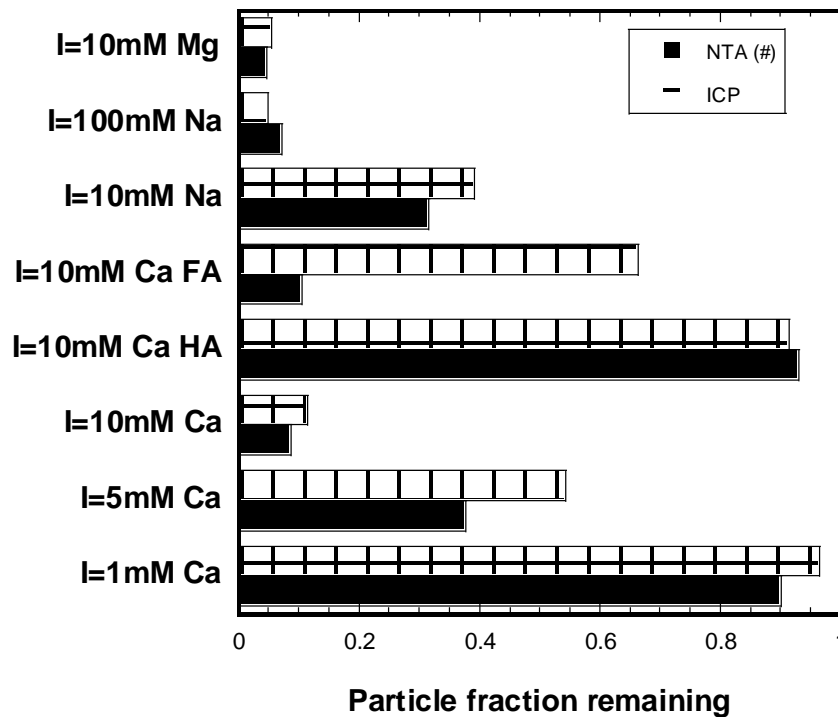
Figure 3.3 Comparison of particle fraction remaining between NTA and ICP-OES from AgNPs removed by granular media filtration in Lawler *et al.*, 2015

In most cases, results from the two measurements were quite consistent. This agreement again indicates that NTA is a promising method to characterize nanoparticles during water treatment processes both qualitatively and quantitatively.

37

3.4.2 Dynamic Light Scattering (DLS)

DLS measures the scattered light that is created by Brownian motion of nanoparticles in a liquid solvent. Fitting the frequency of light fluctuation into different time intervals, diffusion coefficient values of nanoparticles are found (Pecora, 2013). Then, the hydrodynamic diameters are calculated from the obtained diffusion coefficient by using the Stokes-Einstein equation. Amongst the various analytical methods available for measuring particle size, dynamic light scattering (DLS) has been used most frequently for characterization of nanoparticles (Malloy and Carr, 2006; Carr *et al.*, 2008). However, after extensive preliminary studies, DLS is determined to be an unsuitable technique for the present research. DLS only gives relative concentration measurements (*i.e.*, the intensity of light scattering) and creates a Gaussian distribution to fit the ensemble light scattering detected; the objectives of this research require absolute (not relative) size distributions and cannot be constrained by a Gaussian fit.

A set of flocculation data obtained by NTA and DLS (Malvern Zetasizer) is shown in Figure 3.4. For this flocculation experiment, the stock suspension of 50 nm AgNPs with citrate capping was prepared at a concentration of 500 µg/L. The $Ca(NO_3)_2$ stock solution was added at time 0 to achieve the desired ionic strength of 10 mM, and the suspension was rapidly mixed for 30 seconds. Samples were collected at various times thereafter and particle size distributions were measured immediately by NTA and DLS.
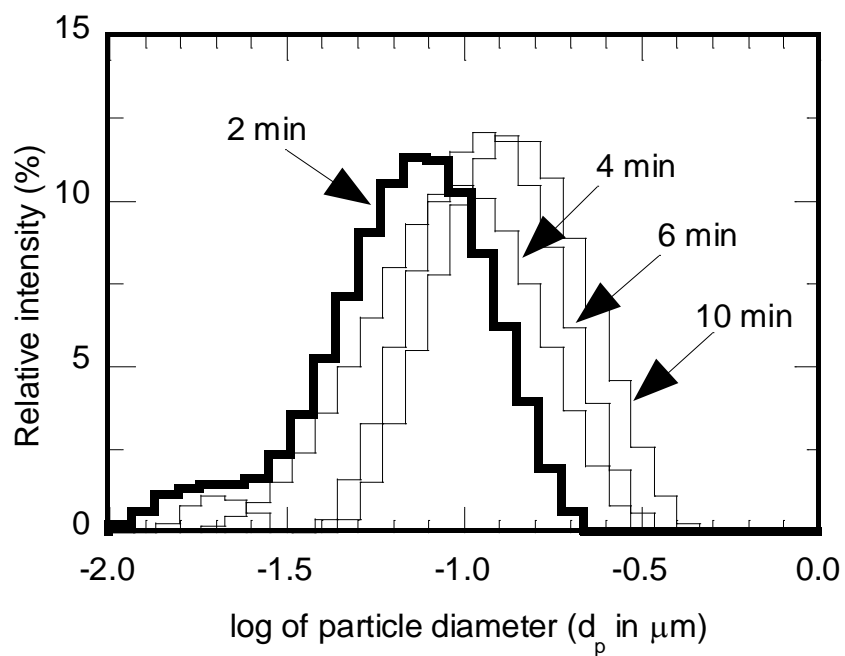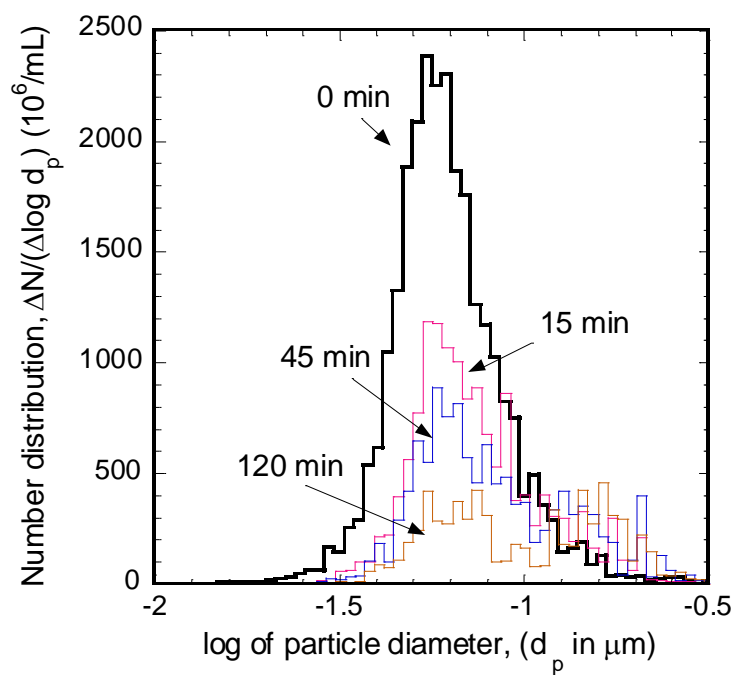
Figure 3.4 Flocculation results from NTA (top) and DLS (bottom)

The NTA result in Figure 3.4. shows the changes in the particle size distributions of destabilized AgNPs with time. The peak of the number distribution shifted to larger particles, both the height of the peak number concentration and the area of the figure (total particle concentration) lowered with time, and the creation of larger flocs is clearly indicated. This result is clear evidence of flocculation and is qualitatively consistent with the Smoluchowski theory of flocculation (*i.e.*, many small particles aggregated to form fewer larger particles). The limitation of DLS measurements is clear when compared with NTA results from the same experiment as shown in the bottom of Figure 3.4. Although DLS also indicated flocculation by the shift to larger sizes, it only shows relative size measurements as a normal distribution; this result is not consistent with Smoluchowski principles.

3.4.3 Tunable Resistive Pulse Sensing (TRPS)

The feasibility of utilizing TRPS technique of qNano (iZon Science) for nanoparticle size measurements was also contemplated for the present research. TRPS is an impedance based technique that employs the Coulter principle at the nanoscale (Kozak *et al.*, 2012). TRPS measures the magnitude of electrical currents across a nano-sized pore of a membrane in a background suspension. Because the background suspension is a salty electrolyte, a constant voltage can be maintained across the pore by the instrument. When a particle passes through the pore, the particle (assumed to be non-conductive in comparison to the electrolyte) alters the resistance between the nano-sized pore of the membrane. Due to the relationship between voltage, current and resistance (V=I*R), if the voltage is constant, a sudden electrical pulse in the currents will be created as the particle passes through. The peak and duration of that pulse are proportional to the volume and the velocity of the particle, respectively (Garza-Licudine *et al.*, 2010). This

technique can be a powerful nano-characterization tool because TRPS technique directly measures the absolute physical volume of each particle rather the hydrodynamic diameter, as DLS and NTA do. The hydrodynamic diameter includes a hydration layer of fluid and capping or other surrounding ions that travel with particles in solutions. The hydrodynamic diameter depends on the properties of the solutions such as ionic strength or pH. According to the operation manual of the qNano, TRPS measurements agree well with transmission electron microscopy (TEM) because they are both independent of electrolyte properties. The NanoSight utilizes laser, and the quality of measurements relies on the refractive index of particle materials whereas TRPS does not have such limitations. In addition, numerical flocculation modeling is based on the absolute volume of particles, not the hydrodynamic diameter. The absolute particle volume that is measured by the qNano would correspond to numerical modeling prediction better.

Despite all these positive aspects, the qNano failed to yield the particle size distributions of the purchased AgNPs for a few reasons. To maintain a constant electric voltage across the membrane pore, the background electrolyte requires relatively high salinity. The standard background electrolyte solution, iZon Tris buffer, provided by the manufacturer has 100 mM of KCl, equivalent to ionic strength of 100 mM. In such ionic strength, the purchased citrate capped AgNPs are highly destabilized and extremely rapid flocculation takes place. Because flocculation is a second order reaction with respect to the particle number concentration, the number concentration of AgNPs decreases dramatically within a few minutes of sampling periods. By the time, the samples are ready to be measured in the instrument, the number concentration falls below the minimum particle count required by the qNano. In addition, due to rapid flocculation, the size of AgNP flocs becomes larger than the size of the membrane pore. Although it is possible to substitute the membrane of the qNano with a larger pore sized membrane, this

procedure requires cleaning and replacement time. Practically speaking the qNano was not able to keep up with the dynamic nature of AgNPs flocculation on a real-time basis. To prevent rapid flocculation of AgNPs, a laboratory synthesized electrolyte that had a lower salinity of 50mM of KNO_3 was attempted for qNano measurements instead of the standard background electrolyte. However, the electric current was not stable at that low of a salinity condition so severe electrical background noise resulted. Ultimately, the TRPS system was determined not suitable for the purchased citrate capped AgNPs.

Alternatively, when latex particles (Duke Scientific Corporation, CA) with a diameter of170 nm were used during a similarly designed flocculation experiment, the qNano was able to deliver the evolution of particle size distributions in laboratory scale flocculation as shown in Figure 3.5.
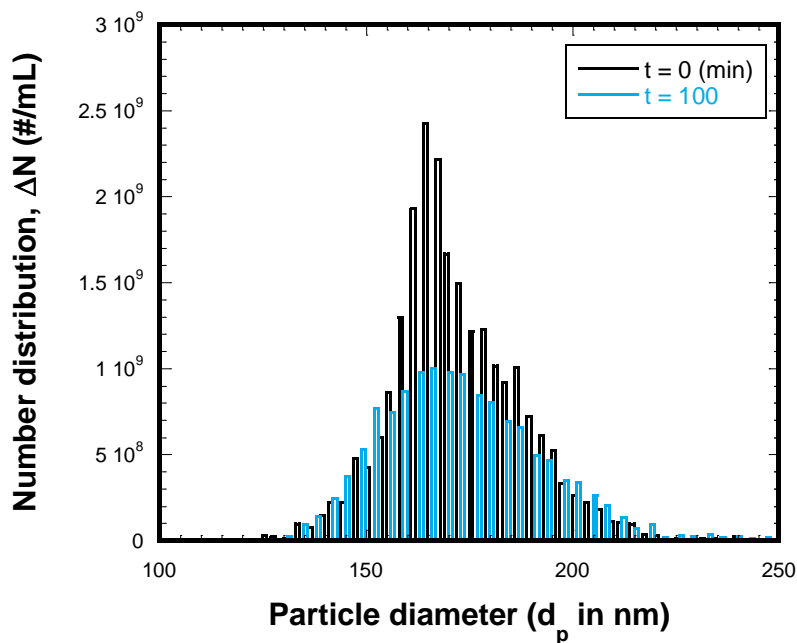
Figure 3.5 Flocculation of latex particles induced by I = 400 mM of KCl from qNano

Latex particles (polystyrene) have a lower Hamaker constant value compared to silver (Israelachvili, 2011); as a result, the vdW attraction of latex is weaker than the purchased AgNPs. In addition, the electrical surface potential of latex particles is estimated to be higher than the citrate capped AgNPs; the EDL repulsion of latex is stronger than AgNPs. For this reason, in the standard background solution of the qNano, latex particles do not form flocs. Flocculation of latex particles were induced by the ionic strength of 400 mM of KCl. The samples were then diluted with standard background solution and particle size distributions were measured at various times. The qNano could be a powerful tool to characterize nanoparticles only if the stability of the target particles is not affected by the high salinity of background electrolytes.

3.4.4 Electrophoretic Mobility

The magnitude of surface charges of particles in water is commonly estimated experimentally by electrokinetic techniques (Elimelech *et al.*, 1998). Among several existing electrokinetic techniques, electrophoretic mobility is most popular for suspended colloidal particles (*i.e.*, velocities of particles over electrical field strengths). Estimated electrophoretic mobility can then be converted to zeta potential. Zeta potential (also known as electrokinetic potential) is defined as the electric potential at the shear plane of the diffuse layer (Kim *et al.*, 2006). Due to the correlation between the zeta potential and the surface potential, the surface potential and the particle stability can be analyzed through measurements of the zeta potential. The zeta potential is a critical parameter for prediction of particle stability in solutions.

In the present study, the zeta potentials of AgNPs were obtained from electrophoretic mobility measurements made with a Zetameter ZetaCompact (CAD,

France). The Zetameter ZetaCompact is a laser illuminated microscopic instrument that utilizes a computer video processing program to track moving particles under various electrical field strengths. In natural conditions, most particles have a heterogeneous distribution of zeta potentials because of the complexity of crystal structure and chemical compositions of the particle surfaces (Kim and Lawler, 2005). This heterogeneous nature of zeta potentials must be carefully taken into account. To have statistically significant data, each measurement must contain the number of tracked particles between 80 and 120 (Kim *et al.*, 2008).

Kim and Yoon (2002) reported the relationships between measured electrophoretic mobility and zeta potentials for deformed spherical particles. However, the effect of non-spherical particles on electrophoretic mobility was not considered in the present study because TEM images confirmed the spherical shape of the purchased AgNPs as shown in Figure 3.6. Similar TEM images from the manufacturer for the other particles confirm the sphericity and small variation in size for those other particles. In addition, the standard deviations in the zeta potential distributions from ZetaCompact can account such variations (Kim *et al.*, 2008).
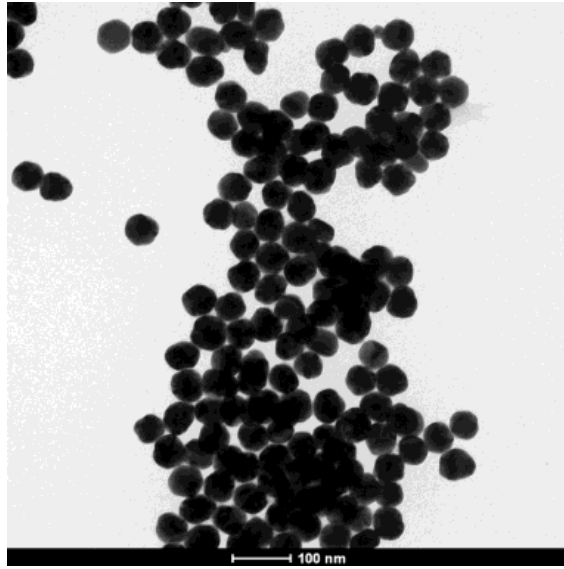
Figure 3.6 TEM image of the purchased 50 nm citrate capped AgNPs

Using the Gouy-Chapman model with a known distance (0.5 nm) between the particle surface and the shear plane (van Oss *et al.*, 1990), the surface potential was estimated from experimentally measured zeta potentials though out the present research.

3.5 INTERPRETATION OF PARTICLE SIZE DISTRIBUTION DATA

Raw data from the NanoSight contains the number of particle tracked in each particle size bin (or channel). Users of the NanoSight can specify whether particle size bins to be spread equivalently either in an arithmetic scale or a logarithmic scale. Using an arithmetic scale squeezes the data at small particle sizes and disseminates the data for large particle sizes. For instance, the distinctions in transport behavior of nanoparticles between 10 and 50 nm (diameter) particles are relatively more important than the distinctions in transport behavior between 1.01 and 1.05 μm sized particles. However, the arithmetic scale assumes that they have the equal importance. To avoid this scale issue, it is conventional to use a logarithmic scale for the abscissa (particle diameter) in size distributions for particles in a suspension (Benjamin and Lawler, 2013). On the

logarithmic scale, nanoparticles of 1 and 5 nm are as equally spaced out as 100 and 500 nm particles; therefore, the relative importance between different sized particles is adjusted.

3.5.1 Presentation of Size Distributions of Nanoparticles

Several different methods of expressing size distributions of particles in a suspension exist and Benjamin and Lawler (2013) thoroughly discussed these methods. In this research, the definition for particle size distributions described by Benjamin and Lawler is used hereafter. The particle size distribution function is defined as follows:

$$n(d_p) = \frac{\Delta N(d_p)}{\Delta(d_p)} \tag{3.2}$$

where, d_p is a mean particle diameter of each particle size bin, and $N(d_p)$ is a cumulative number density function. Hence, $n(d_p)$ is the differential form of the number distribution (*i.e.*, number of particles in each size bin). Along with the abscissa, the logarithmic scale is commonly used for the ordinate in particle size distribution function because the numbers of measured particle in each bin vary over a few orders of magnitude in a sample. Figure 3.7 shows the particle size distribution function from the purchased AgNP stock solution for 100 nm.
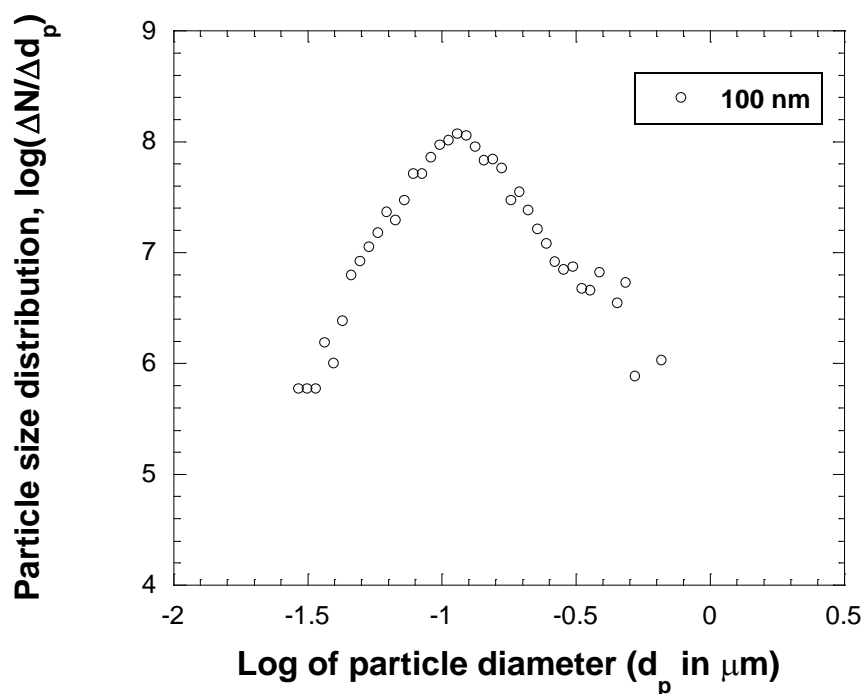
Figure 3.7 Particle size distribution function for the purchased citrate-AgNPs

Particle diameters are reported as micrometers. The logarithmic value of -1 with base 10 corresponds to 0.1 μm (*i.e.*, 100 nm); therefore, the peak of the particle size distribution for the 100 nm sized AgNP stock suspension is approximately at -1 of the logarithmic of the particle diameter. Although the particle size distribution function is a popular method to deliver particle distribution information, it does not work very well with data from NanoSight. NanoSight often measures no particles for a certain size bin. In turn, this results in a zero number concentration for that particular size bin (*i.e.*, $\Delta N(d_p) = 0$). Because the logarithmic of 0 is undefined, particle size distributions cannot be generated with measured data from the NanoSight. To circumvent this issue, the number distribution ($\Delta N/\Delta \log d_p$) was used throughout the present study. Figure 3.8 shows number distribution for the same AgNP stock solution to Figure 3.7.
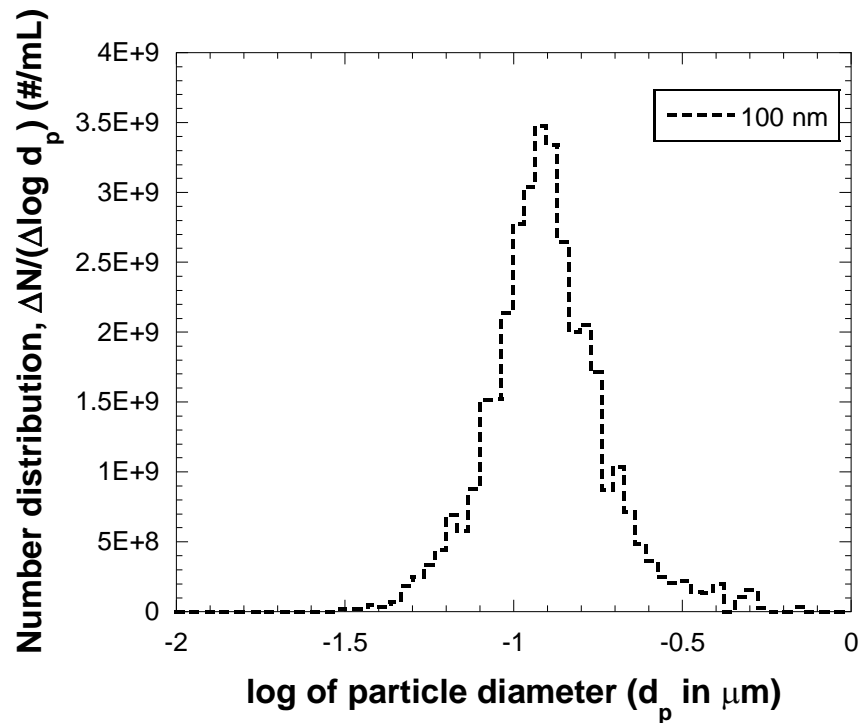
Figure 3.8 Particle number distribution for the purchased citrate-AgNPs as measured using NanoSight

The particular usefulness of this plot is that the total number concentration within a particular size range is given by the integral (area under the curve) of the number distribution over that size range. The particle number distribution functions are somewhat analogous to probability density functions in statistics. According to the Oxford English Dictionary, the probability density function is "a function of a random variable, whose integral across an interval gives the probability that the value of the variable lies within the same interval." Similarly, a number distribution is a function of the particle diameter, whose integral across an interval gives the number concentration that the value of the particle size lays within the same interval. Throughout the present study, number distribution functions were used as a primary method to visualize size distributions of AgNPs in flocculation experiments and mathematical modeling.

48

3.5.2 Data Manipulation

The output summary files from NanoSight include information of sample and instrumental settings. The width of each bin ($\Delta \log d_p$) was set at 0.033 to generate one hundred individual particle size bins that are equally spread out in a logarithmic scale from 1 nm to 2000 nm. Although NanoSight allows fitting the data to a log-normal distribution, the raw data were used in the analysis. The absolute, and not just relative, size distributions reflect the changes brought about by flocculation and filtration more precisely; these processes promote heterodispersity in the distribution, and a log-normal model fit would distort the actual data. The raw data from NanoSight are the number concentration (ΔN) for each size bin. Normalizing the number concentration (ΔN) by the bin width ($\Delta \log d_p$), the number distribution is then generated. Each size measurement measured on NanoSight was run in triplicate. The average values of three measurements were used for the mathematical modeling and further analysis.

3.5.3 Quantifying Flocculation

As shown in Equation 2.3, flocculation is a second-order reaction with respect to the particle number concentration. Even though examining all the number distributions over an entire flocculation experiment could give some general idea about flocculation kinetics, the influence of different experimental conditions on flocculation kinetics can be more readily seen by comparing some characteristic changes in the number distributions among flocculation experiments. Figure 3.9 shows changes in the number fraction (*i.e.*, the ratio of the number concentration of particles in particular diameter ranges to the total number concentration) of 30 nm AgNPs in 10 mM ionic strength at $NaNO_3$.
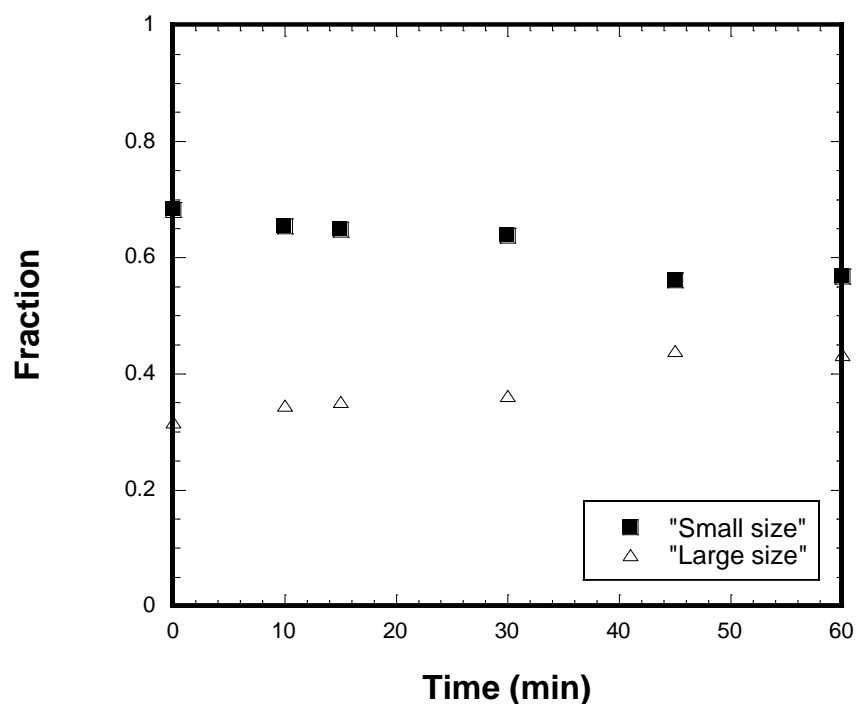
Figure 3.9 Particle number fraction during flocculation of 30 nm AgNPs at I = 10 mM

Two arbitrary particle diameter ranges, equally spaced logarithmically, were chosen as the 'smaller particle range' and 'larger particle range'. The smaller particle range represents particle that include the first 70% of the total particle number concentration in the size distribution and the larger particle range includes the remaining 30% of the distribution. During flocculation, the fraction of smaller particles decreased while the fraction of the larger particles increased. At time 0, the smaller and larger particle accounted for 70% and 30%, respectively. After an hour of flocculation, the fraction of smaller particles decreased to 55% while the fraction of larger particles increased to 45%. By comparing number fractions between flocculation experiments, the effects of experimental conditions are better understood.

50

Chapter 4: Experimental Results

4.1 INTRODUCTION

The main objective of the experimental portion of this research was to examine the evolution of AgNP size distributions under various water chemistry conditions. Through the experimental results of AgNP flocculation, theories of particle destabilization and flocculation processes in water treatment that were initially developed for micron-sized particle can be validated for nano-sized particles. The experimental results would bridge the gap between applications and theory for water treatment in the nanoscale. The work was performed at the laboratory scale using batch flocculation experiments. Independent variables included ionic strength (I), type of electrolytes, presence or absence of natural organic matter (NOM), initial particle number concentration, and initial particle size. These experimental variables were selected on the basis of their fundamental and established influence during flocculation processes in conventional water treatment. This work specifically focuses on their effects on nanoparticle flocculation, an area of research that is not well understood. The experimental procedures for monodisperse suspensions are first discussed in this section, followed by the discussion of heterodisperse suspensions. The particle number distributions obtained from each experimental condition (Table 3.1) are provided in Appendix A. In addition, the reproducibility of the evolution of particle size distributions for the AgNP flocculation experiments was verified. Experimental results from different iterations of the same experimental conditions were compared side by side as shown in Appendix D.

4.2 ANALYSIS OF A TYPICAL LABORATORY SCALE FLOCCULATION EXPERIMENT

Flocculation takes into account both liquid and solid phases. Batch flocculation experiments measured routine liquid properties such as pH and ionic strength, while cutting edge characterization techniques were developed for the solid phase, since incorporating the nano size range is novel to this type of research. This section provides representative figures that illustrate results obtained from each flocculation experiment.

Experiments #1 and #2 from Table 3.1 (flocculation experiments of the 100 nm AgNPs brought about by I = 30 and 50 mM as $NaNO_3$, respectively, in the absence of NOM) were selected to demonstrate analyzed raw data from NanoSight. Figure 4.1 delineates the changes in size and number of AgNPs in Experiment #1 and #2 over sixty minutes of flocculation. As shown in Figures 4.1A and B, the peak of the number distributions at time zero was located approximately at log d_p = -0.9 (d_p = 0.126 μm). Because the NanoSight measures the hydrodynamic diameter, the measured diameters are always slightly greater than the actual diameter of AgNPs reported by the manufacturer. The number distribution of AgNPs initially showed a normal distribution around its peak. Once flocculation was induced by increasing the ionic strength to 30 and 50 mM with $NaNO_3$, the number distributions were measured by NanoSight at various times to scrutinize the evolution of particle number distributions during flocculation.

Poor flocculation would show minimal or no change in the number distributions with time. In Figure 4.1A, the peaks of the number distributions did not appear to be moved at all whereas the height of the peak was slightly reduced during sixty minutes of flocculation. This result is an indication of poor or limited flocculation. On the other hand, successful flocculation transforms a large number of smaller particles into a fewer number of larger particles. This trend could be readily seen in the number distributions of many experiments in this research; in that case, the peak of the number distribution

52

shifted to larger particles, and both the height of the peak and the area under the curve are lowered with time as shown in Figure 4.1B. In addition, the creation of larger flocs is clearly indicated in Figure 4.1B.

Because the area under the number distributions represents the total number concentration of AgNPs in the system, the effectiveness of flocculation becomes apparent by looking at the changes of the area under the number distribution (*i.e.*, the total particle number concentration) as a function of time. The total particle concentrations of AgNPs versus experimental duration were acquired from the number distributions as shown in Figure 4.1C and D. The total number concentrations during Experiments #1 and #2 were reduced approximately from 1.3E9 #/mL to 1.0E9 #/mL and 1.1E9 #/mL to 5.0E8 #/mL, respectively. Because flocculation is a second-order reaction with respect to the number concentration of particles, the particle number concentration decreases quickly in the beginning of flocculation; however, the rate slows down with time by developing a plateau in the later stage of flocculation. By comparing the rate of changes in the total number concentrations of AgNPs with respect to time among each experimental condition, the intensity of flocculation is elucidated.

Figure 4.1E and F represent the changes in the particle number fraction in different parts of the size range during Experiments #1 and #2. The principles behind particle number fraction graphs are discussed in detail in Section 3.5.3. In short, the first 70% of the total particle number concentration in the size distribution is designated as the smaller particle and the remaining 30% of the distribution is classified as the larger particle. Minimal changes in the number fractions of small and large size particles were observed during Experiment #1 as shown in Figure 4.1E. The number fraction of small sized particles was lowered from 70% to 65%, while the fraction of large sized particles was shifted from 30% to 35%. This negligible shift is another confirmation that the ionic

strength of 30 mM as NaNO$_3$ did not induce vigorous flocculation for 100 nm sized citrated capped AgNPs. For Experiment #2, substantial changes in the number fractions occurred as shown in Figure 4.1F. The number fraction of small sized particles went down from 75% to 35%, whereas the fraction of large sized particles soared from 25% to 65%. This dramatic shift is a clear evidence that the ionic strength of 50 mM of NaNO$_3$ induced vigorous flocculation. It can be deduced from all parts of Figure 4.1 that flocculation was somewhat limited under the conditions of Experiment #1 while far more robust flocculation took place in Experiment #2.
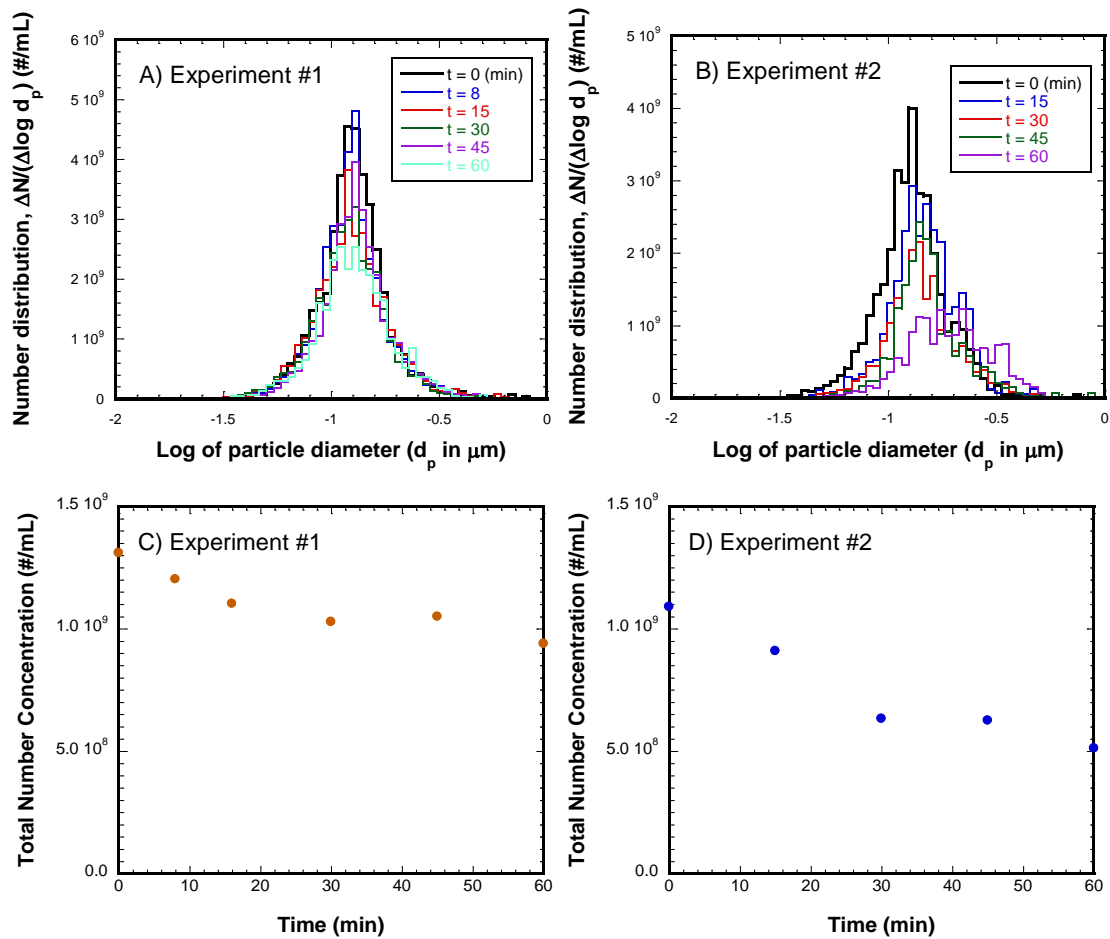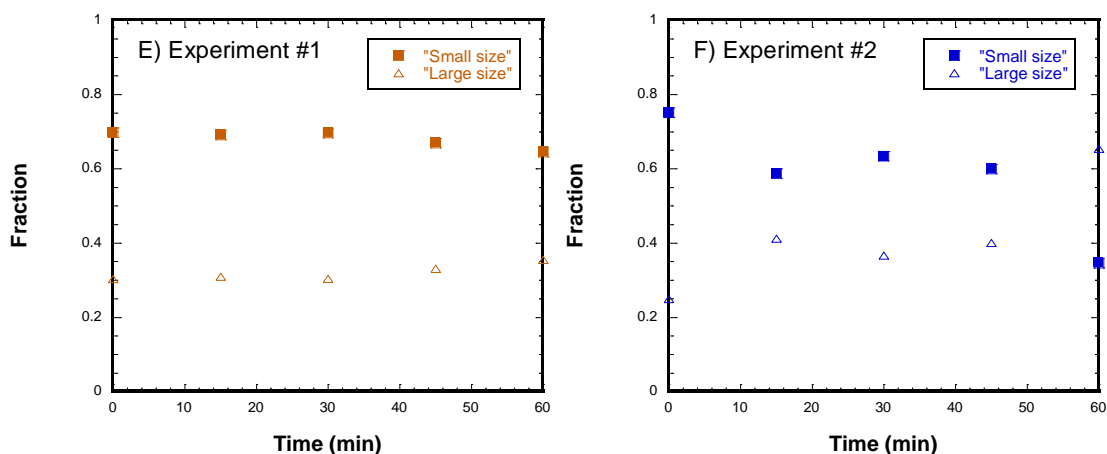
Figure 4.1 A) and B) Number distributions C) and D) Total particle concentrations, and E) and F) Number Fraction for 100 nm sized AgNPs under I = 30 and 50 mM achieved by NaNO$_3$, respectively

Along with the changes in particle sizes, the zeta potentials of AgNPs during flocculation experiments were evaluated as shown in Figure 4.2. Prior to the ionic strength adjustment in Experiment #1, the initial zeta potential of AgNPs was -50 mV. Due to the increased ionic strength, compression of the diffuse layer of AgNPs was achieved; therefore, the absolute value of the measured zeta potential was reduced to approximately -25 mV.
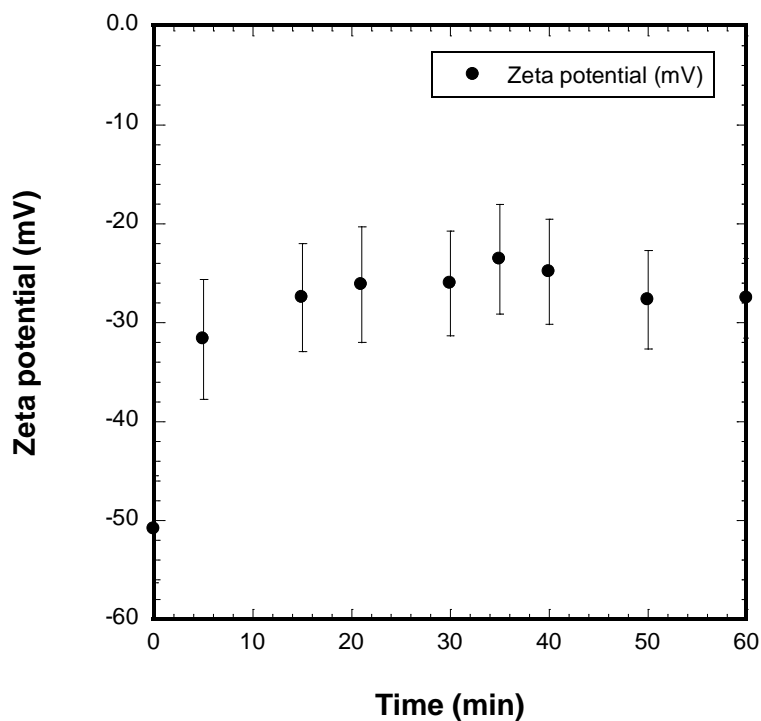
Figure 4.2 Zeta potential measurements from Electrophoresis measurements
    (ZetaCompact, France) performed during Experiment #1

Because of the difficulty of simultaneous measurements of particle sizes and zeta

potentials, and the observation that zeta potential values stabilized during flocculation,

only the initial and final zeta potentials of AgNPs were analyzed and reported for the

other experiments. The measured zeta potentials are tabulated in Appendix E.

Throughout the remainder of Chapter 4, identical data analysis and interpretation

techniques were applied to examine the changes in the distribution of particle sizes and

the zeta potential for each AgNP flocculation experiment.

4.3 FLOCCULATION EXPERIMENTS OF MONODISPERSE SOLUTIONS

4.3.1 Effects of Ionic Strengths of Destabilizing Agents

Because compression of the double layer due to increased ionic strengths is mathematically well understood, this mechanism is widespread in research setting for the field of particle separation processes (Benjamin and Lawler, 2013). By changing the concentration of destabilizing agents in suspensions, which is directly related to the ionic strength, scholars have quantified the critical coagulation concentration (CCC) and the stability of nanoparticles (Li *et al.*, 2011; Zhang *et al.*, 2011; Nason *et al.*, 2012; El Badawy *et al.*, 2012). While these cited works mainly focused on the growth of the mean hydrodynamic particle size as a function of the concentration (or the ionic strength) of the background electrolyte, the present work pinpointed the changes in the absolute particle size distributions under varying ionic strength conditions with respect to time.

Figure 4.3 shows the changes in the particle number distribution of the 30 nm sized citrate stabilized AgNPs over an hour of batch flocculation achieved by the different ionic strengths of $NaNO_3$ (Experiments #8, 9, and 10) while all other conditions remained constant.
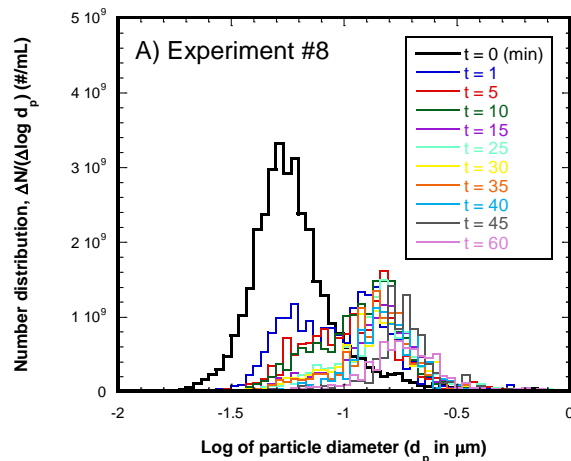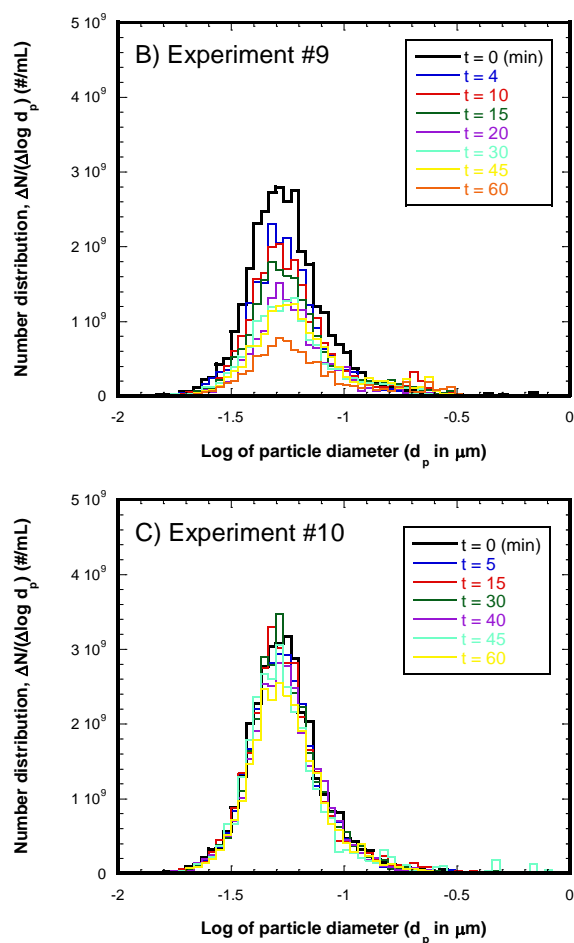
Figure 4.3 Changes in the particle number distributions during flocculation for the 30 nm AgNPs with A) I = 3 mM B) 10 mM and C) 30 mM of NaNO$_3$ which are from Experiment #8, Experiment #9, and Experiment #10, respectively

Different degrees of flocculation between each experiment can be manifested from Figure 4.3. As discussed in Chapter 3, however, it is easier to discern the effectiveness of flocculation by examining the changes in the total number concentrations under each experimental condition. Figure 4.4 displays the changes in the total number concentrations for the three flocculation results for the 30 nm sized AgNPs. As shown in Figure 4.4, the total particle number concentrations of the 30 nm AgNPs fell to various degrees under the three ionic strengths (I = 3, 10, and 30 mM). The particle number

concentrations under I = 10 and 30 mM were lowered almost one order of magnitude from their initial concentrations (from 1.1E9 to 2E8 #/mL) whereas the total number concentrations for of AgNPs with I = 3 mM declined only slightly.
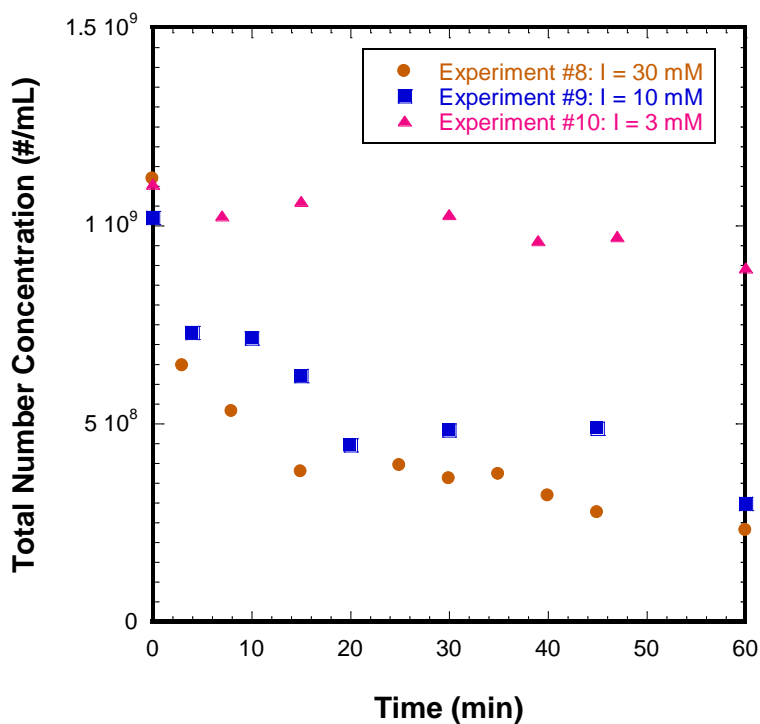
Figure 4.4 Total number concentrations of the 30 nm AgNPs under various ionic
strengths

These results agreed well with the theoretical understanding of compression of the diffuse layer reviewed in Chapter 2. The diffuse layer is more compressed under increased ionic strengths; therefore, weakened repulsive interaction led to an effective destabilization and better flocculation of AgNPs. Examining the interaction energy of two particles provides clear confirmation of this result. The interaction energy of two equal-sized AgNPs as a function of their separation distance (*i.e.*, DLVO curves) was calculated and plotted for the given condition as shown in Figure 4.5.
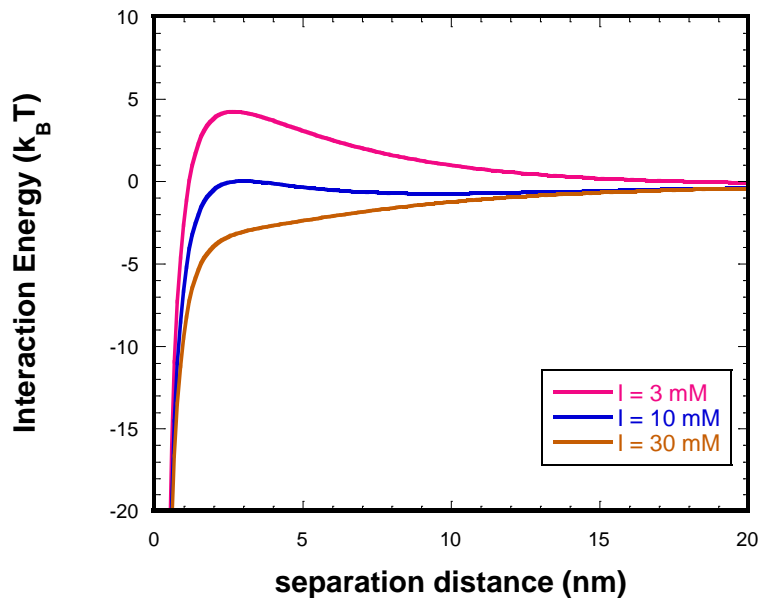
Figure 4.5 DLVO energy between two 30 nm sized AgNPs with a zeta potential of -25.7 mV (A_H was assumed to be 10E20 J)

In Figure 4.5, each line represents the overall interaction energy of AgNPs at the different ionic strengths. The height of energy barrier is inversely related to the magnitude of the ionic strengths (*i.e.*, the energy barrier diminishes with increasing ionic strengths). The energy barrier of 5 k_BT was found at a separation distance of 2 nm when the ionic strength was 3 mM. However, the height of the energy barrier was reduced to 0 k_BT when ionic strength increased to 10 mM. Once the ionic strength was raised to 30 mM, not only the energy barrier, but also the majority of the graph was shifted downward and located in the negative side of interaction energy. Under this condition, AgNPs are attracted to each other over the entire separation distance. These DLVO energy graphs demonstrate that the required momentum in the course of collisions of AgNPs to overcome the energy barrier and reach the primary minimum is reduced with increased ionic strength of the background electrolyte.

The measured number concentrations from the experiments (Figure 4.4) qualitatively agreed with the results of theoretical calculations (Figure 4.5). According to the DLVO calculation (Figure 4.5), superior flocculation should take place with increasing ionic strength. This trend was clearly observed for experimental results at I = 3, 10, and 30 mM when compared to 10 or 30 mM. However, the total number concentrations at I = 30 and 10 mM were quite similar to one another, contrary to the expectations based on the DLVO calculations.

Differences in the extent of flocculation between I = 10 and 30 mM are better demonstrated by the fractional changes in the particle sizes during flocculation, as shown Figure 4.6. Figure 4.6A illustrates the fractional changes in particle sizes under I = 3 mM condition. The fractions of the small and large sized particles maintained their initial fractions of 70% and 30%, respectively. After an hour of flocculation for I = 10 mM (Figure 4.6B), the small and large sized particles represented 55% and 45% of the total particle population detected, respectively. When the ionic strength was set at 30 mM (Figure 4.6C), remarkable fractional changes in the particle size occurred. The fraction of the small sized particles decreased rapidly while the fraction of the large size particles soared. At the end of the flocculation experiment, the large sized particles were approximately 97% whereas the small sized particles were only 3%. This result proves more effective flocculation occurred at the ionic strength of 30 mM than 10 mM.

A) Experiment #10: I = 3 mM

B) Experiment #9: I = 10 mM
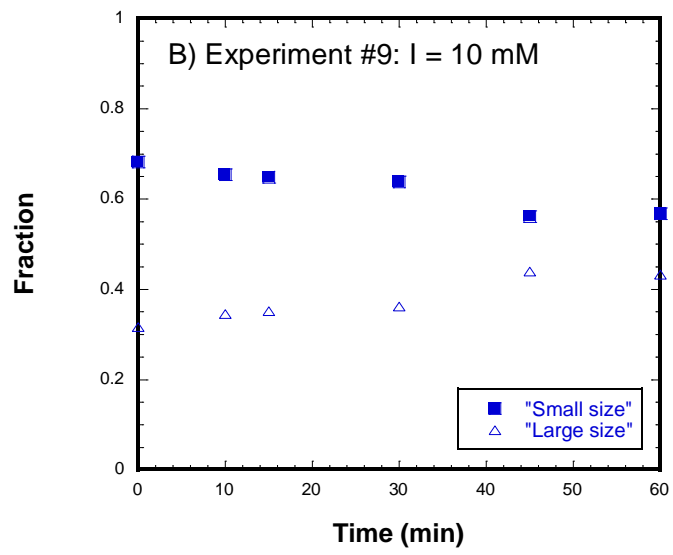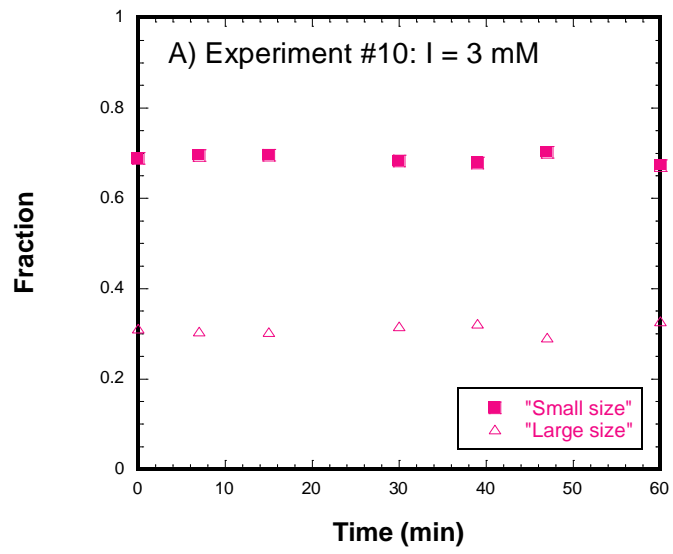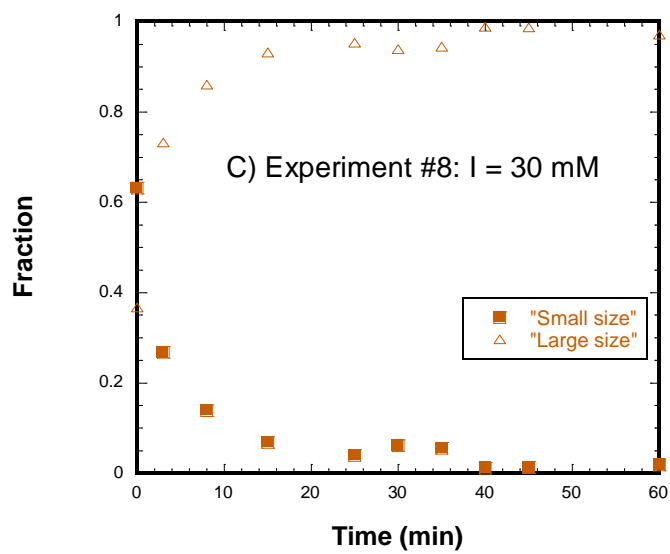
Figure 4.6 Particle Number Fractions during flocculation for the 30 nm AgNPs with A) I = 3 mM B) 10 mM and C) 30 mM of NaNO₃

Comparably designed flocculation experiments for the 50 nm (Experiments #13 and #15) and 100 nm (Experiments #1 and #2) sized AgNPs demonstrated consistent outcomes (The evolution of the particle size distributions for these experiments are exhibited in Appendix A). Figure 4.7 represents the changes in the total number concentrations of the 50 nm and 100 nm sized AgNPs under varying ionic strengths. For both 50 nm and 100 nm sized AgNPs, more successful flocculation was acquired by higher ionic strengths.
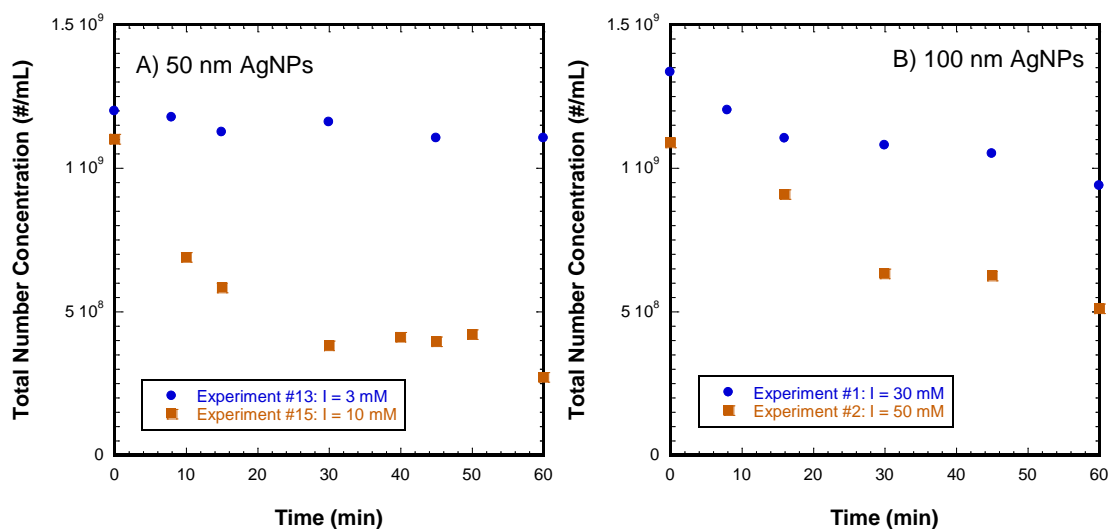
Figure 4.7 Total number concentrations of A) 50 nm and B) 100 nm of AgNPs under
different ionic strengths.

With the identical assumptions used for Figure 4.5 for zeta potential, calculated DLVO
energy at given ionic strengths for the 50 and 100 nm sized AgNPs are plotted in Figure
4.8. Comparable to the previous calculation of the 30 nm sized AgNPs, the height of the
energy barrier is distinctly lower as ionic strength is increased.
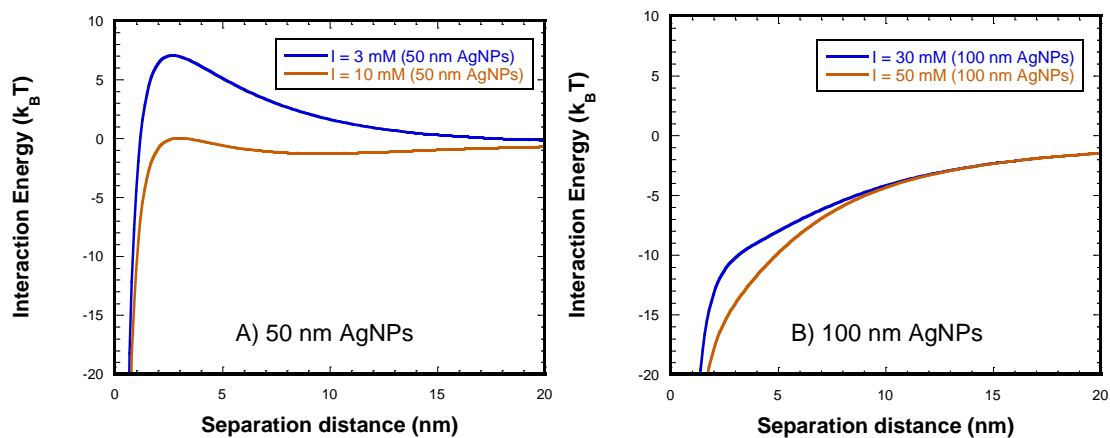
Figure 4.8 DLVO Energy calculations for AgNPs of A) 50 nm and B) 100 nm

The effects of the ionic strength of the destabilizing agents on various sized citrate capped AgNPs were consistent with theoretical understanding of particle destabilization.

4.3.2 Effect of Destabilizing Mechanisms

Calcium ions have a higher affinity than sodium ions to form complexes with citrate ions (Morel and Hering, 1993); therefore, the surface charge of citrate stabilized AgNPs is expected to be more effectively neutralized by $Ca(NO_3)_2$ than $NaNO_3$. That is, $Ca(NO_3)_2$ would destabilize citrate capped AgNPs by adsorption and charge neutralization as well as by compression of the double layer, whereas $NaNO_3$ would only use the latter mechanism. Many previous scholars have experimentally investigated destabilization and flocculation of citrate stabilized AgNPs using different background electrolytes (El Badawy *et al.*, 2009; Cumberland and Lead, 2009; Huynh and Chen, 2011; Baalousha *et al.*, 2013). These cited studies have tried to illuminate the role of capping layers of AgNPs on particle stability with respect to various destabilizing ions such as sodium, calcium, and magnesium. Calcium and magnesium ions were found to be far more effective than sodium ions in reducing the stability of citrate-capped AgNPs; the authors hypothesized that calcium and magnesium complexed with citrate capping layers which led to charge neutralization. In addition, Huynh and Chen (2011) presented experimental results that citrate AgNPs was better destabilized by calcium than magnesium ions because the stability constant of monodentate calcium citrate complexes was higher than that of monodentate magnesium citrate complexes. When AgNPs had poly-vinylpyrrolidone (PVP) capping instead of citrate capping, charge neutralization effects of calcium or magnesium on AgNPs were not observed because there was no complexation between the capping and the destabilizing ions in that scenario. A

preliminary study of our research group verified such relationship between citrate capping layers of AgNPs and sodium and calcium ions (Lawler *et al.*, 2013).

Based on the changes in the mean hydrodynamic diameters of citrated capped AgNPs under the two different electrolytes, theoretical understanding of the destabilization mechanisms between calcium and sodium ions was verified.

In the present study, effects of the destabilization mechanisms of these two electrolytes (sodium and calcium) were studied from the absolute changes in the particle number distributions obtained from NTA instead of the relative size measurements of DLS. The three sets of the flocculation results (Experiments #1-3-4, #10-11, and #13-14) visualized the role of the destabilizing agents on flocculation dynamics of the three sizes of citrate capped AgNPs. Figures 4.9A and B show the evolution of the particle size distributions of the 30 nm sized AgNPs under the ionic strength of 3 mM achieved by NaNO$_3$ and Ca(NO$_3$)$_2$, respectively. The evolution of the particle size distributions for the 50 and 100 nm sized AgNPs are exhibited in Appendix A.
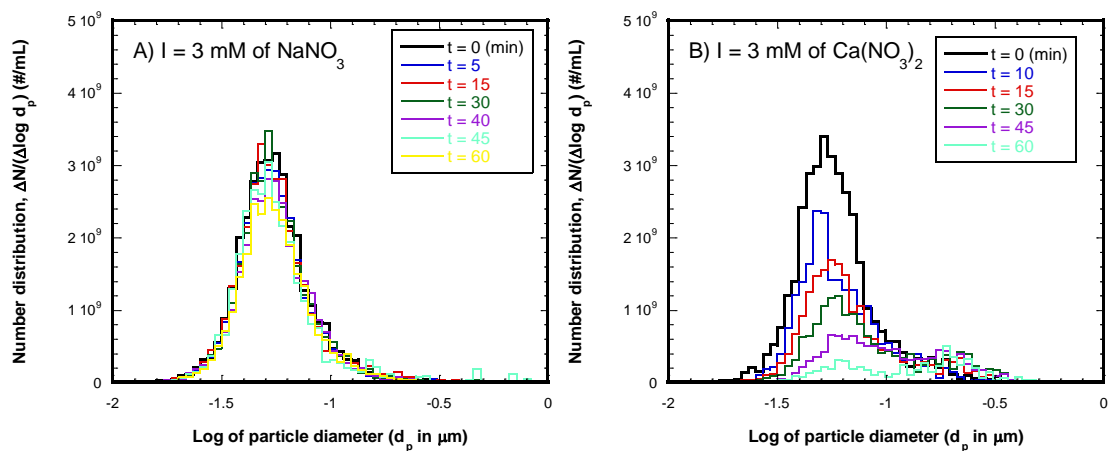
Figure 4.9 The evolution of the particle size distribution of the 30 nm sized AgNPs at I = 3 mM A) of NaNO$_3$ and B) Ca(NO$_3$)$_2$

Figure 4.10 A-C display reductions in the total particle number concentrations for the three sized AgNPs. For each size of AgNPs, the identical ionic strengths were tested with both $NaNO_3$ and $Ca(NO_3)_2$. The target ionic strengths for the 30, 50 and 100 nm sized AgNPs were 3, 3, and 30 mM, respectively. Regardless of the initial size of AgNPs, more significant reductions in the total number concentration of AgNPs were observed under calcium destabilization than sodium destabilization. These results concurred with the conclusions suggested by previous scholars that calcium ions are a better destabilizing agent than sodium ions for citrate capped AgNPs.

Along with $NaNO_3$ and $Ca(NO_3)_2$, $Na_3C_6H_5O_7$ (trisodium citrate) was additionally used for a 100 nm AgNPs flocculation experiment. Trisodium citrate dissolves in water into sodium and citrate ions. The pK_{a1}, pK_{a2}, and pK_{a3} values for citric acid ($C_6H_8O_7$) are 3.13, 4.72, and 6.33, respectively (Benjamin, 2002). Citric acid maintains the least protonated state of -3 (citrate ion) at the experimental pH condition (pH ~ 7.1). The effect of the trivalent ion as a destabilizing agent on flocculation of AgNPs was conducted at an ionic strength of 30 mM of trisodium citrate. Because there should be no complexes formed between the citrate capping layer and background ions of sodium and citrate, the destabilizing mechanism of trisodium citrate was also predicted to be compression of the double layer. Figure 4.10C shows that the flocculation result in the trisodium citrate electrolyte was almost identical to the result in the sodium nitrate electrolyte.

67
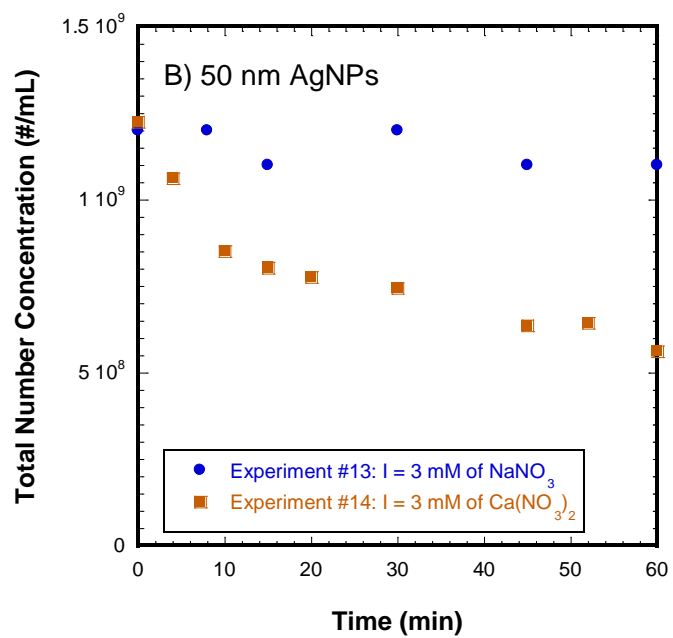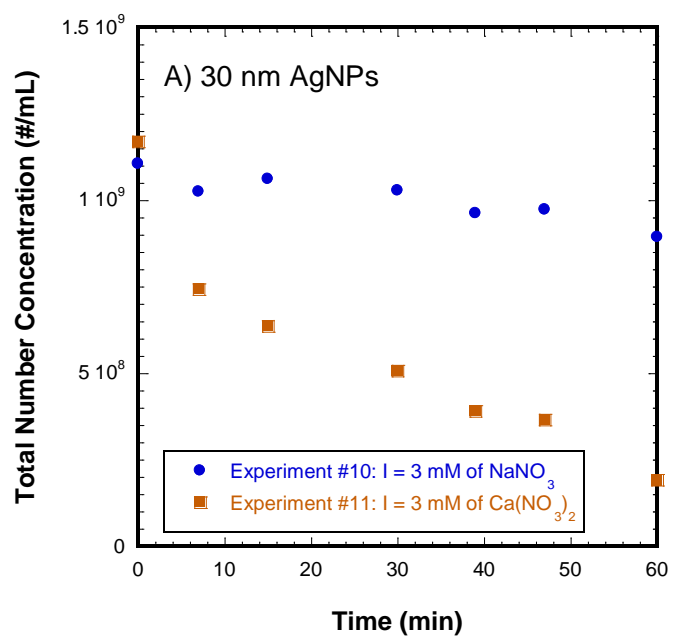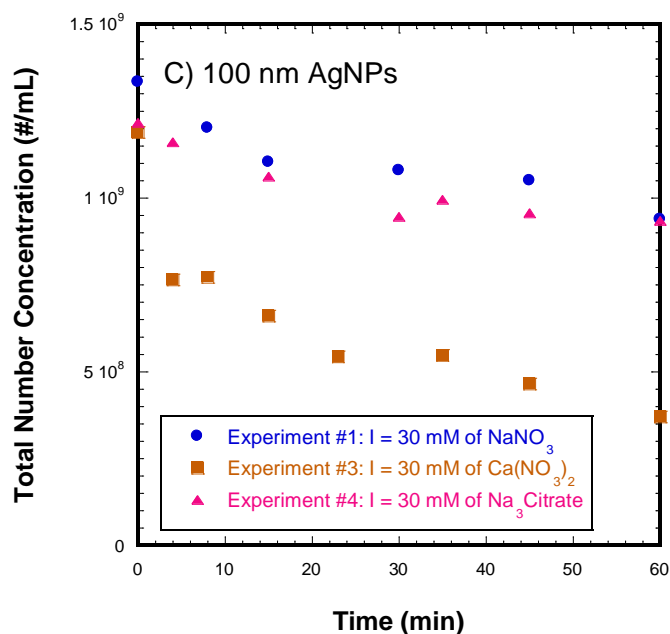
Figure 4.10 Changes in the total number concentrations with different destabilizing agents for the A) 30, B) 50, and C) 100 nm sized AgNPs

The distinction between the two destabilizing mechanisms in AgNP flocculation becomes more prominent when analyzing the changes in the particle number fractions of each experiment. Figure 4.11 shows the changes in the particle fraction for the 30 nm AgNPs when flocculation was induced by $NaNO_3$ and $Ca(NO_3)_2$ at an identical ionic strength of 3 mM. The fractional ratio between small and large size particles did not show much change when $NaNO_3$ was used. However, the percentage of the small particles decreased from 70% to 20% after an hour of flocculation brought about by $Ca(NO_3)_2$. Much more effective flocculation occurred when citrate capped AgNPs were destabilized by $Ca(NO_3)_2$. Consistent results were obtained for the 50 and 100 nm AgNPs (not shown).
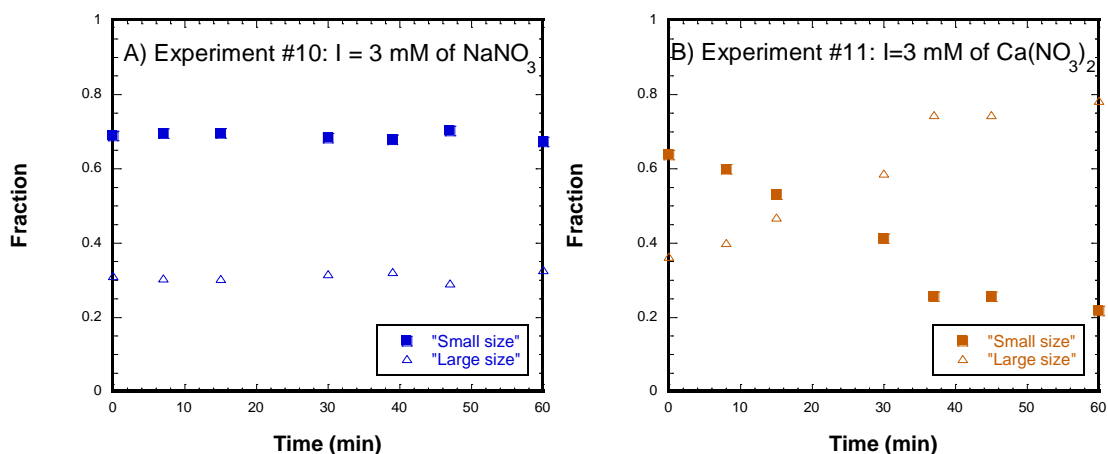
Figure 4.11 Particle fraction for Experiment #10 and #11

The zeta potential measurements from electrophoretic mobility also support the argument that calcium ions destabilize citrate capped AgNPs by charge neutralization (or near neutralization) rather than by compression of the double layer with sodium ions. For example, at an ionic strength of 30 mM, NaNO₃ weakened the initial zeta potential for the 100 nm AgNPs from -50.9 mV to -27.5 mV whereas the zeta potential changed to -8.94 mV for Ca(NO3)₂. Figure 4.12 illustrates the calculated DLVO energy of the measured zeta potentials for 100 nm sized AgNPs. The reduced surface charge (ergo, zeta potentials) for the calcium ion condition lowered the energy barrier of interaction between AgNPs. Under the calcium destabilization, citrate stabilized AgNPs are expected to be favorable to form flocs as demonstrated by having its entire energy curve lie below zero.
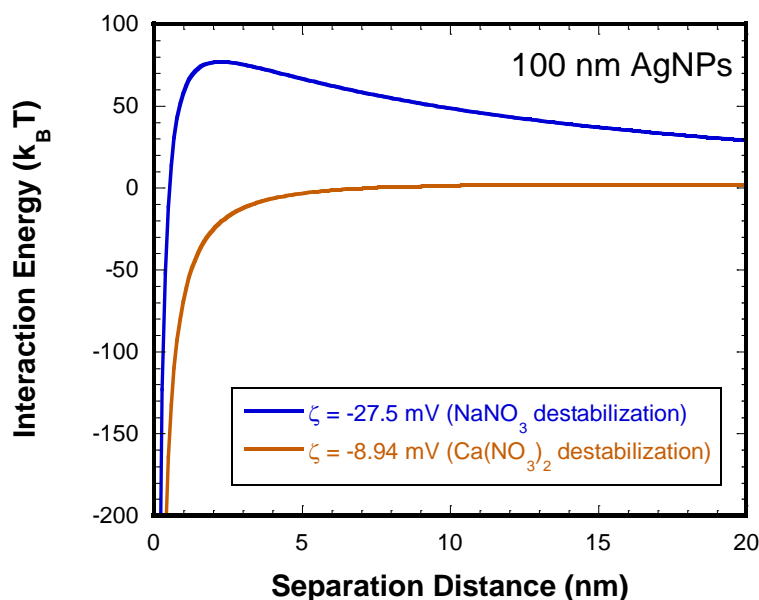
Figure 4.12 Calculated interaction energy for the 100 nm sized AgNPs under two zeta
potential conditions. I = 0.1 mM for both conditions.

4.3.3 Effect of the Initial Concentration of Nanoparticles

As discussed in Chapter 2, flocculation is a second-order reaction with respect to

the particle number concentration. For this reason, the initial concentration of particles

dictates reaction kinetics in flocculation (Benjamin and Lawler, 2013). To comprehend

how the dynamics of nanoparticle flocculation were impacted by different initial

concentrations of AgNPs, the absolute size and number concentrations during

flocculation must be simultaneously acquired. Because DLS only gives the relative value

such as the intensity of scattered light (not the actual number concentration of

nanoparticles), DLS is not suitable to provide the information required for the present

study. The effects of initial concentration of AgNPs on flocculation kinetics were

scrutinized based on the real-time measurements of the size and number concentration of

AgNPs made by NTA. One of the advantages of employing NTA is that the technique

provides the absolute number counts and size measurements at the same time. This is also

71

the major distinction of this work from other scholar's previous nanoparticle aggregation studies which were mainly based on relative measurements (*e.g.*, investigation on changes of mean hydrodynamic sizes of nanoparticles over time).

Figure 4.13 A and B display the evolutions of the particle size distributions of the 100 nm sized AgNPs during flocculation experiments with two different initial number concentration conditions (Experiments #1 and #5).
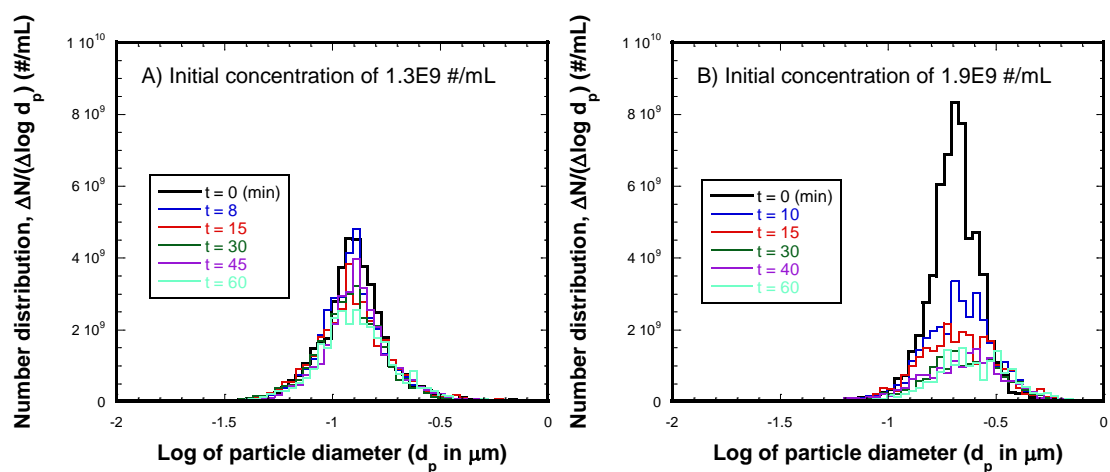
Figure 4.13 The particle size distributions of the 100 nm sized AgNPs for the initial number concentration of A) 1.3E9 #/mL and B) 1.9E9#/mL

Once again, the particle size distributions were converted to the total number concentration for systematic examinations. Figure 4.14A shows the declines in the total number concentration of the 100 nm sized AgNPs with two different initial number concentration conditions (Experiments #1 and #5). Flocculation was achieved by an addition of I = 30 mM of $NaNO_3$. Over an hour of flocculation, the initial concentration of 1.3E9 #/mL was reduced to 1.0E9 #/mL (77% of its initial value) for Experiment #1 whereas the initial concentration of 1.9E9 #/mL was lowered to 5.0E8 #/mL (only 23% of the initial concentration) for Experiment #5. More robust flocculation took place in with the higher initial particle number concentration even though all other experimental conditions were identical for the two experiments.

Similar results were observed when flocculation of the 30 nm sized AgNPs was induced by 3 mM of $NaNO_3$ as shown in Figure 4.14B (The particle size distributions are shown in Appendix A). When the initial particle concentration was set at 1.1E9 #/mL for Experiment #10, the final number concentration (9E8 #/mL) was approximately 82% of its initial concentration. However, the increased initial particle concentration of 2.5E9 #/mL under the exact same experimental conditions (Experiment #12) showed a substantial reduction in the total number concentration. The final number concentration was 9E8 #/mL, which was only 36% of its initial particle number concentration. For both 30 and 100 nm sized AgNPs, more effective flocculation was resulted with the increased initial particle number concentrations.
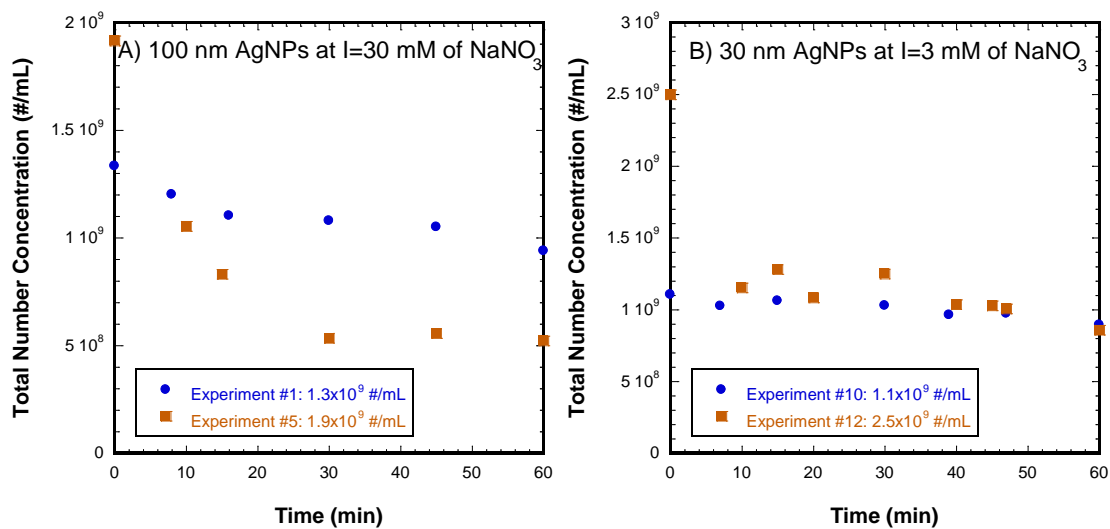
Figure 4.14 The changes of the total number concentration of A) the 100 nm sized and B) the 30 nm sized AgNPs

The influences of the initial concentration on flocculation kinetics can be also readily seen by examining changeovers in the number fraction of the small and large particles during flocculation experiments. Figure 4.15 show the fractional changes of Experiments #1 and #5 (Figure 4.14A) where flocculation of 100 nm sized AgNPs was induced by 30 mM of $NaNO_3$ at two different initial particle number concentration. The fractional ratio between small and large particles was barely altered in Experiment #1 whereas a reversal in the fractional ratio was detected in Experiment #5.
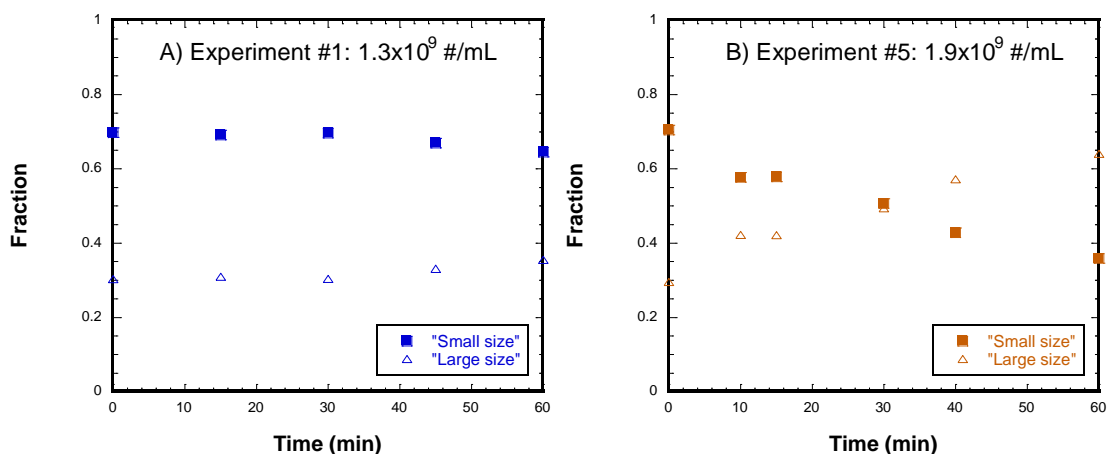
Figure 4.15 The fractional changes during the flocculation experiments of the 100 nm
sized AgNPs brought about by I = 30 mM of $NaNO_3$ with initial number
concentrations of A) 1.3E9 and B) 1.9E9 #/mL

Although these results are consistent with the Smoluchowski principle that flocculation

kinetics depend on the initial number concentration of particles, this result may seem

counterintuitive knowing that the interaction energies (DLVO) are exactly the same for

AgNPs regardless of the particle concentration when destabilization conditions and

particle size are identical. However, recall that in the short-range model proposed by Han

and Lawler (1992), described in Chapter 2, flocculation is a function of the number of

particles in the system and the collision frequency and efficiency correction functions.

The particle destabilization determines the probability of a floc being formed from each

collision between particles (*i.e.*, collision efficiency). If destabilization is achieved by an

identical mechanism for two systems, the likelihood of creating a new floc from each

collision is also identical for the two systems (*i.e.*, the same collision efficiency). If one

system contains a higher number of particles, there will be a greater chance for each

particle to collide with other particles compared to a system that has lower particle

numbers while the probability of forming flocs from each collision is the same. For this

reason, greater flocculation is always expected in a system that has a higher initial particle concentration if all other physiochemical conditions are the same.

4.3.4 Effect of Natural Organic Matter

Particles in engineered systems and natural waters are generally coated with natural organic matter (NOM). NOM originates from various sources including the activity and decay of plants, bacteria, or animals in water. In water treatment, the presence of NOM has been of particular concern for several reasons. First, the reaction between NOM and oxidants (disinfectants) in water treatment causes the formations of disinfection by-products (DBPs) that have negative health impacts. Secondly, the adsorption of NOM onto the surface of particle alters their stability and impacts the fate and transport of the particles in water treatment processes (O'Melia *et al.*, 1999). Lastly, the presence of NOM lowers the treatment efficiency by adsorbing onto filtration media or forming foulants in membrane systems in water and wastewater treatment (Benjamin and Lawler, 2013). A substantial amount of research has been conducted to comprehend the role of NOM in water and wastewater treatment process (Siddiqui *et al.*, 1997; Edzwald and Tobiason, 1999; Craun *et al.*, 2001; Roalson *et al.*, 2003; Sharp *et al.*, 2006; Zularisam *et al.*, 2006; Bull, 2006).

In spite of the extensive research, virtually no study has been conducted for the evolution of the absolute particle size distributions of nanoparticles in the presence of NOM during flocculation in water treatment. The interaction between stabilizing agents of engineered nanoparticles, coagulants, and NOM would modify the stability of nanoparticles; therefore, the fate and transport of nanoparticles in the presence of NOM might be significantly different from the ideal condition where no NOM is present. The aim of this study was to investigate the effect that the presence of Suwannee River

aquatic NOM had on the evolution of the absolute particle size distributions during laboratory scale batch flocculation experiments.

Figure 4.16 shows the evolutions of the particle size distributions during the flocculation experiments of the 100 nm sized citrate stabilized AgNPs that had I = 50 mM of $NaNO_3$ in the presence and absence of NOM (Experiments #2 and #6).
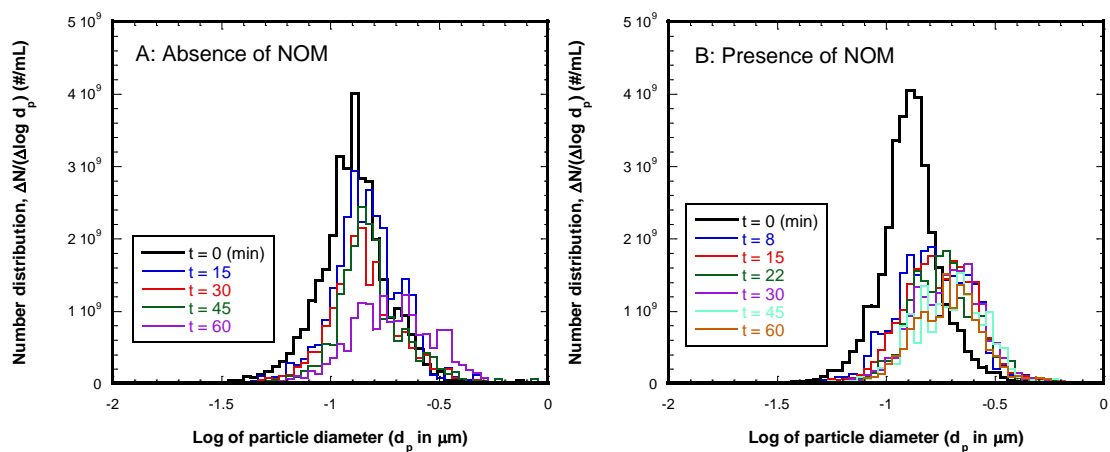
Figure 4.16 The particle size distributions for the 100 nm sized AgNPs in A) the absence of NOM and B) the presence of NOM

Along with the evolution of the particle size distributions, the total number concentrations and fractional changes during the flocculation were plotted as shown in Figures 4.17 and 4.18, respectively. Comparable declining trends were found in the total number concentration graph under the given condition whether NOM was present or not in the system (Figure 4.17). The almost identical initial (1.1E9 #/mL) and final number concentrations (5.0E8 #/mL) were obtained with minor deviations in between. Fractional changes, Figure 4.18, shows the particle size growth of AgNPs appeared to be faster in the presence of NOM (3.5 mg/L as DOC) even though the initial and final fractional ratios were similar regardless of the NOM conditions. The percentages of small and large

particles intersected within the first ten minutes of flocculation when NOM was present whereas the fractional turnover occurred in the last fifteen minutes in the absence of NOM. As mentioned earlier, the compression of the diffuse layer is suggested as the main destabilizing mechanism of the $NaNO_3$ electrolyte on citrate stabilized AgNPs in the absence of NOM. This result (rapid size growth of AgNPs) suggests that in the presence of NOM, there might be additional destabilizing effects along with the compression of the diffuse layer by $NaNO_3$.
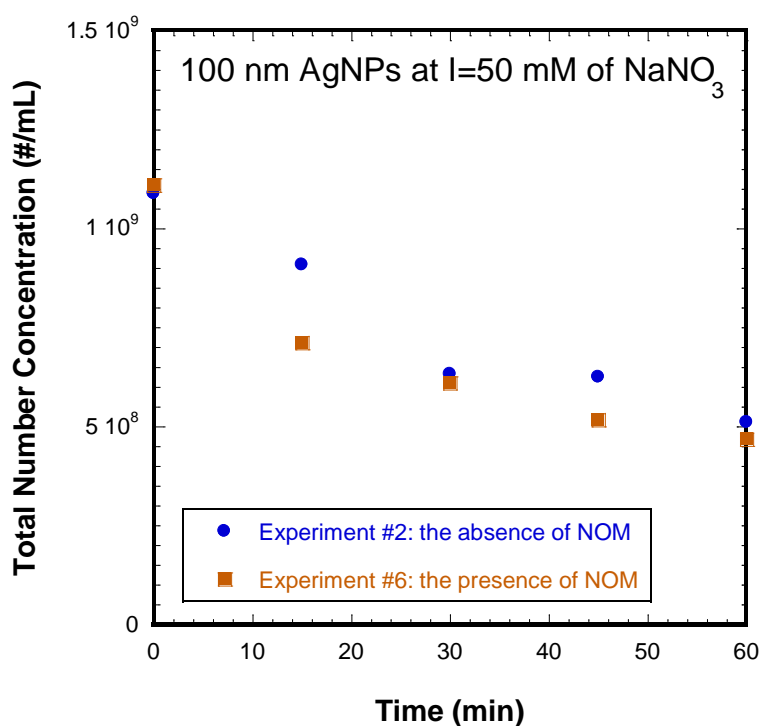
Figure 4.17 The changes in the total number concentration of the 100 nm sized AgNPs in the presence and absence of NOM when flocculation was induced by I = 50 mM of $NaNO_3$
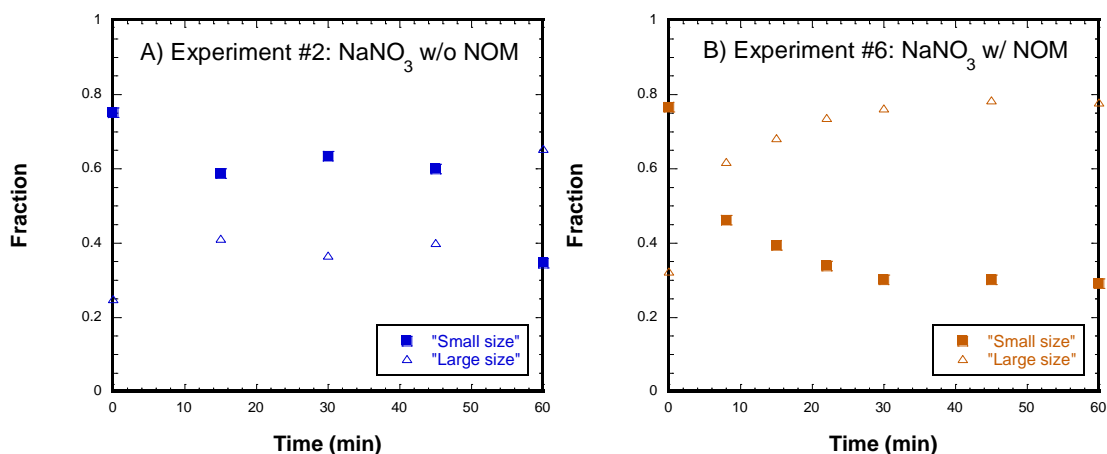
Figure 4.18 The fractional changes during flocculation by $NaNO_3$ for the 100 nm sized AgNPs in A) the presence of NOM and B) absence of NOM

Figures 4.19 and 4.20 display the changes in the total particle number concentration and number fractions, respectively, in the flocculation experiments that were attained by an ionic strength of 30 mM as $Ca(NO_3)_2$ with and without NOM (Experiments #3 and #7). The particle number distributions are attached in Appendix A. The NTA results of both the number concentration and the fractional ratios were indistinguishable whether NOM was present or not. When NOM was absent, citrate AgNPs were likely destabilized through adsorption and charge neutralization and the compression of the diffuse layer by the addition of $Ca(NO_3)_2$. The presence of NOM in the system seemed irrelevant to flocculation dynamics of citrate stabilized AgNPs under calcium destabilization.
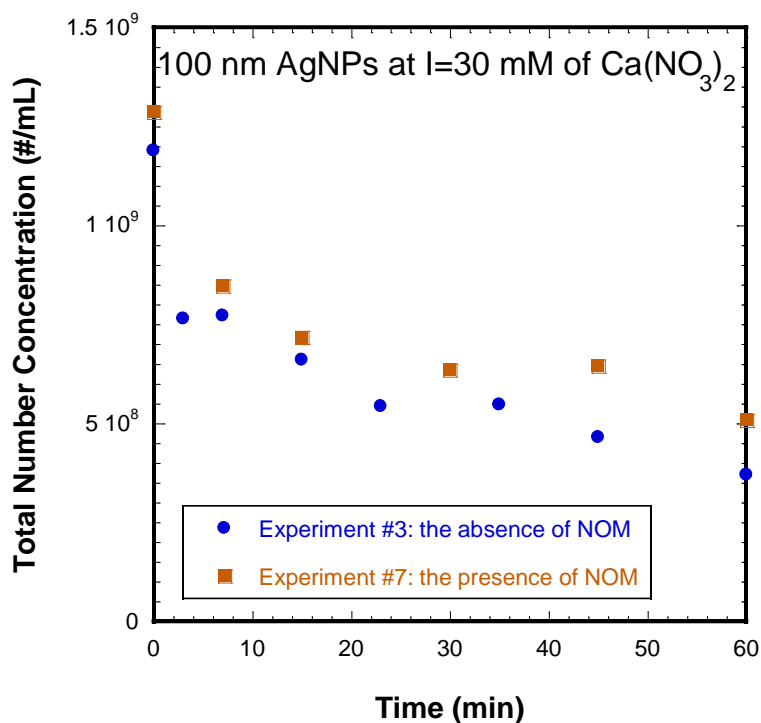
Figure 4.19 The changes in the total number concentration of the 100 nm sized AgNPs in the presence and absence of NOM when flocculation was induced by I = 30 mM of Ca(NO$_3$)$_2$
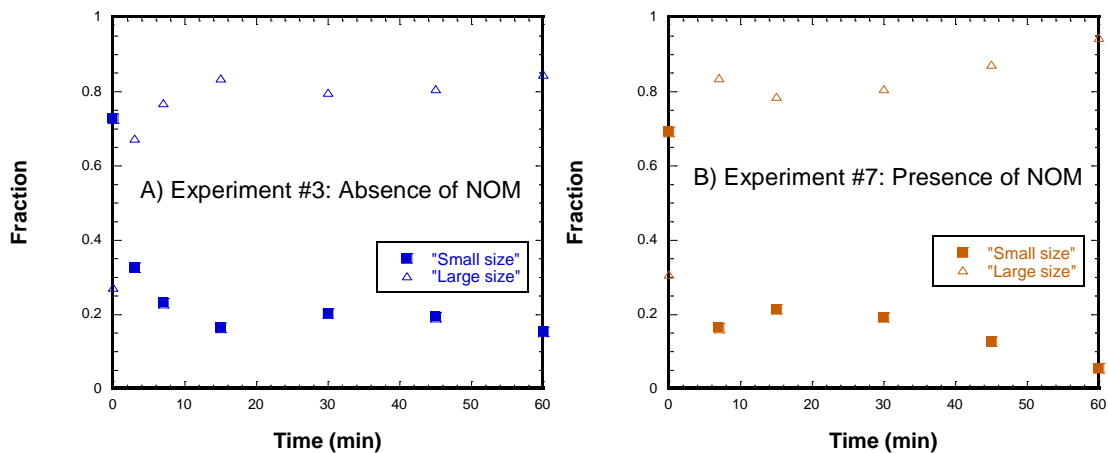
Figure 4.20 The fractional changes during flocculation by I = 30 mM of Ca(NO$_3$)$_2$ for the 100 nm sized AgNPs in A) the presence of NOM (3.5 mg/L as DOC) and B) absence of NOM

According to the International Humic Substances Society, major components of NOM in water include humic acids, fulvic acids, and humin fractions. Previous scholars agreed that the stability of citrate stabilized nanoparticles is strongly influenced by water chemistry such as pH, hardness and ionic strength as well as different types and concentrations of these NOM substances. Many scholars have studied the relation between the adsorption of NOM and the stability of citrate stabilized nanoparticles (Cumberland and Lead, 2009; Stankus *et al*, 2010; Thio *et al.*, 2011; Chinnapongse *et al.*, 2011; Furman *et al.*, 2013; Kim 2014).

Humic acid has received the most attention among these NOM components due to its effects on the stability of citrate capped AgNPs. Huynh and Chen (2011) suggested that the presence of humic acids caused electrosteric hindrance for sodium and calcium (low ionic strengths) destabilization. A preliminary study of our research group confirmed that humic acids improve the stability of citrate AgNPs under calcium destabilization while fulvic acids do not (Lawler *et al.*, 2015). Interestingly, at high concentrations of calcium in the presence of humic acids, enhanced flocculation has been observed and that enhancement has been ascribed to interparticle bridging effects. It is currently widely accepted that calcium ions cause the bridging between humic acids and nanomaterials including AgNPs, fullerene, gold, and silica (Chen and Elimelech, 2007; Huynh and Chen, 2011; Stankus *et al*, 2010; Liu *et al.*, 2011).

However, this effect was not observed in the present experiments. Slightly enhanced flocculation was observed with sodium destabilization in the presence of NOM while no substantial change in stability was noted with calcium destabilization in the presence of NOM. One possible explanation is that the NOM used for the current study was Suwannee river aquatic NOM that contains not only humic acids but also fulvic acids and humin fractions. The bridging phenomenon is dependent on the ratio between humic

and fulvic acids and the type and structure of the NOM (Baalousha *et al.*, 2013). For this reason, the results obtained here might be dissimilar to experimental results reported by other scholars.

In addition, the diffuse layer would be well compressed under I = 50 mM of NaNO$_3$ and the characteristic length of the diffuse layer (*i.e.*, Debye length, κ^{-1}) will only be 1.36 nm which is a size of glucose molecule. Under this condition, the effect of the adsorbed layers of NOM would be more significant than the diffuse layer due to the macromolecular structure of NOM. Further investigation is required to fully understand the destabilization of citrate capped AgNPs in the presence of NOM with various destabilizing mechanisms. The main focus of the present study was to emulate more realistic natural water conditions that have various components of NOM and Suwannee River aquatic NOM was suitable for the present research.

4.3.5 Effect of Particle Size

Destabilized particles in water form flocs through collisions that are caused by a combination of the three main transport mechanisms: Brownian motion, fluid shear, and differential sedimentation. As the colliding particles' size gets smaller, the influences of gravity (sedimentation) and linear shear flow (fluid shear) decrease while the diffusion coefficient (Brownian motion) increases; hence, Brownian motion is the most dominant transport mechanism in collisions of nano-sized particles in water (Han and Lawler, 1991). To scrutinize the effects of particle size on flocculation kinetics at the nanoscale, laboratory batch flocculation experiments for the 30, 50 and 100 nm sized AgNPs were examined under identical experimental conditions.

Figure 4.21 shows the reduction in the total number concentration of the 30 and 100 nm sized citrate stabilized AgNPs during flocculation that was induced by 30 mM of

NaNO$_3$ (Experiments #1 and #8). The graph clearly indicates that flocculation was achieved more successfully with the 30 nm sized AgNPs then the 100 nm sized particles. The initial particle number concentration of the 30 nm AgNPs was reduced almost an order of magnitude (from 1.1E9 to 2.0E8 #/mL) whereas the 100 nm sized AgNPs had only a slight reduction of number concentration from 1.3E9 to 1.0E9 #/mL.
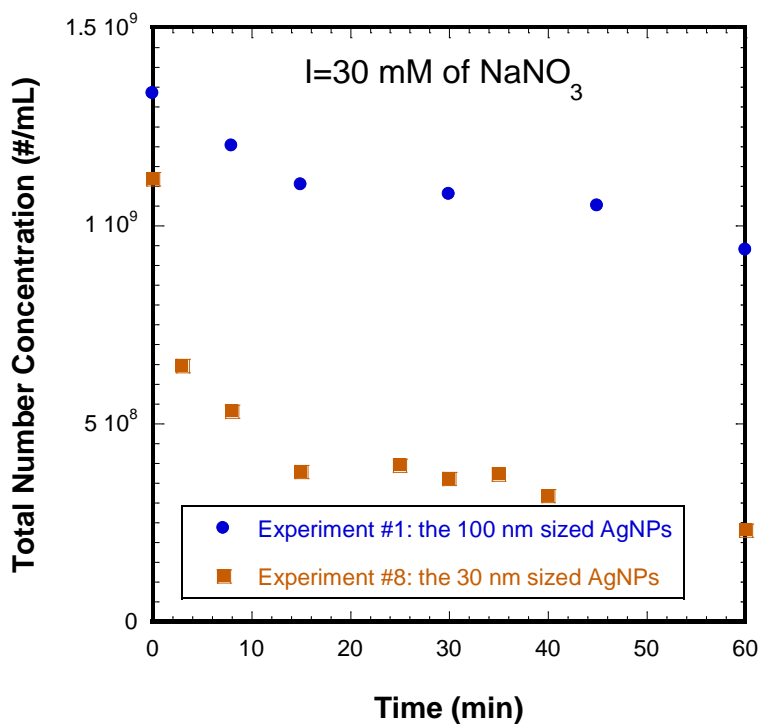
Figure 4.21 The changes in the total number concentrations of the 100 and 30 nm sized AgNPs under I = 30 mM by NaNO$_3$ (Experiments #1 and #8)

At least qualitatively, the result was consistent with theories of particle destabilization and flocculation (A more quantitative explanation is provided in Chapter 5). According to the Stokes-Einstein equation (Equation 3.1), the diffusion coefficient is inversely proportional to the particle diameter. The 30 nm sized AgNPs have a higher diffusion coefficient value than the 100 nm sized particles if all other conditions are

83

identical. The diffusion coefficient represents the ratio of the mean square displacement to time (Einstein, 1905). The 30 nm sized AgNPs, with their higher diffusion coefficient, would travel further than the 100 nm sized AgNPs with their lower diffusion coefficient, if an identical time is given. Therefore, particles with higher diffusion coefficients will have more opportunities to collide with other particles because they move intensely.

Results demonstrating this phenomenon were also obtained when similar flocculation experiments were designed for the 30 and 50 nm sized AgNPs (Experiment #11 and #14). Flocculation was brought about by 3 mM of $Ca(NO_3)_2$. Even though the difference in the size of AgNPs was not great as in the previous case, the effect of particle size between 30 and 50 nm on flocculation was also clearly observed (Figure 4.22).
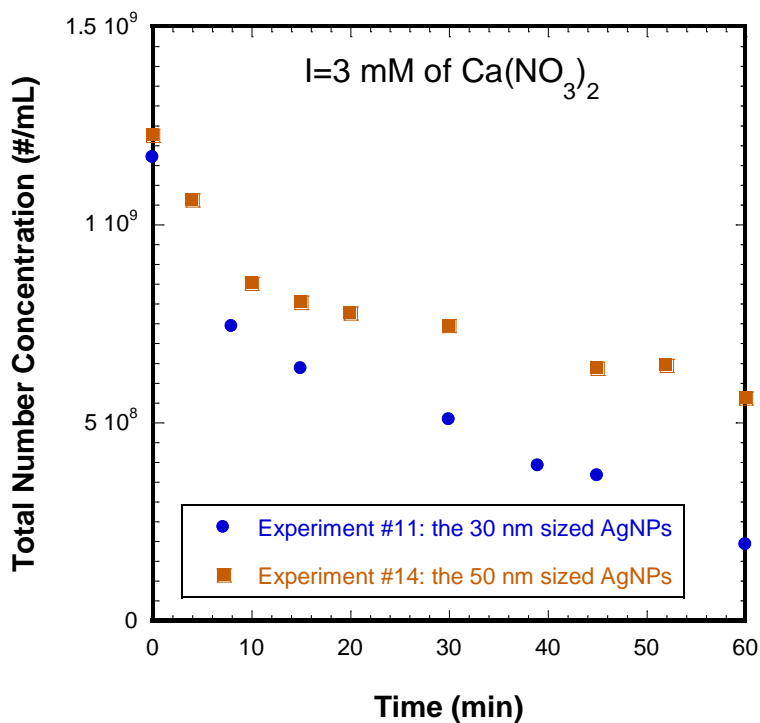
Figure 4.22 The changes in the total number concentrations of the 100 and 30 nm sized AgNPs under I = 3 mM by $Ca(NO_3)_2$ (Experiments #11 and #14)

Because the 30 nm AgNPs have a higher diffusion coefficient than the 50 nm AgNPs, more robust flocculation was found with the 30 nm sized AgNPs. The initial number concentrations were 1.2E9 #/mL for both the 30 and 50 nm AgNPs. The final number concentrations were lowered to 2E8 #/mL, and 6E8 #/mL, respectively.

4.4 FLOCCULATION EXPERIMENTS OF HETERODISPERSE SOLUTIONS

In addition to flocculation of (nearly) monodispersed AgNPs samples, the evolution of the particle size distributions for heterodispersed AgNPs were also investigated. Equal-number mixtures of the 30 and 100 nm sized AgNPs were prepared (*e.g.*, 1:1 particle number ratio between the 30 and 100 nm sized particles) and their flocculation dynamics were evaluated by NTA under the same experimental conditions (I = 10 and 30 mM of $NaNO_3$ and I = 3 mM of $Ca(NO_3)_2$) that were previously used for the monodispersed AgNPs samples. Figure 4.23 shows the evolution of the particle size distributions of the heterodispersed sample during an hour of flocculation at the two different ionic strengths of $NaNO_3$.
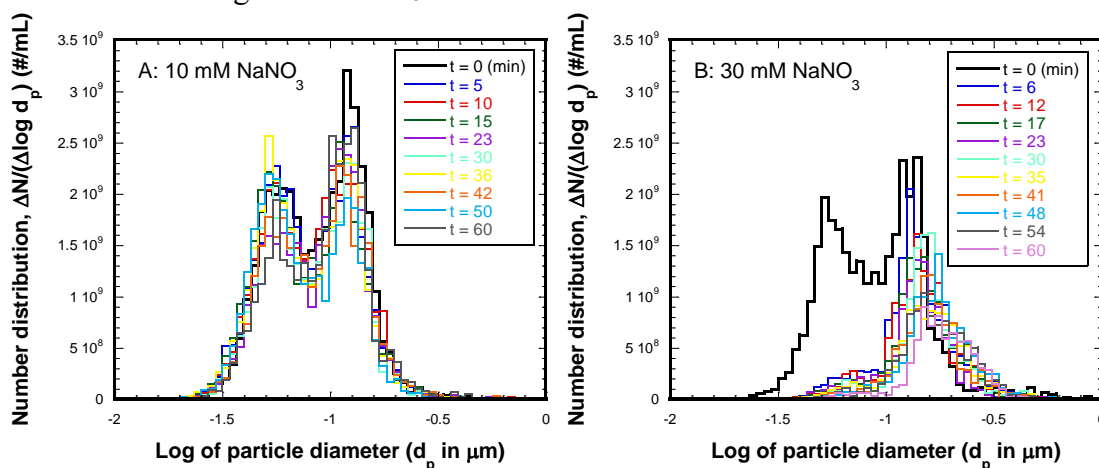
Figure 4.23 The particle size distribution of heterodispersed AgNPs at A) I =10 mM and B) 30 mM of $NaNO_3$

In addition, Figure 4.24 shows the changes in the total number concentrations AgNPs when particles were destabilized by the addition of NaNO$_3$. When the ionic strength was 10 mM, the total number concentration of the heterodispersed sample reduced to 85% of its initial values (*i.e.*, from 1.3E9 #/mL to 1.1E9 #/mL). More dramatic reduction of the initial particle number concentration was observed under the ionic strength of 30 mM of NaNO$_3$. The total number concentration became 27% of the initially value (changed from 1.1E9 to 3.0E8 #/mL) in an hour of flocculation in I = 30 mM condition.
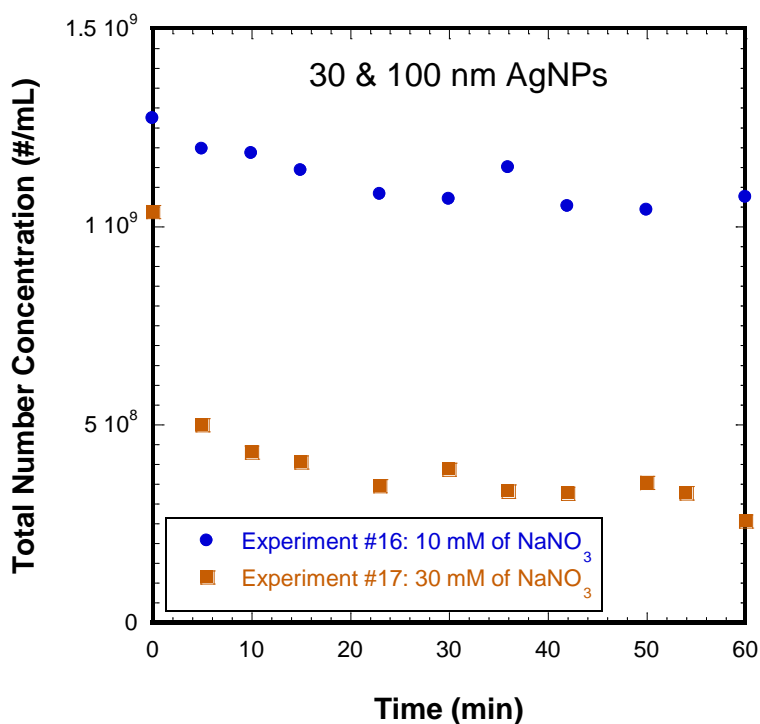
Figure 4.24 The changes in the total number concentrations of the heterodispersed
AgNPs with two ionic strengths of 10 and 30 mM by NaNO$_3$

As destabilization of monodisperse AgNPs were consistent with DLVO theory, destabilization of heterodispersed samples also corresponds to DLVO theory. Figure 4.25 shows the interaction energy of the 30 and 100 nm sized AgNPs for two ionic strengths

of 10 (Figure 4.25A) and 30 mM of $NaNO_3$ (Figure 4.25B), respectively. Under I = 10 mM condition, the 30 nm sized AgNPs are attracted to each other at any separation distance while the 100 nm sized AgNPs has an energy barrier at the separation distance of 3 nm. Therefore, the 30 nm sized AgNPs are favorable for flocculation while the 100 nm sized AgNPs are not fully destabilized. For I = 30 mM, both the 30 and 100 nm sized AgNPs are attractive and favorable for flocculation regardless of the separation distance.
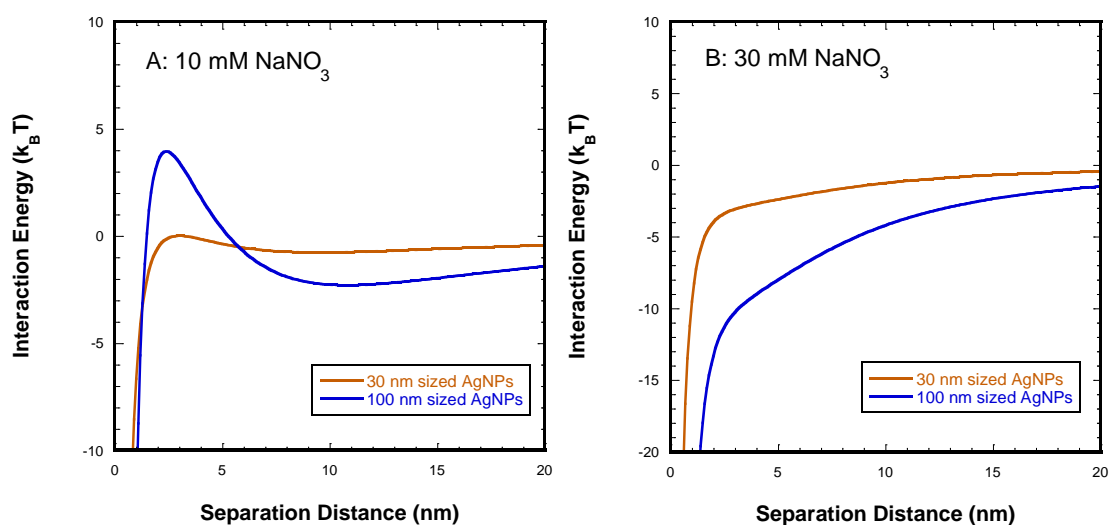
Figure 4.25 The interaction energy calculations for the 30 and 100 nm sized AgNPs when the ionic strengths were A) 10 and B) 30 mM by $NaNO_3$

It can be deduced from the interaction energy calculations that the limited flocculation was resulted under the I = 10 mM condition because only the 30 nm sized AgNPs in the heterodispersed solution form flocs. More successful flocculation took place under the ionic strength of 30 mM by $NaNO_3$ where both 30 and 100 nm sized particles were destabilized to create flocs.

In addition to $NaNO_3$, flocculation of the heterodispersed AgNPs was induced by the ionic strength to 3 mM of $Ca(NO_3)_2$. Figures 4.26 and 4.27 present the particle

distributions and the total number concentration of the heterodispersed AgNPs at the ionic strength of 3 mM by Ca(NO₃)₂, respectively. The total number concentration of the mixture of the 30 and 100 nm sized AgNPs showed almost an identical reduction trend as the flocculation result of the 30 nm AgNPs under the I = 3 mM of Ca(NO₃)₂ condition (Experiment #10). Compared to the previous experimental condition for the heterodispersed sample (I = 10 mM of NaNO₃), a more significant particle number reduction (better flocculation) is observed with the ionic strength of 3 mM of Ca(NO₃)₂. As already discussed earlier, calcium ions are a better destabilizing agent than sodium for citrate capped AgNPs because calcium ions form complexes with citrate capping ions. Calcium ions destabilize citrate capped AgNPs more effectively by adsorption and charge neutralization. For this reason, the ionic strength of calcium (3 mM) induced greater flocculation of the heterodispersed AgNPs that the sodium ions at I=10 mM.
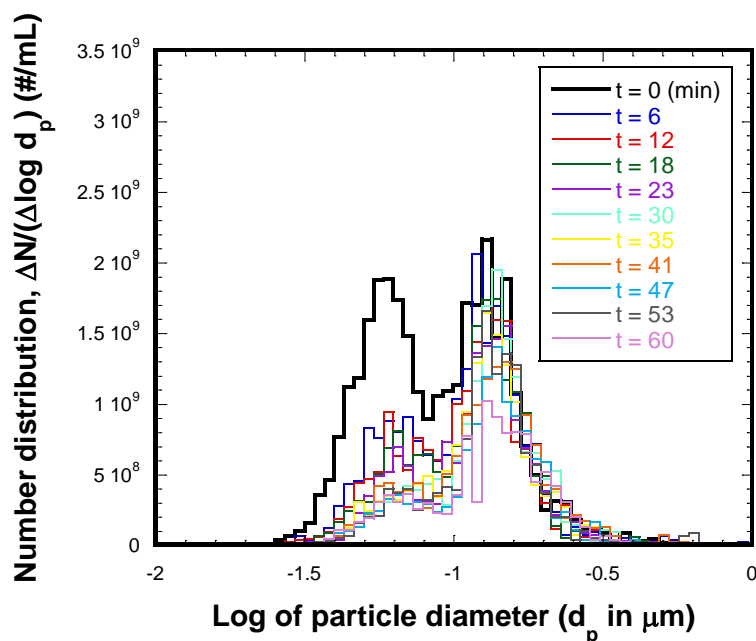
Figure 4.26 The evolution of the particle size distribution of the heterodispersed AgNPs at the ionic strength of 3 mM of Ca(NO₃)₂
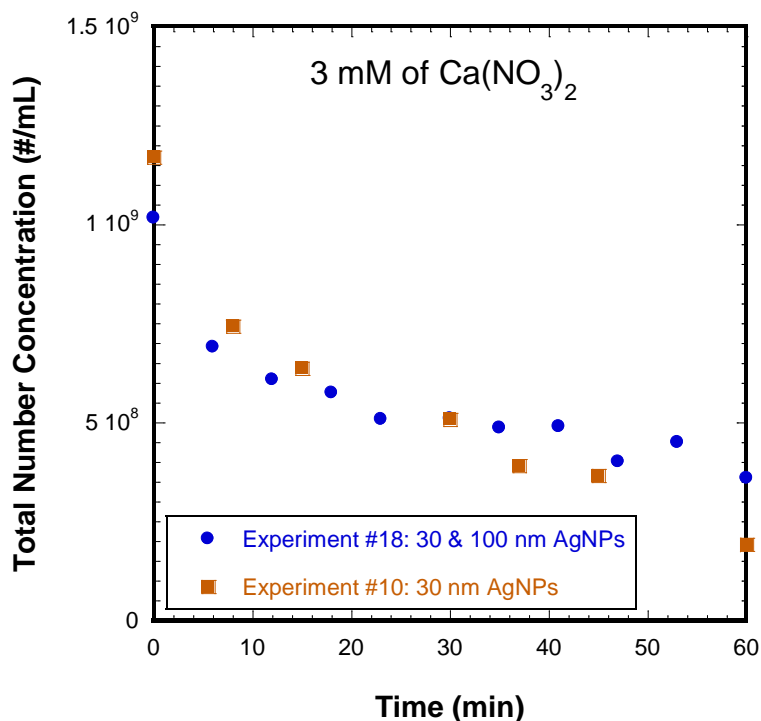
Figure 4.27 The changes in the total number concentrations of the heterodispersed AgNPs with two ionic strengths of 3 mM by Ca(NO₃)₂

4.5 SUMMARY

In previous research done by the Lawler research group, the flocculation dynamics for micro-sized particles were quantitatively explained and modelled by the short-range force model. The experimental investigations presented in this Chapter were designed to improve the understanding of how the evolution of particle number distributions changes at the nanoscale during well-controlled laboratory scale flocculation of AgNPs. The main focus was to identify the effects of operative variables on the nanoparticle flocculation rates. The findings from the experimental results have allowed further development of the mathematical model (Chapter 6).

The experimental data showed more successful flocculation of AgNPs in the electrolyte of $Ca(NO_3)_2$ than $NaNO_3$. It is thought that, due to the complexation of calcium with the citrate capping layer of AgNPs, two destabilizing mechanisms (charge neutralization and compression of the double layer) were simultaneously applied to AgNPs with $Ca(NO_3)_2$. In addition, as the ionic strength of destabilizing agents increased, more effective destabilization by compression of the double layer occurred, and therefore, successful flocculation occurred regardless of their initial particle sizes.

When Suwannee River aquatic NOM was added to the system, the flocculation dynamics of AgNPs altered to some extent. The destabilization of $NaNO_3$ seemed more efficient for citrate capped AgNPs in the presence of NOM than in the absence of NOM, whereas the effect of NOM was not noticeable in the destabilization of $Ca(NO_3)_2$. It appears that NOM is an important factor to consider for the fate and transport of AgNPs.

Because flocculation is a second-order reaction with respect to particle number concentration, the flocculation rate was strongly influenced by the initial number concentration of AgNPs. More robust flocculation took place in a sample of a higher particle number concentration.

The experimental data also revealed the relationship between the initial particle size and the flocculation dynamics. If all other conditions are identical, flocculation was more vigorous with the 30 nm sized AgNPs than the 50 nm or 100 nm particles. Even, when the mixtures of the 30 and 100 nm sized AgNPs were tested, the reductions of the 30 nm sized occurred before the 100 nm.

The qualitative results of this Chapter are broadly applicable to water treatment processes: nanoparticles can be expected to be flocculated into much larger sizes in conventional water treatment plants regardless of their initial sizes if they are properly destabilized.

Chapter 5: Results of Numerical Computation and Trajectory Analysis

5.1 INTRODUCTION

For the short-range force model to accurately predict the flocculation process in water treatment, the collision efficiency function, α for the three collision mechanisms (Brownian motion (Br), fluid shear (Sh), and differential sedimentation (Ds)) must be quantified carefully. However, calculating the α values is rather demanding due to the complexity of hydrodynamic and interparticle forces between two interacting particles (Benjamin and Lawler, 2013). Han and Lawler (1991, 1992) performed numerical analysis to calculate the collision efficiency functions for Brownian motion and differential sedimentation (α_{Br}, and α_{Ds}, respectively) when the larger particle in the two-particle collision was one micrometer or larger. They also reported the collision efficiency function for fluid shear, α_{Sh} based on Adler's global capture efficiency (1981b). Han and Lawler published third order polynomial fits to the numerical solutions of the α_{Br}, α_{Ds}, and α_{Sh} values. Since then, by using the polynomial equations, the α values can be easily quantified without performing arduous numerical analysis. Later, it was confirmed that the predictions of particle collisions made from the α_{Br}, α_{Ds}, and α_{Sh} values from the polynomial fits were in close agreement with experimental results (Li, 1996; Lawler and Nason, 2005; Nason, 2006).

The main objective of the present study is to extend the α values to correspond for collisions between nano-sized particles or nano- and micro- sized particles. Because nano-sized particles were not initially included in Han and Lawler's work, it is necessary to execute numerical analysis to acquire the α_{Br}, α_{Ds}, and α_{Sh} values at the nanoscale. The mathematical derivation and solutions for numerical calculation and trajectory analysis for collision efficiency function (α) at the nanoscale are detailed here.

5.2 MATHEMATICAL FRAMEWORK

First of all, to precisely emulate particle collisions in water through the three principal transport mechanisms, the movement of the fluid around the two interacting particles must be taken into account during the course of collisions. In addition to hydrodynamics, the interparticle potential energy between the two interacting particles must be incorporated. In this Chapter, detailed mathematical derivations for the hydrodynamics and potential energy of interacting particles are given first. These fundamentals underlie the numerical computations and trajectory analysis that follow. The mathematical derivations closely follow pioneering works of previous scholars. For example, the derivations for collision efficiency functions of Brownian motion and differential sedimentation stems from Han and Lawler's original work (1991, 1992) and the deductions of the collision efficiency functions for fluid shear come from Adler (1981b) and Tandon and Diamond's works (1997).

5.2.1 Governing Equations for Two Particle Movement

The famous Navier-Stokes equations explain the dynamics of an incompressible Newtonian fluid. Creeping motion of an incompressible fluid around moving bodies far from containing boundaries at low Reynolds number can be represented by simplified Navier-Stokes equations. Leaving out the time dependence and the advective terms in the original Navier-Stokes equations, the simplified equations can be derived, which are called Stokes flow, as follows (Lautrup, 2011):

$$\nabla^2 \mathbf{v} = \frac{1}{\mu} \nabla p \qquad\qquad (5.1)$$

$$\nabla \cdot \mathbf{v} = 0 \qquad\qquad (5.2)$$

where **v** is fluid velocity, p is dynamic pressure, and μ is dynamic viscosity. The fluid movements around a spherical particle in an incompressible fluid can be obtained by solving Equations (5.1) and (5.2).

Since the development of the Navier-Stokes equations, many scholars have expanded the theory for the hydrodynamic of a single spherical particle to the theory for the hydrodynamics of two spherical particles. Jeffery (1915) first derived the solutions to hydrodynamics for two equal-sized rotating spheres. The hydrodynamic solutions were then extended by other scholars to more complex conditions such as unequal-size particles, both rotational and translational motions, and both far and near fields (Stimson and Jeffrey, 1923; Goldman *et al.*, 1966; Majumdar, 1967; Cooley and O'Neill, 1969; Davis, 1969, O'Neill, 1969; O'Neill and Majumdar, 1970; Spielman, 1970; Nir and Acrivors, 1973; Jeffery, 1982; Jeffrey and Onishi, 1984). However, the numerical solutions (in series forms) to Equations (5.1) and (5.2) yields very poor convergence at the small separation distance of the two particles because the near-field solution was initially derived (Brenner 1966; Goldman et al., 1966) for the boundary condition where a sphere approaches a wall. To avoid this shortcoming, Jeffery and Onishi (1984) took an innovative method that utilized the concepts of resistance and mobility tensors to represent the torque vector (force) and spin vector (velocity). They summarized all the reported hydrodynamic solutions as the elements of these tensors. Although some solutions at near field did not produce completely explicit solution forms, Jeffrey and Onishi's hydrodynamic solutions are useful because their solutions are a superset of all the previously known solutions prior to them. Batchelor's method (1982) is used to relate Jeffrey and Onishi's mobility tensor to the velocities.

94

5.2.2 Velocities of Two Particles

Consider a system of two spheres that have radii of a_1 and a_2 with their centers located at $\mathbf{x_1}$ and $\mathbf{x_2}$, respectively. The velocity field of each particle is the summation of velocities caused by external forces such as gravity, interparticle forces, or Brownian motion:

$$\mathbf{U} = \mathbf{U_{gravity}} + \mathbf{U_{interparticle\ force}} + \mathbf{U_{Brownian\ motion}} \qquad (5.3)$$

Because of a symmetrical configuration about the center-to-center direction $\mathbf{r}$, mobility tensors are written as:

$$\mathbf{b_{ij}} = \frac{1}{3\pi\mu(a_i+a_j)}\left\{A_{ij}\frac{\mathbf{rr}}{r^2} + B_{ij}\left(\mathbf{I} - \frac{\mathbf{rr}}{r^2}\right)\right\} \qquad (5.4)$$

where i and j refer to the two spherical particles (i, j = 1 or 2), $\mathbf{b_{ij}}$ is a component of a mobility tensor describing sphere i's motion due to a force applied to sphere j, ($\mathbf{b_{ii}}$ or $\mathbf{b_{jj}}$ expresses the particle's own response to an external force), r=|$\mathbf{r}$|, $\mathbf{I}$ is the second rank unit tensor, and A_{ij} and B_{ij} are the mobility functions. The properties and details of these mobility functions can be found in the published works of Jeffrey and Onishi (1984) and Batchelor (1982). The mobility functions (A_{ij} and B_{ij}) are the dimensionless scalar coefficients for the movements of the two spherical particles and they are the functions of the dimensionless separation distance s and size ratio of the two particles (smaller to larger) λ.

Once the mobility tensors are known, the velocities of the two particles at a single point in time and space in the presence of an external force $\mathbf{F}$ can be written as:

$$\mathbf{U_1} = \mathbf{b_{11}F_1} + \mathbf{b_{12}F_2} \qquad (5.5a)$$

$$\mathbf{U_2} = \mathbf{b_{21}F_1} + \mathbf{b_{22}F_2} \qquad (5.5b)$$

5.2.2.1 Velocity of Particles Under Influence of Gravity

When two spherical particles, sphere 1 and 2, are at infinite separation, the hydrodynamic effects for the two particles are negligible. The relative velocity of two spheres under the influence of gravity at infinite separation is then:

$$\mathbf{V}_{12}^{\infty}(\mathbf{r}) = \mathbf{U}_{2}^{\infty} - \mathbf{U}_{1}^{\infty} = (\lambda^2\gamma - 1)\mathbf{U}_{1}^{\infty} \tag{5.6}$$

where U_1^{∞} and U_2^{∞} are the velocity fields of a single particle at the infinite separation and γ is the reduced density ratio of the two spherical particles,

$$\gamma = \frac{(\rho_1 - \rho_L)}{(\rho_2 - \rho_L)} \tag{5.7}$$

where ρ_1 and ρ_2 are densities of sphere 1 and 2, respectively, and ρ_L is the density of the fluid.

The hydrodynamic effects for the two particles must be considered if they are not at infinite separation. In that case, the relative velocity of sphere 2 with respect to sphere 1 under the influence of gravity can be derived from Equations (5.5) as follows:

$$\mathbf{V}_{12}(\mathbf{r}) = \mathbf{U}_2 - \mathbf{U}_1 = 6\pi\mu a_1 \mathbf{U}_1^{(0)}(\mathbf{b}_{21} - \mathbf{b}_{11}) + 6\pi\mu a_2 \mathbf{U}_2^{(0)}(\mathbf{b}_{22} - \mathbf{b}_{12}) \tag{5.8}$$

The final expression for $\mathbf{V}_{12}$ was further deduced from plugging the mobility tensors of Equation (5.4) into Equation (5.8) as follows:

$$\mathbf{V}_{12}(\mathbf{r}) = \mathbf{V}_{12}^{\infty}\left\{\frac{\mathbf{rr}}{r^2}L(s,\lambda) + \left(\mathbf{I} - \frac{\mathbf{rr}}{r^2}\right)M(s,\lambda)\right\} \tag{5.9}$$

where:

$$L(s,\lambda) = \frac{\lambda^2\gamma A_{22} - A_{11}}{\lambda^2\gamma - 1} + \frac{2(1 - \lambda^3\gamma)A_{12}}{(1+\lambda)(\lambda^2\gamma - 1)} \tag{5.10}$$

$$M(s,\lambda) = \frac{\lambda^2\gamma B_{22} - B_{11}}{\lambda^2\gamma - 1} + \frac{2(1 - \lambda^3\gamma)B_{12}}{(1+\lambda)(\lambda^2\gamma - 1)} \tag{5.11}$$

Equation (5.9) using the hydrodynamic mobility coefficients describes the relative velocity between two spherical settling particles under the influence of gravity in arbitrary location. For the ease of tensor computation, Han and Lawler (1991) resolved

V_{12} into velocities in the two-dimensional polar coordinate or the Cartesian coordinate systems.

5.2.2.2 Velocity of Particles under Interparticle Potential Energy

The net potential energy acting on two spherical interacting particles is equal in the opposite direction, $\mathbf{r}$ (center-to-center). The negative gradient of the interparticle potential energy with respect to the separation distance is the net interparticle force acting on each particle and it can be written as shown below:

$$-\nabla\Phi_{12} = \mathbf{F_1} = -\mathbf{F_2} \tag{5.12}$$

The relative velocity of the two particles under the influence of this interparticle force is then derived by Han (1989) as follows:

$$
\begin{aligned}
\mathbf{V_{12}(r)} = \mathbf{U_2} - \mathbf{U_1} &= -(\mathbf{b_{11}} + \mathbf{b_{22}} - \mathbf{b_{12}} - \mathbf{b_{21}})\nabla\Phi_{12} \\
&= -\frac{1}{6\pi\mu}\left(\frac{1}{a_1} + \frac{1}{a_2}\right)\left\{\frac{\mathbf{rr}}{r^2}G(s,\lambda) + \left(\mathbf{I} - \frac{\mathbf{rr}}{r^2}\right)H(s,\lambda)\right\}\Phi_{12}
\end{aligned} \tag{5.13}
$$

where:

$$G(s,\lambda) = \frac{\lambda A_{11} + A_{22}}{1+\lambda} - \frac{4\lambda A_{12}}{(1+\lambda)^2} \tag{5.14}$$

$$H(s,\lambda) = \frac{\lambda B_{11} + B_{22}}{1+\lambda} - \frac{4\lambda B_{12}}{(1+\lambda)^2} \tag{5.15}$$

The DLVO energy, which is the sum of van der Waals attraction and electric repulsion energies, was used to calculate interparticle potential, Φ_{12}, between the two particles; the calculation of DLVO energy is explained in Chapter 2.

5.2.2.3 Velocity of Particles under Brownian Motion

Han (1989) also derived the relative velocity of the two spherical particles under the influence of Brownian motion. Using the pair distribution function, $\mathbf{P_{12}}$, the net forces acting on each particle due to Brownian motion are written as:

$$\mathbf{F_1} = -\mathbf{F_2} = k_B T \nabla \log \mathbf{P_{12}(r)} \tag{5.16}$$

where $P_{12}(r)$ is the pair distribution function that indicates the probability of finding particle 2 at the separation distance r from particle 1 with the center of particle 1 taken as the origin of coordinates. When the monodispersed particles are in a mechanical equilibrium, this system can be represented by the Boltzmann distribution. The relative velocity between particle 1 and 2 due to Brownian motion becomes:

$$\mathbf{V_{12}(r)} = \mathbf{U_2} - \mathbf{U_1} = -k_B T(\mathbf{b_{11}} + \mathbf{b_{22}} - \mathbf{b_{12}} - \mathbf{b_{21}})\nabla \log \mathbf{P_{12}(r)}$$

$$= -\mathbf{D(r)}\nabla \log \mathbf{P_{12}(r)} \tag{5.17}$$

The relative diffusivity tensor $\mathbf{D(r)}$ is defined as:

$$\mathbf{D(r)} = D_{12}\left\{\frac{\mathbf{rr}}{r^2}G(s,\lambda) + \left(\mathbf{I} - \frac{\mathbf{rr}}{r^2}\right)H(s,\lambda)\right\} \tag{5.18}$$

where D_{12} is the relative diffusion coefficient that is from the assumption that the relative motion of the two spherical particles is the sum of the individual diffusion coefficients as:

$$D_{12} = \frac{k_B T}{6\pi\mu}\left(\frac{1}{a_1} + \frac{1}{a_2}\right) \tag{5.19}$$

5.2.3 The Collision Efficiency Functions

As mentioned earlier, the short-range force model is more realistic than the long-range force model due to the inclusion of the hydrodynamics and interparticle potential energy through the collision efficiency functions, α. The collision efficiency functions are obtained from solving Equation 2.9 - 2.13 numerically. The relative velocity tensors derived in Chapter 5.2.2. are embedded in the deduction of Equation 2.9 - 2.13. Here, the derivation of Equations 2.9- 2.13 is detailed. The material presented in this section is, in fact, reproduced in brief from Han's dissertation (1989).

5.2.3.1 Collision Efficiency Functions for Brownian Motion (α_{Br})

The rate of the Brownian collision between two spherical particles 1 and 2 is explained by Smoluchowski (1917) through the diffusion equation as shown below:

$$\frac{\partial n_2}{\partial r} = \frac{1}{r^2}\frac{\partial}{\partial r}r^2\left(D_{12}\frac{\partial n_2}{\partial r}\right) \tag{5.20}$$

where D_{12} is the relative diffusion coefficient as defined in Equation 5.19, and n_2 is the number distribution of sphere 2 in the vicinity of sphere 1. To calculate the rate of the Brownian collision under the influence of interparticle interactions, Fuchs (1937) expanded Smoluchowski's diffusion equation by incorporating the net interparticle energy between the two particles as follows:

$$\frac{\partial n_2}{\partial r} = \frac{1}{r^2}\frac{\partial}{\partial r}r^2\left(D_{12}\frac{\partial n_2}{\partial r} + \frac{D_{12}n_2}{k_BT}\frac{dV_T}{dr}\right) \tag{5.21}$$

where V_T is the net interparticle energy acting on the two interacting particles.

By definition, a stability ratio (W) is the ratio of the aggregation rate in the absence of colloidal interactions to the aggregation rate in the presence of interparticle energy between the particles (Elimelech $et\ al.$, 1998). From the definition, the collision efficiency functions for Brownian motion is the inverse of the stability ratio ($\alpha_{Br} = 1/W$). When attraction between the interacting particles is more significant, the Brownian collision can be expected to be more frequent than Smoluchowski's estimation (W < 1.0 or $\alpha_{Br} > 1.0$). If repulsion is more important, then the collision can be expected to be less frequent than Smoluchowski's prediction (W > 1.0 or $\alpha_{Br} < 1$). The stability ratio (W) is then calculated as shown:

$$W = \frac{1}{\alpha_{Br}} = \left(1 + \frac{a_2}{a_1}\right)\int_2^\infty \frac{\exp\left(\frac{V_T}{k_BT}\right)}{s^2}ds \tag{5.22}$$

where s is the dimensionless separation distance defined by normalizing the absolute separation distance by the average radii of the two particles.

Spielman (1970) discovered that the hydrodynamic effect is not negligible in a Brownian collision, and he introduced the hydrodynamic interaction between the particles into the stability calculation. Spielman indicated that the diffusivity is a function of particle size and the size ratio of two colliding particles rather than the sum of the

diffusivities of the two individual particles. Therefore, Spielman redefined the stability ratio ($W_{hydrodynamic}$) as the ratio of Smoluchowski's diffusion equation to the Spielman's diffusion equation which considers two particle hydrodynamics. Spielman's stability equation is given as Equation 2.9 and the boundary conditions are shown as:

$$n_2 = 0 \text{ and } V_T = -\infty \text{ when } r = a_1 + a_2$$

$$n_2 = n_2^\infty \text{ and } V_T = 0 \text{ when } r = \infty \tag{5.23}$$

The hydrodynamic coefficient function in the center-to-center direction, $G(s,\lambda)$ is already derived for any particle size ratio and separation distance using Jeffrey and Onishi's tensor solution in Equation 5.14. Equation 2.9 is further deduced as follows:

$$W_{hydrodynamic} = \left(1 + \frac{a_2}{a_1}\right) \int_2^\infty \frac{1}{G(s,\lambda)} \frac{\exp\left(\frac{V_T}{k_B T}\right)}{s^2} ds = \frac{1}{\alpha_{Br}} \tag{5.24}$$

Solving Equation 5.24 numerically, the stability and the collision efficiency functions for the two interacting particles under the effect of Brownian motion is obtained.

5.2.3.2 Collision Efficiency Functions for Differential Sedimentation (α_{Ds})

An illustrative diagram for the relative trajectory of two non-Brownian settling particles that have radii of a_1 and a_2 was given in Figure 2.2. The center of the larger particle (a_1) is the origin of the polar coordinate system. The separation distance, r is the absolute distance between the two centers of the particles and the angle between them is θ. In order to calculate the relative settling velocity, gravity and interparticle forces must be considered along with hydrodynamic effects between the two particles. The relative settling velocity can be obtained from the sum of the gravity (Equation 5.9) and interparticle velocity (Equation 5.13) vectors. The equation is formulated for the relative trajectory of the smaller particle (a_2) with respect to the large particle (Han and Lawler, 1991). First, the relative velocity into r and θ direction can be written as following:

In r direction:

$$V_r = V_{r,gravity} + V_{r,interparticle} \tag{5.25}$$

$$= -\cos\theta L(s,\lambda)U_{12} - D_{12}G(s,\lambda)F(s,\lambda)$$

In θ direction

$$V_\theta = V_{\theta,gravity} + V_{\theta,interparticle} \tag{5.26}$$

$$= \sin\theta M(s,\lambda)U_{12} + 0$$

Then the two equations (5.25) and (5.26) can be combined to yield equation (2.10):

$$\frac{dr}{d\theta} = r\frac{V_r}{V_\theta} = r\frac{[-\cos\theta L(s,\lambda)U_{12} - D_{12}G(s,\lambda)F(s,\lambda)]}{\sin\theta M(s,\lambda)U_{12}} \tag{2.10}$$

where all variables are defined in Chapter 2. U_{12} represents relative settling velocity of the two particles as shown in the following equation:

$$U_{12} = \frac{2g(\rho_p - \rho_f)a_1{}^2(1-\lambda^2)}{9\mu} \tag{5.27}$$

where, ρ_p and ρ_f are densities of the particles and fluid, respectively, a_1 is the radius of the larger particle, λ is the size ratio between the two particles, and μ is viscosity of the fluid.

Solving the first order non-linear differential equation (2.10) with various initial values (*e.g.*, different locations of the smaller particle, a_2 with respect to the center of the larger particle, a_1), different trajectories can be found. Depending on the initial location of the smaller particle, some trajectory simulations end up with collisions of the two particles (*i.e.*, closed trajectory) and others end up with separations of the two particles (*i.e.*, open trajectory) as shown in Figure 2.3. In the numerical calculations, the initial separation distance between the two particles in the y-direction was set as s = 20 (dimensionless distance), which is far enough that the initial interaction between the two particles is negligible. The critical distance in the x-direction which determines the open and closed trajectory was found by trial-and-error method. By changing the initial x coordinates from x = 0, the critical distance in the x direction is obtained. The collision

efficiency function is defined as the ratio of the circular area determined by a radius of the critical distance to the circular area defined by the sum of two settling particles as shown in Figure 2.3. The numerical computation was made using ODE Solvers in MATLAB.

5.2.3.3 Collision Efficiency Functions for Fluid Shear (α_{Sh})

When the sizes of two spherical particles moving in a linear shear flow are sufficiently small, they have low Reynolds numbers and inertia forces are insignificant. In this case, the hydrodynamic problem is linear and the solutions can be obtained by the standard methods (Brenner and O'Neill, 1972). Figure 2.4 illustrates the relative position of two spherical particles that move in a linear flow where the origin of the polar coordinate is at the center of Particle 2. The velocity of the fluid (V_x) is assumed to be linearly proportional to the separation distance in the y-direction (G*y), where G is a velocity gradient. The equations of relative particle location were derived by Adler (1981b and c) as shown in Chapter 2.

$$\frac{dr}{dt} = Gr(1 - A) \sin^2 \theta \sin \phi \cos \phi + F_r \tag{2.11}$$

$$r\frac{d\theta}{dt} = (1 - B) \sin \theta \cos \theta \sin \phi \cos \phi + F_\theta \tag{2.12}$$

$$r \sin \theta \frac{d\phi}{dt} = Gr \sin \theta \left(\cos^2 \phi - \frac{B}{2} \cos 2\phi \right) \sin \theta + F_\phi \tag{2.13}$$

A and B are dimensionless mobility functions that describe the hydrodynamic interaction between the particles (Batchelor and Green, 1972). A and B are functions of the radii of the two particles and the separation distance between them and they are fully explained by Adler (1981b and c). To reduce the computational burden, Tandon and Diamond (1997) developed matching hydrodynamic functions at the intermediate separation that yield less than 2% errors from the detailed hydrodynamic calculations of Batchelor and

102

Green (1972) and Adler (1981a). Tandon and Diamond's simpler hydrodynamic functions can account for a wide range of λ values ($0.03 \leq \lambda \leq 1$), which are suitable to generate extreme cases of particle size ratios. However, as Adler (1981b) mentioned, the precision of hydrodynamic solutions at small λ values ($\lambda < 0.1$) can be low even if they are numerically calculated because the number of equations that need to be considered dramatically increases at short separation distances between two interacting particles. The simpler hydrodynamic functions inherited this shortcoming as well; therefore, hydrodynamic functions for smaller λ values ($\lambda < 0.1$) need to be used with caution.

The relative trajectories of the two spherical particles in a linear shear flow were simulated by numerical integration of these equations (Equations 2.11-13) in MATLAB using ODE Solvers. Similar to the numerical computation results of differential sedimentation, the results of trajectories in fluid shear are either open or closed. The critical trajectories which separates the open and closed trajectories are found through trial-and-error method. The global capture efficiency is defined from the limiting trajectories and the global capture efficiency is converted to the collision efficiency functions.

5.3 SOLUTIONS OF COLLISION EFFICIENCY FUNCTIONS

5.3.1 In the Absence of Surface Potential

5.3.1.1 Brownian Motion

First, α was calculated under the assumption of the complete particle destabilization where the EDL repulsive forces are negligible. Using two different Hamaker constant (A_H) values (10 and 50 $k_B T$, which are equivalent to 4.11E-20 and 2.06E-19 J, respectively), the collision efficiency functions under Brownian motion (α_{Br}) for various particle sizes were calculated as shown in Figure 5.1. The computed

Brownian collision efficiencies for A_H of 10 k_BT (Figure 5.1A) are consistent with the previously reported values (Han 1989), except for the two additional lines for $a_1 = 0.5$ and 5 nm which are the new results of this study. When A_H was raised to 50 k_BT, the lines in the graph shifted upward (Figure 5.1B). Particle collisions are expected to be more favorable in short-range transport with a higher Hamaker constant value because of the stronger vdW attraction force between the two colliding particles. In this figure (and in all subsequent figures), the points shown were calculated directly from the numerical analysis, but the lines represent polynomial fits of those points. The polynomial fitting equations for each figure are tabulated in Appendix B: Table B.1-7.

Intriguingly, α_{Br} increased as the size of the smaller particle (a_2) in the two-particle collision decreased while the size of the bigger particle (a_1) was fixed (*i.e.*, the particle size ratio λ decreased). This result is due to a higher diffusivity of the smaller particle which causes more chances of particle collisions. For a similar reason, α_{Br} surged as a_1 decreased when a_2 was maintained constant. However, α_{Br} values never exceeded or became unity at any particle sizes or size ratios. This result shows that the hydrodynamic (viscous) forces acting against collisions are more significant than the vdW force that promotes collisions under the given Brownian conditions.
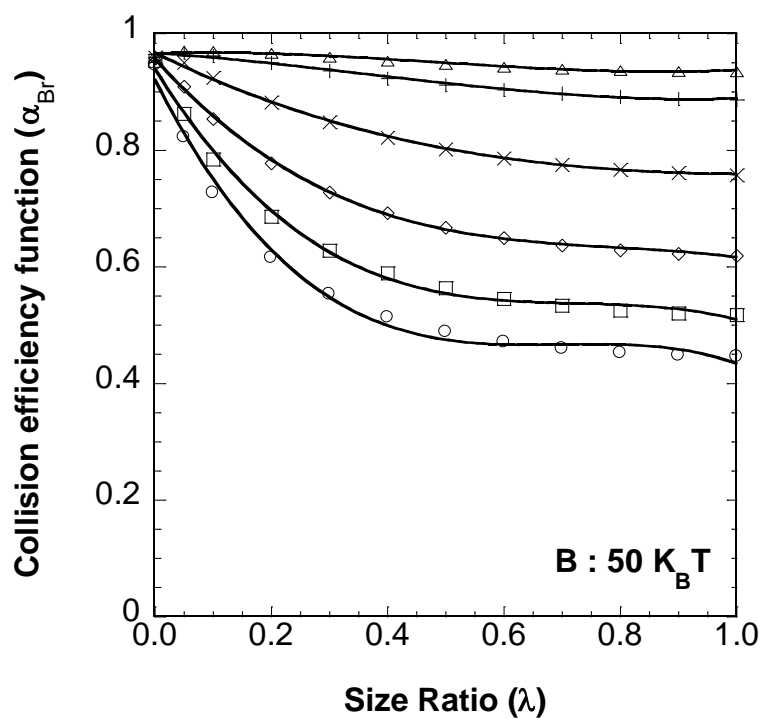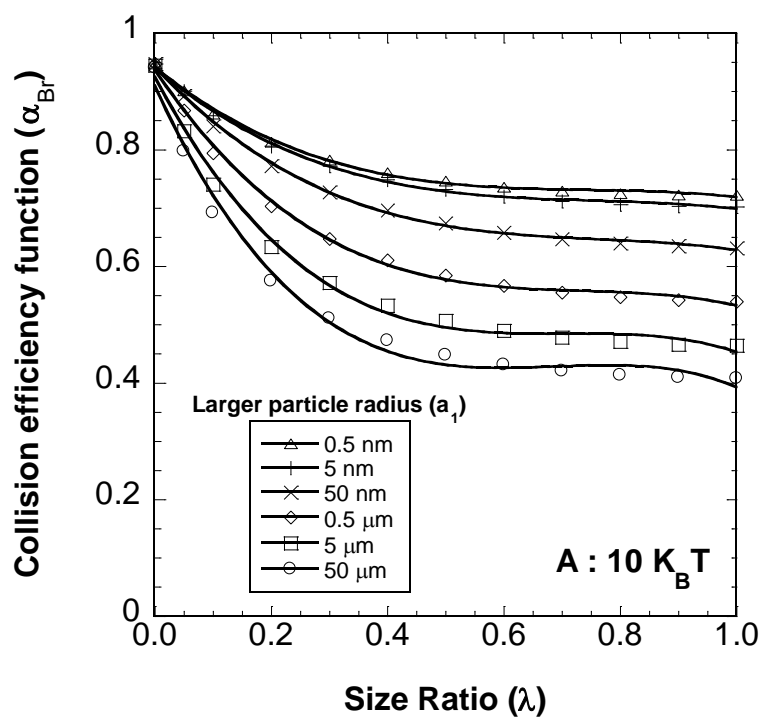
Figure 5.1 The collision efficiency functions in Brownian motion under two different Hamaker constant values of A) 10 k_BT and B) 50 k_BT.

5.3.1.2 Differential Sedimentation

The calculated collision efficiency functions of differential sedimentation (α_{Ds}) in the absence of the EDL repulsion is presented in Figure 5.2. Traditionally, a dimensionless number, N_g is used to incorporate all of the influencing variables in differential sedimentation transport (Han and Lawler, 1992). This number is defined as follows:

$$N_g = \frac{3A_H}{\pi(\rho_P - \rho_L)ga_1^4} \tag{5.28}$$

where g is the gravitational constant, and ρ_P and ρ_L are the densities of the particles and fluid, respectively. Various N_g values were selected by changing the radius of the larger particle in the collision while all the other variables remained constant. Figure 5.2 shows α_{Ds} for $\log(N_g)$ values from -6 to 6. When α_{Ds} values were first reported by Han, trajectory analysis was performed only up to $\log(N_g) = 1$, which was enough to deal with the relevant particle sizes at the time of study. At that time, it was thought that the upper limit of α_{Ds} was unity when $\log(N_g) > 1$. However, Figure 5.2 shows that α_{Ds} gradually ascended as $\log(N_g)$ increased and eventually exceeded unity. This result reveals that short-range transport processes could be more significant than the long-range transport process in differential sedimentation. That is, as a larger particle falls, a smaller particle below can be drawn toward and collide with the larger particle, even if the smaller particle starts outside the area associated with the critical trajectory in the long-range model depicted in Figure 2.3. Because N_g is inversely proportional to the fourth power of the size of the larger particle (a_1) in the collision, $\log(N_g)$ goes up dramatically with smaller values of a_1. Therefore, this behavior more likely occurs in the collisions of submicron-sized particles where $\log(N_g)$ values are greater than 2.
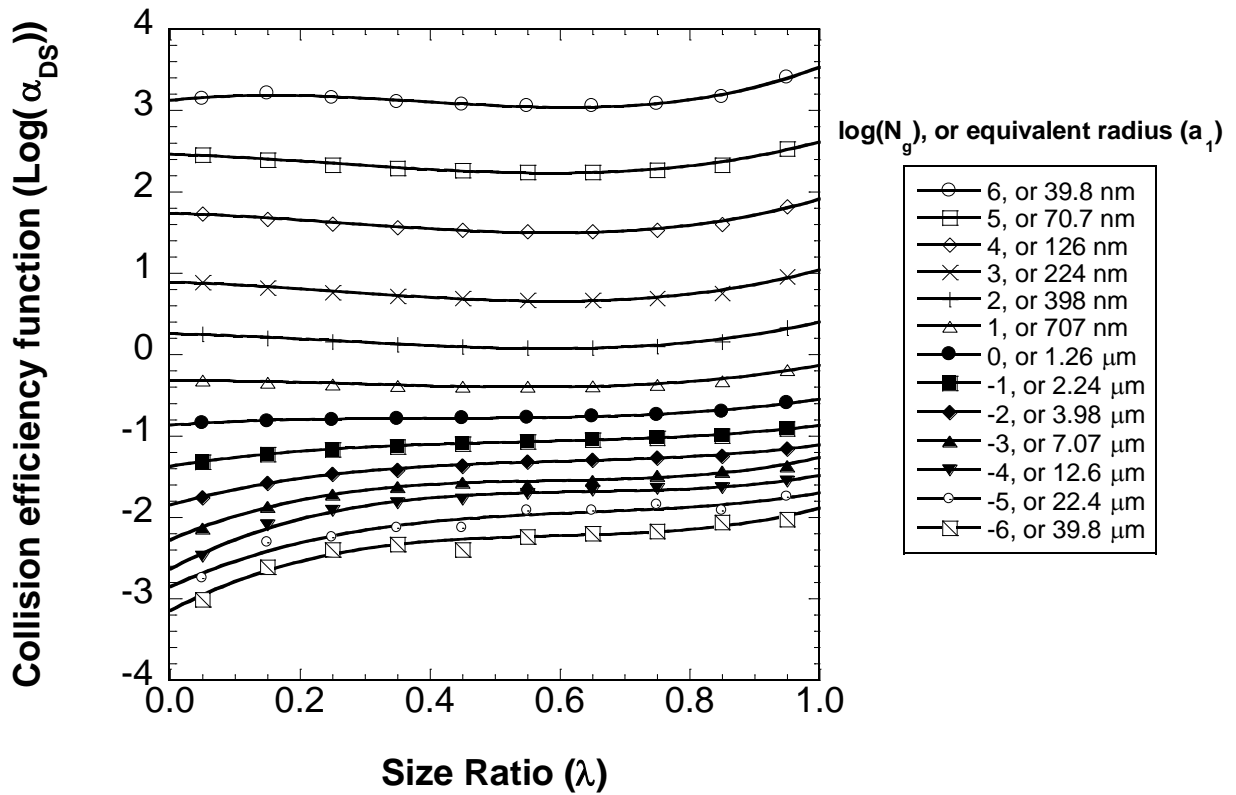
Figure 5.2 The collision efficiency functions in differential sedimentation. (The calculations were made with $A_H = 10 \ k_BT$, $\rho_P = 2.6 \ g/cm^3$, and $\rho_L = 1 \ g/cm^3$ and the larger particle radius varied as shown in the legend but any combination of values that leads to the same N_g value leads to the same result.)

5.3.1.3 Fluid Shear

The calculated collision efficiency values in a linear shear flow (α_{Sh}) in the absence of the EDL repulsion are presented in Figure 5.3. Similar to differential sedimentation, a dimensionless number, H_A, is used to integrate all of the controlling variables in fluid shear transport (Adler, 1981a). H_A is defined as follows:

$$H_A = \frac{A_H}{144\pi\mu a_1{}^3 G} \tag{5.29}$$

107

where G is the velocity gradient and μ is the absolute viscosity of the fluid. In Figure 5.3, the values of $\log(H_A)$ were varied from -5 to 1 by changing the radius of the larger particle (a_1) in the collision while all the other variables were fixed.

Figure 5.3 shows slightly different α_{Sh} values than those reported by Han and Lawler (1992) although they are from exactly the same trajectory analysis. Han and Lawler obtained the collision efficiency functions for fluid shear by interpolation and extrapolation of Adler's global capture efficiency results (1981a). Because Adler's global capture efficiency was generated under narrow computational conditions, Han and Lawler's work inherited this limitation. For this research, Adler's trajectory analysis for global capture efficiency was performed with a wider range of computational conditions and the results were converted to α_{Sh} values. The discrepancies between Han and Lawler values and the recalculated α_{Sh} values shown here are very small. In fact, the general trends and the actual values are similar, except that, as H_A and λ increase, α_{Sh} values became greater than 1 in the same manner as shown above for differential sedimentation; that is, the vdW attraction dominates at the submicron-scale in short-range transport. At the other extreme (*i.e.*, when $\log(H_A) \leq -4$), the result confirms Han and Lawler's conclusion that collisions with particles that are much smaller ($\lambda < 0.4$) rarely occur.
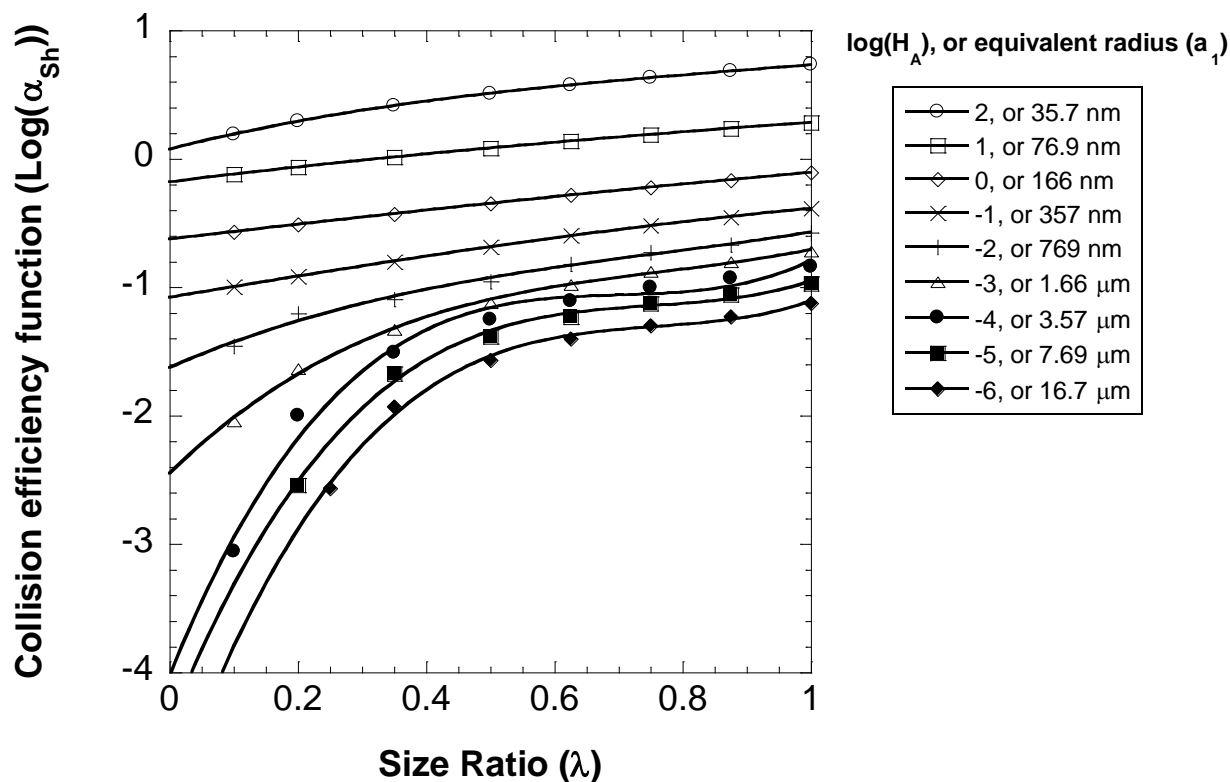
Figure 5.3 The collision efficiency functions in fluid shear (The calculations were made with $A_H = 10\ k_BT$, $G = 20\ s^{-1}$, and $\mu = 0.01$ g/cm-s and the larger particle radius varied as shown in the legend but any combination of values that leads to the same H_A value leads to the same result.)

5.3.2 In the Presence of Surface Potential

5.3.2.1 Brownian Motion

When a constant surface potential of -25 mV in the ionic strength of 1 mM was integrated into the identical condition of Figure 5.1A (where A_H was 10 k_BT), α_{Br} was lowered substantially by the presence of the EDL repulsion, as shown in Figure 5.4. Interestingly, the degree of α_{Br} reduction due to the EDL repulsion varies dramatically with the size of the larger particle (a_1) in the collision. The EDL repulsion reduces α_{Br} more significantly as a_1 increases. For any particle with a radius greater than 50 nm, α_{Br} was negligible in the presence of the constant surface potential of -25 mV. It is known

that the heights of interaction energy barriers (*i.e.*, DLVO energy barrier) due to the EDL repulsion are strongly influenced by the sizes of two interacting particles even under the identical surface potential and electrolyte conditions (Benjamin and Lawler, 2013). When the size of the larger particle (a_1) in the collision gets larger, particle diffusion coefficients decrease while the DLVO energy barrier rises. Conversely, if a_1 gets smaller, diffusion coefficients increase while the DLVO energy barrier falls. For this reason, collisions between smaller particles through short-range transport were less hindered by the presence of the EDL repulsion.
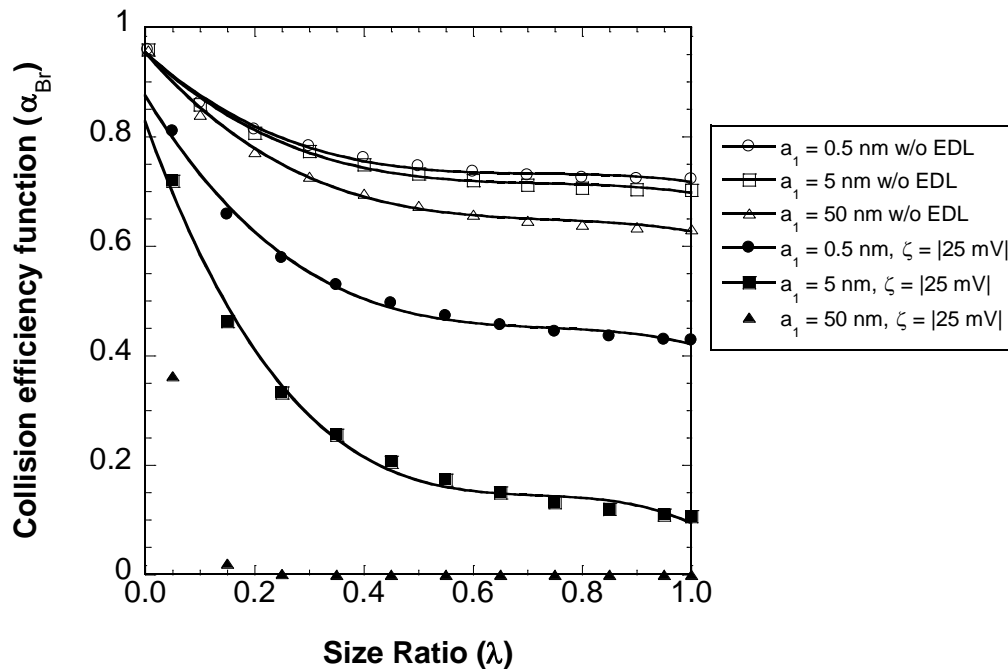
Figure 5.4 α_{Br} in the presence/absence of the constant surface potential of |25 mV|

The influence of surface potentials and the ionic strength of electrolytes on collision efficiency functions were also studied while a_1 was fixed at 5 nm as shown in Figure 5.5.

The results in Figures 5.5A and 5.5B confirmed that α_{Br} is a function of the magnitude of the surface potential and the ionic strength of the electrolytes. In the presence of the EDL, α_{Br} is a function of the ionic strength, the surface potential, and the colliding particle sizes.
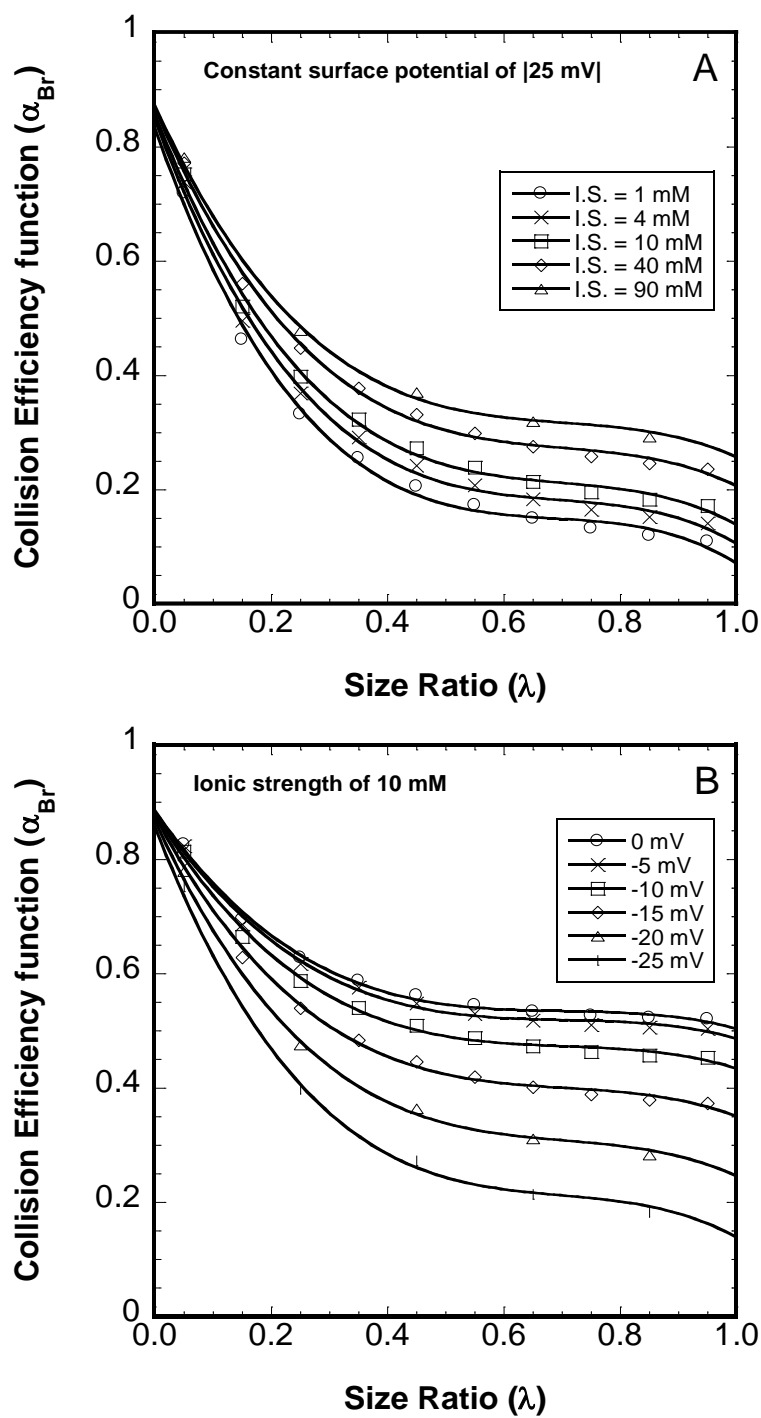
Figure 5.5 α_{Br} with A) various ionic strength and B) surface potential for $a_1 = 5$ nm

5.3.2.2 Differential Sedimentation

With the constant surface potential of -25 mV, particle trajectories in differential sedimentation were simulated for four distinct a_1 values (a_1 = 5 nm, 500 nm, 5 μm, and 50 μm, which are equivalent to $\log(N_g)$ = 5.6, 1.6, -2.4, and -6.4, respectively, under the identical conditions that were assumed in producing Figure 5.2). As expected, the presence of the EDL repulsion reduces α_{Ds}. When a_1 was smaller than or equal to 5 μm with any size of a_2, no collisions were predicted to occur (*i.e.*, α_{Ds} = 0). That is, below some size particle, two approaching particles never collide in differential sedimentation in the presence of the EDL repulsion. More interestingly, at the nano/submicron-scale (a_1 < 0.5 μm), simulated trajectories showed that two settling particles never collide in the course of settling, but particles orbit each other with a fixed separation distance. This phenomenon, the formation of so-called "secondary doublets," has been discussed by other scholars, particularly for particle collisions in a linear shear flow (Adler, 1981b; Van de Ven, 1989), but secondary doublets have not been noted in differential sedimentation before. The results of this trajectory analysis suggest that the interparticle forces dictate the transport behavior more significantly than the settling forces for submicron-sized particles. The separation distance of the two particles in doublets is found to be at the secondary minimum of DLVO energy curve. An example of a simulated trajectory of secondary doublets in differential sedimentation is depicted from the Lagrangian view on the large particles (a_1) in Figure 5.6.
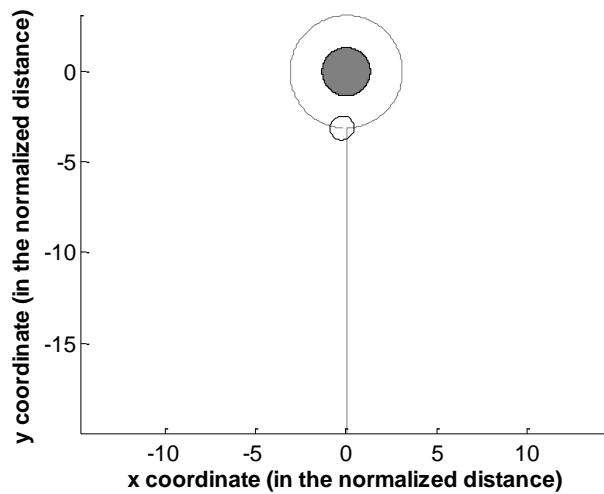
Figure 5.6 Simulated trajectory result from MATLAB (the size of the gray colored particle (a_1) was 100 nm, and the size of the small clear particle (a2) was 25 nm, the dotted line is the pathway of the center of the small particle, and the calculations were made with the surface potential of |25| mV when log(Ng) = 5.3)

The explanation for secondary doublets in differential sedimentation is that, as a_1 decreases, the settling force rapidly drops and becomes negligible compared to the interparticle forces. The interparticle forces (vdW and EDL) are linearly proportional to the particle radius while Stokes' settling force due to gravity is directly proportional to the third order of the particle radius. At the submicron-scale, the differential settling force is simply not sufficient enough to overcome the DLVO energy barrier.

Some could argue that, if the two particles are settling together at the same velocity in a secondary doublet, they should be considered as one entity (*e.g.*, a floc or an aggregate); however, in trajectory analysis for this work, secondary doublets were not considered as permanent flocs. Van de Ven and Mason (1976a-b) calculated the lifespan of secondary doublets. Their experimental results showed that the orbital period of

114

secondary doublets in a linear shear flow was shorter than the theoretically calculated values. Van de Ven and Mason thought that the imbalance in the surface charge distribution causes particles to break apart. Similar to this argument, the instability of secondary doublets in differential settling was observed in trajectory analysis and an illustrating figure is depicted in Appendix B: Figure B.1. For this reason, in this study, secondary doublets are considered as reversible products and not as flocs.

When a_1 was greater than 50 μm, direct particle collisions were observed occasionally even in the presence of the constant surface potential of -25 mV. The settling force (or momentum) at these particles sizes was large enough to overcome the DLVO energy barriers. When the direct collisions occurred at these particle sizes, α_{Ds} was substantially lowered in comparison to the non-EDL case and the maximum values of α_{Ds} were estimated to be on the order of 10^{-4}.

However, it was not feasible to create a generalized graph of α_{Ds} with polynomial fittings in the presence of a constant surface potential. Several influencing variables that control α_{Ds} values in numerical trajectory analysis are not incorporated into the dimensionless number, N_g; those variables include ionic strength, valency of background electrolyte, magnitude of surface charge, and boundary conditions of surface charge. To get an accurate value of α_{Ds}, each specific physical and chemical condition requires separate runs of numerical calculation.

5.3.2.3 Fluid Shear

Because Adler (1981a) already presented the influence of the EDL repulsion on global capture efficiencies regarding micro-sized particles, the main focus of this work is α_{Sh} of submicron-sized particles under the influence of the EDL. When the surface potential of -25 mV was included in the trajectory analysis, the critical cross-sectional

area that can result in particle collisions is effectively minimized. At the nano/submicron-scale, the external shear force acting on the particles is insignificant to overcome the DLVO energy barrier, and particle transport is primarily governed by the interparticle forces. Similar to α_{Ds}, particle doublets are frequently observed due to the DLVO energy barrier. To provide a qualitative explanation, two hypothetical collision scenarios of two large particles ($a_1 = a_2$) and two small particles ($a_1' = a_2'$) in a linear shear flow in the xy-plane are plotted in Figure 5.7. In trajectory analysis, the separation distance between two particles is normalized by the average of the two particle radii (*i.e.*, $s = 2*r/(a_1+a_2)$). In Figure 5.7, the component of that separation distance that is perpendicular to the flow direction is depicted as δ for two pairs of possible colliding particles with the distance of 2δ in the x direction from each other. For equivalent values of the dimensionless δ, the smaller particles (a_1' and a_2') have a lower differential shear velocity than the larger particles (a_1 and a_2) because of the shorter (actual) separation distance. As a result, the presence of the EDL hinders particle collision in short-range transport to a greater extent for submicron-sized particles than micro-sized particles. Just as for α_{Ds} in the presence of the EDL, the polynomial fits for α_{Sh} as a function of the sizes and the size ratio of the two colliding particles could not be easily generated in the presence of the EDL. The dimensionless number, H_A does not include factors that affect α_{Sh}. For each specific physiochemical condition, individual trajectory analysis needs to be performed.
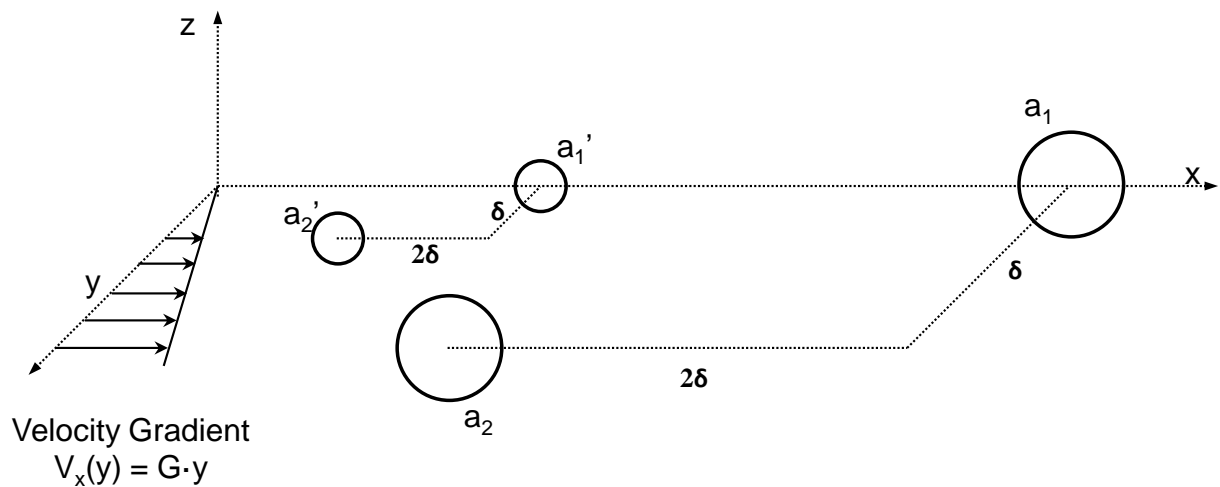
Figure 5.7 Difference in shear velocities for large particles and small particles

5.3.3 Summary

To visualize the relative importance of the three transport mechanisms in flocculation for a submicron-sized particle with a wide range of particle sizes, the calculated collision efficiency functions (α) are combined with the collision frequency functions (β) and illustrated in Figure 5.8. Figure 5.8A displays the total collision frequency values ($\gamma = \alpha*\beta$) of two-particle collisions considering well-destabilized (no EDL) silver particles (AH = 50 k_BT, density = 10.49 g/cm3, and G = 32 s^{-1}). The diameter of the first particle in the collision (a_1) was fixed at 200 nm while the size of the second particle in the collision (a_2) was varied. Brownian motion is the dominant transport mechanism where the diameter of the second particle is smaller than approximately 1 μm. However, fluid shear and differential sedimentation becomes the most significant mechanism when the size of the second particle becomes larger than 1 and 2 μm, respectively.

Figure 5.8B shows the total collision frequency values in the presence of the constant surface potential of -25 mV while all the other settings are maintained identical

as in Figure 5.8A. The total collision frequency was lower than in conditions without EDL repulsion for all three transport mechanisms, as expected. Brownian motion is still the most significant mechanism when the diameter of the second particle is below 200 nm. The importance of fluid shear became more noticeable when the diameter of the second particle is between 200 nm and 10 µm. Differential sedimentation is important when the second particle is larger than 10 µm. The three transport mechanisms displayed a varying degree of their importance in flocculation in the presence of the EDL. The Hamaker constant value ($A_H = 50$ k_BT) that was used in the numerical computation contributed to these interesting results. The repulsive energy from the constant surface potential of -25 mV is well compromised by the attractive energy caused by the relatively high Hamaker constant.
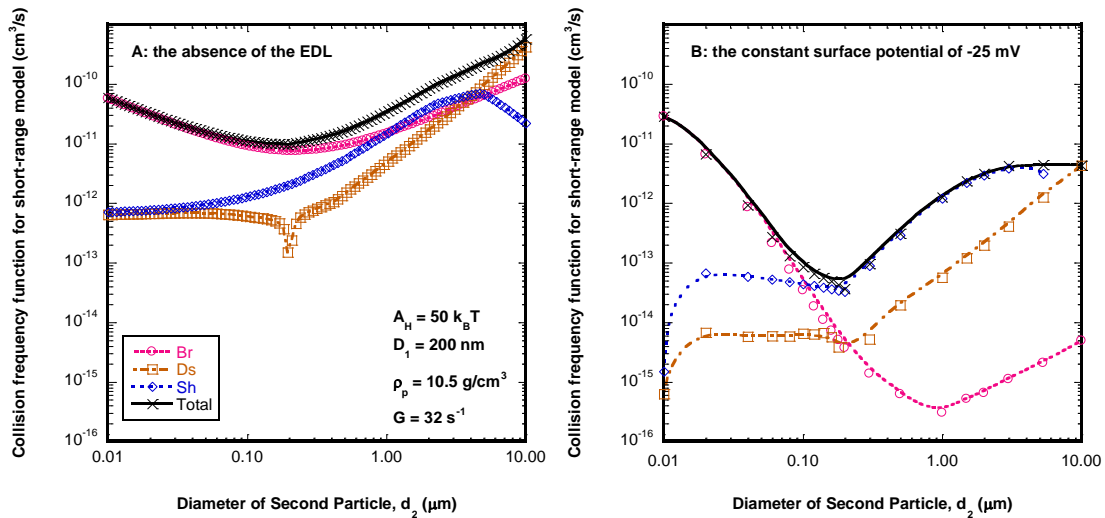
Figure 5.8 Total collision correction function: A) in the absence and B) in the presence of constant surface potential of -25 mV (the calculated values are indicated with points and the smooth curves fitting was generated between the points)

The numerical calculation results of two extreme cases were presented in this Chapter: no surface potential at all and the surface potential of -25 mV. For the accurate quantification of transport mechanisms in flocculation, the numerical analysis must be performed at the corresponding particle/solution conditions. At the nanoscale, Brownian motion is the most important transport mechanism, as expected. However, differential sedimentation and fluid shear mechanisms could also be as important as Brownian motion transport in some cases. For submicron-sized particles, more caution is necessary not to overlook differential sedimentation or fluid shear mechanisms over Brownian motion. The presence of the EDL repulsion reduces the collision efficiency functions (α) for the three fundamental transport mechanisms.

Temporary secondary doublets are frequently observed at the nano/submicron-scale in the presence of the EDL. As the sizes of the two colliding particles decrease, the settling force and shear force diminish more than the interparticle forces (vdW and EDL). Secondary doublets are formed when the particle separation is at the secondary minimum of DLVO energy curve.

The results presented in this Chapter extend the ranges of size and surface charge for which the changes in particle size distributions during flocculation in water treatment can be modeled quantitatively. Evaluating the mechanisms of particle transport and attachment at the nanoscale will be a cornerstone of flocculation modeling as those particle physics in flocculation have not been explained previously. The identified trends in the results of trajectory analyses allowed further development of the mathematical model of flocculation at the nanoscale (Chapter 6).

Chapter 6: Flocculation Modeling and Results

6.1 INTRODUCTION

The mathematical flocculation model described in Chapter 2 is capable of predicting the evolution of particle size distributions brought about by flocculation for micro-sized particles (Han, 1989; Li, 1996; Nason, 2006). This Chapter focuses on comparing experimental results from laboratory-scale AgNP flocculation tests with model predictions derived from the updated short-range force model described in the previous Chapters. The hypothesis is that the established mathematical theory of flocculation for micro-sized particles could be applied to nano-sized particles as well. It was assumed that updating the collision efficiency functions, α, for short-range transport mechanisms (*i.e.*, the term that captures the physics of particle collisions and is described in Chapter 5) would successfully forecast the evolution of particle number distributions at the nanoscale. The objective of this Chapter is to illuminate aspects of flocculation at the nanoscale that are and are not quantitatively well understood through systematic comparisons of experimental data with the model predictions.

6.2 FLOCCULATION MODEL

As introduced in Chapter 2, the most advanced flocculation model is the short-rage force model, which considers interparticle interactions, including the hydrodynamic and DLVO energy experienced between colliding particles. The short-range force model is as follows:

$$r_k^{Short-range} = \frac{dn_k}{dt} = \frac{1}{2}\alpha_{emp}\sum_{\substack{all\ i\ and\ j \\ Vi+Vj=Vk}}\gamma_{ij}^{tot}n_in_j - \alpha_{emp}n_k\sum_{all\ i}\gamma_{ij}^{tot}n_i \qquad (2.8)$$

$$\gamma_{ij}^{tot} = \alpha_{ij}^{Br}\beta_{ij}^{Br} + \alpha_{ij}^{Sh}\beta_{ij}^{Sh} + \alpha_{ij}^{Ds}\beta_{ij}^{Ds}$$

where, i, j and k are size classes of particles; n_i is the number concentration of i-sized particles (L^{-3}), Vi is the volume of a size i particle (L^3), β_{ij} is the collision frequency function for particles of size i and j (L^3/T), α_{emp} is the empirical collision efficiency factor, and α_{ij} is the (theoretically calculated) collision efficiency function for particle size i and j.

Equation 2.8 evaluates the rate at which the number concentration of k-sized particles changes with respect to time. As discussed in Chapter 3, for this research, the NanoSight particle size analyzer was set to generate one hundred individual particle size bins (N = 100) that were equally spaced on a logarithmic scale. Equation 2.8 applies to each particle size bin in a continuous particle size distribution. For each time increment (Δt = 10s), Equation 2.8 is integrated by Heun's method for each bin (*i.e.*, computing one hundred integrals for every ten second increment). The collision frequency functions, β, can be analytically calculated using the equations tabulated in Table 2.1. The collision efficiency functions, α, for the three transport mechanisms at the nanoscale were obtained in Chapter 5. To minimize the computational burden (time), AgNPs are assumed to be completely destabilized (*i.e.*, without surface charge); therefore, the values of the collision efficiency functions (α_{Br}, α_{DS}, and α_{Sh}) are as shown in Figures 5.1, 5.2, and 5.3, respectively, rather than calculated anew. This choice means that any DLVO energy barrier and all chemical aspects of flocculation such as the degree of destabilization of AgNPs were accounted for by the empirical collision efficiency factor (α_{emp}) in the short-range force model.

6.2.1 Inputs for the Model

The short-range force model requires various physical parameters including temperature, density of particles, mixing intensity, and the initial particle number

distribution. Collision frequency functions for Brownian Motion (β_{Br}) and the viscosity of water are influenced by the temperature of water. A constant room temperature of 298.25 K (25 Celsius) was applied throughout this modeling. In addition, the collision frequency function for fluid shear (β_{Sh}) is controlled by the mixing intensity, G. Throughout each flocculation experiment, gentle mixing (with G values estimated by Camp's method (1955) as 10 s^{-1}) was applied. The densities of particles and flocs affect the collision frequency for differential sedimentation (β_{DS}). However, the density of Ag-flocs is not easy to measure because Ag-flocs consist of both water and silver and their composition and porosities may vary. Although applying the actual density for Ag-flocs for the model would produce more realistic and accurate results, the bulk density of silver (10.5 g/cm^3) was used for both AgNPs and Ag-flocs. The short-range force model inherited the coalescence assumption that was made by Smoluchowski (*i.e.*, particle volume is conserved during particle collisions) and, for this reason, the use of the bulk density of silver is more consistent with the flocculation model. Lastly, the particle number distributions that were measured by NanoSight at time zero were used as the model input. NanoSight allows users to specify the number and size of each bin on a logarithmic scale. It was manually set so that data from NanoSight had one hundred bins for sizes ranging from 1 nm to 2000 nm.

6.2.2 Model Performance

The original computer code for flocculation was developed by Lawler (1979) in PL/1 to study the evolution of particle size distributions in thickening processes. Since then, the computer code has been used and improved by his successors. The existing short-range force model was written in C Language by Nason (2005), which is a modified version of the first short-range force model developed by Han (1989). For this

research, Nason's model was rewritten in MATLAB modernizing outdated functions in C Language.

For each model run, the mathematical calculations at four selected times (t = 15, 30, 45, and 60 minutes) were obtained based on the initial number distribution of AgNPs that had been measured by NanoSight (*i.e.*, inputs for the model). The model predictions were plotted against experimental data at the four times to examine if model predictions agreed with measured number distributions. By adjusting the empirical fitting parameter (α_{emp}), the short-range force model was tuned to produce the best-fit number distribution curves.

Figure 6.1 shows the predictions made by the short-range force model against NanoSight data from Experiment #14. Although the model slightly deviated from experimental data at 60 minutes, the predictions of the flocculation model (α_{emp}= 0.06) agreed with experimental data generally well by showing the decreasing number of smaller size particles and the increasing number of larger size particles. Consistent with the experimental results, the peak of the model in the number distribution shifted to larger size particles while both the height of the peak and the area under the curve (total particle concentration) lowered with time. By looking at the four different times from Figure 6.1A through 6.1D, the creation of larger flocs is also indicated in the model. This result is evidence that the model predictions are consistent with the experimental data and that flocculation of AgNPs can be explained by the Smoluchowski theory of flocculation.
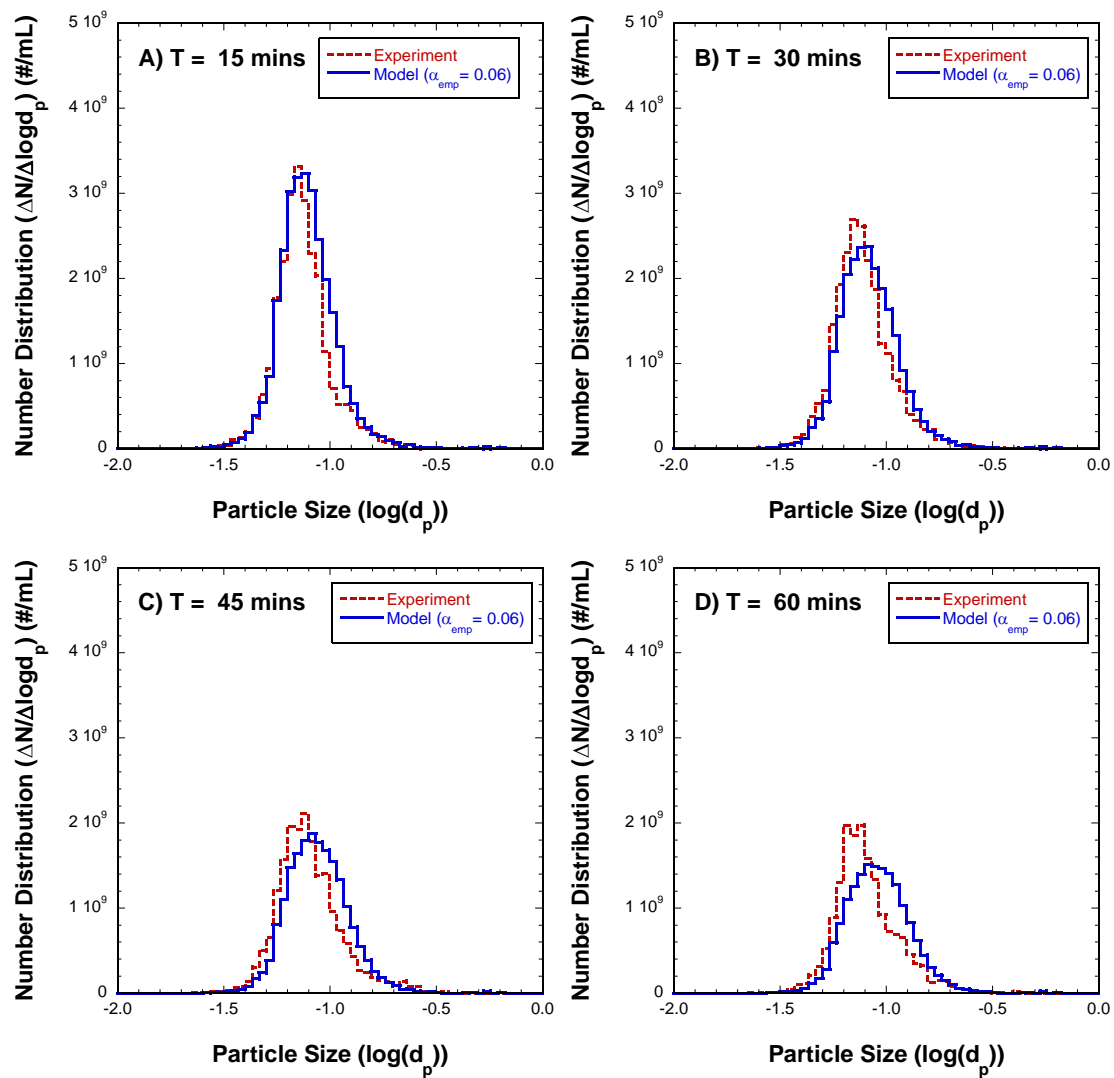
Figure 6.1. Flocculation model (α_{emp} = 0.06) vs. experimental data (EXP #14: 50 nm, $Ca(NO_3)_2$, I = 3 mM, and 1.2E9 #/mL) at t= A) 15, B) 30, C) 45, and D) 60 minutes

6.2.3 Collision Efficiency Factor (α_{emp})

The short-range force model takes particle transport (the physical aspects) into account through the collision frequency and efficiency functions (β and α) with the assumption that all particles are well-destabilized and do not have repulsive interaction. In practice, however, complete destabilization is not always achieved and particles are

124

left with some surface potential. In this case, particle collisions do not guarantee the formation of flocs due to incomplete destabilization. For this reason, an empirical fitting parameter was incorporated into the short-range force model that is known as the empirical collision efficiency factor (α_{emp}). The collision efficiency factor (α_{emp}) is mainly regarded as a chemical correction factor that accounts for the fraction of predicted collisions that result in flocs.

In this research, a maximum likelihood estimator that measures the agreement between the model predictions and the experimental results was used to determine α_{emp}. The least square estimator is a standard regression analysis and small values of the sum of squared error (SSE) represent close agreement. The following equation was used to quantify the goodness of fit:

$$\text{SSE} = \frac{\sum_{i=1}^{N}(E_i - M_i)^2}{N} \tag{6.1}$$

where, E_i is the experimental data (*i.e.*, the measured number concentration of i-sized particles), M_i is the model predictions (*i.e.*, the predicted number concentration of i-sized particles), and N is the total number of size bins (N= 100).

A minimum value of SSE for the four selected times (t= 15, 30, 45, and 60 minutes) was sought through trial-and-error, and α_{emp} was correspondingly adjusted to yield best-fit number distributions. Because α_{emp} depends mainly on chemical conditions, in theory, an identical value of α_{emp} should be obtained for all experiments with the same chemical condition. By comparing α_{emp} values between experimental results that have the same chemical conditions, the validity of the flocculation model for nanoparticles was investigated. In addition to SSE, the goodness of fit was also checked by comparing total particle numbers in the model predictions to the data; however, the model fits were not nearly good as the estimations from SSE method.

6.2.4 Sensitivity to α_{emp}

To check the sensitivity of the flocculation model to α_{emp}, the short-range force model was tested at several different collision efficiency factors (α_{emp} = 0.01, 0.05, 0.1, and 0.2) using the identical particle number distribution functions as input data and keeping all other parameters identical. Figure 6.2 shows various predictions made by the short-range force model with different α_{emp} values for 50 nm sized AgNPs under I = 3 mM of $Ca(NO_3)_2$ and flocculation times of 15 and 60 minutes (identical conditions as Figure 6.1). Higher α_{emp} values in the short-range force model predicted greater flocculation at both 15 and 60 minutes. Interestingly, the lower α_{emp} value (0.01) differed from experimental data to a larger degree at the later time (t = 60 minutes) whereas the two larger α_{emp} values (0. 1 and 0.2) differed more at 15 minutes.
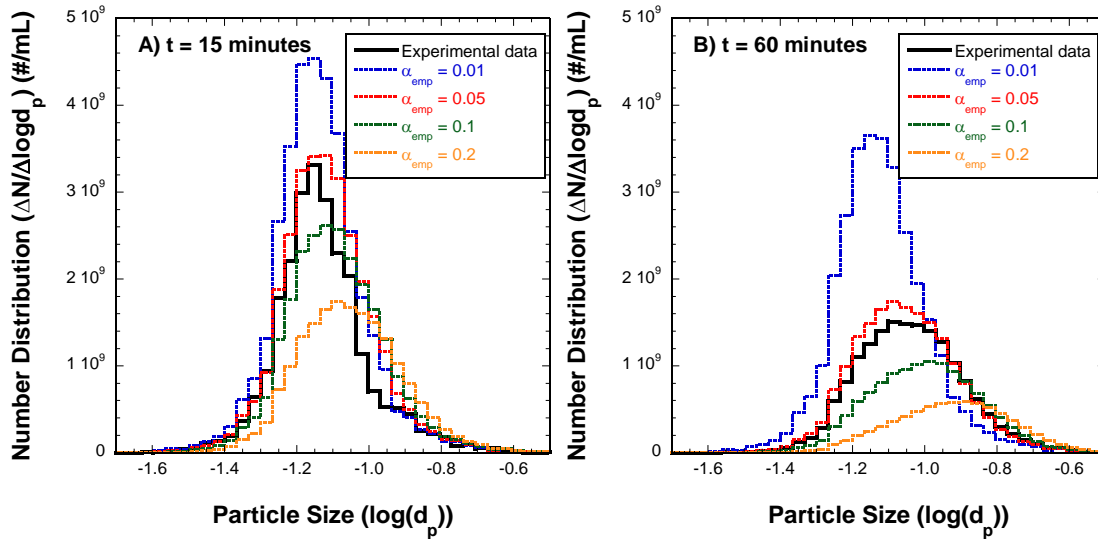
Figure 6.2 Sensitivity of the short-range force model to α_{emp} at = A) 15 and B) 60 minutes

The short-range force model is sensitive to the collision efficiency factor because the predicted rate of successful collisions is directly proportional to its value within the second order flocculation rate expression.

6.3 MODEL PREDICTIONS FOR THE EXPERIMENTAL RESULTS

To inspect the validity of the flocculation model at the nanoscale under various conditions, the short-range force model was tested against all of the laboratory scale flocculation data obtained from NanoSight in Chapter 4. The collision efficiency factor, α_{emp}, for each experiment was obtained using the least square estimator method to find the best-fit number distributions for the four selected time points during each experiment. The values of α_{emp} are tabulated as presented in Table 6.1; in subsequent sections of this Chapter, it is shown that some experiments are better fit with two values of α_{emp}, one for the first time period and the other for later times.

Table 6.1 The collision efficiency factors for each experiment

	Particle size (nm)	Ionic Strength (mM)	Valency	Initial Particle Concentration (#/mL)	NOM*	α_{emp}
1	100	30	1	1.3E+09	X	0.02
2	100	50	1	1.1E+09	X	0.06
3	100	30	2	1.2E+09	X	0.14
4	100	30	3	1.2E+09	X	0.02
5	100	30	1	1.9E+09	X	0.12
6	100	50	1	1.1E+09	O	0.15
7	100	30	2	1.3E+09	O	0.16
8	30	30	1	1.1E+09	X	0.25
9	30	10	1	1.0E+09	X	0.07
10	30	3	1	1.1E+09	X	0.01
11	30	3	2	1.2E+09	X	0.13
12	30	3	1	2.5E+09	X	0.06
13	50	3	1	1.2E+09	X	0.005
14	50	3	2	1.2E+09	X	0.06
15	50	10	1	1.1E+09	X	0.15
16	30 & 100	10	1	1.3E+09	X	0.01
17	30 & 100	30	1	1.0E+09	X	0.27
18	30 & 100	3	2	1.0E+09	X	0.12

*NOM = Natural Organic Matter, X= the absence of NOM, and O= the presence of NOM

6.3.1 Model Predictions for Different Ionic Strength of Destabilizing Agents

Figure 6.3 shows the modeling results for flocculation of the 100 nm sized AgNPs at an ionic strength of 30 mM of $NaNO_3$ at the four chosen times (t= 15, 30, 45, and 60 minutes, Experiment #1). The best-fit curves were found when the collision efficiency factor (α_{emp}) was 0.02. The model predictions matched the experimental data fairly well

128

for the four selected times, with the height and location (log d_p value) of the peaks and the widths of the number distributions nearly identical to the measured data. However, the model seems to consistently underestimate smaller size particles and overestimate larger size particles.
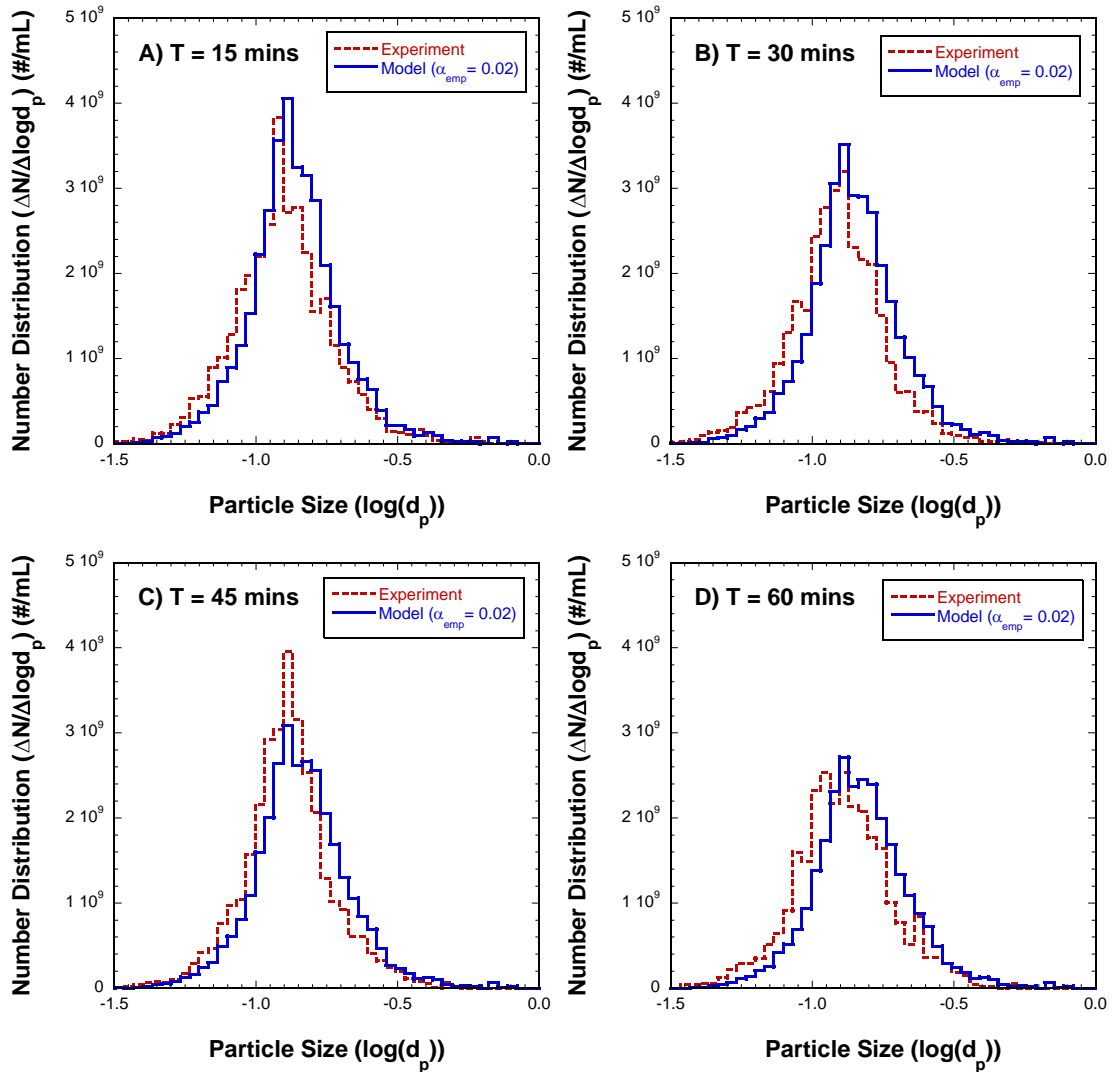
Figure 6.3 Flocculation model ($\alpha_{emp} = 0.02$) vs. experimental data (EXP #1: 100 nm NaNO$_3$, I = 30 mM 1.3E9 #/mL)

Running the short-range force model with a lowered α_{emp} value could fix the issue of under and overestimating for smaller and larger size particles. For example, using the α_{emp} value of 0.005 instead of 0.02, the short-range force model estimated weaker flocculation, and the best-fit curves for the number distributions were shifted to smaller size particles as shown in Figure 6.4. However, the lowered α_{emp} also produced higher estimations for the number concentrations due to weaker flocculation (*i.e.*, the heights of each bet-fit curve were more elevated with $\alpha_{emp} = 0.005$ than 0.02). The benefits of not having under/overestimating on each tail with the lowered α_{emp} value was overpowered by the greater sum of squared error from the higher peak number concentrations. Hence, the best-fit α_{emp} values was determined to be 0.02.
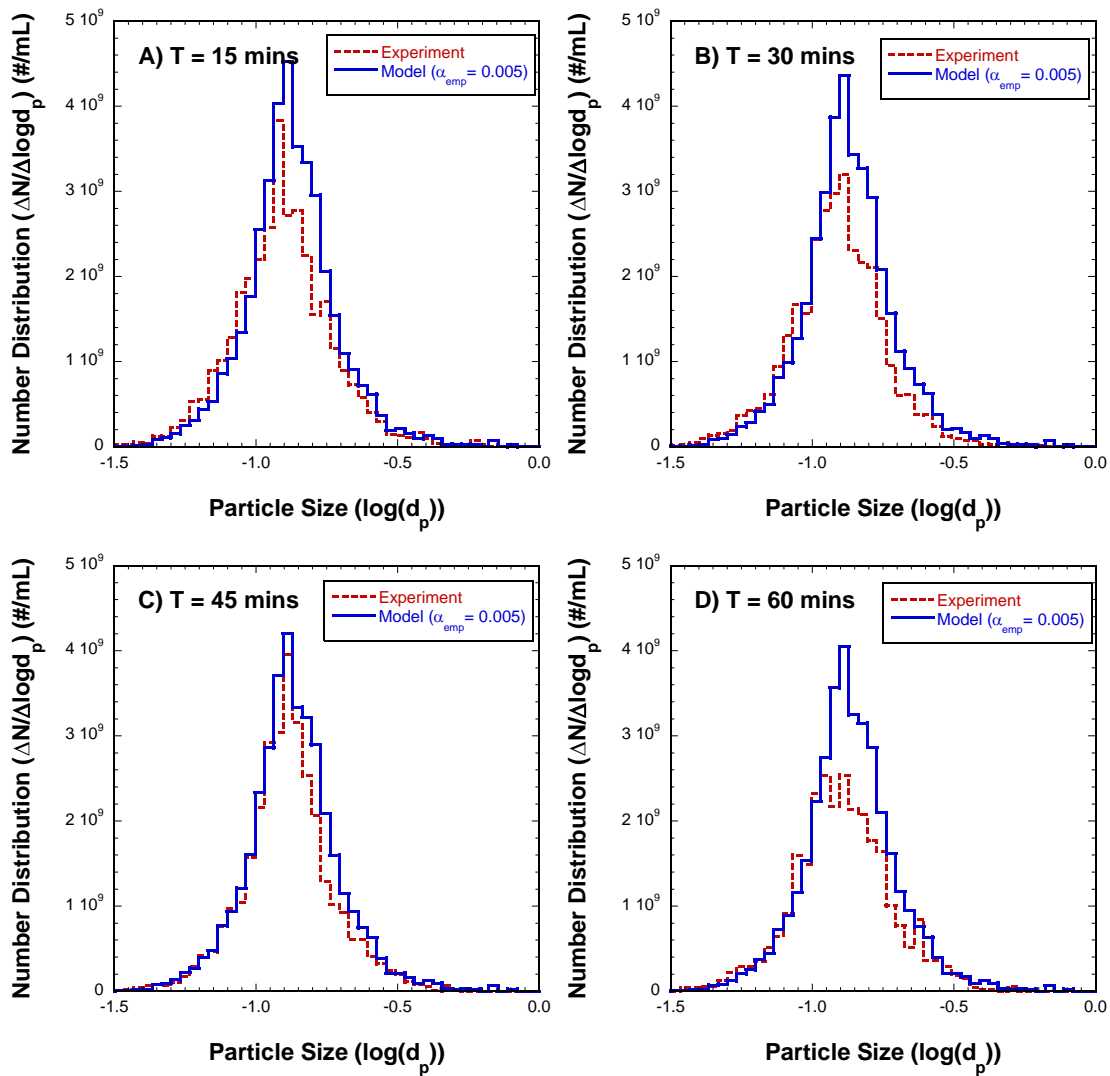
Figure 6.4 Flocculation model (α_{emp} = 0.005) vs. experimental data (EXP #1: 100 nm NaNO₃, I = 30 mM 1.3E9 #/mL)

When the model was executed against the data from Experiment #2, where the ionic strength was set to 50 mM instead of 30 mM of NaNO₃, the α_{emp} value was found to be 0.06 as shown in Figure 6.5. Again, the model showed the peaks and heights that are comparable to the experimental results for the selected times. Minor deviations between

the model and the experimental data were observed at larger size particles and the

discrepancy became more apparent with time.
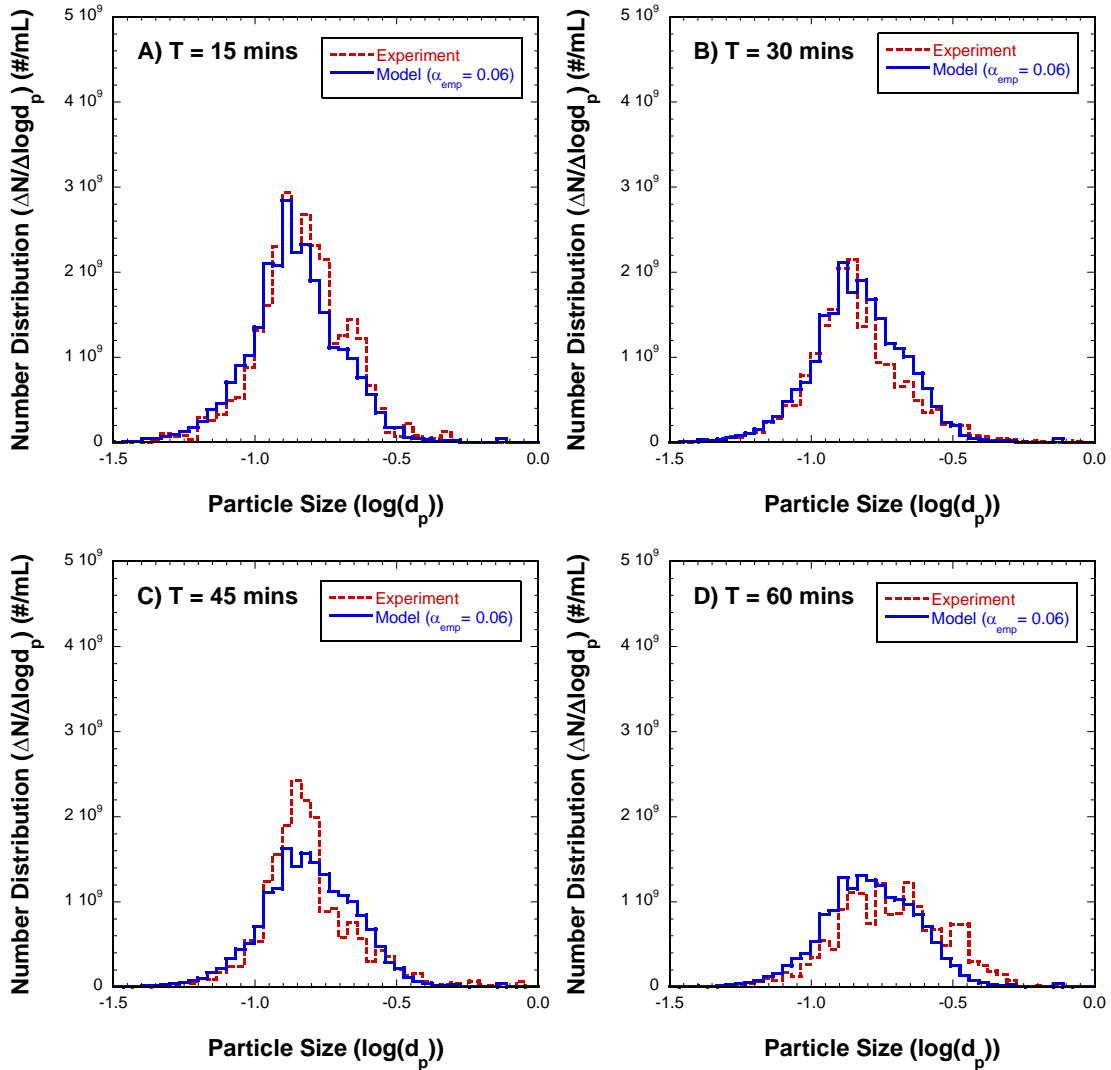

Figure 6.5 Flocculation model vs. experimental data (EXP #2: 100 nm NaNO₃, I = 50
mM 1.1E9 #/mL)

The comparisons between the model predictions and the two experiments above

confirmed that the collision efficiency factors were affected mainly by the chemical

conditions. As the ionic strength was raised from 30 mM to 50 mM of NaNO₃, the α_{emp}

value was adjusted from 0.02 to 0.06 to generate the best-fit curves. Under these two conditions, as discussed in Chapter 4, the higher ionic strength of sodium ions produced a higher degree of destabilization due to compression of the double layer, so that this trend of increasing value of α_{emp} with increasing ionic strength was expected from theory. When AgNPs were better destabilized, the fraction of collisions that resulted in attachment was also greater, reflected in the higher values of α_{emp}. This trend was observed regardless of the initial size of AgNPs. When flocculation of the 30 and 50 nm sized AgNPs was induced by only varying ionic strength, the α_{emp} values grew with increased ionic strength (Experiments #8, 9, and 10 for the 30 nm sized AgNPs; Experiments # 13 and 15 for the 50 nm sized AgNPs). The model predictions for the 30 and 50 nm sized AgNPs are exhibited in Appendix C.

6.3.2 Model Predictions for Different Destabilizing Mechanisms

Along with ionic strength, the ability of the short-range force model to predict the evolution of particle size distributions brought about by different destabilizing mechanisms was evaluated in this research. As discussed in Chapter 4, when the identical ionic strength of $NaNO_3$ and $Ca(NO_3)_2$ was applied to citrate capped AgNPs, more robust flocculation was induced under the $Ca(NO_3)_2$ condition. This occurred because calcium ions and the citrate capping layer form complexes. As a result, $Ca(NO_3)_2$ can destabilize AgNPs by adsorption and charge neutralization as well as by compression of the double layer, whereas $NaNO_3$ only utilizes the mechanism of compression of the double layer.

Because Experiment #1 and #3 were designed so that AgNPs were subjected to identical chemical conditions except for the destabilizing agent, the capability of the model to forecast flocculation dynamics with different destabilizing mechanisms can be manifested by comparing α_{emp} values between the two experiments. Figure 6.6 displays

133

the model predictions for the 100 nm sized AgNPs at an ionic strength of 30 mM as Ca(NO$_3$)$_2$ (Experiment #3). The short-range force model generated the best-fit curves when the α_{emp} value was 0.14 with some overestimations for smaller size particles and underestimations for larger size particles. This α_{emp} value of 0.14 is substantially greater than the α_{emp} value of 0.02 that was attained in Figure 6.3 (Experiment #1). This result agreed with the experimental observations that more successful flocculation took place in under the calcium destabilization and agrees with particle destabilization theory; calcium ions are a better destabilizer than sodium ions for citrate capped AgNPs.

As was expected, the model results for the 30 and 50 nm sized AgNPs showed consistent results (Experiments #10 with sodium and #11 with calcium for the 30 nm sized AgNPs; Experiments # 13 with sodium and #14 with calcium for the 50 nm sized AgNPs). The α_{emp} values were always greater with calcium than sodium ions irrespective of the size of AgNPs if the same ionic strength was applied. The model predictions that are plotted for the 30 and 50 nm sized AgNPs are included in Appendix C.
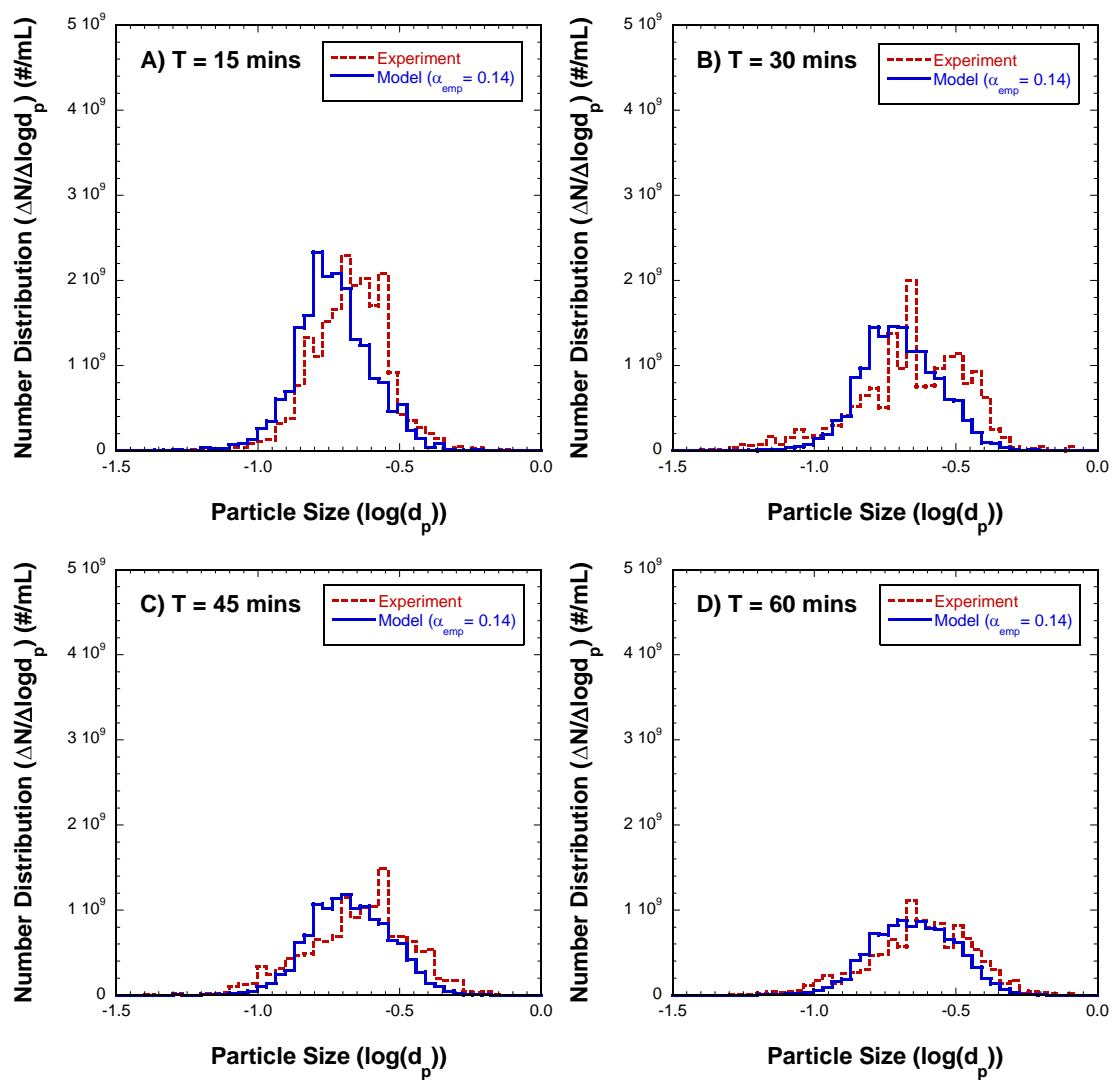
Figure 6.6 Flocculation model vs. experimental data (EXP #3: 100 nm Ca(NO$_3$)$_2$, I = 30 mM 1.2E9 #/mL)

6.3.3 Model Predictions for the Presence of NOM

The effect of NOM on flocculation dynamics of citrate capped AgNPs was experimentally investigated in Chapter 4. The experimental results suggested that more rapid flocculation occurred in the presence of NOM when $I = 50$ mM of $NaNO_3$ was used as a destabilizing salt (Experiment #6). The presence of NOM seemed irrelevant to flocculation dynamics when the destabilization of AgNPs was achieved by $I = 30$ mM of $Ca(NO_3)_2$ (Experiment #7). Although these results seemed contradictory to widely accepted theory that calcium causes interparticle bridging with humic acids, Suwannee River aquatic NOM that was used in the present experiments include fulvic acids and humin fractions; therefore, their behavior can differ from humic acids.

To gain quantitative understanding, the model predictions were generated to simulate these experimental results for the four selected times (t= 15, 30, 45, and 60). Figure 6.7 shows the model predictions for flocculation induced by $I = 50$ mM of $NaNO_3$ in the presence of NOM (Experiment #6). The α_{emp} value for the best-fit curves was 0.15 which was 2.5 times the α_{emp} value under the identical experimental condition without NOM (Experiment #2). This result is consistent with the qualitative analysis of experimental data given earlier; $NaNO_3$ destabilized citrate capped AgNPs to a greater extent in the presence of NOM.

On the other hand, the presence of NOM did not affect the degree of destabilization of citrate capped AgNPs when $Ca(NO_3)_2$ was used as a destabilizing agent. The α_{emp} value was 0.16 in the presence of NOM (Experiment #7) as shown in Figure 6.8. Previously, the α_{emp} value for the identical condition without NOM was found 0.14 (Experiment #3). The α_{emp} values from the model agreed with the experimentally observed phenomenon that NOM had a limited influence on flocculation of citrate capped AgNPs under the calcium destabilization condition.

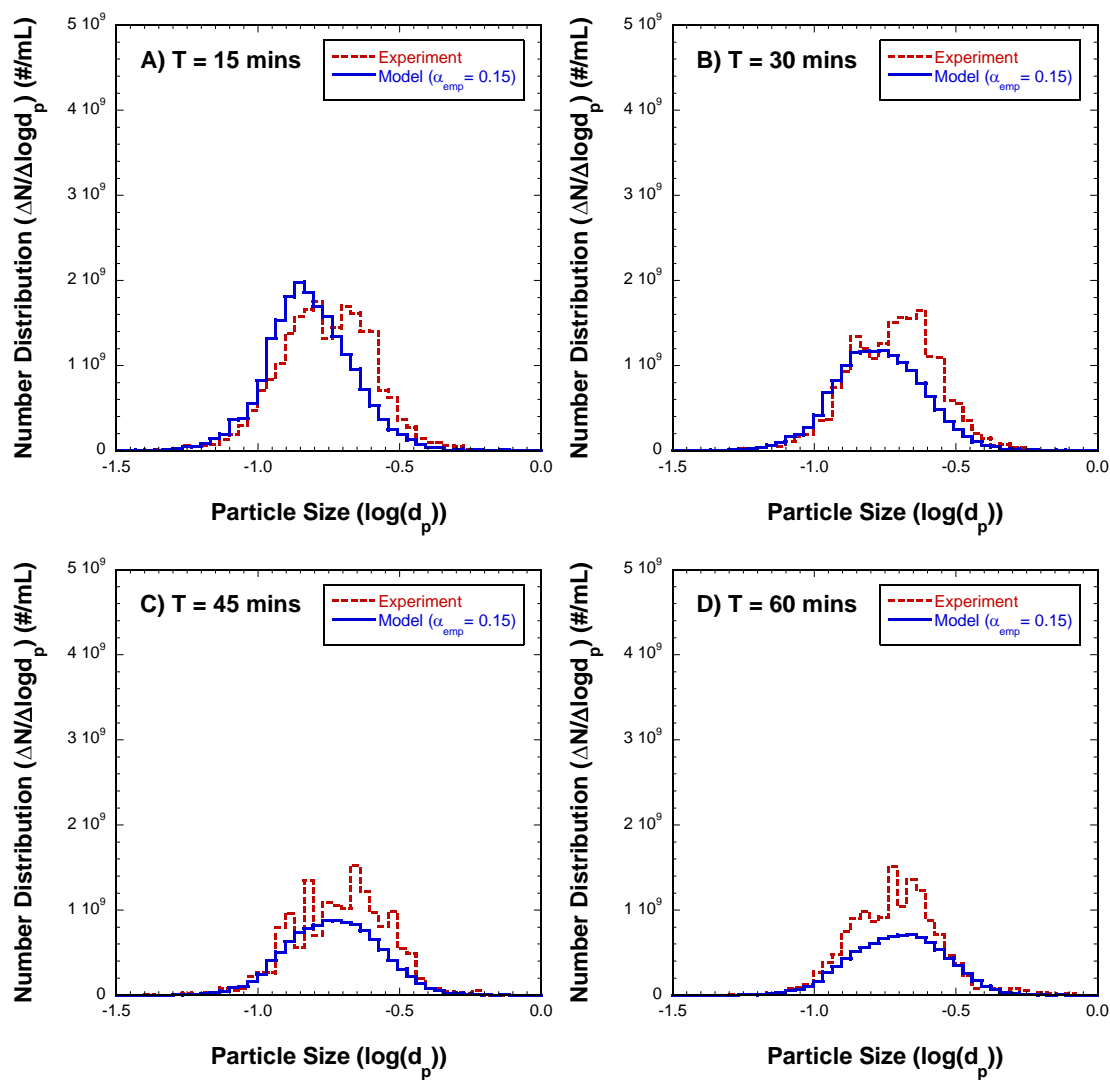Figure 6.7 Flocculation model vs. experimental data (EXP #6: 100 nm NaNO$_3$, I = 50 mM 1.1E9 #/mL in the presence of NOM)
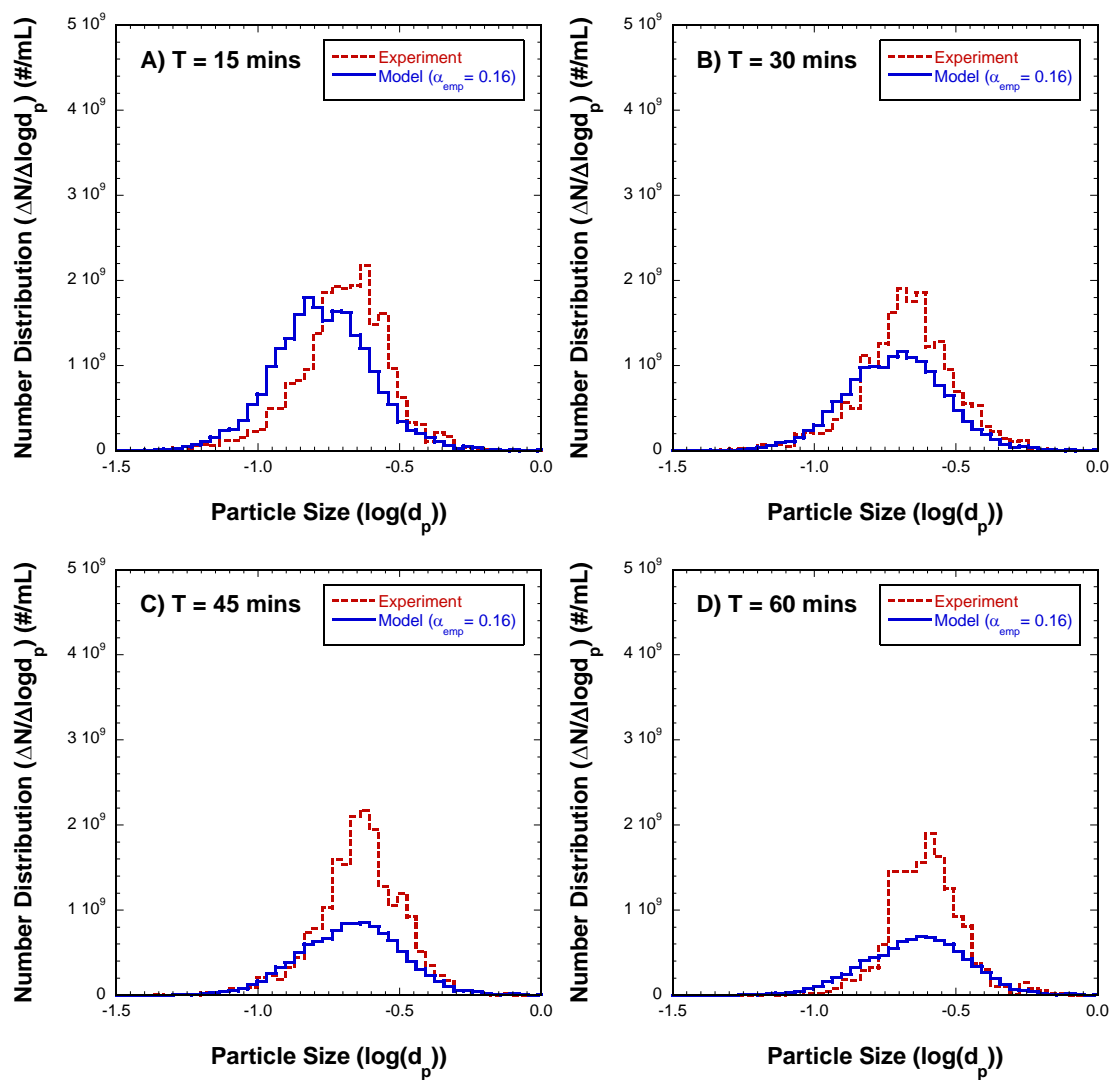
Figure 6.8 Flocculation model vs. experimental data (EXP #7: 100 nm $Ca(NO_3)_2$, I = 30 mM 1.3E9 #/mL in the presence of NOM)

Interestingly, in the presence of NOM, the model predictions started to deviate from the experimental data around t = 30 minutes. Although the model showed fairly good estimations at t=15 minutes, the discrepancy between the model and the data became more severe with time for both destabilizing agents (Figures 6.7 and 6.8). At t = 60 minutes, the heights of the peaks of experimental data were almost twice high as the peaks of the model predictions.

The escalating deviations with time between the experimental data and the model indicated that the evolution of the particle number distributions for the flocculation experiments in the presence of NOM actually slowed down at some point while the flocculation model continuously progressed. For further analysis, a two-step modeling approach was performed for the flocculation experiment under I= 50 mM of $NaNO_3$ in the presence of NOM (Experiment #6). The two-step modeling had two separate time periods for modeling. The first period used the initial number distribution measured at time zero as input for the model to predict the first 15 minutes of flocculation. Then, the number distribution at t = 15 minutes that was experimentally obtained was used as input for the model to predict the number distributions at 30, 45, and 60 minutes.

Figure 6.9 shows the two-step modeling result for Experiment #6 (comparable to Figure 6.7). During the first 15 minutes of flocculation, the best-fit curve was generated by an α_{emp} value of 0.22. The model then found the α_{emp} value of 0.06 for 30, 45, and 60 minutes. The two-step modeling procedure produced results that matched the experimental data far better; the results do not have the escalating deviation that was initially observed in Figure 6.7. Taking the α_{emp} value as an indicator of the degree of destabilization, flocculation in the presence NOM appears to be more robust in the first 15 minutes than the last 45 minutes.
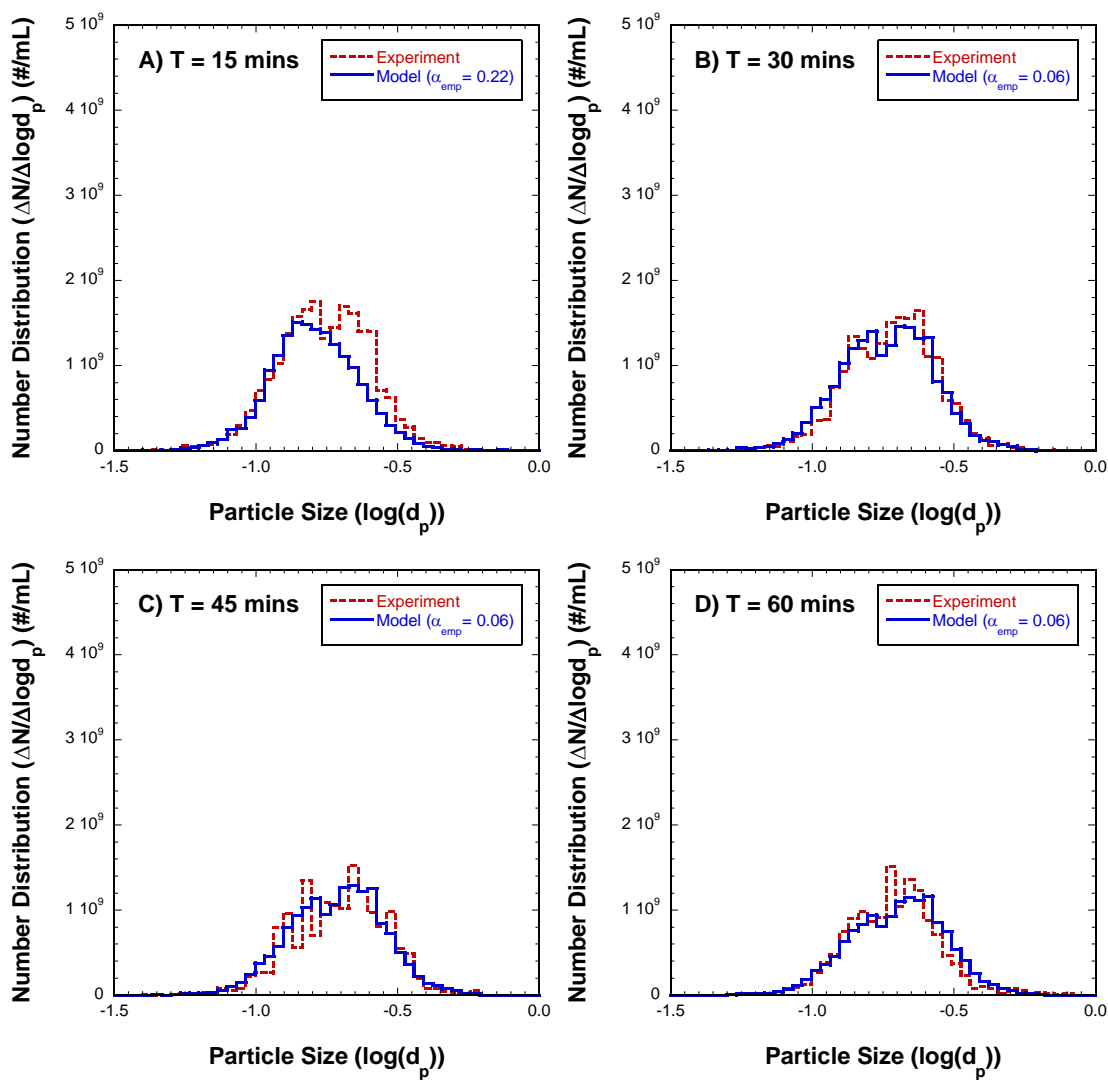
Figure 6.9 Flocculation model vs. experimental data with varying α_{emp} (EXP #6: 100 nm NaNO₃, I = 50 mM 1.1E9 #/mL in the presence of NOM)

Further experimentation is required to fully understand why flocculation dynamics changes in the presence of NOM. Along with the experiments in the presence of NOM (Experiments #6 and #7), there were also a few other experiments that could be modelled only (or far better) by the two-step modeling approach (Experiments #8 and #17). Intriguingly, AgNPs were highly destabilized in those experiments because they

were under relatively high ionic strengths (I > 30 mM), and more rapid flocculation took place in them compared to the other experimental conditions that were tested. Although the fundamental reasons for this apparent two-step flocculation rate were not clear, two conjectures are suggested here.

First, the rapid growth in sizes could have increased the height of the energy barrier for flocs, which allowed flocs to restabilize in the system. In those experiments, the mean particle size of AgNPs became 2 or 3 times its initial mean size within the first 15 minutes of flocculation. As already shown in Chapter 4, larger sized particles have a greater energy barrier in DLVO interactions than smaller sized particles in the identical conditions. Figure 6.10 shows the energy barrier of DLVO curves for the 100 nm sized pristine AgNPs and the 300 nm and 500 nm sized AgNP flocs (with the coalescence assumption, meaning flocs are perfectly spherical). The DLVO calculation suggested that the energy barrier between AgNPs and Ag-flocs will increase as the floc size gets larger during flocculation process. For this reason, for the last 45 minutes in the rapid flocculation experiments, values of α_{emp} needed to be readjusted to account for the changes in the particle interaction energy due to the size growth.
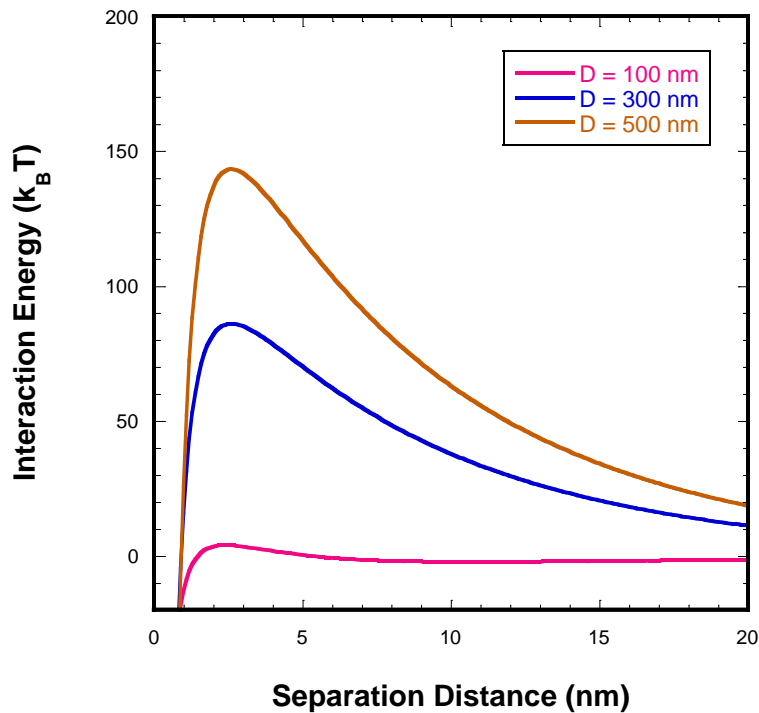
Figure 6.10 The DLVO energy curves for three different sizes of AgNPs in the identical condition (with the assumptions that the surface potential -25.7 mV, the ionic strength of 1 mM, and Hamaker constant of 20 k_BT)

Secondly, floc breakup might have become more significant in the last 45 minutes during the rapid flocculation experiments. In the current flocculation model, flocs are considered as an irreversible product (*i.e.*, no flocs break up). While this assumption helps to simplify a mathematical derivation, it clearly incorporates errors that could be critical in predicting the evolution of particle number distributions at the nanoscale. Due to its complexity, floc breakup is not incorporated in the current flocculation modeling. Floc breakup would need to be included for future research to improve quantitative understanding of nanoparticle flocculation.

6.3.4 Model Predictions for Different Initial Particle Concentrations

Because flocculation is a second-order reaction with respect to the particle number concentration, particle concentration dictates the rate of flocculation. In Chapter 4, the influence of the initial number concentration on flocculation rate was investigated by comparing some characteristic changes in the number distributions among the experiments that varied the initial number concentrations while all other conditions were fixed (Experiments #1 and #5 and Experiments #10 and #12).

In this Chapter, the short-range force model was tested to predict the evolution of particle number distributions for the flocculation experiments that had different initial number concentrations. Figure 6.11 shows the model predictions for the flocculation data of the 100 nm sized AgNPs under $I = 30$ mM of $NaNO_3$ with the initial number concentration of 1.9E9 #/mL (Experiment #5). The best-fit curves for the four times were initially found at an α_{emp} value of 0.12 (not shown in the figure), but an escalating deviation between the model and the experimental data was observed with time, similar to the flocculation results in the presence of NOM. To solve the evolving discrepancy, the two-step model technique was performed for the first fifteen minutes and the last forty-five minutes, separately. The two-step model produced improved best-fit curves with the α_{emp} values of 0.16 and 0.08 for the first fifteen minutes and the last forty-five minutes, respectively (Figure 6.11). This result is further evidence that flocculation was more robust during the first fifteen minutes than the last forty-five minutes. Hence, the same conjecture provided earlier can be applied to this experimental result as well; that is, the EDL might be changing when the particles are growing dramatically bigger by flocculation.
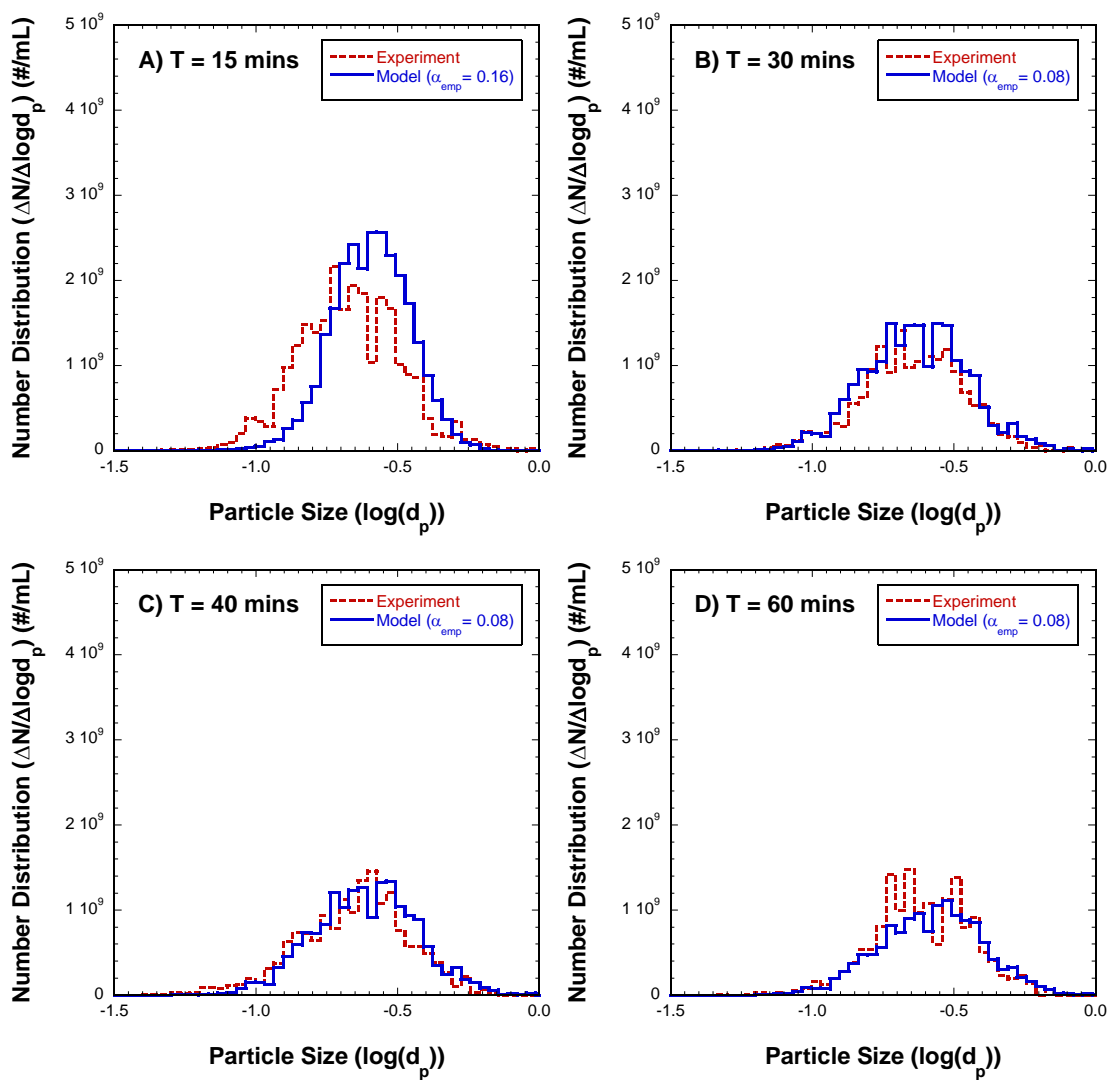
Figure 6.11 Flocculation model vs. experimental data with varying α_{emp} (EXP #5: 100 nm NaNO$_3$, I = 30 mM 1.9E9 #/mL)

The α_{emp} values from the two-step model were compared to the α_{emp} value from Experiment #1, which had the identical chemical conditions but a lower initial particle number concentration of 1.3E9 #/mL (Figure 6.3). Recall that, the α_{emp} value was 0.02 in Experiment #1; the α_{emp} values obtained from the two-step modeling with the higher initial concentration were 8 and 4 times the values obtained for the first fifteen and the

last forty-five minutes, respectively. Comparable results were obtained for the 30 nm sized AgNPs as well (Experiments #10 and #12). The α_{emp} value was greater under the higher initial concentration of the 30 nm AgNPs (Experiment #12) than the lower initial concentration (Experiment #10) while all other conditions remained constant.

Having the higher α_{emp} value with the higher initial number concentration might seem reasonable because more successful flocculation occurred with the higher initial number concentration; however, this statement is rather contradictory to the underlying theory of the flocculation model. The α_{emp} value in the short-range force model is a correction factor for chemical aspects of flocculation while physical aspects (particle transport) are (theoretically) fully accounted for by collision frequency and efficiency functions. Therefore, the α_{emp} value should be identical for two systems regardless of their initial particle number concentrations if the same chemical conditions are applied. This result could possibly indicate that the physics of particle collisions for higher number concentrations were not perfectly incorporated in the flocculation model. Hence, the α_{emp} value was adjusted to accommodate physical aspects of flocculation.

One possible source of inaccuracy in the current flocculation model is that the physical behavior of particles was simulated based on the two-particle system. Classical flocculation research for micron-sized particles were typically performed in the range of the particle number concentration of 1E5 #/cm^3. Taking the inverse of that particle concentration shows that there is one particle per 1E-5 cm^3 of water. This volume of water can be translated into a cube with sides that are roughly 215 μm, which becomes the average distance between particles in water.

However, typical measurements of nanoparticles (*e.g.*, NanoSight or DLS, or TEM) require number concentrations greater than 1E9 #/mL. For example, in Experiment #12, the initial number concentration of 2.5E9 #/mL of AgNPs was used. This number

concentration is converted into the average distance of 7.4 μm between AgNPs. It can be shown with a quick approximation using characteristic diffusion time ($t = x^2/D$, where x is the mean distance, and D is the diffusion coefficient), that it takes only ten seconds for AgNPs to travel 7.4 μm. Therefore, in such high particle concentrations, nanoparticles might already be under the influence of more than two particles nearby at the same time, suggesting a two-particle system might not fully explain the physical behavior of nanoparticles. It will be difficult to incorporate the three-particle problem into flocculation modeling because it has been shown by many scholars and physicists that most three body-problem in quantum mechanics are not solvable. Further experiment is required to pinpoint how the α_{emp} changes with various initial number concentrations.

6.3.6 Model Predictions for Heterodisperse Samples

The efficacy of the short-range force model for flocculation of heterodispersed AgNPs was also studied. Figure 6.12 shows the model results for the heterodispersed sample that consisted of the 30 and 100 nm sized citrate capped AgNPs. Flocculation was induced by $I = 3$ mM of $Ca(NO_3)_2$ in the absence of NOM. The model prediction corresponded with the experimental data fairly well with an α_{emp} value of 0.12. The best-fit curves were established without the two-step modeling approach. In the first thirty minutes, the model closely predicted the reduction of the 30 nm peak in the particle number distributions. For the last thirty minutes of flocculation, the decrease of the 100 nm peak and the creation of larger size particles were predicted well by the model. This result is promising in indicating that the short-range force model could successfully predict the evolution of particle number distributions for the heterodisperse sample. More results of the model predictions for the heterodispersed AgNP sample are included in Appendix C.

146
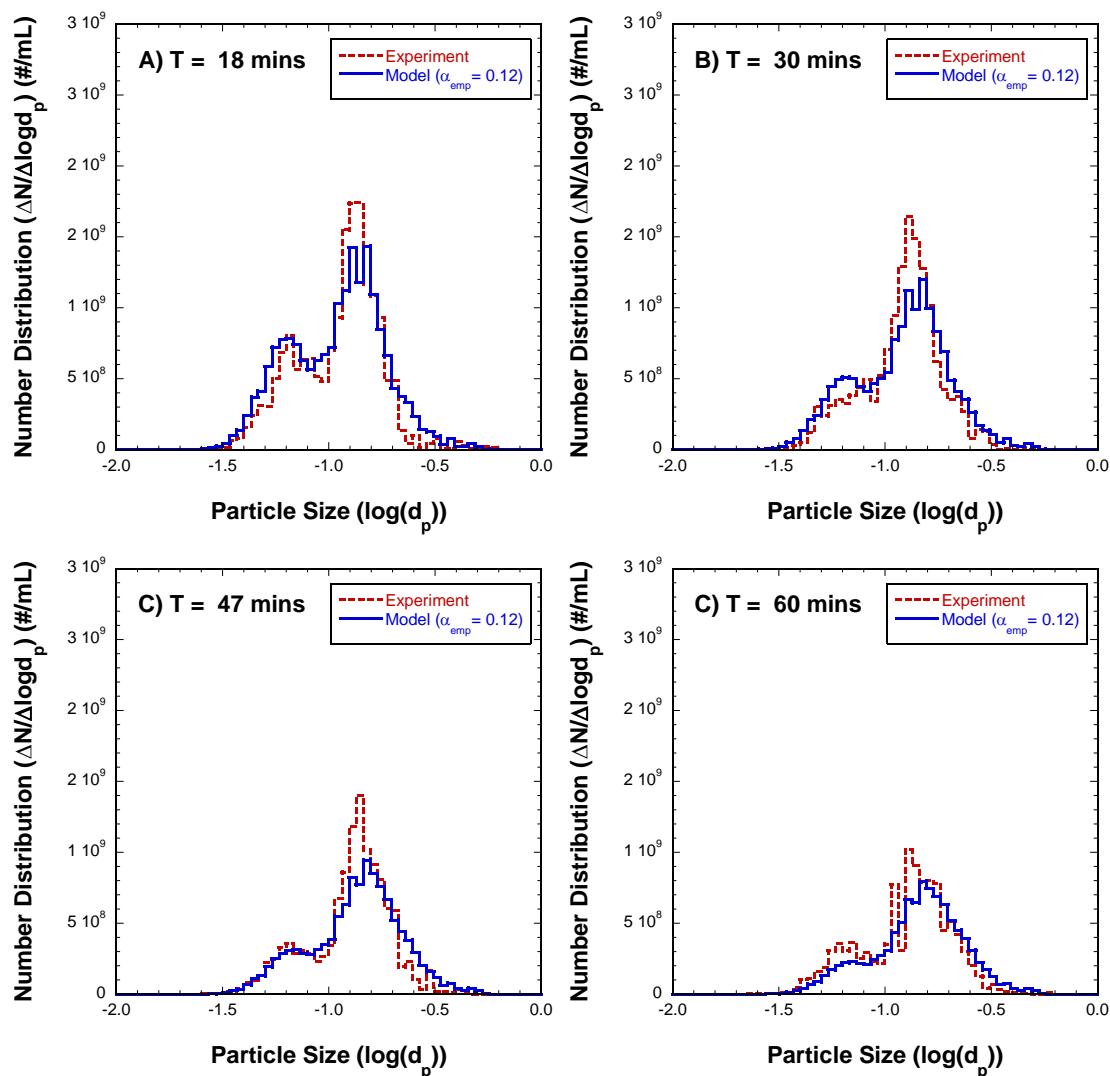
Figure 6.12 Flocculation model vs. experimental data (EXP #18: 30+100 nm Ca(NO$_3$)$_2$ 3 mM 1.3E9 #/mL)

Lastly, to check the compatibility of the α_{emp} values for different particle distributions, the α_{emp} values that were obtained from monodisperse experiments were used to predict flocculation of heterodisperse samples. Under I = 30 mM of NaNO$_3$ for the 30 and 100 nm sized monodisperse samples, the α_{emp} values were 0.25 and 0.02,

respectively (Experiments # 8 and #1). Figure 6.13 shows the model predictions for flocculation of heterodisperse AgNPs under the identical operative conditions. (Experiment #17: I = 30 mM of NaNO$_3$ for the mixture of the 30 & 100 nm AgNPs). While the α_{emp} value of 0.02 underestimated flocculation, the α_{emp} value of 0.25 showed somewhat close predictions to the experimental results. In fact, the best-fit curves were found with the α_{emp} value of 0.27. This result suggested that the flocculation dynamics of the mixture of the 30 and 100 nm sized AgNPs were more closely represented by the 30 nm sized AgNPs. The 30 nm sized AgNPs will control flocculation rate because the 30 nm sized AgNPs were better destabilized compared to the 100 nm sized AgNPs under the identical destabilization. However, the better fitting curve can be found using two-step modeling approach.
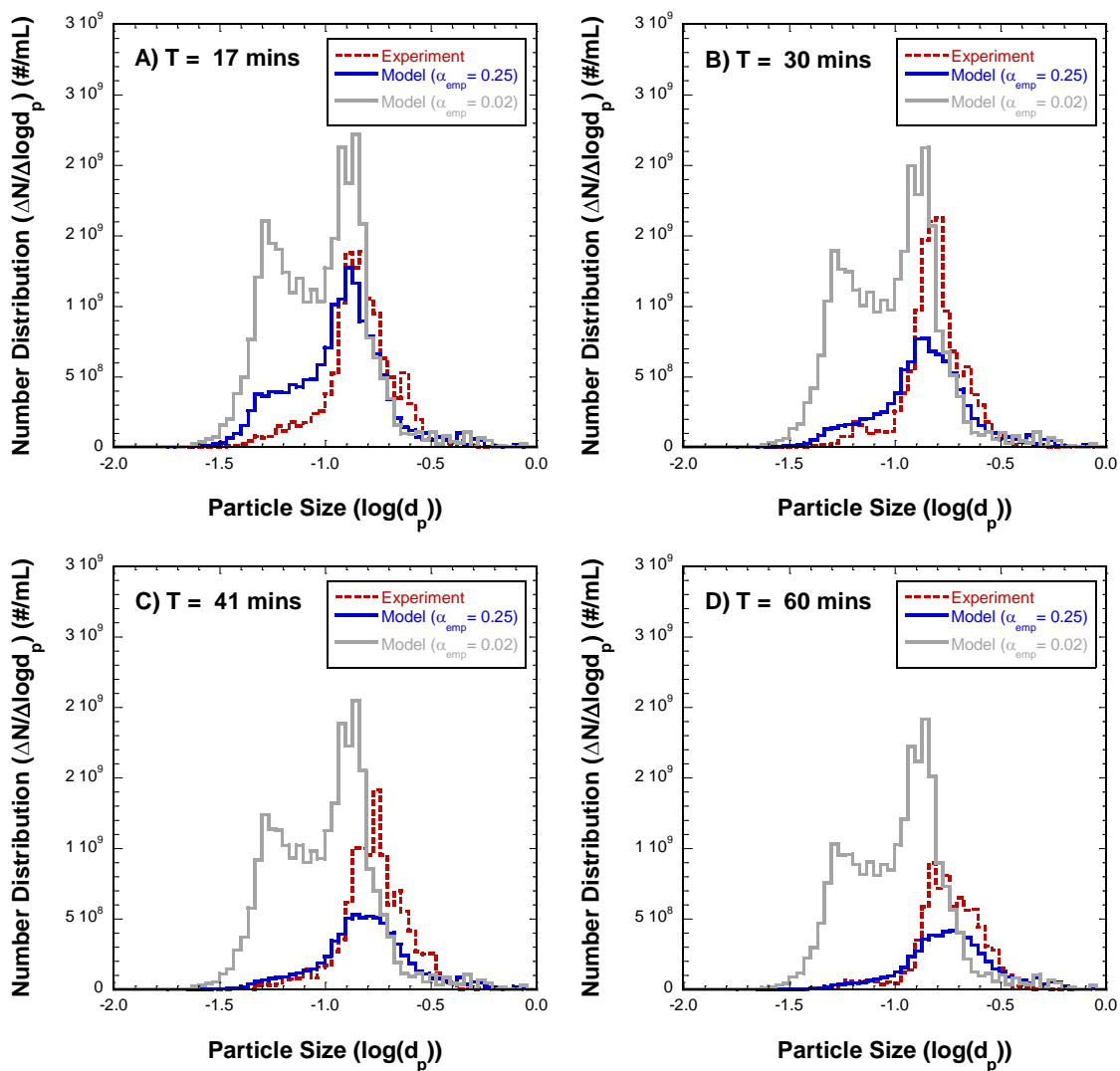
Figure 6.13 Flocculation model predictions for heterodisperse AgNPs (EXP #17: 30+100 nm NaNO$_3$ 30 mM 1.0E9 #/mL) with the α_{emp} values obtained from monodisperse experiments

6.4 DISCUSSION AND CONCLUSIONS

The predictions made by the short-range force model were tested for the flocculation experiments of citrate capped AgNPs. Having the short-range force model tested under various operating conditions, the initial hypothesis of the present research was verified. Comparisons of the short-range model with the experimental data from NanoSight disclosed the areas of the flocculation process at the nanoscale that are well understood, and some that require further investigation.

Generally, the short-range force model with the updated collision efficiency functions does an excellent job of predicting the evolution of particle number distributions at the nanoscale. Successful accounting of AgNPs during laboratory-scale batch flocculation experiments shows that the updated collision efficiency functions are effective. Updating collision efficiency functions for nanoparticles was a critical improvement to the existing flocculation model because, previously, there was no way to account for physics of collisions of nano-sized particles in the flocculation process.

In terms of the agreements between the model predictions and the experimental data, modeling results can be separated into two scenarios. First, the short-range force model agreed well with the experiment results with just one α_{emp} value for the entire sixty minutes of flocculation, suggesting that flocculation rate or the degree of destabilization did not change during the flocculation experiments for both monodispersed and heterodispersed AgNP samples.

The second scenario is that the experimental data could be predicted better by the two-step modeling, having two different α_{emp} values for two separate periods, indicating that flocculation rate or the degree of destabilization had changed during the flocculation experiments. These experiments are listed following:

- the 30 nm AgNPs (1.1E09 #/mL) with I = 30 mM of $NaNO_3$ without NOM (Experiment #8)

- the 100 nm AgNPs (1.1E09 #/mL) with I = 50 mM of $NaNO_3$ with NOM (Experiment #6)

- the 100 nm AgNPs (1.3E09 #/mL) with I = 30 mM of $Ca(NO_3)_2$ with NOM (Experiment #7)

- the 100 nm AgNPs (1.9E09 #/mL) with I = 30 mM of $NaNO_3$ without NOM (Experiment #5)

- the 30 and 100 nm AgNPs with I = 30 mM of $NaNO_3$ without NOM (Experiment #17)

Although fundamental relationships were not clear, these experiments had relatively high ionic strengths of the destabilizing agents compared to other experiments. These results suggest that the degree of destabilization of AgNPs can change during the sixty minutes of flocculation when flocculation is induced by such a high ionic strength (I > 30 mM). Further examination is necessary to delineate the cause and effect for the changes of the degree of the destabilization during flocculation of AgNPs. One suggestion in interpreting these results is that the increasing size of the particles during flocculation could increase the electrostatic repulsion and the consequent energy barrier, and that this would be much more obvious in the rapid flocculation experiments than in those with slower flocculation.

The current mathematic modeling effort advanced the quantitative understanding of flocculation at the nanoscale. Although there were some minor deviations, very good agreement between the measured and predicted particle size distributions was observed. From these results, it can be concluded that flocculation of nanoparticles can be quantitatively explained using standard theory that was originally developed for micro-

sized particles. From a water treatment point of view, this conclusion is optimistic: nanoparticles can be effectively removed in typical water treatment as long as nanoparticles are well destabilized to reduce surface potential.

Chapter 7: Conclusions

7.1. CONCLUSIONS

The main objective of this research was to improve the quantitative understanding of how nanoparticle size distributions change during flocculation. Both experimental examination and mathematical modeling were performed. Well controlled laboratory scale batch flocculation experiments with citrate capped AgNPs were performed under a variety of physiochemical conditions to evaluate the impacts of controlling variables, such as initial particle size, initial particle number concentration, ionic strength, destabilizing mechanism, and inclusion of natural organic matter on the measured nanoparticle size distributions.

Mathematical modeling consisted of two parts. First, mathematical expressions of particle collisions for the three main transport mechanisms at the nanoscale were developed by numerical trajectory analysis. The results of trajectory analysis were reported in terms of collision efficiency functions for two extreme cases: no repulsive energy between particles and the surface potential of -25 mV. As expected, Brownian motion is the most significant transport mechanism for the nano-sized particles. In some cases, however, differential sedimentation and fluid shear could be as important as Brownian motion at the nanoscale; therefore, caution is required not to underestimate differential sedimentation and fluid shear transport during flocculation at the nanoscale.

The second part of mathematical modeling was to verify the proposed hypothesis: the well-known mathematical theory of flocculation for micro-sized particles can be applied to nano-sized particles. The Smoluchowski theory for particle collisions and the updated collision efficiency functions were used together to predict the evolution of particle number distributions at various time during flocculation of nanoparticles. Comparisons between the model predictions and the experimental data revealed the areas

of the flocculation process for nanoparticles that are quantitatively well understood, and some that require further study. Overall, the short-range force model with the updated collision efficiency functions was able to consistently match the measured particle number distributions at various times.

Based on the results of the experimental investigation, mathematical modeling, and iterative comparison between the data and the model, the following conclusions can be drawn:

1. Calcium ions are more effective than sodium ions as a destabilizing agent for citrate capped AgNPs regardless of their initial particle sizes. If the same ionic strength of calcium and sodium ions is applied to citrate capped AgNPs, calcium ions induce better flocculation, apparently because calcium citrate complexes are formed and neutralize the surface charge of the nanoparticles, whereas the sodium nitrate works only by compression of the electrical double layer.

2. If all other conditions are identical, more successful flocculation will take place in a system with a higher particle number concentration. Because flocculation is a second-order reaction, the flocculation rate is strongly dependent on the particle number concentration.

3. Flocculation of AgNPs brought about by $NaNO_3$ was slightly more rapid in the presence of Suwannee River aquatic NOM than in the absence of it. However, flocculation induced by $Ca(NO_3)_2$ did not show such effect. These results suggested that the presence of NOM could affect particle destabilization; therefore, NOM is an important parameter to be understood.

4. Due to higher diffusion coefficients, smaller sized AgNPs are more favorable to form flocs than larger sized AgNPs under the identical operative conditions.

5. The stability of both monodispersed and heterodispersed AgNPs can be estimated by DLVO energy curves, and their destabilization by various mechanisms was consistent with conventional theory.

6. Brownian motion is the most significant transport mechanism at the nanoscale; however, the other two transport mechanisms (differential sedimentation and fluid shear) could also be as important as Brownian motion in some cases.

7. If nanoparticles are completely destabilized, then collision efficiency functions for differential sedimentation and fluid shear (α_{DS} and α_{Sh}) can be greater than 1, indicating the vdW attraction can become a governing force in short-range transport at the nanoscale.

8. In the presence of EDL, temporary secondary doublets are frequently observed in trajectory analysis for differential sedimentation and fluid shear at the nanoscale.

9. The short-range force model with the updated collision efficiency functions (α_{Br}, α_{DS}, and α_{Sh}) can accurately predict the evolution of particle number distributions of AgNPs, suggesting that the updated collision efficiency functions are effective and practical.

10. Some flocculation experimental results of AgNPs can be predicted better by the model through a two-step modeling approach (a higher α_{emp} at early times and a lower value later) because the dynamics of flocculation changes during the hour of flocculation experiments. The first fifteen minutes shows more rapid flocculation than the last forty-five minutes.

7.2. SIGNIFICANCE

This research contributed new knowledge of particle destabilization and flocculation processes in water treatment be extending ideas of previous researchers into

the nanoscale. The primary objective of understanding the evolution of the particle number distributions at the nanoscale during flocculation processes was achieved through both experimental investigation and mathematical modeling. From the conclusions stated above, it is clear that the dynamics of flocculation at the nanoscale is consistent with standard theories of particle destabilization and transport. Direct observations of changes in absolute particle number distributions from NTA and numerical trajectory analysis enhance both qualitative and quantitative understanding of particle separation processes of nanoparticles. Previously, the dynamics of flocculation at the nanoscale could not be modeled using available flocculation models. The product of this research, updated collision efficiency functions that account for the collision mechanisms of nanoparticles, allows prediction of the evolution of nanoparticle number distributions brought about by flocculation. The fact that experimentally observed flocculation results for AgNPs were accurately estimated by the model represents an enhancement in the quantitative understanding of flocculation.

The findings of this research are relevant to design and operation of flocculation processes that would encounter nanoparticles. If particle destabilization is well performed, nano-sized particles will flocculate into larger particles rapidly. Although no experiments were performed with both nano- and micro-sized particles in the same suspension, the fact that the results of this research on nanoparticle flocculation were completely consistent with the well-established theory for micro-sized particles suggests that flocculation between nano- and micro-sized particles would work well. Therefore, nanoparticles can be expected to be flocculated into much larger sizes that will be well removed in conventional water treatment plants, as long as proper destabilization is achieved.

7.3. RECOMMENDATIONS FOR FUTURE WORK

This research was initiated from the concern that the increasing use of engineered nanomaterials would eventually reach drinking water sources and water treatment systems. While the present research results have improved the quantitative understanding of the flocculation dynamics at the nanoscale, they also have revealed areas requiring further study. A more fundamental understanding and an enhanced ability to predict the evolution of particle size distributions at the nanoscale in flocculation could be achieved through improvements and extensions to the present research. The following specific tasks are recommendations for future work:

1. Performing flocculation experiments under more complex operational conditions that emulate more practical flocculation processes would help developing fundamental understanding at the nanoscale for engineering practice. For example, experiments with more practical destabilizing mechanisms, such as enmeshment in a precipitate (widely used in water treatment plants), can be performed.

2. Expanding laboratory scale flocculation to full scale by measuring the evolution of particle number distributions of samples from a treatment plant would be beneficial to support the findings from laboratory scale experiments.

3. More experimental research efforts are required to comprehend other nanomaterials. AgNPs were chosen for this research mainly because silver was the most popular nanomaterial being produced and used. Along with silver, other materials are widely used, such as carbon nanotubes, silica, and iron.

4. The main reason of the escalating discrepancies between the model and the experimental results was that the flocculation rate slowed down after some time during laboratory scale flocculation experiments. As flocs gets larger, an

increasing energy barrier in DLVO interaction is expected. However, this physical effect is not accounted for in the current flocculation modeling.

5. The flocculation model might be enhanced by addition of the effect of floc breakup and the fractal nature of flocs. The effect of floc breakup and the fractal nature of flocs could be investigated further and incorporated into the existing model.

Appendix A: Particle Number Distributions

Every particle number distribution that was obtained during the laboratory scale flocculation experiments is displayed here.
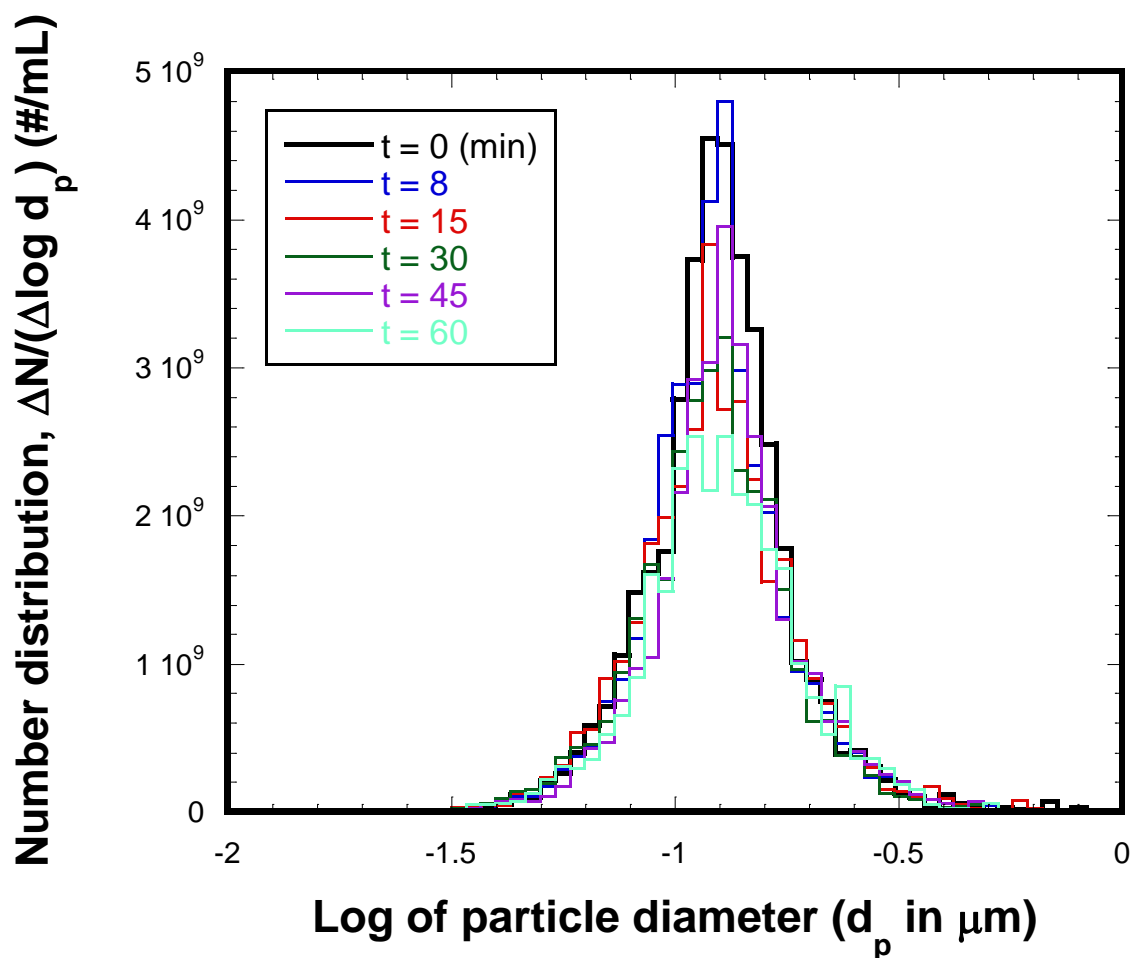
Figure A.1 Particle number distribution from Experiment #1

Experiment #1: the 100 nm sized citrate capped AgNPs under I =30 mM of NaNO$_3$, with an initial number concentration of 1.3E9 #/mL in the absence of NOM. The experiment was performed on May 20, 2016.
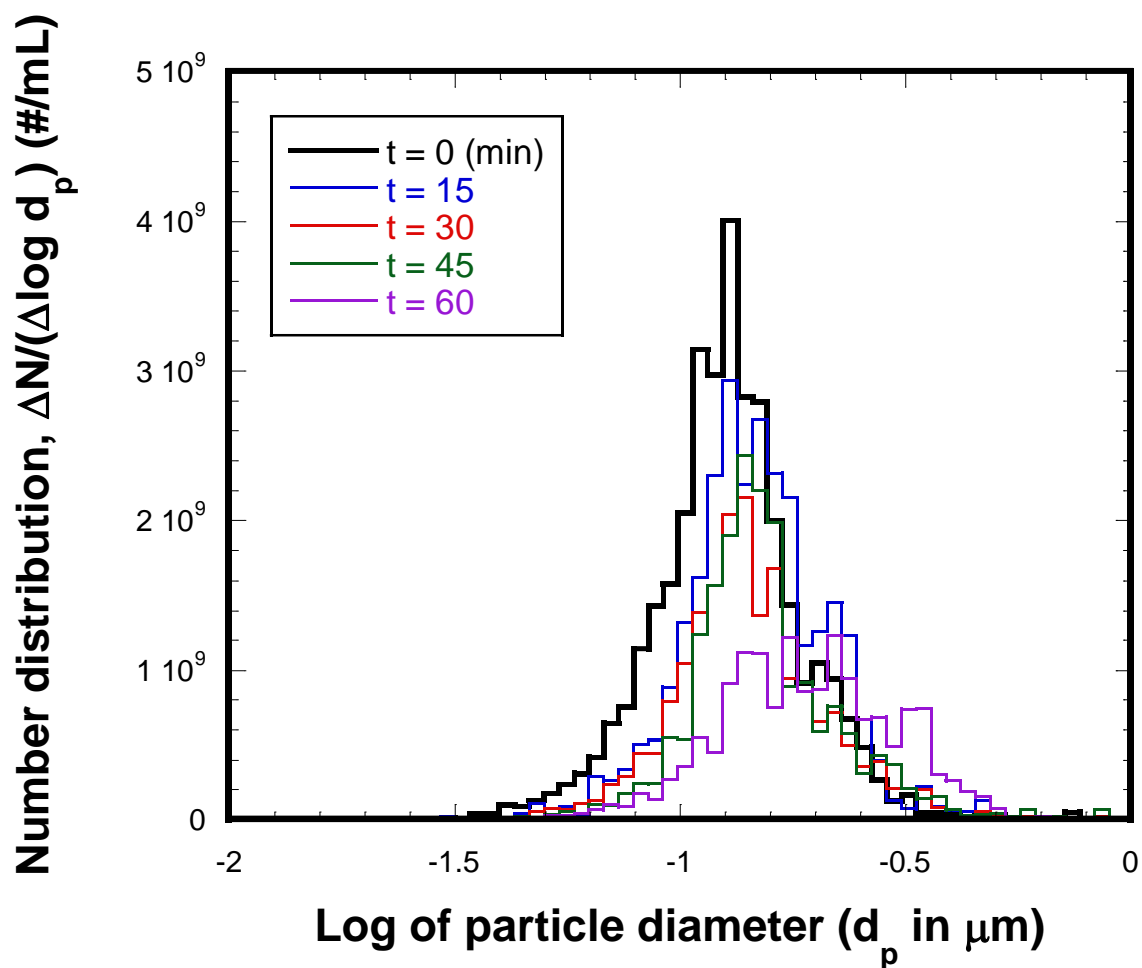
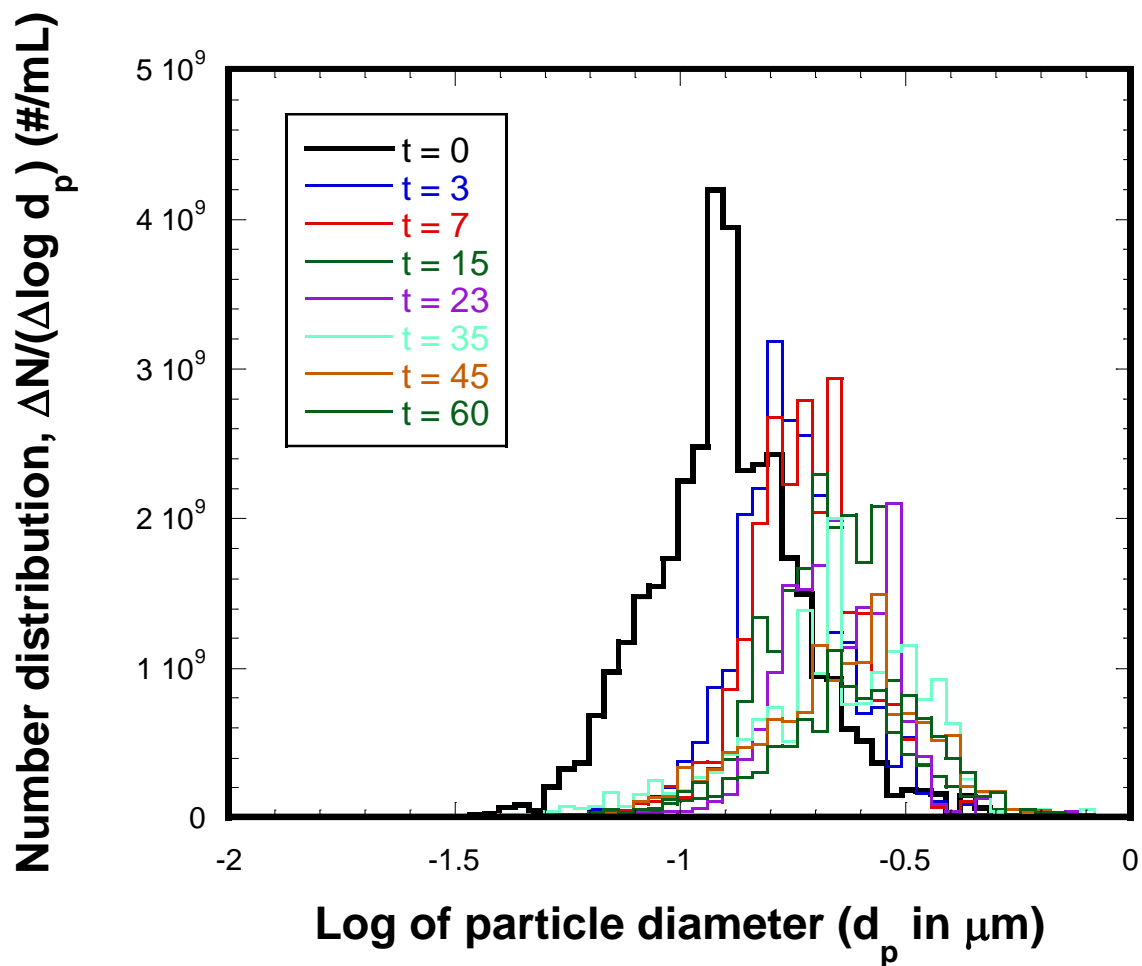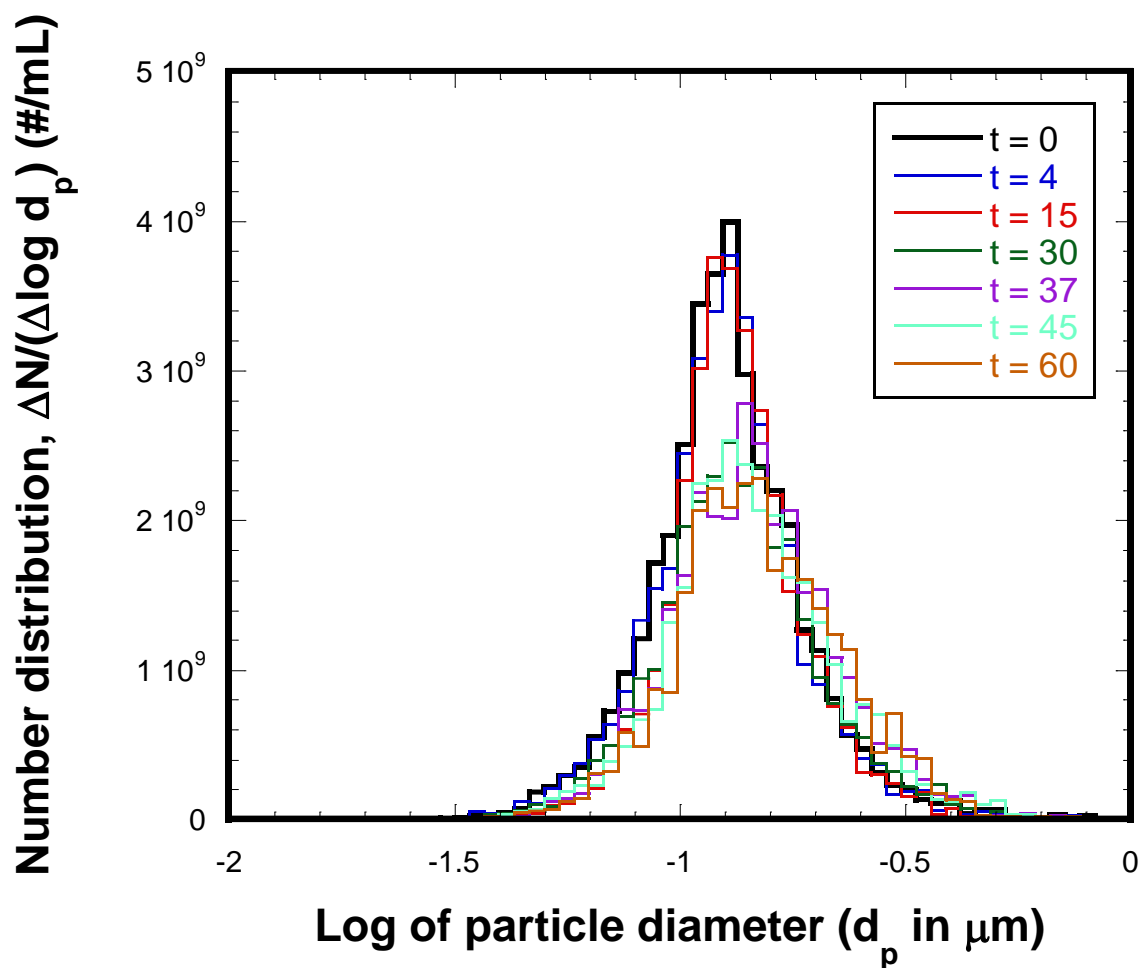Figure A.2 Particle number distribution from Experiment #2

Experiment #2: the 100 nm sized citrate capped AgNPs under I =50 mM of NaNO₃, with an initial number concentration of 1.1E9 #/mL in the absence of NOM. The experiment was performed on May 23, 2016.

Figure A.3 Particle number distribution from Experiment #3

Experiment #3: the 100 nm sized citrate capped AgNPs under I =30 mM of $Ca(NO_3)_2$, with an initial number concentration of 1.2E9 #/mL in the absence of NOM. The experiment was performed on May 24, 2016.

Figure A.4 Particle number distribution from Experiment #4

Experiment #4: the 100 nm sized citrate capped AgNPs under I =30 mM of Na$_3$-Citrate, with an initial number concentration of 1.2E9 #/mL in the absence of NOM. The experiment was performed on May 26, 2016.
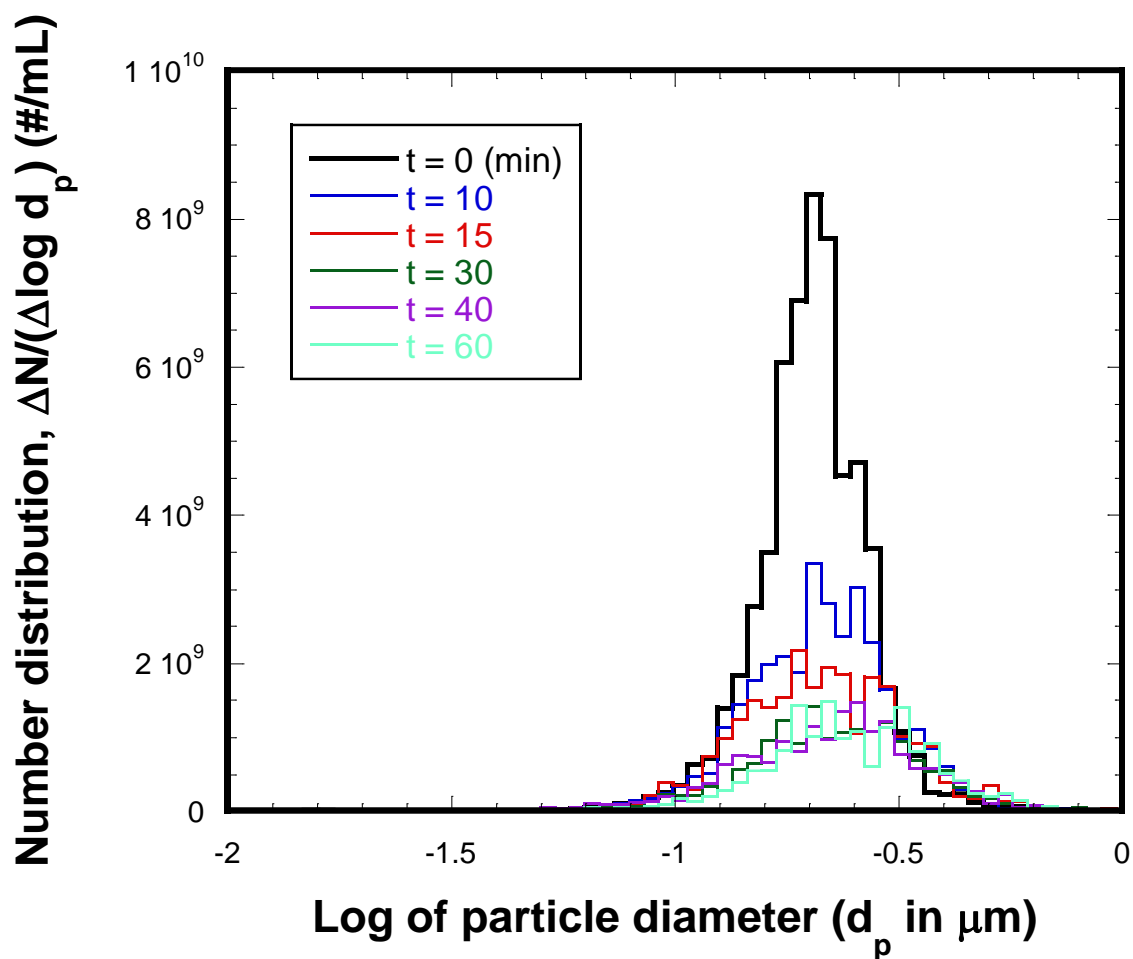
Figure A.5 Particle number distribution from Experiment #5

Experiment #5: the 100 nm sized citrate capped AgNPs under I =30 mM of $NaNO_3$, with an initial number concentration of 1.9E9 #/mL in the absence of NOM. The experiment was performed on April 28, 2016.
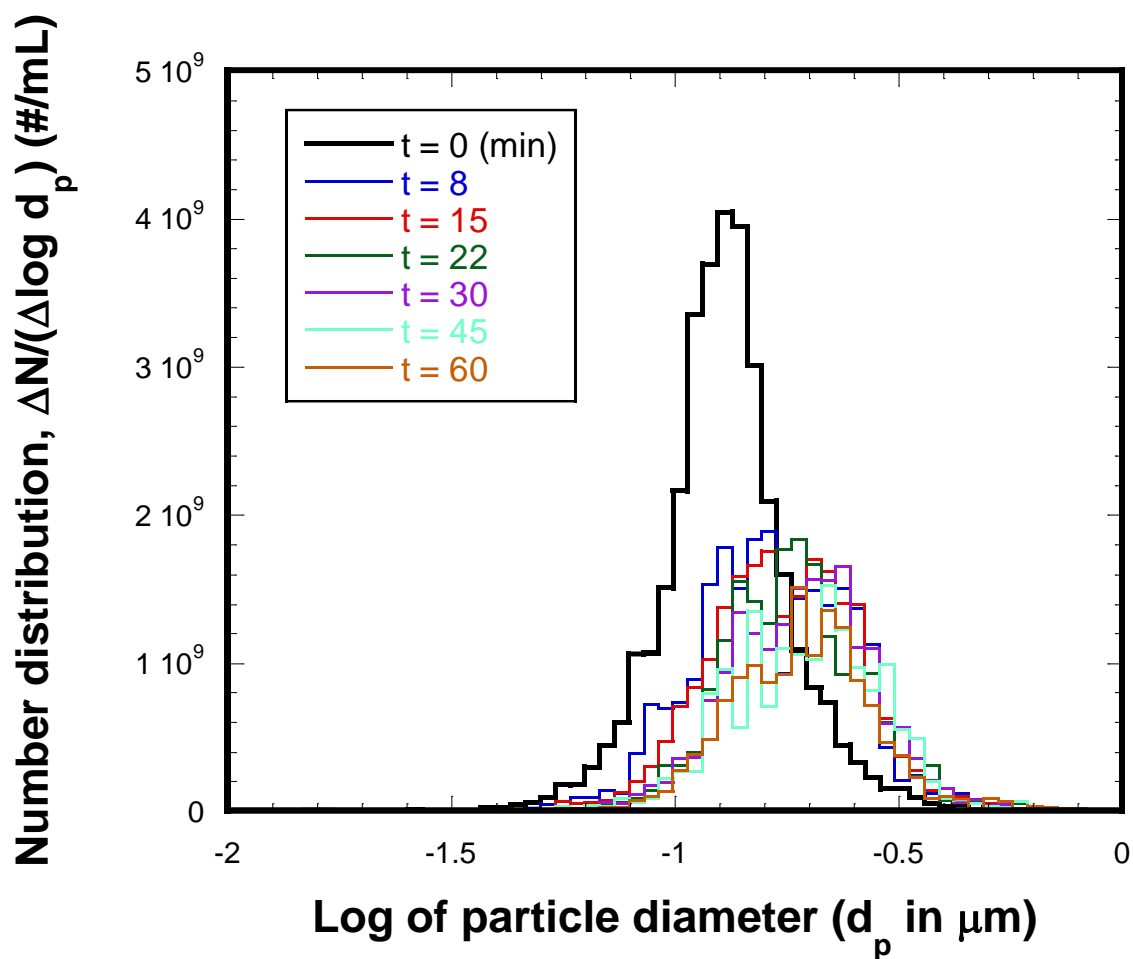
Figure A.6 Particle number distribution from Experiment #6

Experiment #6: the 100 nm sized citrate capped AgNPs under I =50 mM of NaNO$_3$, with an initial number concentration of 1.1E9 #/mL in the presence of NOM. The experiment was performed on Jun 1, 2016.
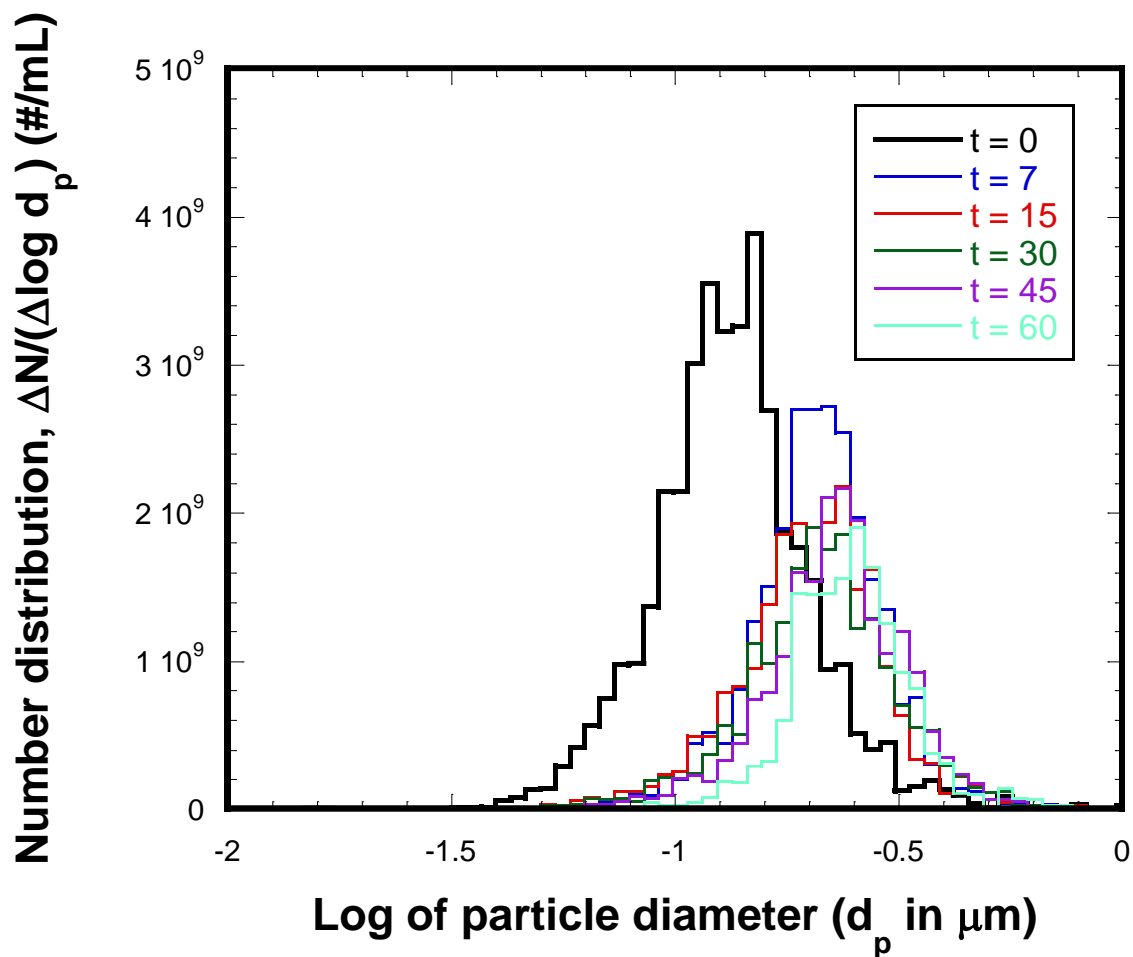
Figure A.7 Particle number distribution from Experiment #7

Experiment #7: the 100 nm sized citrate capped AgNPs under I =30 mM of Ca(NO₃)₂, with an initial number concentration of 1.3E9 #/mL in the presence of NOM. The experiment was performed on May 27, 2016.
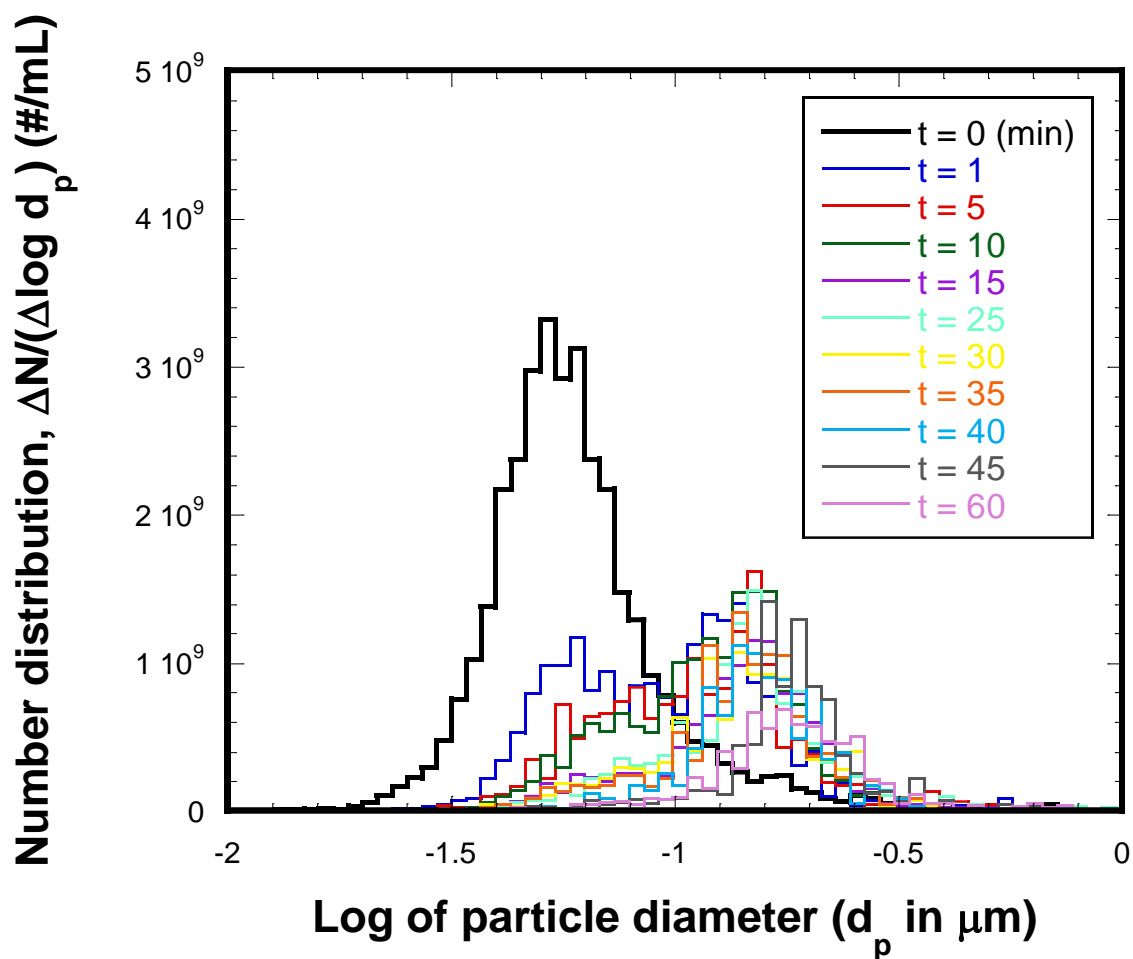
Figure A.8 Particle number distribution from Experiment #8

Experiment #8: the 30 nm sized citrate capped AgNPs under I =30 mM of NaNO₃, with an initial number concentration of 1.1E9 #/mL in the absence of NOM. The experiment was performed on Jun 9, 2016.
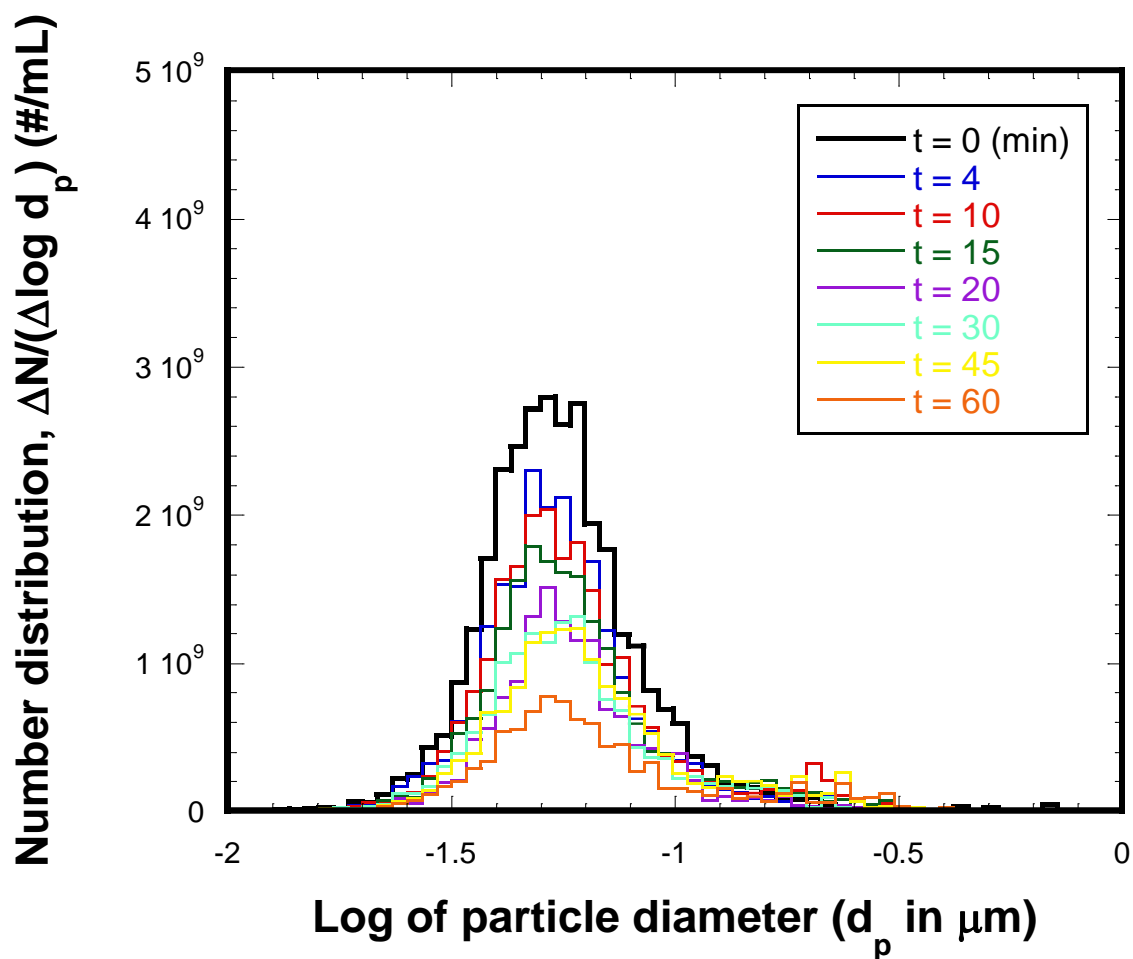
Figure A.9 Particle number distribution from Experiment #9

Experiment #9: the 100 nm sized citrate capped AgNPs under I =10 mM of $NaNO_3$, with an initial number concentration of 1.0E9 #/mL in the absence of NOM. The experiment was performed on Jun 15, 2016.

Figure A.10 Particle number distribution from Experiment #10

Experiment #10: the 30 nm sized citrate capped AgNPs under I =3 mM of NaNO3, with an initial number concentration of 1.1E9 #/mL in the absence of NOM. The experiment was performed on Jun 16, 2016.

Figure A.11 Particle number distribution from Experiment #11

Experiment #11: the 30 nm sized citrate capped AgNPs under I =3 mM of Ca(NO$_3$)$_2$, with an initial number concentration of 1.2E9 #/mL in the absence of NOM. The experiment was performed on Jun 17, 2016.
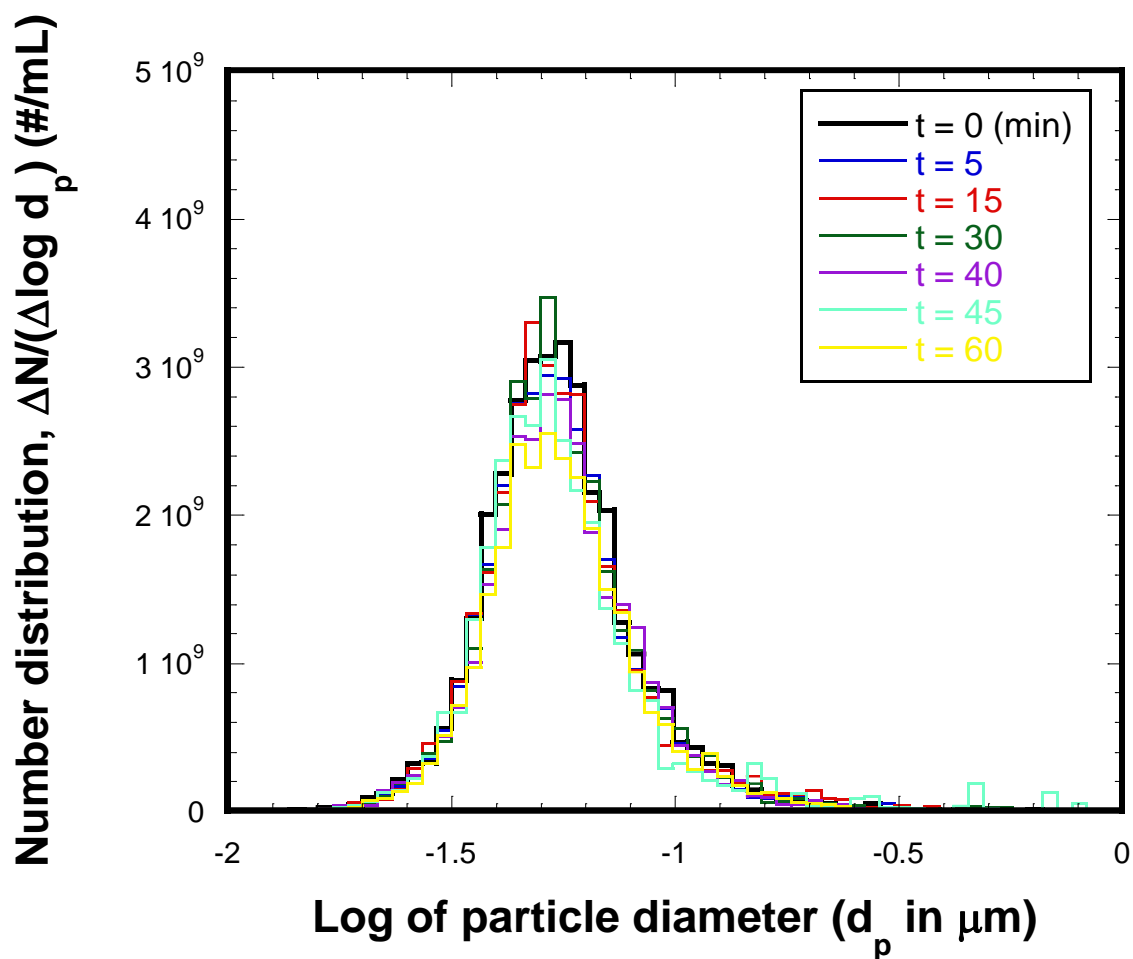
Figure A.12 Particle number distribution from Experiment #12

Experiment #12: the 30 nm sized citrate capped AgNPs under I =3 mM of NaNO₃, with an initial number concentration of 2.5E9 #/mL in the absence of NOM. The experiment was performed on Jun 22, 2016.
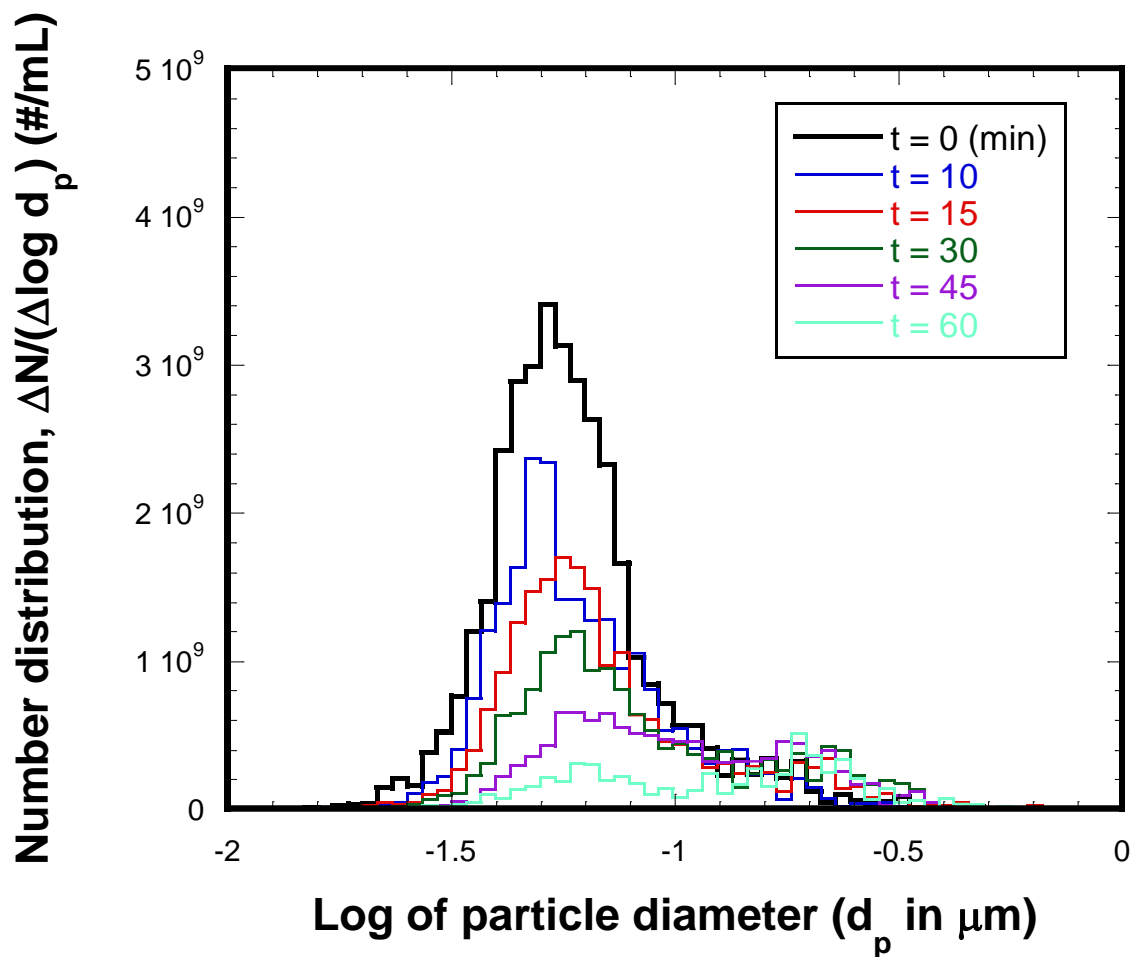
Figure A.13 Particle number distribution from Experiment #13

Experiment #13: the 50 nm sized citrate capped AgNPs under I =3 mM of NaNO₃, with an initial number concentration of 1.2E9 #/mL in the absence of NOM. The experiment was performed on Jun 29, 2016.
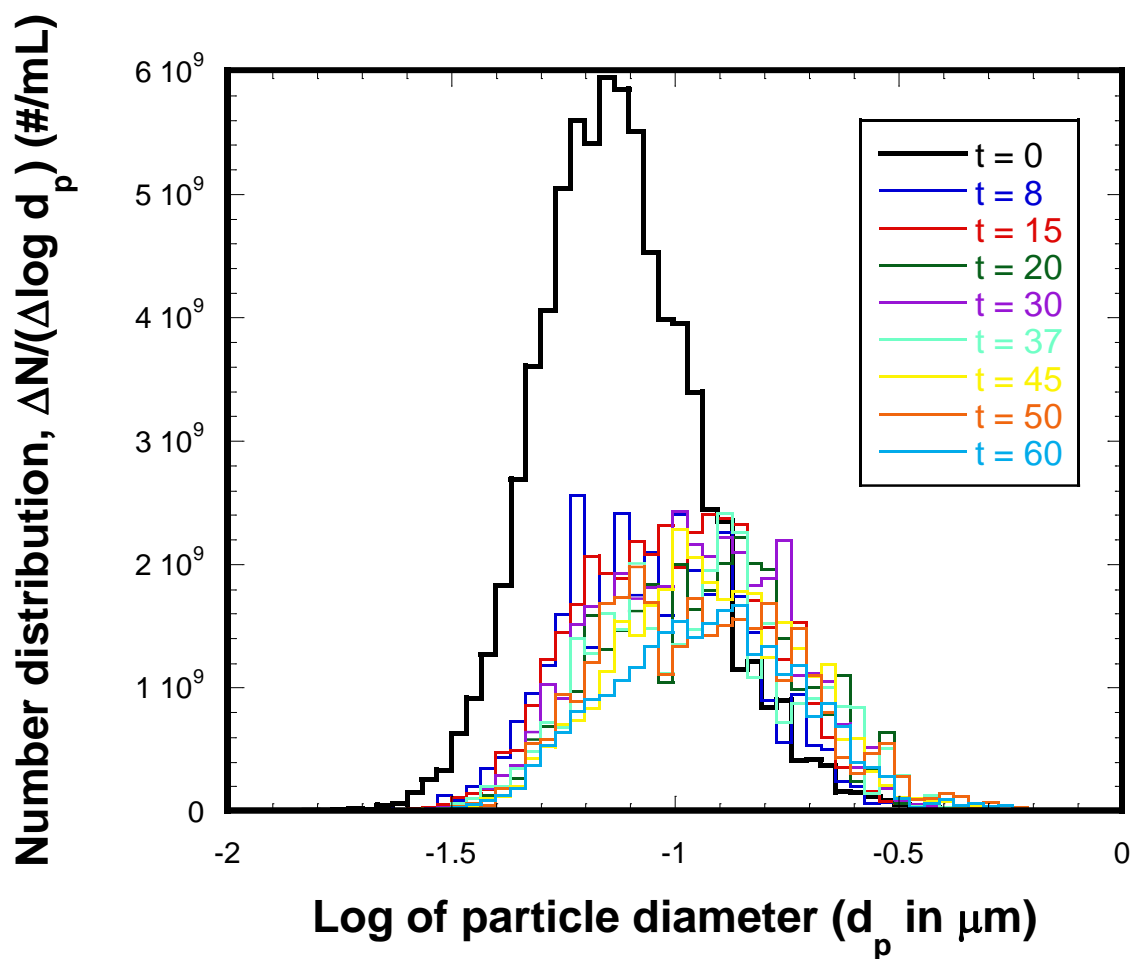
Figure A.14 Particle number distribution from Experiment #14

Experiment #14: the 50 nm sized citrate capped AgNPs under I =3 mM of Ca(NO$_3$)$_2$, with an initial number concentration of 1.2E9 #/mL in the absence of NOM. The experiment was performed on Jun 30, 2016.

Figure A.15 Particle number distribution from Experiment #15

Experiment #15: the 50 nm sized citrate capped AgNPs under I =10 mM of NaNO₃, with an initial number concentration of 1.1E9 #/mL in the absence of NOM. The experiment was performed on Jun 23, 2016.
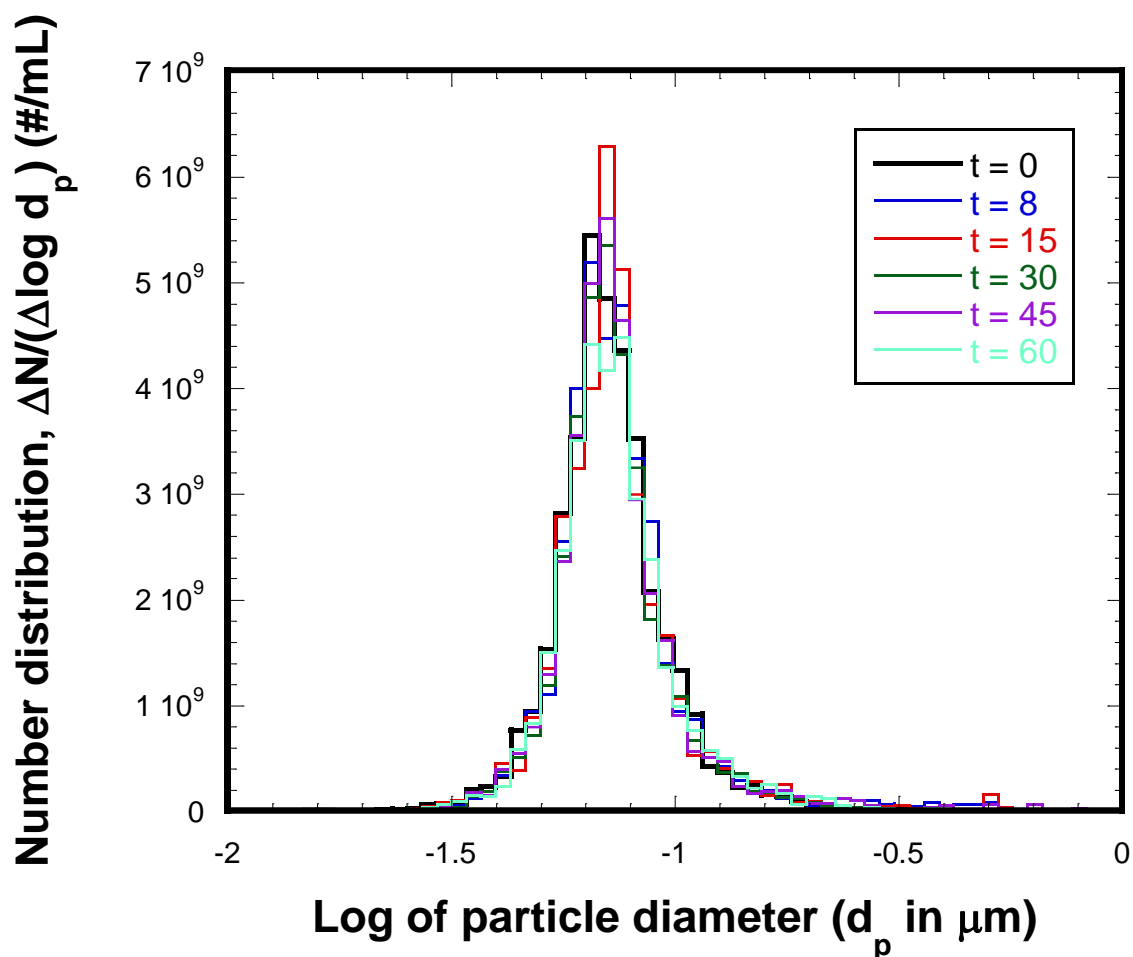
Figure A.16 Particle number distribution from Experiment #16

Experiment #16: the 30 & 100 nm sized citrate capped AgNPs under I =10 mM of NaNO₃, with an initial number concentration of 1.3E9 #/mL in the absence of NOM. The experiment was performed on July 18, 2016.

Figure A.17 Particle number distribution from Experiment #17

Experiment #17: the 30 & 100 nm sized citrate capped AgNPs under I =30 mM of NaNO₃, with an initial number concentration of 1.0E9 #/mL in the absence of NOM. The experiment was performed on July 21, 2016.
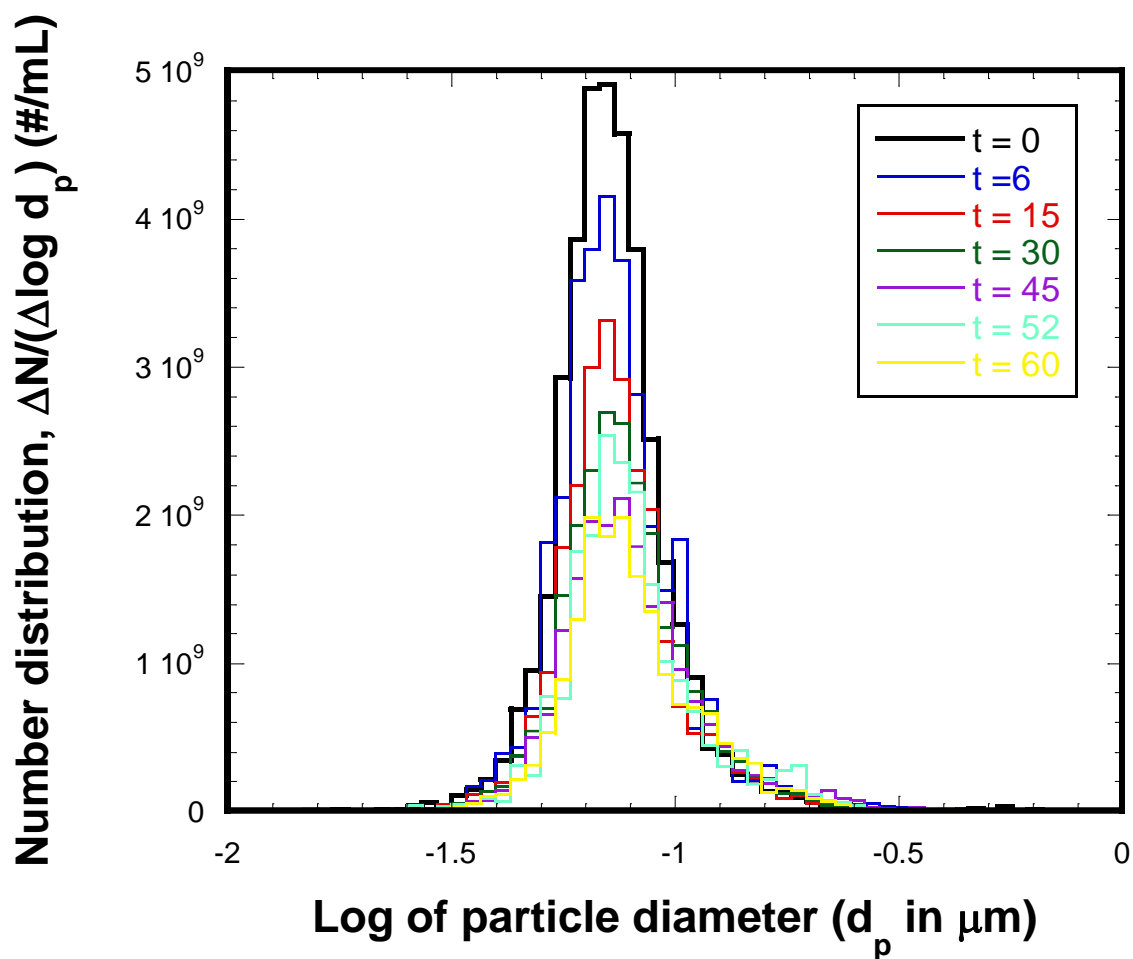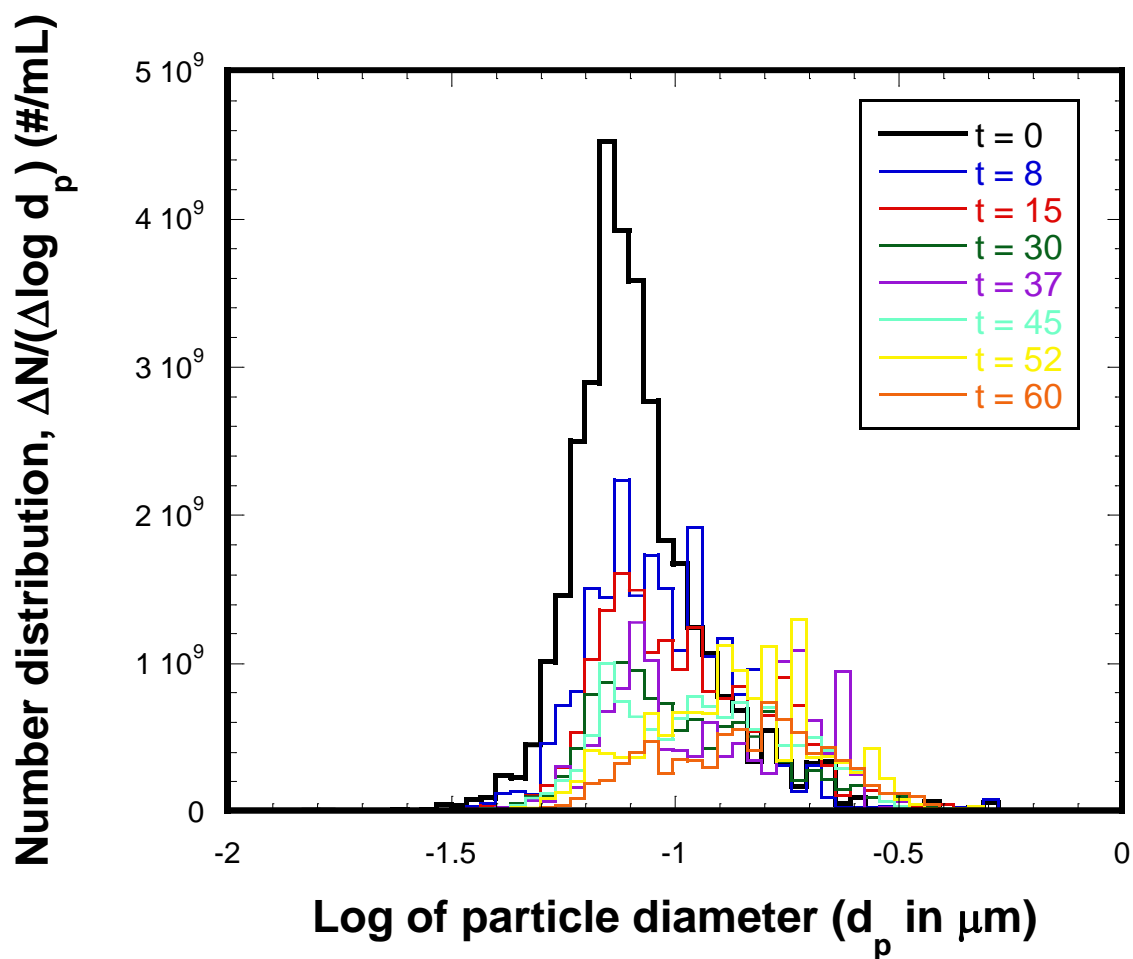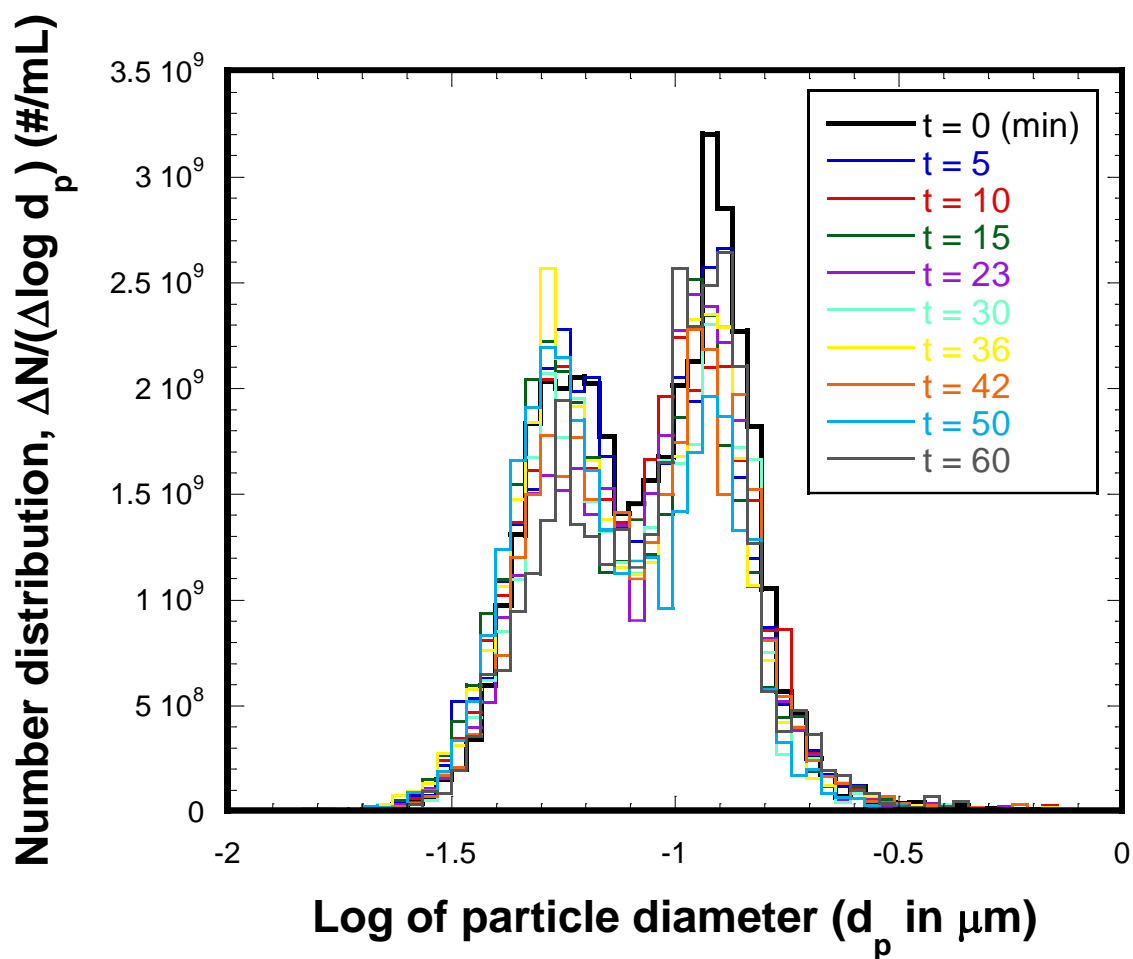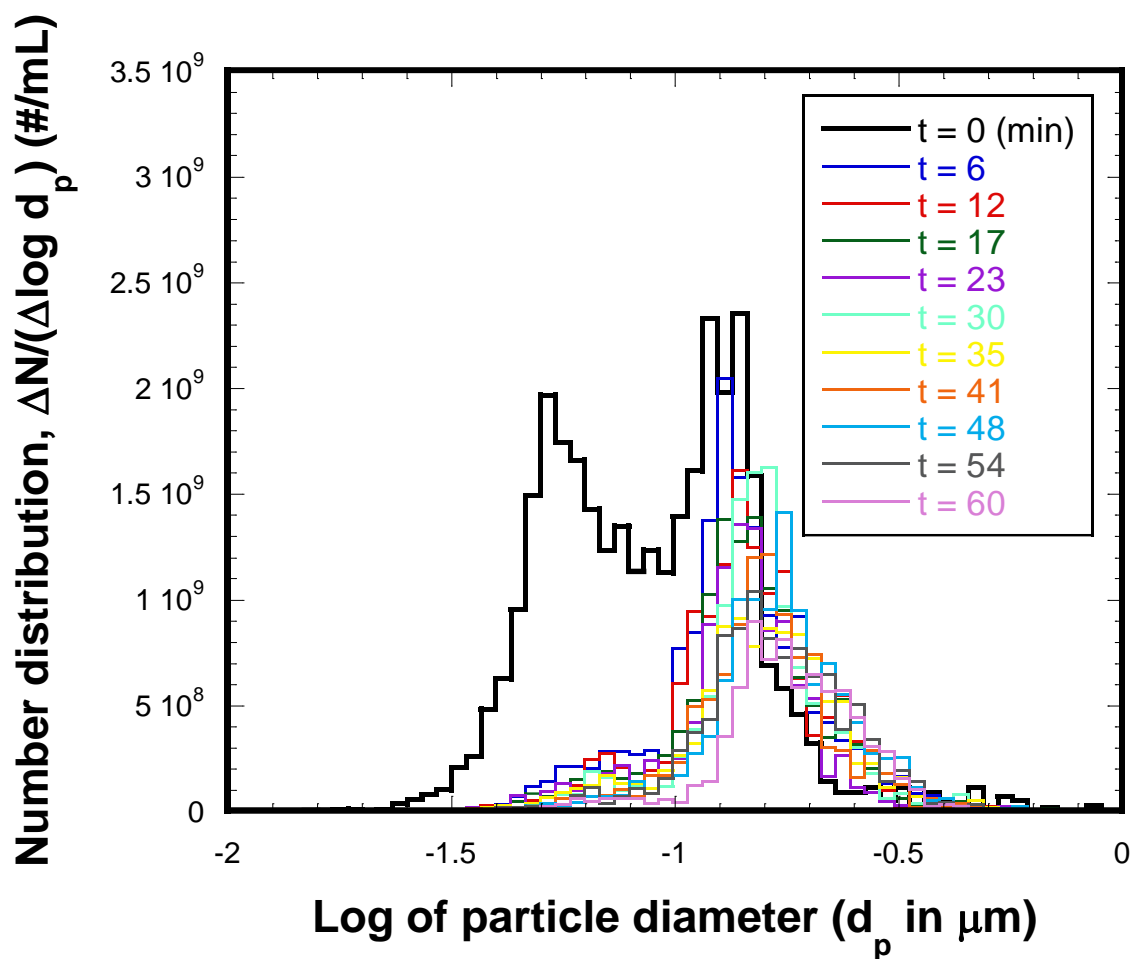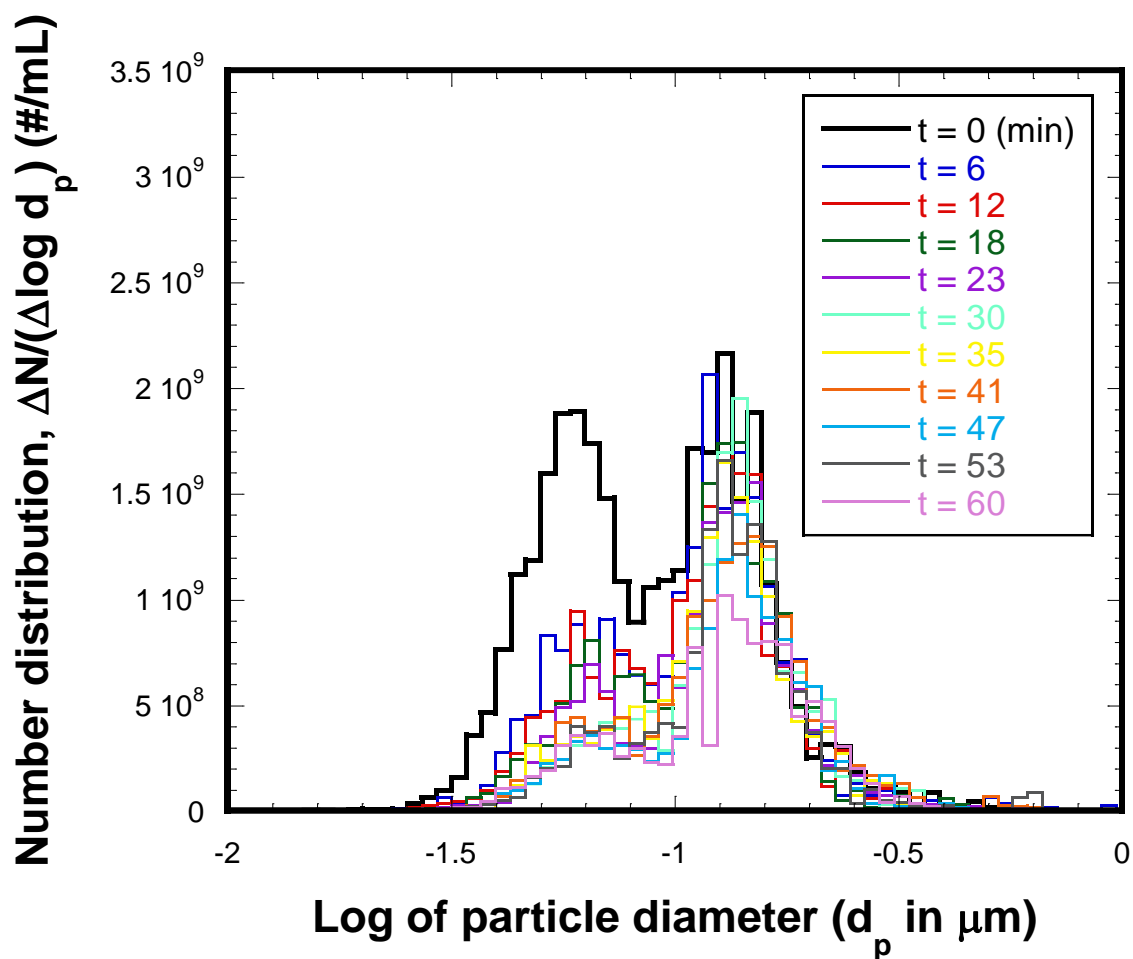
Figure A.18 Particle number distribution from Experiment #18

Experiment #18: the 30 & 100 nm sized citrate capped AgNPs under I =3 mM of Ca(NO₃)₂, with an initial number concentration of 1.0E9 #/mL in the absence of NOM. The experiment was performed on July 19, 2016.

Appendix B: Results of Trajectory analysis

Table B.1 The collision efficiency functions in Brownian motion of $A_H = 10$ k_BT (Figure 5.1A)

Radius of Large Particles, a_1 (nm)	a	b	c	d
0.5	0.94082	-0.80865	1.0576	-0.47159
5	0.94132	-0.8492	1.0826	-0.47671
50	0.94233	-1.0656	1.3259	-0.57494
500	0.93739	-1.4822	1.9666	-0.88943
5000	0.92504	-1.8764	2.6573	-1.2531
50000	0.91010	-2.1807	3.2254	-1.5623

$\alpha^{Br}(i,j) = a + b\lambda + c\lambda^2 + d\lambda^3$
λ = size ratio $(0 \leq \lambda \leq 1)$

Table B.2 The collision efficiency functions in Brownian motion of $A_H = 50$ k_BT (Figure 5.1B)

Radius of Large Particles, a_1 (nm)	a	b	c	d
0.5	0.96501	0.033444	-0.19822	0.13652
5	0.96617	-0.067786	-0.13258	0.12240
50	0.96690	-0.49374	0.37404	-0.089132
500	0.95736	-1.1132	1.3294	-0.55783
5000	0.94061	-1.6181	2.1913	-1.0048
50000	0.92239	-1.9813	2.8482	-1.3558

$\alpha^{Br}(i,j) = a + b\lambda + c\lambda^2 + d\lambda^3$
λ = size ratio $(0 \leq \lambda \leq 1)$

Table B.3 The collision efficiency functions in differential sedimentation (Figure 5.2)

Log N_g	a	b	c	d
6	3.1159	0.88018	-3.5330	3.0808
5	2.4554	-0.24752	-1.1716	1.5715
4	1.7289	-0.18501	-1.4298	1.7890
3	0.88628	-0.24523	-1.2051	1.5981
2	0.25206	-0.16510	-1.0413	1.3472
1	-0.32737	0.060718	-0.98325	1.1113
0	-0.87308	0.56060	-1.3029	1.0592
-1	-1.3799	1.2634	-1.9532	1.1915
-2	-1.8559	2.2140	-3.2739	1.7988
-3	-2.2849	3.4287	-5.5778	3.1605
-4	-2.6446	4.1969	-6.3365	3.2925
-5	-2.8613	3.6070	-5.0766	2.6243
-6	-3.1575	4.2355	-6.7535	3.7801

$$\alpha^{DS}(i,j) = 10^{(a+b\lambda+c\lambda^2+d\lambda^3)}$$
$$N_g = \frac{3\ A_H}{\pi g(\rho_p - \rho_l)a_i^4}$$

λ = size ratio ($0 \leq \lambda \leq 1$); a_i = radius of larger particle; A_H = Hamaker constant; ρ_p, ρ_L = density of particle and fluid, respectively; g = gravitational constant.

Table B.4 The collision efficiency functions in fluid shear (Figure 5.3)

Log H_A	a	b	c	d
2	0.075155	1.2549	-0.94647	0.34894
1	-0.18053	0.62092	-0.21078	0.053507
0	-0.62591	0.58511	-0.046965	-0.019519
-1	-1.0801	0.84297	-0.076939	-0.072626
-2	-1.6270	2.1801	-1.9887	0.86313
-3	-2.4514	4.8616	-5.485	2.3666
-4	-4.0305	12.390	-17.452	8.2989
-5	-4.4083	12.369	-16.028	7.1154
-6	-5.036	14.006	-17.969	7.8903

$$\alpha^{Sh}(i,j) = \frac{8}{(1+\lambda)^3} 10^{(a+b\lambda+c\lambda^2+d\lambda^3)}$$
$$H_A = \frac{A_H}{18\pi\mu a_i^3 G}$$

λ = size ratio ($0 \leq \lambda \leq 1$); a_i = radius of larger particle; A_H = Hamaker constant; μ = absolute viscosity; G = velocity gradient.

Table B.5 The collision efficiency functions in Brownian motion of $A_H = 10\ k_BT$ with the constant surface potential $|25|$ mV (Figure 5.4)

Radius of Large Particles, a_1 (nm)	Surface Potential (mV)	a	b	c	d
0.5	0	0.94082	-0.80865	1.0576	-0.47159
5	0	0.94132	-0.8492	1.0826	-0.47671
50	0	0.94233	-1.0656	1.3259	-0.57494
0.5	-25	0.87463	-1.6328	2.1504	-0.97150
5	-25	0.82678	-2.7618	3.7793	-1.7508
50	-25	-	-	-	-

* The third order polynomial curve could not fit data for the 50 nm w EDL because the values are near zero

$$\alpha^{Br}(i,j) = a + b\lambda + c\lambda^2 + d\lambda^3$$
λ = size ratio $(0 \leq \lambda \leq 1)$

Table B.6 The collision efficiency functions in Brownian motion of $A_H = 10\ k_BT$ with the constant surface potential $|25|$ mV and a_1 is 5 nm (Figure 5.5A)

Ionic Strength (mM)	a	b	c	d
1	0.83357	-2.857	4.0562	-1.9621
4	0.84858	-2.7161	3.7895	-1.8163
10	0.85764	-2.5923	3.5780	-1.7050
40	0.86818	-2.3643	3.2355	-1.5333
90	0.87213	-2.2168	3.0422	-1.4410

$$\alpha^{Br}(i,j) = a + b\lambda + c\lambda^2 + d\lambda^3$$
λ = size ratio $(0 \leq \lambda \leq 1)$

Table B.7 The collision efficiency functions in Brownian motion of $A_H = 10 \, k_BT$ with the constant surface potential $|25|$ mV and a_1 is 5 nm (Figure 5.5B)

Surface Potential (mV)	a	b	c	d
0	0.88461	-1.4615	2.0528	-0.97265
-5	0.88376	-1.5110	2.1120	-0.99920
-10	0.88108	-1.6570	2.2887	-1.0794
-15	0.87630	-1.8942	2.5852	-1.2173
-20	0.86882	-2.2119	3.0101	-1.4216
-25	0.85764	-2.5923	3.5780	-1.7050

$\alpha^{Br}(i,j) = a + b\lambda + c\lambda^2 + d\lambda^3$
λ = size ratio $(0 \leq \lambda \leq 1)$
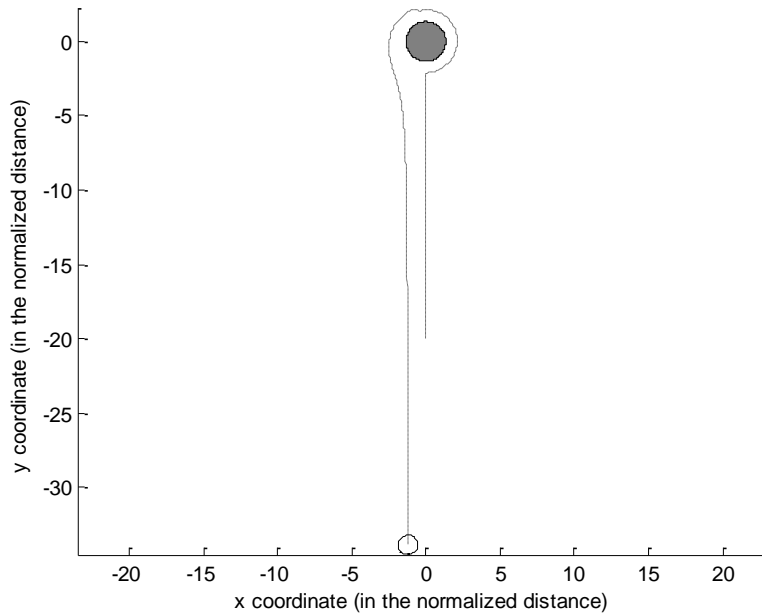

Figure B.1 Simulated trajectory result (the size of the gray colored particle (a_1) was 1 μm, and the size of the small clear particle (a_2) was 500 nm, the dotted line is the pathway of the center of the small particle, and the calculations were made with the surface potential of $|25|$ mV when log(Ng) = 3.4)

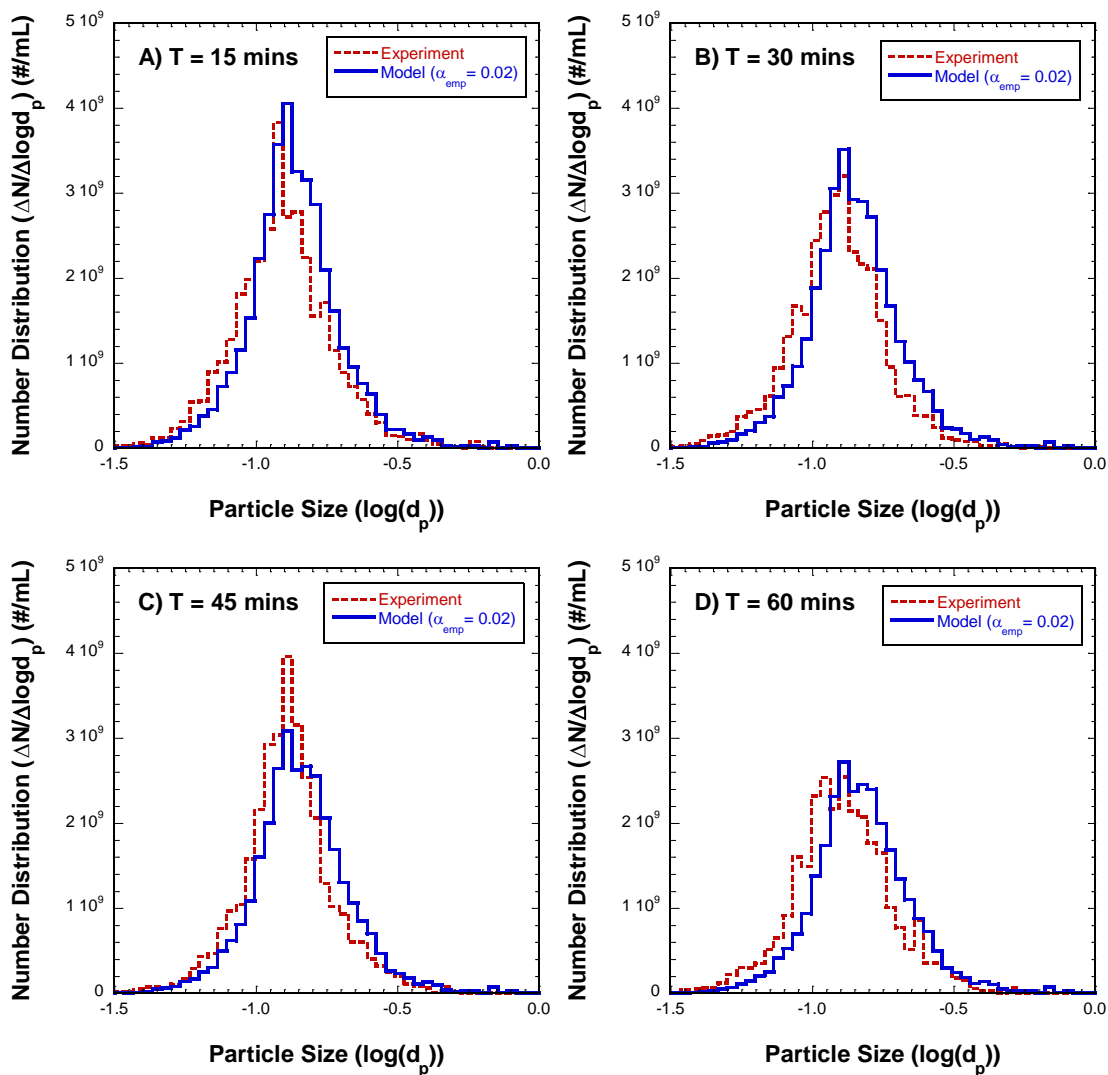# Appendix C: Model Estimations for Total Number Concentrations

Figure C.1 Model predictions for Experiment #1

Experiment #1: the 100 nm sized citrate capped AgNPs under I = 30 mM of NaNO₃, with an initial number concentration of 1.3E9 #/mL in the absence of NOM.

Figure C.2 Model predictions for Experiment #2

Experiment #2: the 100 nm sized citrate capped AgNPs under I =50 mM of $NaNO_3$, with an initial number concentration of 1.1E9 #/mL in the absence of NOM.

Figure C.3 Model predictions for Experiment #3

Experiment #3: the 100 nm sized citrate capped AgNPs under I =30 mM of Ca(NO$_3$)$_2$, with an initial number concentration of 1.2E9 #/mL in the absence of NOM.

Figure C.4 Model predictions for Experiment #4

Experiment #4: the 100 nm sized citrate capped AgNPs under I =30 mM of Na₃-Citrate, with an initial number concentration of 1.2E9 #/mL in the absence of NOM.
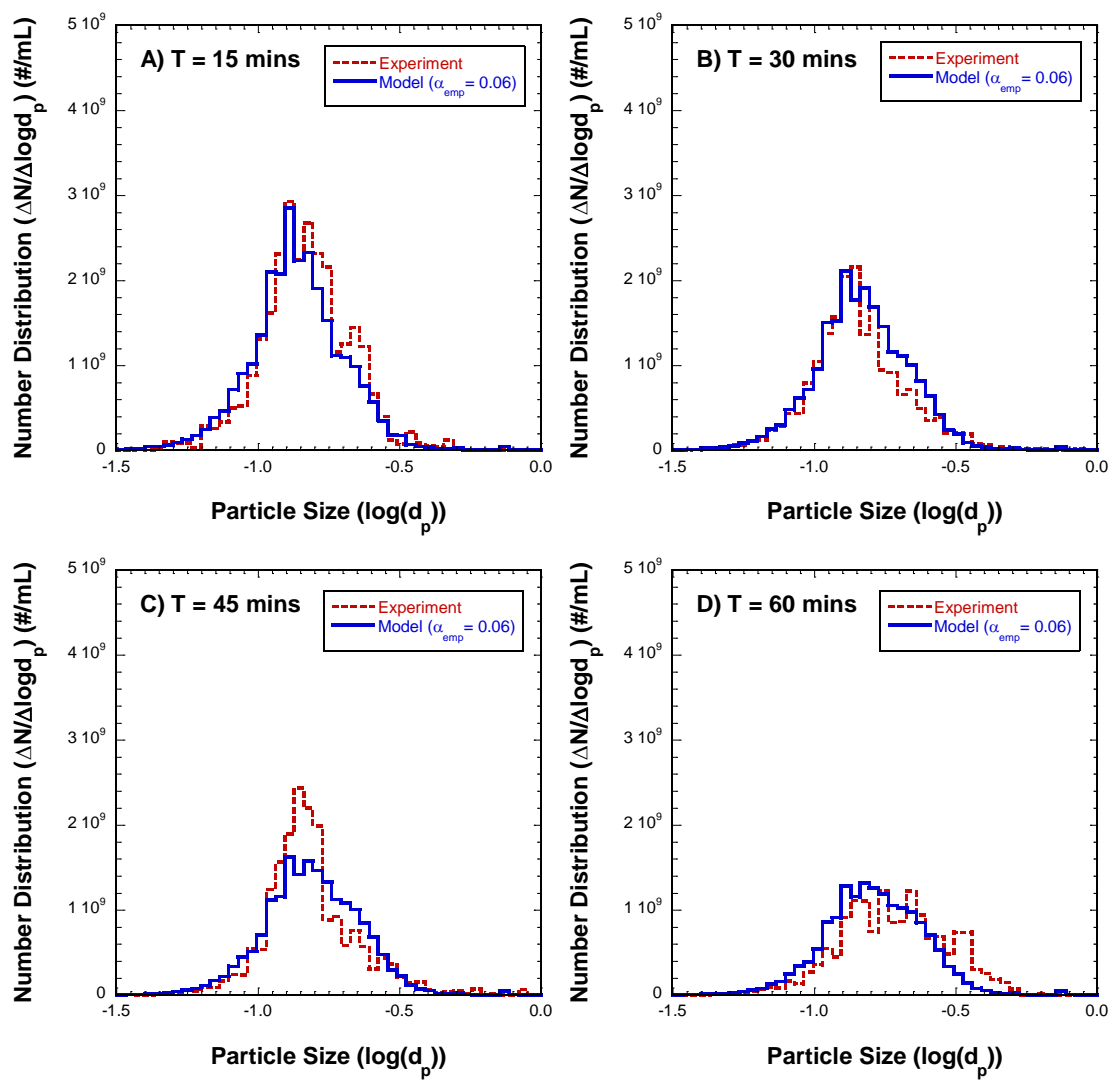
Figure C.5 Model predictions for Experiment #5

Experiment #5: the 100 nm sized citrate capped AgNPs under I =30 mM of NaNO₃, with an initial number concentration of 1.9E9 #/mL in the absence of NOM.
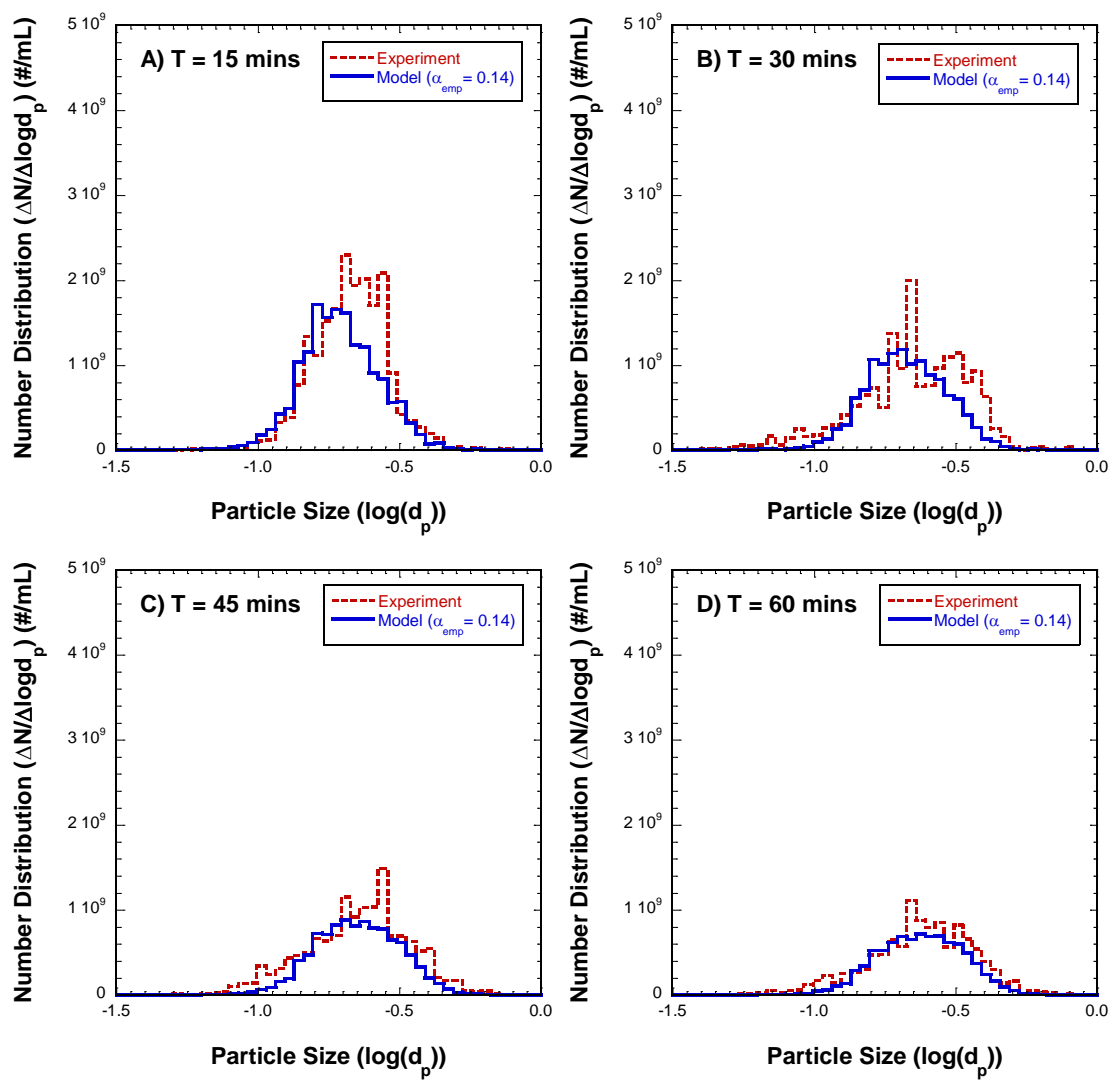
Figure C.6 Model predictions for Experiment #6

Experiment #6: the 100 nm sized citrate capped AgNPs under I =50 mM of NaNO$_3$, with an initial number concentration of 1.1E9 #/mL in the presence of NOM.

Figure C.7 Model predictions for Experiment #7

Experiment #7: the 100 nm sized citrate capped AgNPs under I =30 mM of Ca(NO$_3$)$_2$, with an initial number concentration of 1.3E9 #/mL in the presence of NOM.
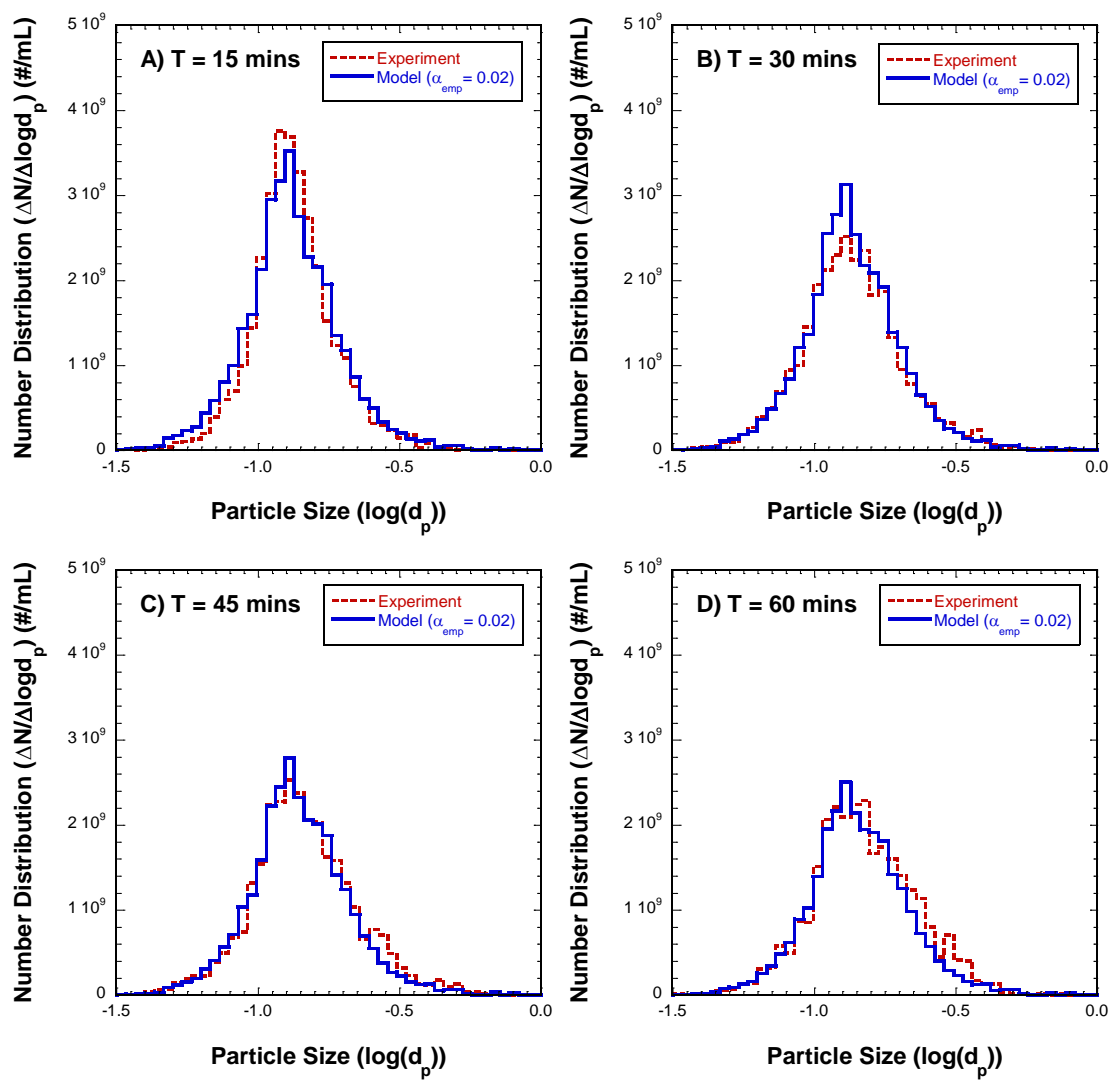
Figure C.8 Model predictions for Experiment #8

Experiment #8: the 30 nm sized citrate capped AgNPs under I =30 mM of NaNO₃, with an initial number concentration of 1.1E9 #/mL in the absence of NOM.
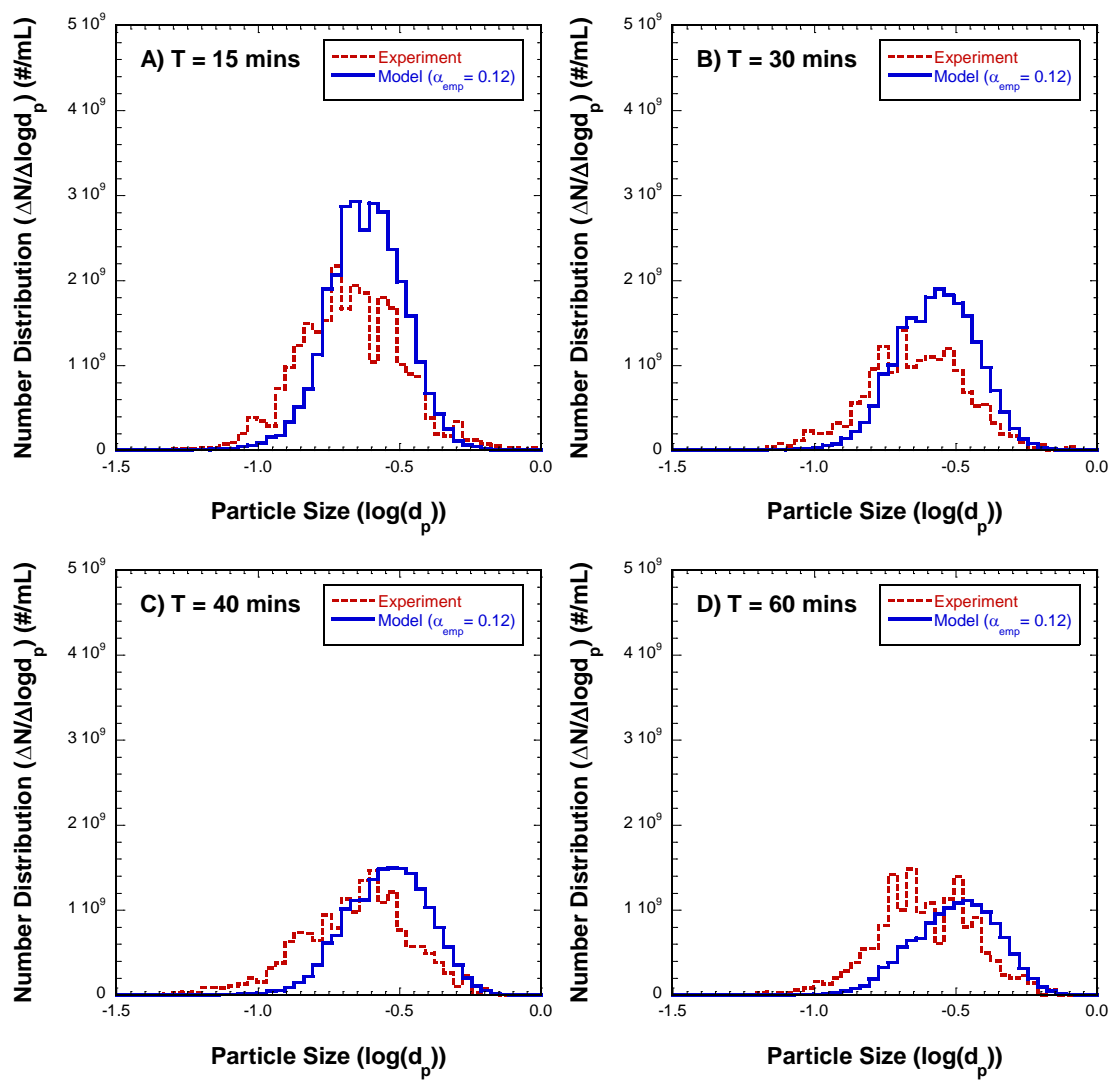
Figure C.9 Model predictions for Experiment #9

Experiment #9: the 100 nm sized citrate capped AgNPs under I =10 mM of NaNO$_3$, with an initial number concentration of 1.0E9 #/mL in the absence of NOM.
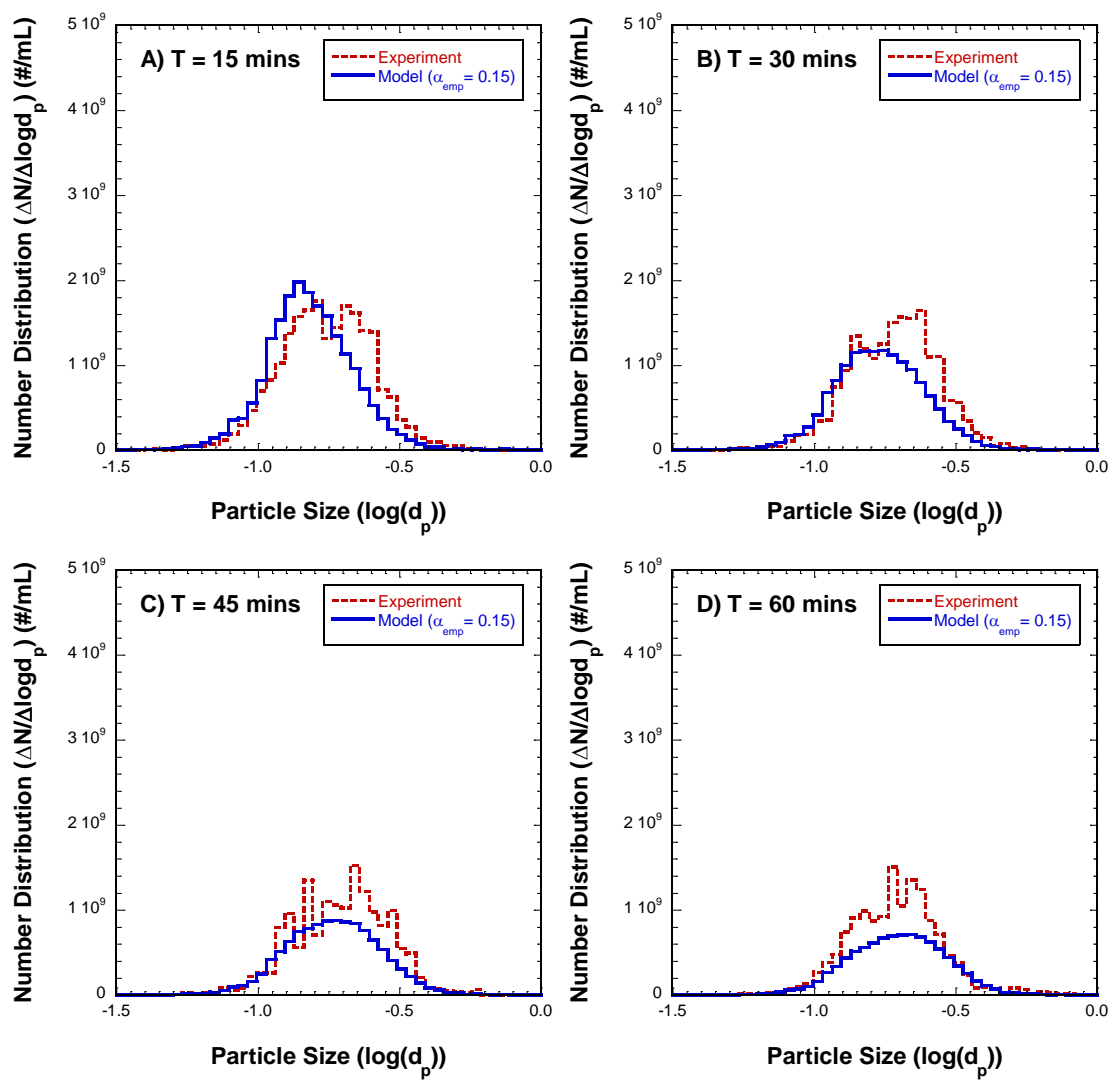
Figure C.10 Model predictions for Experiment #10

Experiment #10: the 30 nm sized citrate capped AgNPs under I =3 mM of NaNO3, with an initial number concentration of 1.1E9 #/mL in the absence of NOM.

Figure C.11 Model predictions for Experiment #11

Experiment #11: the 30 nm sized citrate capped AgNPs under I =3 mM of Ca(NO$_3$)$_2$, with an initial number concentration of 1.2E9 #/mL in the absence of NOM.
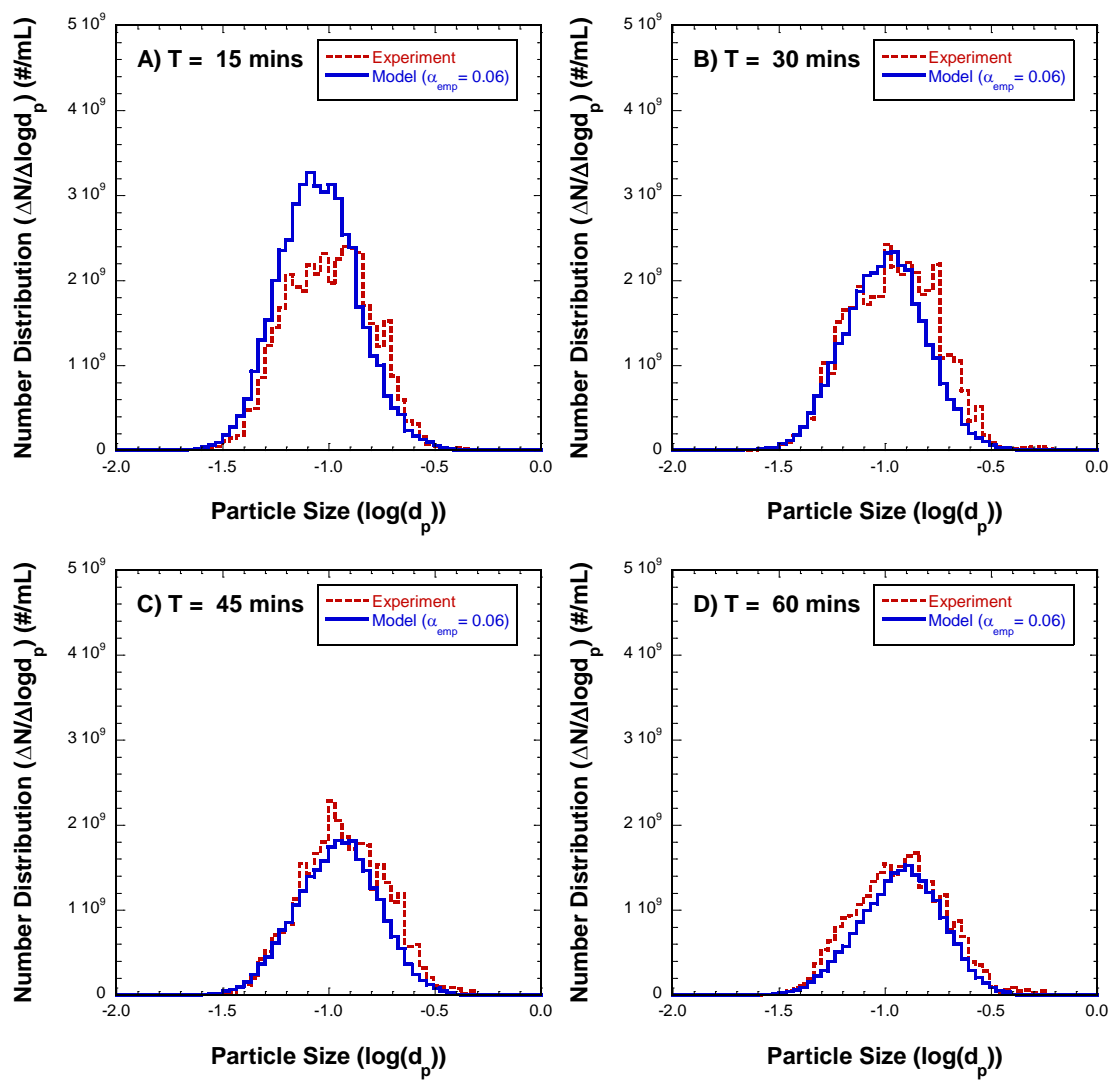
Figure C.12 Model predictions for Experiment #12

Experiment #12: the 30 nm sized citrate capped AgNPs under I =3 mM of NaNO$_3$, with an initial number concentration of 2.5E9 #/mL in the absence of NOM.

Figure C.13 Model predictions for Experiment #13

Experiment #13: the 50 nm sized citrate capped AgNPs under I =3 mM of NaNO$_3$, with an initial number concentration of 1.2E9 #/mL in the absence of NOM.
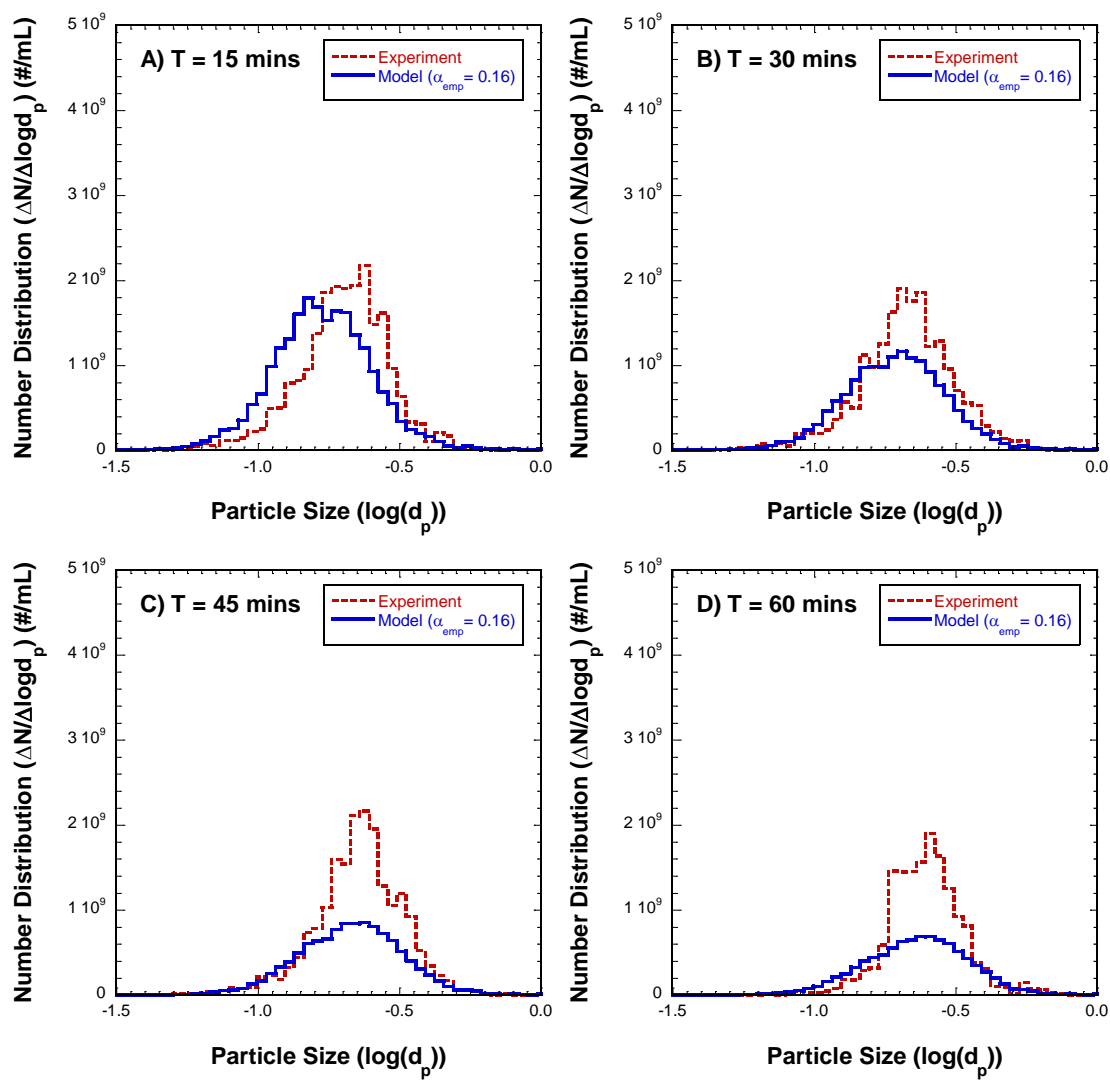
Figure C.14 Model predictions for Experiment #14

Experiment #14: the 50 nm sized citrate capped AgNPs under I =3 mM of Ca(NO$_3$)$_2$, with an initial number concentration of 1.2E9 #/mL in the absence of NOM.
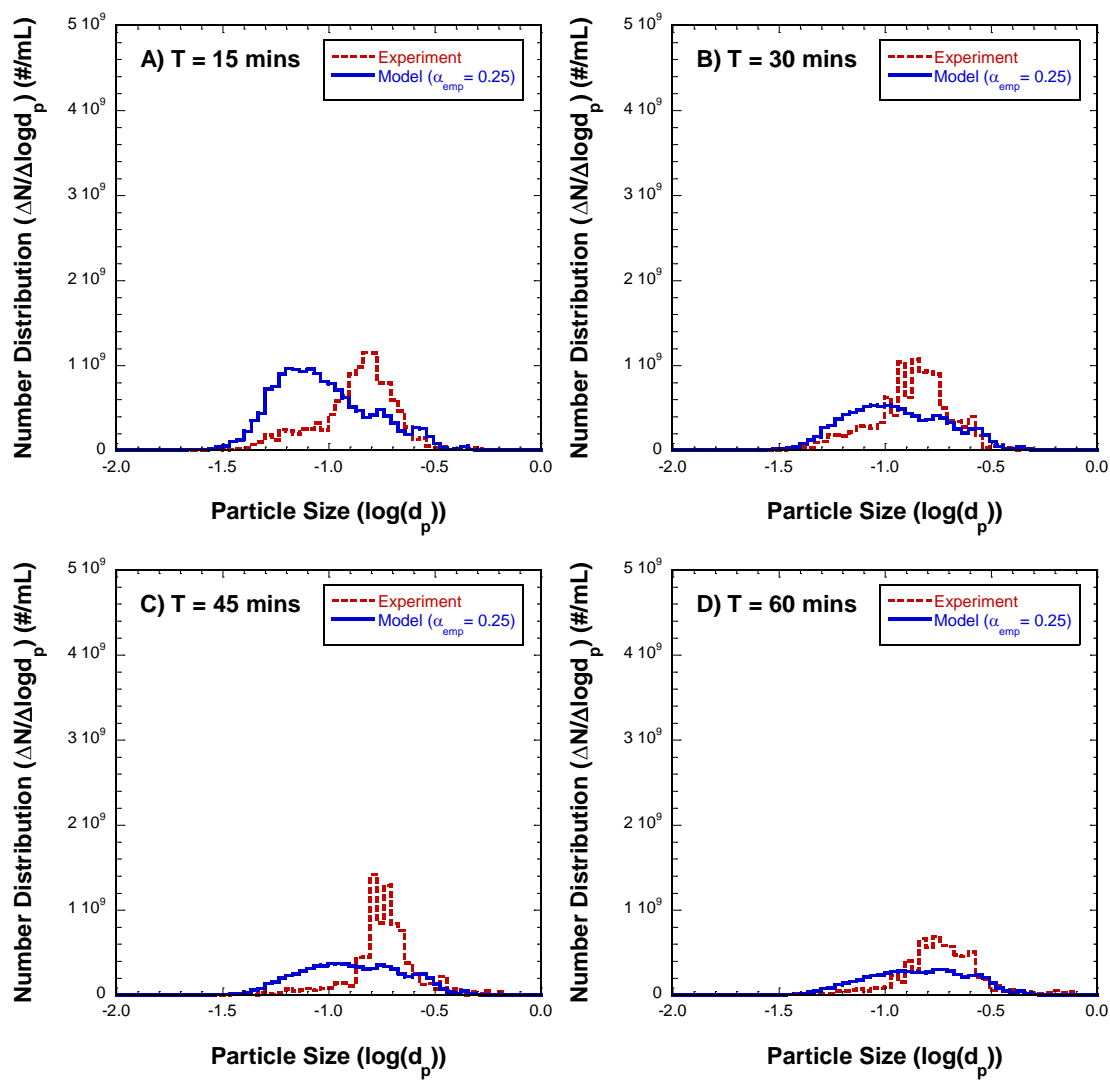
Figure C.15 Model predictions for Experiment #15

Experiment #15: the 50 nm sized citrate capped AgNPs under I =10 mM of NaNO₃, with an initial number concentration of 1.1E9 #/mL in the absence of NOM.
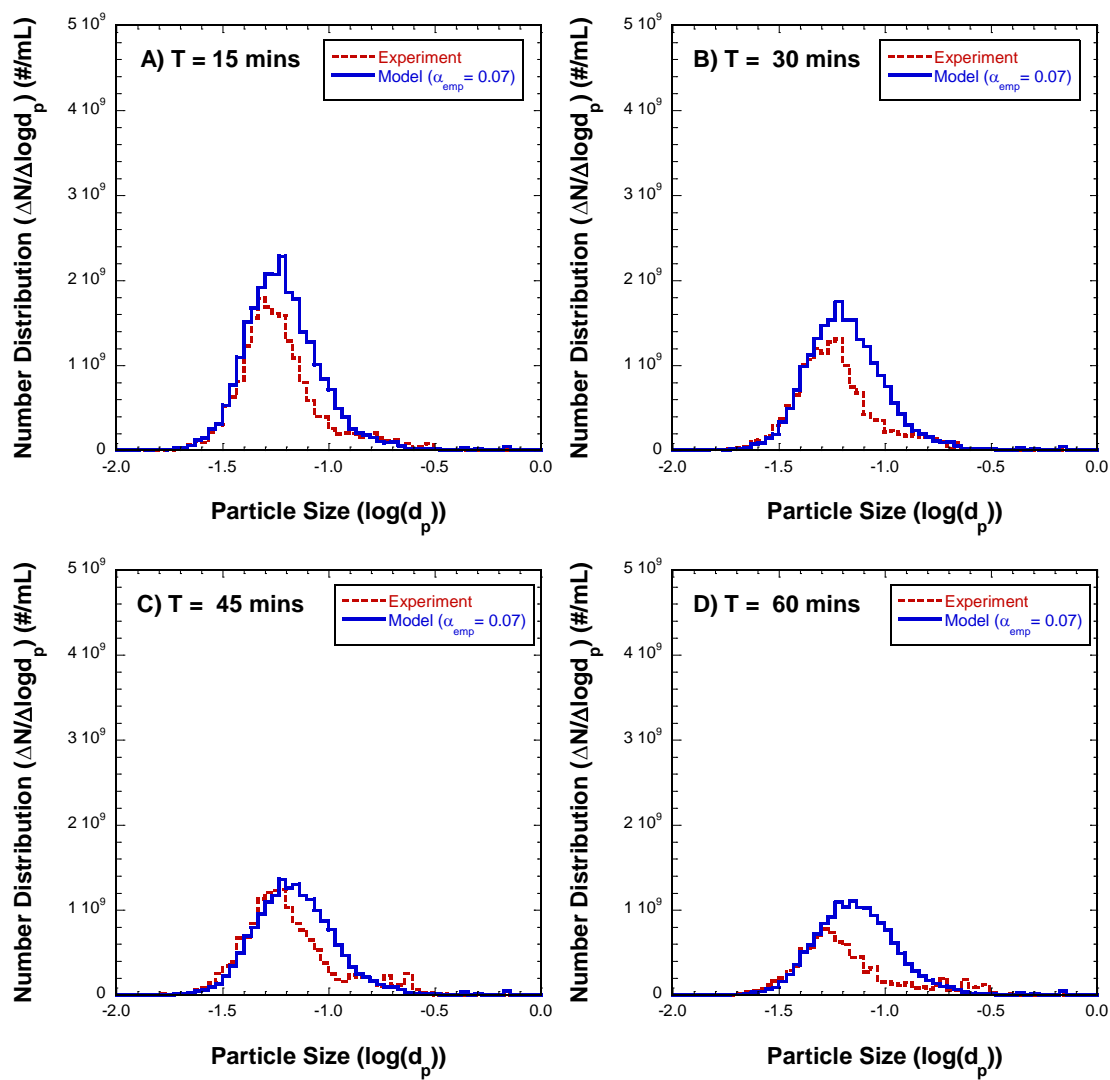
Figure C.16 Model predictions for Experiment #16

Experiment #16: the 30 & 100 nm sized citrate capped AgNPs under I =10 mM of NaNO₃, with an initial number concentration of 1.3E9 #/mL in the absence of NOM.
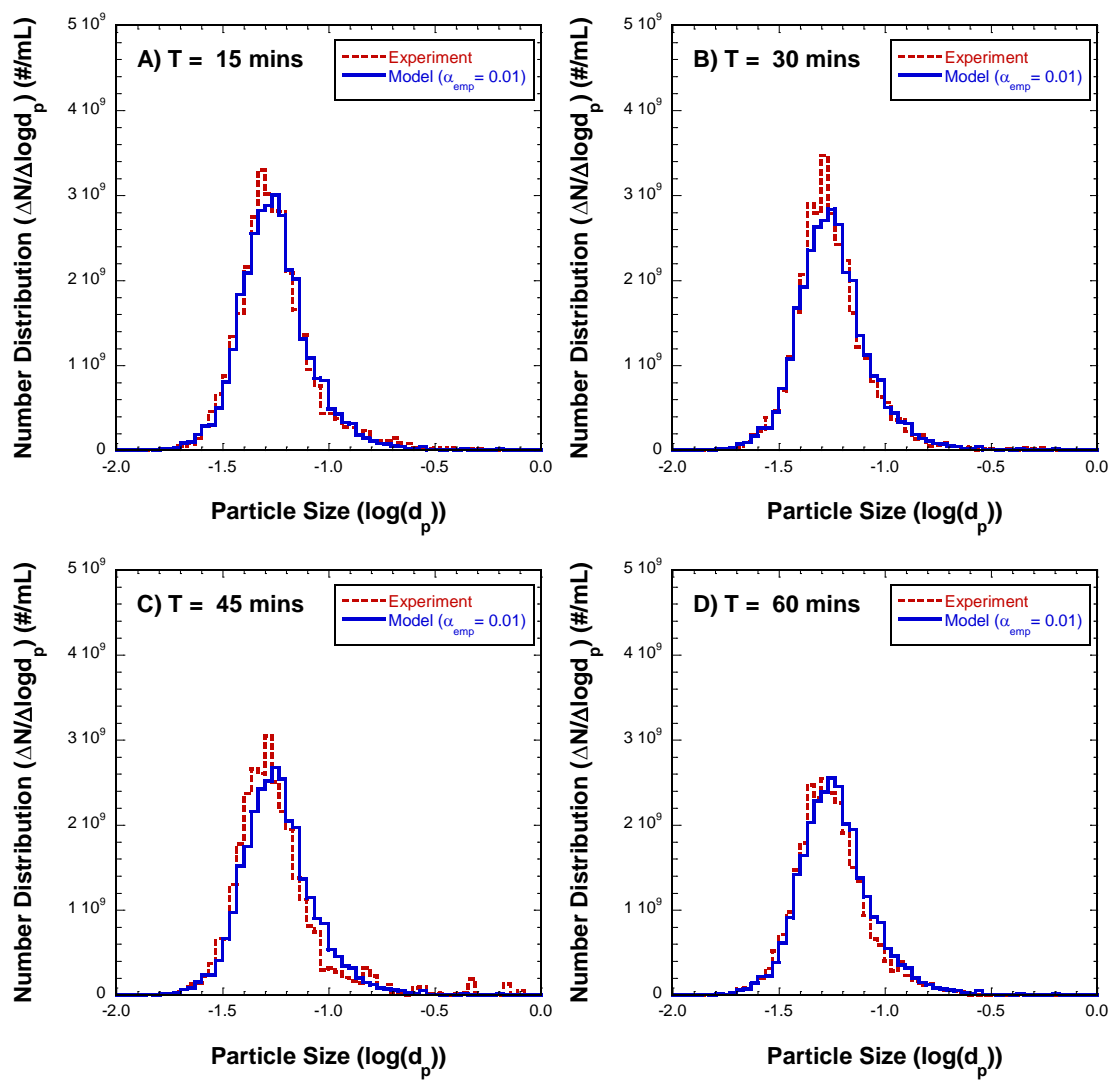
Figure C.17 Model predictions for Experiment #17

Experiment #17: the 30 & 100 nm sized citrate capped AgNPs under I =30 mM of

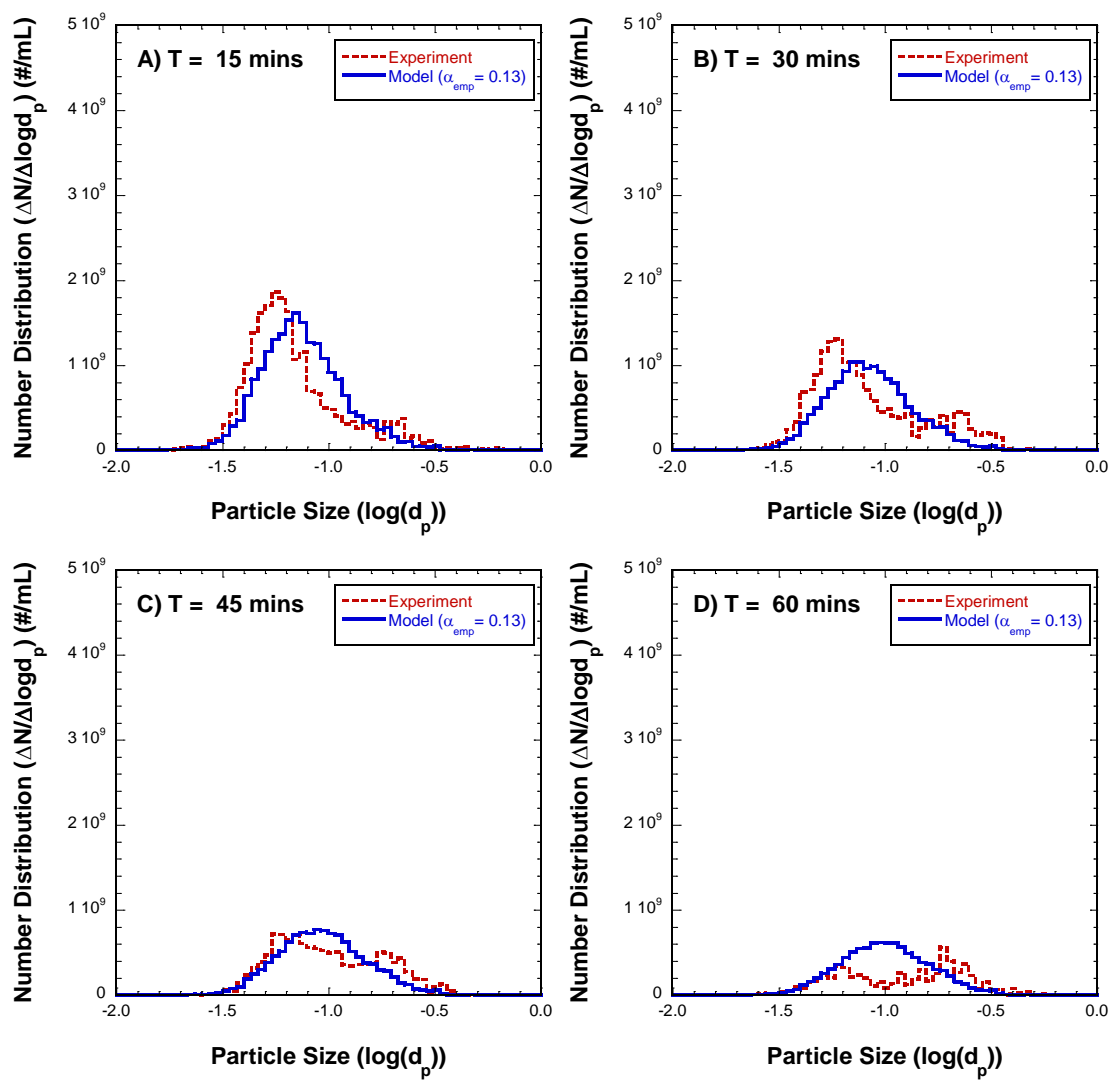NaNO₃, with an initial number concentration of 1.0E9 #/mL in the absence of NOM.
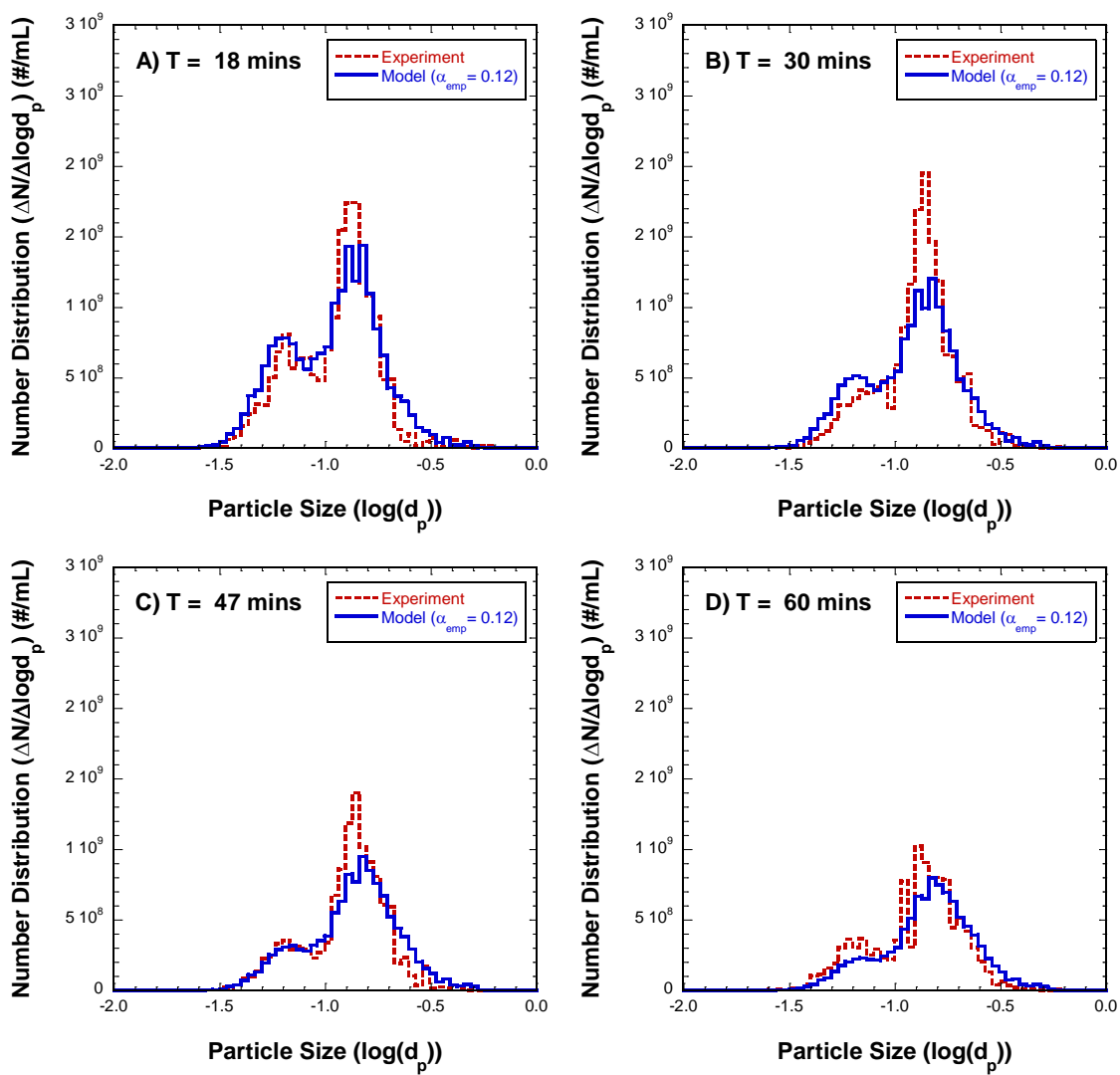
Figure C.18 Model predictions for Experiment #18

Experiment #18: the 30 & 100 nm sized citrate capped AgNPs under I =3 mM of

Ca(NO$_3$)$_2$, with an initial number concentration of 1.0E9 #/mL in the absence of NOM.

Appendix D: The Reproducibility of Experimental Data
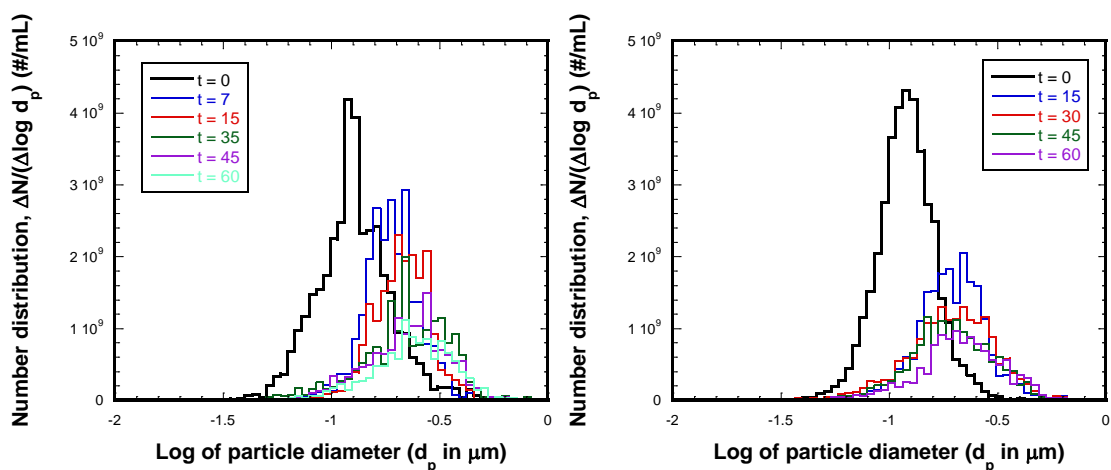
Figure D.1 Particle number distribution from Experiment #3
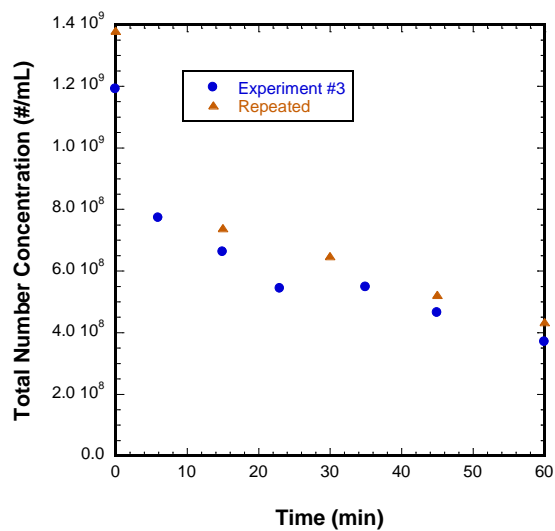
Figure D.2 Total Particle number concentration measured A) in Experiment #3 and B) in the second iteration (reproduced data from)

Experiment #3: the 100 nm sized citrate capped AgNPs under $I = 30$ mM of $Ca(NO_3)_2$, with an initial number concentration of 1.2E9 #/mL in the absence of NOM.
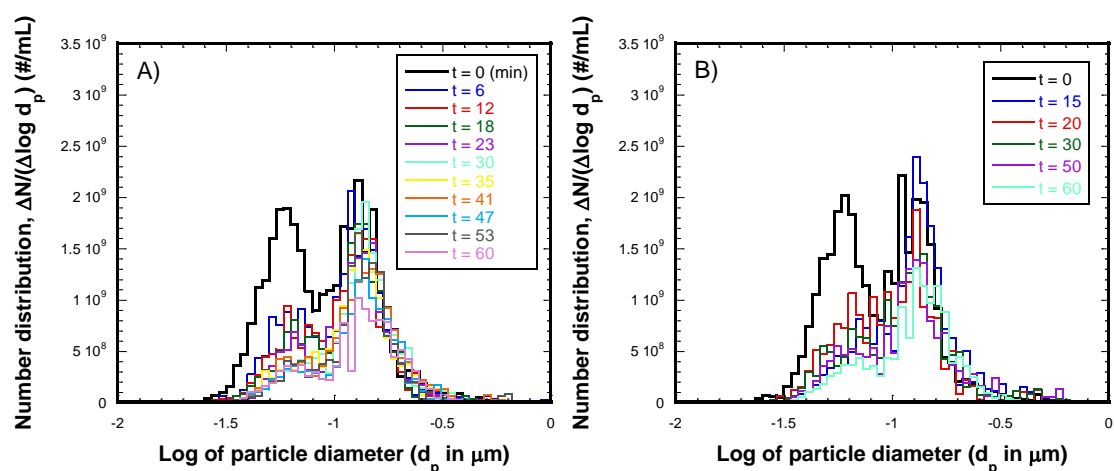
Figure D.3 Particle number distributions measured A) in Experiment #18 and B) in the second iteration (reproduced data from)
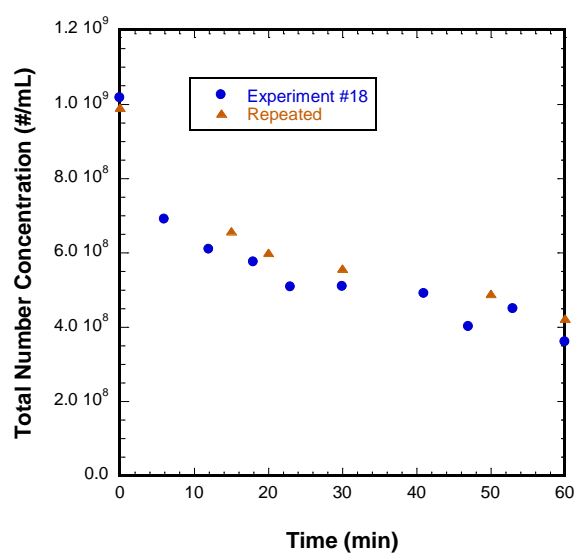
Figure D.4 Total Particle number concentration measured A) in Experiment #18 and B) in the second iteration (reproduced data from)

Experiment #18: the 30 & 100 nm sized citrate capped AgNPs under I =3 mM of

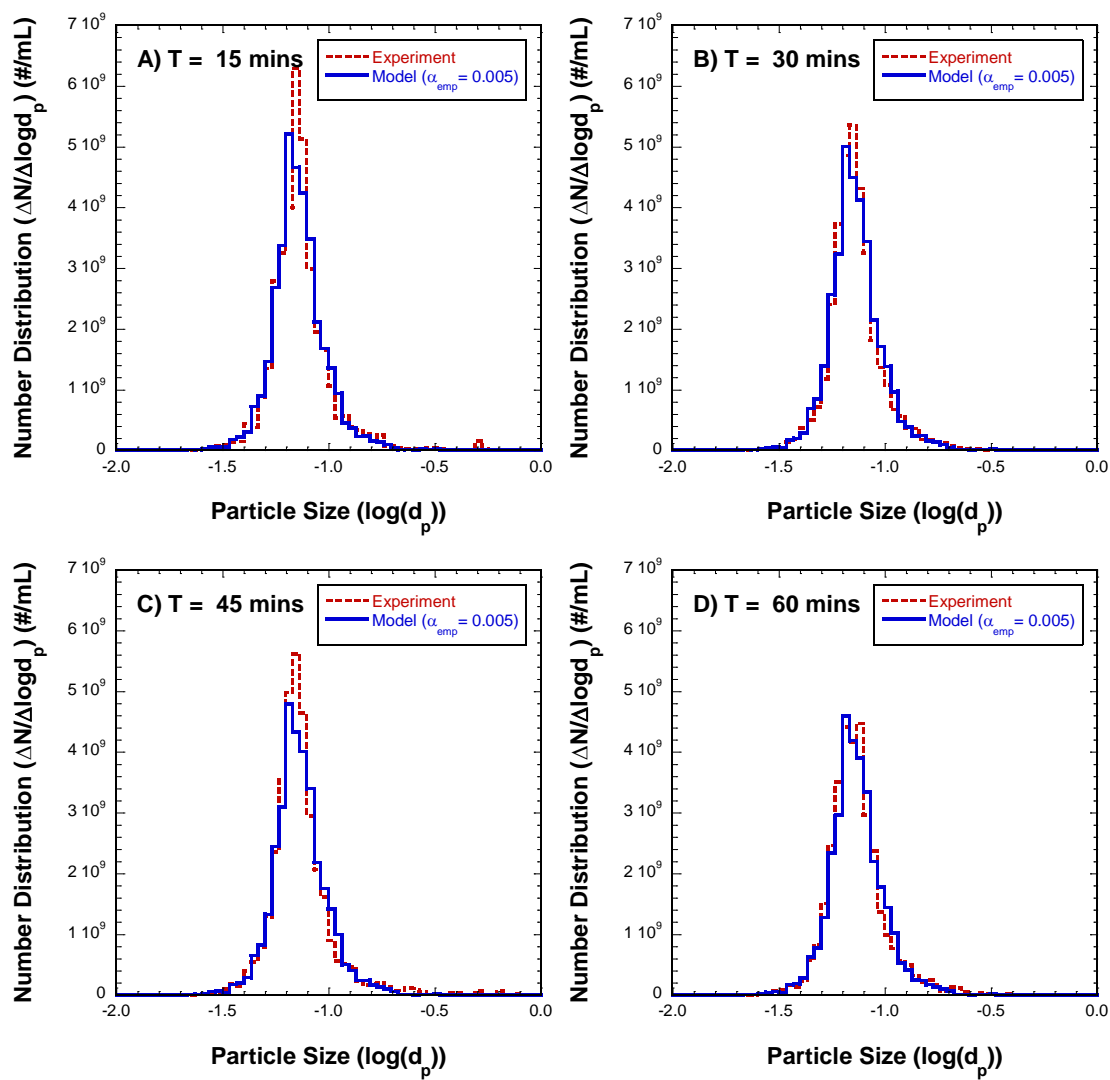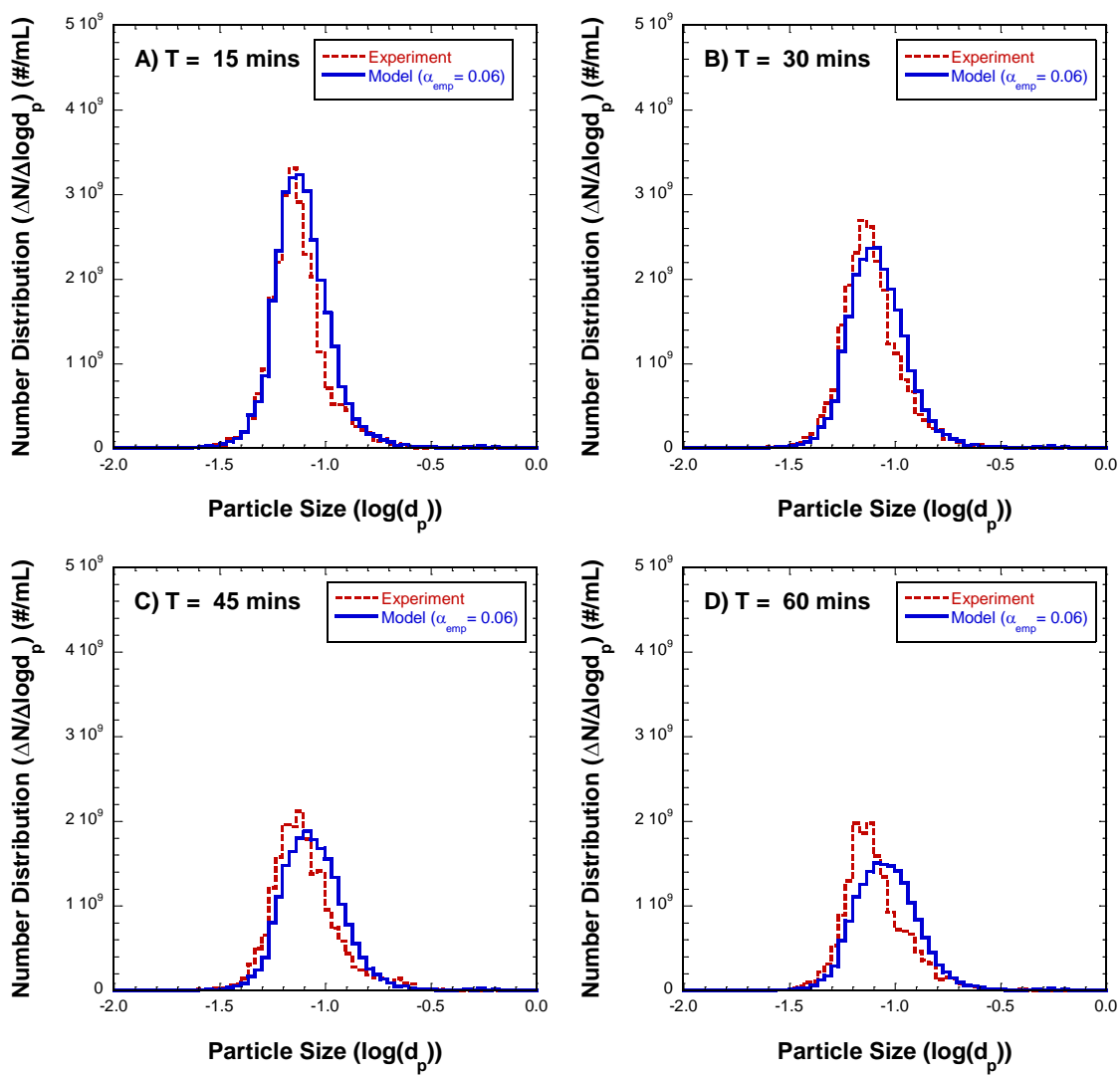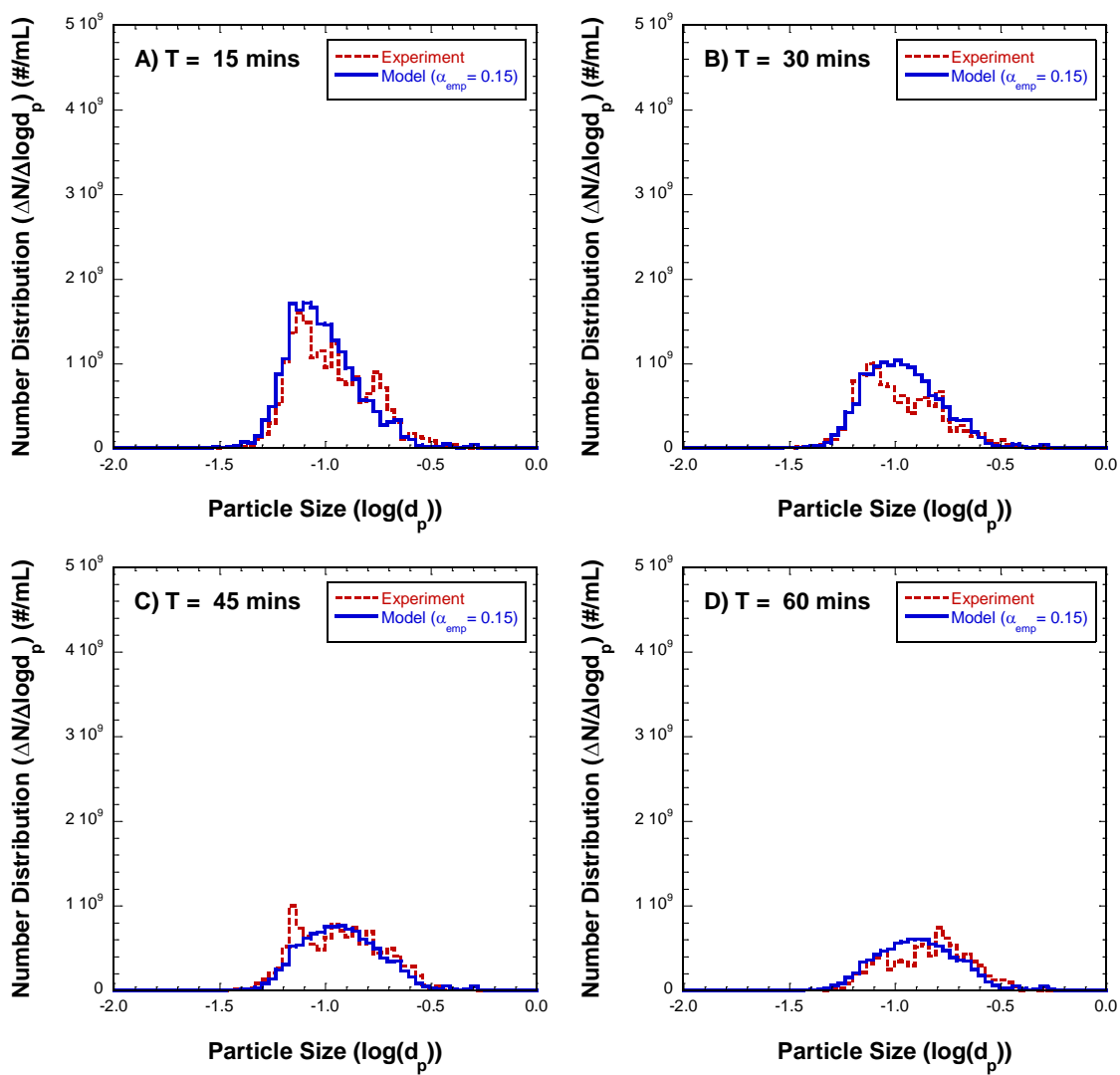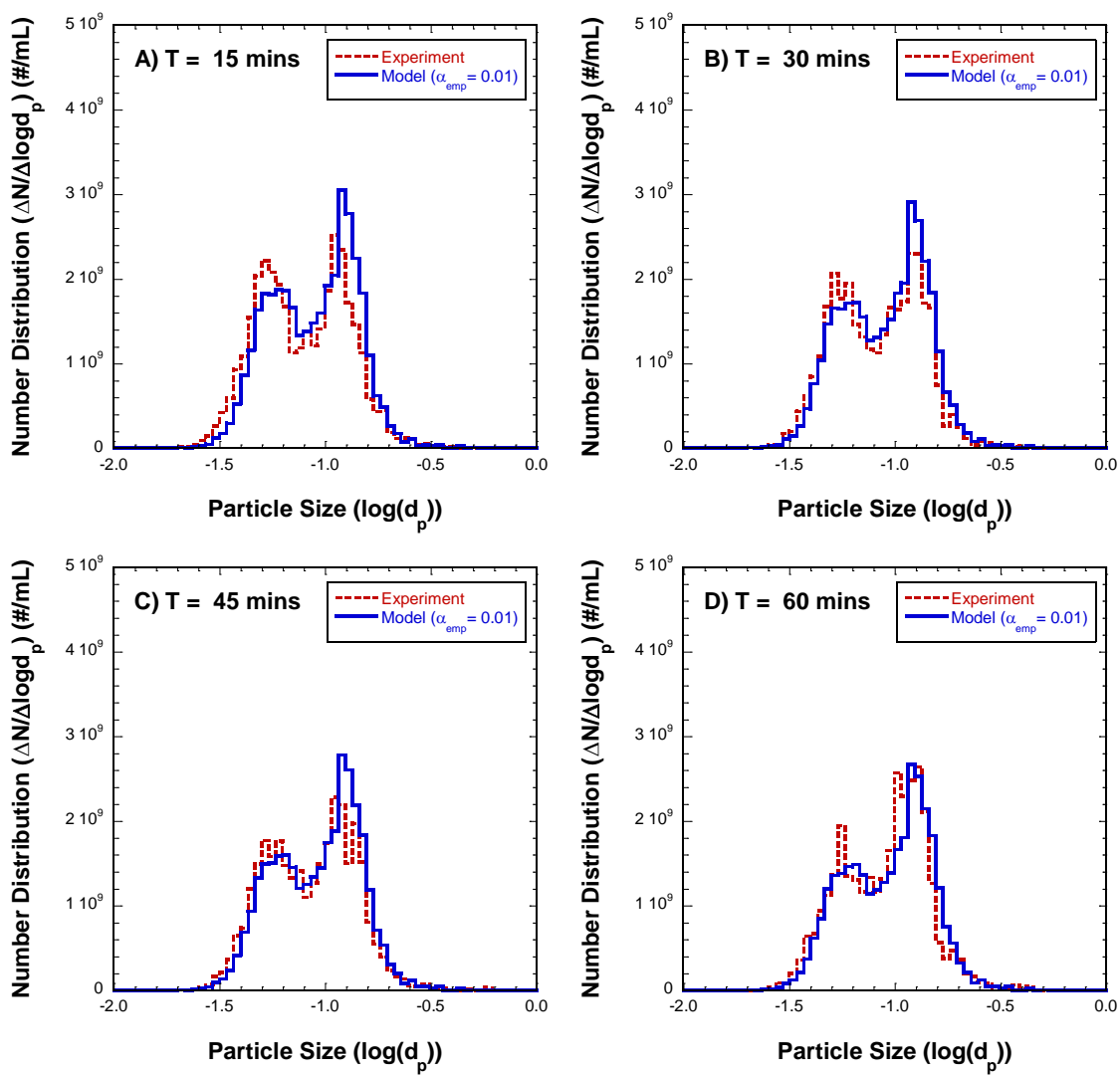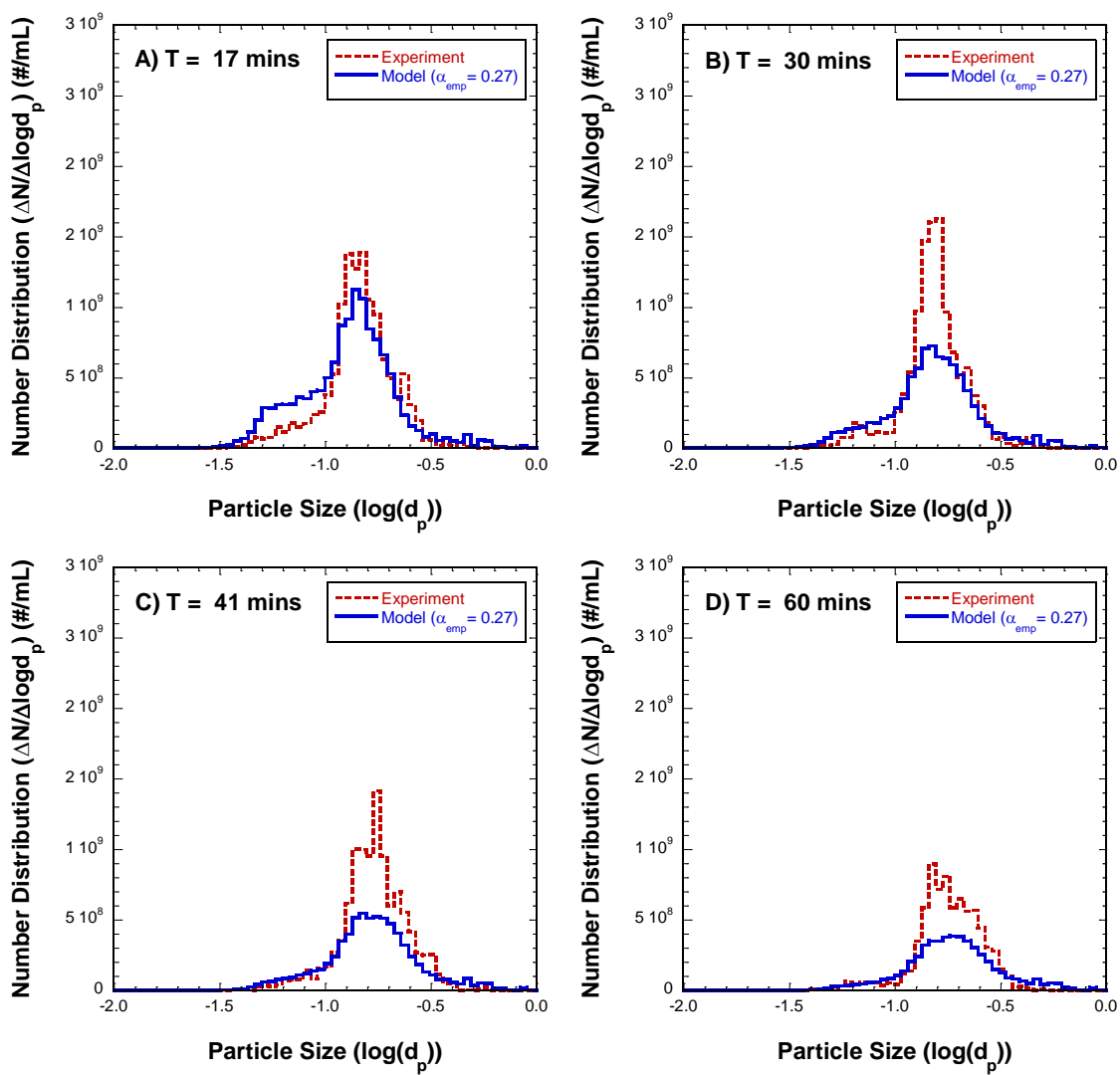Ca(NO$_3$)$_2$, with an initial number concentration of 1.0E9 #/mL in the absence of NOM.

200

Appendix E: Zeta Potentials

The measured zeta potentials at the end of each laboratory scale flocculation experiment are tabulated here.

Table E.1 Measured Zeta Potentials

	Particle size (nm)	Ionic Strength (mM)	Valency	Initial Particle Concentration (#/mL)	NOM*	Zeta Potential (mV)
1	100	30	1	1.3E+09	X	-27.52
2	100	50	1	1.1E+09	X	-13.01
3	100	30	2	1.2E+09	X	-8.94
4	100	30	3	1.2E+09	X	-32.30
5	100	30	1	1.9E+09	X	-25.91
6	100	50	1	1.1E+09	O	-8.36
7	100	30	2	1.3E+09	O	-7.42
8	30	30	1	1.1E+09	X	-4.31
9	30	10	1	1.0E+09	X	-15.82
10	30	3	1	1.1E+09	X	-31.98
11	30	3	2	1.2E+09	X	-12.06
12	30	3	1	2.5E+09	X	-
13	50	3	1	1.2E+09	X	-33.48
14	50	3	2	1.2E+09	X	-21.96
15	50	10	1	1.1E+09	X	-14.58
16	30 & 100	10	1	1.3E+09	X	-
17	30 & 100	30	1	1.0E+09	X	-
18	30 & 100	3	2	1.0E+09	X	-

*NOM = Natural Organic Matter, X = the absence of NOM, and O = the presence of NOM

References

Adler, P.M., 1981a. Heterocoagulation in shear flow. *Journal of Colloid and Interface Science*, *83*(1), pp.106-115.

Adler, P.M., 1981b. Interaction of unequal spheres: I. Hydrodynamic interaction: Colloidal forces. *Journal of Colloid and Interface Science*, *84*(2), pp.461-473.

Adler, P.M., 1981c. Interaction of unequal spheres: II. Conducting spheres. *Journal of Colloid and Interface Science*, *84*(2), pp.475-488.

Adler, P.M., 1981d. Interaction of unequal spheres: III. Experimental. *Journal of Colloid and Interface Science*, *84*(2), pp.489-496.

Anandarajah, A. and Chen, J., 1995. Single correction function for computing retarded van der Waals attraction. *Journal of colloid and interface science*, *176*(2), pp.293-300.

Baalousha, M., Nur, Y., Römer, I., Tejamaya, M. and Lead, J.R., 2013. Effect of monovalent and divalent cations, anions and fulvic acid on aggregation of citrate-coated silver nanoparticles. *Science of the Total Environment*, *454*, pp.119-131.

Badawy, A.M.E., Luxton, T.P., Silva, R.G., Scheckel, K.G., Suidan, M.T. and Tolaymat, T.M., 2010. Impact of environmental conditions (pH, ionic strength, and electrolyte type) on the surface charge and aggregation of silver nanoparticles suspensions. *Environmental science & technology*, *44*(4), pp.1260-1266.

Batchelor, G.K. and Green, J.T., 1972. The hydrodynamic interaction of two small freely-moving spheres in a linear flow field. *Journal of Fluid Mechanics*, *56*(02), pp.375-400.

Batchelor, G.K., 1982. Sedimentation in a dilute polydisperse system of interacting spheres. Part 1. General theory. *Journal of Fluid Mechanics*, *119*, pp.379-408.

Benjamin, M. M., & Lawler, D. F., 2013. Water quality engineering: physical/chemical treatment processes. John Wiley & Sons., Hoboken, NJ.

Benjamin, M. M., 2002. Water Chemistry. McGraw-Hill

Brenner, H. and O'Neill, M.E., 1972. On the Stokes resistance of multiparticle systems in a linear shear field. *Chemical Engineering Science*, *27*(7), pp.1421-1439.

Bull, R.J., 2006. Use of toxicological and chemical models to prioritize DBP research. American Water Works Association.

Camp, T.R., 1955. Flocculation and flocculation basins. *Transactions of the American Society of Civil Engineers*, 2722, p.1.

Camp, T.R. and Stein, P.C., 1943. Velocity gradients and internal work in fluid motion. *Journal of the Boston Society of Civil Engineers*, *85*, pp.219-37.

Carr, R., Hole, P., Malloy, A., Smith, J., Weld, A. and Warren, J., 2008. The real-time, simultaneous analysis of nanoparticle size, zeta potential, count, asymmetry and fluorescence. *Nanotechnology*, *1*, pp.866-870.

Casimir, H.B.G. and Polder, D., 1948. The influence of retardation on the London-van der Waals forces. *Physical Review*, *73*(4), p.360.

Chakraborti, R.K., Gardner, K.H., Atkinson, J.F. and Van Benschoten, J.E., 2003. Changes in fractal dimension during aggregation. *Water Research*, 37(4), pp.873-883.

Chalew, T.E.A., Ajmani, G.S., Huang, H. and Schwab, K.J., 2013. Evaluating nanoparticle breakthrough during drinking water treatment. *Environmental Health Perspectives (Online)*, *121*(10), p.1161.

Chen, K.L. and Elimelech, M., 2007. Influence of humic acid on the aggregation kinetics of fullerene (C 60) nanoparticles in monovalent and divalent electrolyte solutions. *Journal of Colloid and Interface Science*, 309(1), pp.126-134.

Chinnapongse, S.L., MacCuspie, R.I. and Hackley, V.A., 2011. Persistence of singly dispersed silver nanoparticles in natural freshwaters, synthetic seawater, and simulated estuarine waters. *Science of the total environment*, *409*(12), pp.2443-2450.

Christenson, H.K., 1988. Non-DLVO forces between surfaces-solvation, hydration and capillary effects. *Journal of Dispersion Science and Technology*, *9*(2), pp.171-206.

Clayfield, E.J., Lumb, E.C. and Mackey, P.H., 1971. Retarded dispersion forces in colloidal particles—Exact integration of the casimir and polder equation. *Journal of Colloid and Interface Science*, *37*(2), pp.382-389.

Considine, R.F., Hayes, R.A. and Horn, R.G., 1999. Forces measured between latex spheres in aqueous electrolyte: Non-DLVO behavior and sensitivity to dissolved gas. *Langmuir*, *15*(5), pp.1657-1659.

Cooley, M.B.A. and O'neill, M.E., 1969, September. On the slow motion of two spheres in contact along their line of centres through a viscous fluid. In *Mathematical*

Proceedings of the Cambridge Philosophical Society (Vol. 66, No. 02, pp. 407-415). Cambridge University Press.

Craun, G. F., Hauchman, F. S., and Robinson, D. E., 2001. Microbial Pathogens and Disinfection By-Products in Drinking Water: Health Effects and Management of Risks. International Life Science Institute, Washington, DC.

Cumberland, S.A. and Lead, J.R., 2009. Particle size distributions of silver nanoparticles at environmentally relevant conditions. *Journal of chromatography A*, *1216*(52), pp.9099-9105.

Davis, M.H., 1969. The slow translation and rotation of two unequal spheres in a viscous fluid. *Chemical Engineering Science*, 24(12), pp.1769-1776.

Derjaguin, B.V. and Landau, L., 1941. Colloidal stability of protein-polymer systems: A possible explanation by hydration forces. *Acta Physiocochim USSR*, *14*, p.663.

Edzwald, J.K. and Tobiason, J.E., 1999. Enhanced coagulation: US requirements and a broader view. *Water Science and Technology*, *40*(9), pp.63-70.

Einstein, A., 1905. On the movement of small particles suspended in stationary liquids required by the molecular-kinetic theory of heat. *Annalen der Physik*, *17*, pp.549-560.

El Badawy, A.M., Scheckel, K.G., Suidan, M. and Tolaymat, T., 2012. The impact of stabilization mechanism on the aggregation kinetics of silver nanoparticles. *Science of the total environment*, *429*, pp.325-331.

Elimelech, M., Jia, X., Gregory, J., & Williams, R., 1998. Particle deposition & aggregation: measurement, modelling and simulation. Butterworth-Heinemann., Woburn, MA.

Filipe, V., Hawe, A. and Jiskoot, W., 2010. Critical evaluation of Nanoparticle Tracking Analysis (NTA) by NanoSight for the measurement of nanoparticles and protein aggregates. *Pharmaceutical research*, *27*(5), pp.796-810.

Foss Hansen, S., Larsen, B.H., Olsen, S.I. and Baun, A., 2007. Categorization framework to aid hazard identification of nanomaterials. *Nanotoxicology*, *1*(3), pp.243-250.

Frens, G. and Overbeek, J.T.G., 1972. Repeptization and the theory of electrocratic colloids. *Journal of Colloid and Interface Science*, *38*(2), pp.376-387.

Fuchs, V.N., 1934. Über die stabilität und aufladung der aerosole. *Zeitschrift für Physik* 89(11-12), 736-743.

Furman, O., Usenko, S. and Lau, B.L., 2013. Relative importance of the humic and fulvic fractions of natural organic matter in the aggregation and deposition of silver nanoparticles. *Environmental science & technology*, *47*(3), pp.1349-1356.

Garza-Licudine, E., Deo, D., Yu, S., Uz-Zaman, A. and Dunbar, W.B., 2010, August. Portable nanoparticle quantization using a resizable nanopore instrument-The IZON qNano™. In *Engineering in Medicine and Biology Society (EMBC), 2010 Annual International Conference of the IEEE* (pp. 5736-5739).

Goldman, A.J., Cox, R.G. and Brenner, H., 1966. The slow motion of two identical arbitrarily oriented spheres through a viscous fluid. *Chemical Engineering Science*, *21*(12), pp.1151-1170.

Grasso, D., Subramaniam, K., Butkus, M., Strevett, K. and Bergendahl, J., 2002. A review of non-DLVO interactions in environmental colloidal systems. *Reviews in Environmental Science and Biotechnology*, *1*(1), pp.17-38.

Gregory, J., 1973. Rates of flocculation of latex particles by cationic polymers. *Journal of Colloid and Interface Science*, *42*(2), pp.448-456.

Gregory, J., 1975. Interaction of unequal double layers at constant charge. *Journal of Colloid and Interface Science*, *51*(1), pp.44-51.

Gregory, J., 1981. Approximate expressions for retarded van der Waals interaction. *Journal of Colloid and Interface Science*, *83*(1), pp.138-145.

Hamaker, H.C., 1937. The London—van der Waals attraction between spherical particles. *physica*, *4*(10), pp.1058-1072.

Han, M., & Lawler, D. F., 1991. Interactions of two settling spheres: Settling rates and collision efficiency. *Journal of Hydraulic Engineering*, 117(10), 1269-1289.

Han, M., & Lawler, D. F., 1992. The (relative) insignificance of G in flocculation. *Journal of American Water Works Association*, 79-91.

Han, M., 1989. Mathematical modeling of heterogeneous flocculent sedimentation (Doctoral dissertation, University of Texas at Austin).

Hendricks, D. W., 2006. Water treatment unit processes: physical and chemical. CRC press., Boca Raton, FL.

Hettler, E.N., Gulliver, J.S. and Kayhanian, M., 2011. An elutriation device to measure particle settling velocity in urban runoff. *Science of the Total Environment*, *409*(24), pp.5444-5453.

Hogg, R.T.W.D.W., Healy, T.W. and Fuerstenau, D.W., 1966. Mutual coagulation of colloidal dispersions. *Transactions of the Faraday Society*, *62*, pp.1638-1651.

Huynh, K.A. and Chen, K.L., 2011. Aggregation kinetics of citrate and polyvinylpyrrolidone coated silver nanoparticles in monovalent and divalent electrolyte solutions. *Environmental science & technology*, *45*(13), p.5564.

Israelachvili, J.N., 2011. *Intermolecular and surface forces*. Academic press: Waltham, MA.

Jeffery, G.B., 1915. On the steady rotation of a solid of revolution in a viscous fluid. *Proceedings of the London Mathematical Society*, *2*(1), pp.327-338.

Jeffrey, D., 1982. Low-Reynolds-number flow between converging spheres. *Mathematika*, 29(1), 58-66. doi:10.1112/S002557930001216X

Jeffrey, D.J. and Onishi, Y., 1984. Calculation of the resistance and mobility functions for two unequal rigid spheres in low-Reynolds-number flow. *Journal of Fluid Mechanics*, *139*, pp.261-290.

Kim, B., Park, C.S., Murayama, M. and Hochella Jr, M.F., 2010. Discovery and characterization of silver sulfide nanoparticles in final sewage sludge products. *Environmental science & technology*, 44(19), pp.7509-7514.

Kim, I., 2014. Transport and Retention of Silver Nanoparticles in Granular Media Filtration (Doctoral dissertation, University of Texas at Austin).

Kim, J., Nason, J.A. and Lawler, D.F., 2006. Zeta potential distributions in particle treatment processes. *Journal of Water Supply: Research and Technology-Aqua*, *55*(7-8), pp.461-470.

Kim, J., Nason, J.A. and Lawler, D.F., 2008. Influence of surface charge distributions and particle size distributions on particle attachment in granular media filtration. *Environmental science & technology*, *42*(7), pp.2557-2562.

Kim, J.K. and Lawler, D.F., 2005. Characteristics of zeta potential distribution in silica particles. *Bulletin of the Korean Chemical Society*, *26*(7), pp.1083-1089.

Kim, J.Y. and Yoon, B.J., 2002. Electrophoretic motion of a slightly deformed sphere with a nonuniform zeta potential distribution. *Journal of colloid and interface science*, *251*(2), pp.318-330.

Kozak, D., Anderson, W., Vogel, R., Chen, S., Antaw, F. and Trau, M., 2012. Simultaneous size and ζ-potential measurements of individual nanoparticles in dispersion using size-tunable pore sensors. *ACS nano*, *6*(8), pp.6990-6997.

Kramer, T.A. and Clark, M.M., 1999. Incorporation of aggregate breakup in the simulation of orthokinetic coagulation. *Journal of colloid and interface science*, *216*(1), pp.116-126.

Kramer, T.A. and Clark, M.M., 2000. Modeling orthokinetic coagulation in spatially varying laminar flow. *Journal of colloid and interface science*, *227*(2), pp.251-261.

Lautrup, B., 2011. *Physics of continuous matter: exotic and everyday phenomena in the macroscopic world*. CRC press.

Lawler, D. F., & Nason, J. A., 2005. Integral water treatment plant modeling: improvements for particle processes. *Environmental science & technology*, 39(17), 6337-6342.

Lawler, D. F., & Wilkes, D. R., 1984. Flocculation model testing: particle sizes in a softening plant. *Journal of American Water Works Association*, 90-97.

Lawler, D. F., O'Melia, C. R., & Tobiason, J. E., 1980. Integral water treatment plant design: particle size and plant performance. Particulates in water. *Advances in Chemistry Series*, 189, 353-388.

Lawler, D.F., Mikelonis, A.M., Kim, I., Lau, B.L. and Youn, S., 2013. Silver nanoparticle removal from drinking water: flocculation/sedimentation or filtration?. *Water Science and Technology: Water Supply*, *13*(5), pp.1181-1187.

Lawler, D.F., Youn, S., Zhu, T., Kim, I. and Lau, B.L., 2015. Comprehensive understanding of nano-sized particle separation processes using nanoparticle tracking analysis. *Water Science and Technology*, *72*(12), pp.2318-2324.

Lee, D.G., Bonner, J.S., Garton, L.S., Ernest, A.N. and Autenrieth, R.L., 2000. Modeling coagulation kinetics incorporating fractal theories: a fractal rectilinear approach. *Water Research*, *34*(7), pp.1987-2000.

Lee, D.G., Bonner, J.S., Garton, L.S., Ernest, A.N. and Autenrieth, R.L., 2002. Modeling coagulation kinetics incorporating fractal theories: comparison with observed data. *Water Research*, *36*(4), pp.1056-1066.

Levard, C., Reinsch, B.C., Michel, F.M., Oumahi, C., Lowry, G.V. and Brown Jr, G.E., 2011. Sulfidation processes of PVP-coated silver nanoparticles in aqueous solution: impact on dissolution rate. *Environmental science & technology*, 45(12), pp.5260-5266.

Li, J., 1996. Rectilinear vs. curvilinear models of flocculation: Experimental tests (Doctoral dissertation, University of Texas at Austin).

Li, W.R., Xie, X.B., Shi, Q.S., Zeng, H.Y., You-Sheng, O.Y. and Chen, Y.B., 2010. Antibacterial activity and mechanism of silver nanoparticles on Escherichia coli. *Applied microbiology and biotechnology*, *85*(4), pp.1115-1122.

Li, X., Lenhart, J.J. and Walker, H.W., 2011. Aggregation kinetics and dissolution of coated silver nanoparticles. *Langmuir*, *28*(2), pp.1095-1104.

Lifshitz, E.M., 1956. The theory of molecular attractive forces between solids. Pergamon Press: New York.

Limbach, L. K., Bereiter, R., Müller, E., Krebs, R., Gälli, R., & Stark, W. J., 2008. Removal of oxide nanoparticles in a model wastewater treatment plant: influence of agglomeration and surfactants on clearing efficiency. *Environmental science & technology*, 42(15), 5828-5833.

Lin, S. and Wiesner, M.R., 2012. Theoretical investigation on the steric interaction in colloidal deposition. *Langmuir*, *28*(43), pp.15233-15245.

Linnert, T., Mulvaney, P., Henglein, A. and Weller, H., 1990. Long-lived nonmetallic silver clusters in aqueous solution: preparation and photolysis. *J. Am. Chem. Soc*, *112*(12), pp.4657-4664.

Liu, J. and Hurt, R.H., 2010. Ion release kinetics and particle persistence in aqueous nano-silver colloids. *Environmental science & technology*, 44(6), pp.2169-2175.

Liu, X., Wazne, M., Chou, T., Xiao, R. and Xu, S., 2011. Influence of Ca 2+ and Suwannee River Humic Acid on aggregation of silicon nanoparticles in aqueous media. *Water research*, 45(1), pp.105-112.

Majumdar, S.R., 1967. Slow motion of an incompressible viscous liquid generated by the rotation of two spheres in contact. *Mathematika*, *14*(1), pp.43-46.

Malloy, A. and Carr, B., 2006. Nanoparticle tracking analysis–the Halo™ system. *Particle & Particle Systems Characterization*, *23*(2), pp.197-204.

Mikelonis, A.M., Youn, S. and Lawler, D.F., 2016. DLVO approximation methods for predicting the attachment of silver nanoparticles to ceramic membranes. *Langmuir*, *32*(7), pp.1723-1731.

Morel, F.M. and Hering, J.G., 1993. *Principles and applications of aquatic chemistry*. John Wiley & Sons.

Nason, J. A., 2006. Particle aspects of precipitative softening: Experimental measurement and mathematical modeling of simultaneous precipitation and flocculation (Doctoral dissertation, University of Texas at Austin).

208

Nason, J.A., McDowell, S.A. and Callahan, T.W., 2012. Effects of natural organic matter type and concentration on the aggregation of citrate-stabilized gold nanoparticles. *Journal of Environmental Monitoring*, *14*(7), pp.1885-1892.

Nir, A. and Acrivos, A., 1973. On the creeping motion of two arbitrary-sized touching spheres in a linear shear field. *Journal of Fluid Mechanics*, 59(02), pp.209-223.

O'Brien, N. and Cummins, E., 2010. Nano-scale pollutants: fate in Irish surface and drinking water regulatory systems. *Human and Ecological Risk Assessment*, *16*(4), pp.847-872.

O'Melia, C. R., 1978 Coagulation in wastewater treatment. In the scientific basis of flocculation; Springer Netherlands, pp 219-268.

O'melia, C.R., Becker, W.C. and Au, K.K., 1999. Removal of humic substances by coagulation. *Water Science and Technology*, *40*(9), pp.47-54.

O'Melia, C. R., & Stumm, W., 1967. Theory of water filtration. *Journal of American Water Works Association*, 1393-1412.

O'Neill, M.E. and Majumdar, R., 1970. Asymmetrical slow viscous fluid motions caused by the translation or rotation of two spheres. Part I: The determination of exact solutions for any values of the ratio of radii and separation parameters. *Zeitschrift für angewandte Mathematik und Physik ZAMP*, *21*(2), pp.164-179.

O'Neill, M.E., 1969, March. On asymmetrical slow viscous flows caused by the motion of two equal spheres almost in contact. In *Mathematical Proceedings of the Cambridge Philosophical Society* (Vol. 65, No. 02, pp. 543-556). Cambridge University Press.

Overbeek, J.T.G. and Verwey, E.J.W., 1948. Theory of the Stability of Lyophobic Colloids: The interaction of Sol Particles Having an Electric Double Layer.

Pecora, R. ed., 2013. *Dynamic light scattering: applications of photon correlation spectroscopy*. Springer Science & Business Media.

Reijnders, L., 2006. Cleaner nanotechnology and hazard reduction of manufactured nanoparticles. *Journal of Cleaner Production*, 14(2), 124-133.

Roalson, S.R., Kweon, J., Lawler, D.F. and SPEITEL, G.E., 2003. Enhanced softening: effects of lime dose and chemical additions. *Journal of American Water Works Association*, *95*(11), pp.97-109.

Sharp, E.L., Jarvis, P., Parsons, S.A. and Jefferson, B., 2006. Impact of fractional character on the coagulation of NOM. *Colloids and Surfaces A: Physicochemical and Engineering Aspects*, *286*(1), pp.104-111.

Siddiqui, M.S., Amy, G.L. and Murphy, B.D., 1997. Ozone enhanced removal of natural organic matter from drinking water sources. *Water Research*, *31*(12), pp.3098-3106.

Smoluchowski, M., 1917 Versuch Einer Mathematischen Theorie der Koagulations-Kinetic Kolloider Losungen. Z. *Physik Chem*., 92, 129.

Song, J.E., Phenrat, T., Marinakos, S., Xiao, Y., Liu, J., Wiesner, M.R., Tilton, R.D. and Lowry, G.V., 2011. Hydrophobic interactions increase attachment of gum arabic- and PVP-coated Ag nanoparticles to hydrophobic surfaces. *Environmental science & technology*, *45*(14), pp.5988-5995.

Spielman, L.A., 1970. Viscous interactions in Brownian coagulation. *Journal of Colloid and Interface Science*, *33*(4), pp.562-571.

Stankus, D.P., Lohse, S.E., Hutchison, J.E. and Nason, J.A., 2010. Interactions between natural organic matter and gold nanoparticles stabilized with different organic capping agents. *Environmental science & technology*, *45*(8), pp.3238-3244.

Stimson, M. and Jeffery, G.B., 1926. The motion of two spheres in a viscous fluid. *Proceedings of the Royal Society of London. Series A, Containing Papers of a Mathematical and Physical Character*, 111(757), pp.110-116.

Stoller, M., 2009. On the effect of flocculation as pretreatment process and particle size distribution for membrane fouling reduction. *Desalination*, 240(1-3), pp.209-217.

Stumm, W., & O'Melia, C. R., 1968. Stoichiometry of coagulation. *Journal of American Water Works Association*, 514-539.

Stumm, W., Morgan, J.J., 1996. Chemical equilibria and rates in natural waters. In *Aquatic chemistry*. John Wiley & Sons: New York, pp.1022.

Tandon, P. and Diamond, S.L., 1997. Hydrodynamic effects and receptor interactions of platelets and their aggregates in linear shear flow. *Biophysical journal*, *73*(5), pp.2819-2835.

Thill, A., Moustier, S., Aziz, J., Wiesner, M.R. and Bottero, J.Y., 2001. Flocs restructuring during aggregation: experimental evidence and numerical simulation. *Journal of Colloid and Interface Science*, *243*(1), pp.171-182.

Thio, B.J.R., Montes, M.O., Mahmoud, M.A., Lee, D.W., Zhou, D. and Keller, A.A., 2011. Mobility of capped silver nanoparticles under environmentally relevant conditions. *Environmental science & technology*, *46*(13), pp.6985-6991.

Tiehm, A., Herwig, V. and Neis, U., 1999. Particle size analysis for improved sedimentation and filtration in waste water treatment. *Water science and technology*, 39(8), pp.99-106.

Tolaymat, T.M., El Badawy, A.M., Genaidy, A., Scheckel, K.G., Luxton, T.P. and Suidan, M., 2010. An evidence-based environmental perspective of manufactured silver nanoparticle in syntheses and applications: a systematic review and critical appraisal of peer-reviewed scientific papers. *Science of the Total Environment*, *408*(5), pp.999-1006.

Usui, S., 1973. Interaction of electrical double layers at constant surface charge. *Journal of Colloid and Interface Science*, *44*(1), pp.107-113.

Van de Ven, T.G. Colloidal hydrodynamics. Academic Press: San Diego, CA, 1989

Van de Ven, T.G.M. and Mason, S.G., 1976a. The microrheology of colloidal dispersions: IV. Pairs of interacting spheres in shear flow. *Journal of Colloid and Interface Science*, *57*(3), pp.505-516.

Van de Ven, T.G.M. and Mason, S.G., 1976b. The microrheology of colloidal dispersions: V. Primary and secondary doublets of spheres in shear flow. *Journal of Colloid and Interface Science*, *57*(3), pp.517-534.

Van Oss, C.J., Giese, R.F. and Costanzo, P.M., 1990. DLVO and non-DLVO interactions in hectorite. *Clays Clay Miner*, *38*(2), pp.151-159.

Voorhees, P.W., 1985. The theory of Ostwald ripening. *Journal of Statistical Physics*, *38*(1), pp.231-252.

Wiesner, M.R., Lowry, G.V., Alvarez, P., Dionysiou, D. and Biswas, P., 2006. Assessing the risks of manufactured nanomaterials. *Environ. Sci. Technol*, *40*(14), pp.4336-4345.

Yotsumoto, H. and Yoon, R.H., 1993. Application of extended DLVO theory: I. Stability of rutile suspensions. *Journal of Colloid and Interface Science*, *157*(2), pp.426-433.

Zhang, H., Smith, J.A. and Oyanedel-Craver, V., 2012. The effect of natural water conditions on the anti-bacterial performance and stability of silver nanoparticles capped with different polymers. *Water research*, *46*(3), pp.691-699.

Zhang, Y., Chen, Y., Westerhoff, P., Hristovski, K., & Crittenden, J. C., 2008. Stability of commercial metal oxide nanoparticles in water. *Water research*, 42(8), 2204-2212.

Zhang, Z., Yang, X., Shen, M., Yin, Y. and Liu, J., 2015. Sunlight-driven reduction of silver ion to silver nanoparticle by organic matter mitigates the acute toxicity of silver to Daphnia magna. *Journal of Environmental Sciences*, 35, pp.62-68.

Zularisam, A.W., Ismail, A.F. and Salim, R., 2006. Behaviours of natural organic matter in membrane filtration for surface water treatment—a review. *Desalination*, *194*(1-3), pp.211-231.

Vita

Sungmin Youn was born and raised in Seoul, South Korea. After graduating from Cheongwon High School, Sungmin attended Calvin College in Grand Rapids, Michigan where he earned a B.S. in Engineering. Upon graduating, Sungmin began the graduate program in the Department of Civil, Architectural and Environmental Engineering at the University of Texas at Austin. Sungmin obtained a M.S.E in 2013 and continued his studies for a Ph.D. under the supervision of Dr. Desmond F. Lawler.

Permanent email: youn.sungmin@gmail.com

This dissertation was typed by Sungmin Youn.